Vol. 274 No. 1, March 1, 1993 ISSN 0003-2670

ANALYTICA CHIMICA ACTA

An international journal devoted to all branches of analytical chemistry

ELSEVIER

ANALYTICA CHIMICA ACTA

Scope. *Analytica Chimica Acta* publishes original papers, preliminary communications and reviews dealing with every aspect of modern analytical chemistry. Reviews are normally written by invitation of the editors, who welcome suggestions for subjects. Preliminary communications of important urgent work can be printed within four months of submission, if the authors are prepared to forego proofs.

Submission of Papers

Americas

Prof. Harry L. Pardue
Department of Chemistry
1393 BRWN Bldg, Purdue University
West Lafayette, IN 47907-1393
USA
Tel:(+1-317) 494 5320
Fax:(+1-317) 496 1200

Computer Techniques

Prof. J.T. Clerc
Universität Bern
Pharmazeutisches Institut
Baltzerstrasse 5, CH-3012 Bern
Switzerland
Tel:(+41-31) 654171
Fax:(+41-31) 654198

Other Papers

Prof. Alan Townshend
Department of Chemistry
The University
Hull HU6 7RX
Great Britain

Tel:(+44-482) 465027
Fax:(+44-482) 466410

Prof. Willem E. van der Linden
Laboratory for Chemical Analysis
Department of Chemical Technology
Twente University of Technology
P.O. Box 217, 7500 AE Enschede
The Netherlands
Tel:(+31-53) 892629
Fax:(+31-53) 356024

Prof. Paul Worsfold
Dept. of Environmental Sciences
University of Plymouth
Plymouth PL4 8AA
Great Britain

Tel:(+44-752) 233006
Fax:(+44-752) 233009

Submission of an article is understood to imply that the article is original and unpublished and is not being considered for publication elsewhere. *Anal. Chim. Acta* accepts papers in English only. There are no page charges. Manuscripts should conform in layout and style to the papers published in this issue. See inside back cover for "Information for Authors".

Publication. *Analytica Chimica Acta* appears in 14 volumes in 1993. The subscription price for 1993 (Vols. 267–280) is Dfl. 4214.00 plus Dfl. 462.00 (p.p.h.) (total approx. US$ 2672.00). *Vibrational Spectroscopy* appears in 2 volumes in 1993. The subscription price for *Vibrational Spectroscopy* (Vols. 4 and 5) is Dfl. 700.00 plus Dfl. 66.00 (p.p.h.) (total approx. US$ 437.75). The price of a combined subscription (*Anal. Chim. Acta* and *Vib. Spectrosc.*) is Dfl. 4592.00 plus Dfl. 528.00 (p.p.h.) (total approx. US$ 2925.75). All earlier volumes (Vols. 1–266) except Vols. 23 and 28 are available at Dfl. 259.50 (US$ 148.25), plus Dfl. 18.00 (US$ 10.25) p.p.h., per volume. The Dutch guilder price is definitive. The U.S. dollar price is subject to exchange-rate fluctuations and is given only as a guide. Subscriptions are accepted on a prepaid basis only, unless different terms have been previously agreed upon.
Our p.p.h. (postage, packing and handling) charge includes surface delivery of all issues, except to subscribers in the U.S.A., Canada, Australia, New Zealand, China, India, Israel, South Africa, Malaysia, Thailand, Singapore, South Korea, Taiwan, Pakistan, Hong Kong, Brazil, Argentina and Mexico, who receive all issues by air delivery (S.A.L.–Surface Air Lifted) at no extra cost. For Japan, air delivery requires 25% additional charge of the normal postage and handling charge; for all other countries airmail and S.A.L. charges are available upon request.

Subscription orders. Subscription orders can be entered only by calendar year and should be sent to: Elsevier Science Publishers B.V., Journals Department, P.O. Box 211, 1000 AE Amsterdam, The Netherlands. Tel: (+31-20) 5803 642, Telex: 18582, Telefax: (+31-20) 5803598, to which requests for sample copies can also be sent. Claims for issues not received should be made within six months of publication of the issues. If not they cannot be honoured free of charge. Readers in the U.S.A. and Canada can contact the following address: Elsevier Science Publishing Co. Inc., Journal Information Center, 655 Avenue of the Americas, New York, NY 10010, U.S.A. Tel: (+1-212) 6333750, Telefax: (+1-212) 6333990, for further information, or a free sample copy of this or any other Elsevier Science Publishers journal.
Advertisements. Advertisement rates are available from the publisher on request.

Detailed "Instructions to Authors" for *Analytica Chimica Acta* was published in Volume 256, No. 2, pp. 373–376. Free reprints of the "Instructions to Authors" of *Analytica Chimica Acta* and *Vibrational Spectroscopy* are available from the Editors or from: Elsevier Science Publishers B.V., P.O. Box 330, 1000 AH Amsterdam, The Netherlands. Telefax: (+31-20) 5862845.

US mailing notice – Analytica Chimica Acta (ISSN 0003-2670) is published biweekly by Elsevier Science Publishers (Molenwerf 1, Postbus 211, 1000 AE Amsterdam). Annual subscription price in the USA US$ 2672.00 (subject to change), including air speed delivery. Second class postage paid at Jamaica, NY 11431. *USA Postmasters*: Send address changes to Anal. Chim. Acta, Publications Expediting, Inc., 200 Meacham Av., Elmont, NY 11003. Airfreight and mailing in the USA by Publication Expediting.

ANALYTICA CHIMICA ACTA

An international journal devoted to all branches of analytical chemistry

(Full texts are incorporated in CJELSEVIER, a file in the Chemical Journals Online database available on STN International; Abstracted, indexed in: Aluminum Abstracts; Anal. Abstr.; Biol. Abstr.; BIOSIS; Chem. Abstr.; Curr. Contents Phys. Chem. Earth Sci.; Engineered Materials Abstracts; Excerpta Medica; Index Med.; Life Sci.; Mass Spectrom. Bull.; Material Business Alerts; Metals Abstracts; Sci. Citation Index)

VOL. 274 NO. 1 CONTENTS MARCH 1, 1993

Electroanalytical Chemistry and Sensors

Screen-printed electrodes for stripping measurements of trace mercury
J. Wang and B. Tian (Las Cruces, NM, USA) 1
Modelling of coulometric sensor–actuator systems based on ISFETs with a porous actuator covering the gate
J. Luo, W. Olthuis, P. Bergveld, M. Bos and W.E. Van der Linden (Enschede, Netherlands) 7
Crayfish walking leg neuronal biosensor for the detection of pyrazinamide and selected local anesthetics
D. Leech and G.A. Rechnitz (Honolulu, HI, USA) 25
Potentiometric ion- and bioselective electrodes based on asymmetric polyurethane membranes
D. Liu, M.E. Meyerhoff, H.D. Goldberg and R.B. Brown (Ann Arbor, MI, USA) 37
Multiple-indicator fiber-optic sensor for high-resolution pCO_2 sea water measurements
D.R. Walt, G. Gabor (Medford, MA, USA) and C. Goyet (Woods Hole, MA, USA) 47
L-Lactate oxidase electrode based on methylene green and carbon paste
J. Kulys, L. Wang and A. Maksimoviene (Vilnius, Lithuania) 53
Determination of methamphetamine in urine in situ using a methamphetamine-sensitive membrane electrode
K. Watanabe, K. Okada and T. Katsu (Okayama, Japan) 59
Adsorption voltammetry of the gallium–morin system
L. Qu and W. Jin (Shandong, China) 65

Chemometrics

Evaluation and correction of signal model errors in a matched filter for the quantification of chromatographic data
B. Van den Bogaert, H.F.M. Boelens and H.C. Smit (Amsterdam, Netherlands) 71
Quantification of chromatographic data using a matched filter: robustness towards noise model errors
B. Van den Bogaert, H.F.M. Boelens and H.C. Smit (Amsterdam, Netherlands) 87

Enzymatic Methods

Approaches to the development of spectrophotometric reaction-rate methods by use of immobilized enzymes in continuous-flow systems
J.M. Fernández-Romero, M.D. Luque de Castro and M. Valcárcel (Córdoba, Spain) 99
Enzymatic determination of alcohol mixtures at the nanogram level by the stopped-flow technique
E. Förster (Freiberg, Germany), M. Silva (Córdoba, Spain), M. Otto (Freiberg, Germany) and D. Pérez-Bendito (Córdoba, Spain) 109

Flow-Injection Analysis

Flow-injection analysis for the measurement of penicillin V in fermentation media
M. Carlsen, L.H. Christensen and J. Nielsen (Lyngby, Denmark) 117
Segmental flow injection with ion-selective electrodes for the determination of fluoride in water
J.A. Borzitsky, A.V. Dvinin (Sillamae, Estonia), O.M. Petrukhin and Yu.I. Urusov (Moscow, Russia) 125

Chromatography and other Separation Methods

Solid-phase extraction procedure for the determination of selenium by capillary gas chromatography
K. Johansson, U. Örnemark and Å. Olin (Uppsala, Sweden) 129

(Continued overleaf)

Contents (continued)

Liquid–liquid extraction of transition metal ions with macrocyclic Schiff bases containing phenol or thiophene subunits
S. Abe, T. Sone, K. Fujii and M. Endo (Yonezawa, Japan) 141
Linear solvation energy relationships in reversed-phase liquid chromatography. Prediction of retention from a single solvent and a single solute parameter
M. Rosés and E. Bosch (Barcelona, Spain) 147
Simultaneous determination of trace metals in human hair by dynamic ion-exchange chromatography
A. Sturaro, G. Parvoli, L. Doretti, S. Zanchetta, G. Allegri and G. Battiston (Padova, Italy) 163

Gas Analysis

Effect of relative humidity on the performance of a platinum–lead denuder for the adsorption of nitrobenzene
C.L.P. Thomas and J.F. Alder (Manchester, UK) 171
Precision humidifier for dynamic test atmosphere generators
C.L.P. Thomas, J.F. Alder, P.R. Fielden, A.R.M. Przybylko, R.D. Snook and A.F.R. Watson (Manchester, UK) 179

ANALYTICA CHIMICA ACTA
VOL. 274 (1993)

ANALYTICA CHIMICA ACTA

An international journal devoted to all branches of analytical chemistry
Revue internationale consacrée à tous les domaines de la chimie analytique
Internationale Zeitschrift für alle Gebiete der analytischen Chemie

---

Anal. Chim. Acta, Vol. 274 (1993)

ELSEVIER, Amsterdam–London–New York–Tokyo

© 1993 ELSEVIER SCIENCE PUBLISHERS B.V. ALL RIGHTS RESERVED

0003-2670/93/$06.00

No part of this publication may be reproduced, stored in a retrieval system or transmitted in any form or by any means, electronic, mechanical, photocopying, recording or otherwise, without the prior written permission of the publisher, Elsevier Science Publishers B.V., Copyright and Permissions Dept., P.O. Box 521, 1000 AM Amsterdam, The Netherlands.

Upon acceptance of an article by the journal, the author(s) will be asked to transfer copyright of the article to the publisher. The transfer will ensure the widest possible dissemination of information.

Special regulations for readers in the U.S.A.–This journal has been registered with the Copyright Clearance Center, Inc. Consent is given for copying of articles for personal or internal use, or for the personal use of specific clients. This consent is given on the condition that the copier pays through the Center the per-copy fee for copying beyond that permitted by Sections 107 or 108 of the U.S. Copyright Law. The per-copy fee is stated in the code-line at the bottom of the first page of each article. The appropriate fee, together with a copy of the first page of the article, should be forwarded to the Copyright Clearance Center, Inc., 27 Congress Street, Salem, MA 01970, U.S.A. If no code-line appears, broad consent to copy has not been given and permission to copy must be obtained directly from the author(s). All articles published prior to 1980 may be copied for a per-copy fee of US $2.25, also payable through the Center. This consent does not extend to other kinds of copying, such as for general distribution, resale, advertising and promotion purposes, or for creating new collective works. Special written permission must be obtained from the publisher for such copying.

No responsibility is assumed by the publisher for any injury and/or damage to persons or property as a matter of products liability, negligence or otherwise, or from any use or operation of any methods, products, instructions or ideas contained in the material herein.

Although all advertising material is expected to conform to ethical (medical) standards, inclusion in this publication does not constitute a guarantee or endorsement of the quality or value of such product or of the claims made of it by its manufacturer.

This issue is printed on acid-free paper.

PRINTED IN THE NETHERLANDS

Analytica Chimica Acta, 274 (1993) 1–6
Elsevier Science Publishers B.V., Amsterdam

Screen-printed electrodes for stripping measurements of trace mercury

Joseph Wang and Baomin Tian

Department of Chemistry, New Mexico State University, Las Cruces, NM 88003 (USA)

(Received 12th October 1992)

Abstract

Screen-printed carbon-strip electrodes, coated with a thin gold film, are used for highly sensitive potentiometric stripping measurements of trace levels of mercury. The stripping response toward mercury at these inexpensive and disposable electrodes compares favorably with that common at conventional gold electrodes. Various experimental variables have been optimized to yield low detection limits (e.g., 0.5 μg l^{-1} mercury for 4 min deposition) and good precision (e.g., R.S.D. of 2.5% for 20 repetitive measurements of 25 μg l^{-1} mercury). Applicability to trace measurements of alkyl mercury and selenium is also demonstrated. Such adaptation of screen-printing technology for the development of reliable sensors for trace mercury should benefit numerous field applications.

Keywords: Potentiometry; Sensors; Stripping voltammetry; Field monitor; Mercury; Trace metals

Mercury is well known as one of the most toxic metals in the environment. The reliable measurement of trace levels of mercury is thus of great significance for clinical screening, environmental monitoring and food quality tests. It is highly desired to move these measurements from the central laboratory to the field. Spectroscopic techniques, commonly used for trace measurements of mercury in the central laboratory, are not suitable for the task of on-site assays. In contrast, the portable nature and remarkable sensitivity of electrochemical stripping techniques [1] are very attractive for field monitoring of trace metals. Both stripping voltammetry [2–4] and potentiometry [5] have been used successfully in central laboratories for measuring low levels of mercury. The adaptation of these stripping procedures to on-site and single-use measurements of mercury is thus a logical extension of their scope.

In this paper we describe the performance of disposable screen-printed electrodes for on-site quantitation of low mercury levels. Stripping measurements of trace mercury in central laboratories have been traditionally carried out at various carbon [2,3] and gold [4–6] disk electrodes. Best performance has been achieved with rotating gold disk [3] and twin gold disk [6] electrodes. On-site (and particularly "one-shot") applications require the development of significantly cheaper, simpler and mass-produced electrodes for mercury. Screen-printing technology represents a simple approach for mass production of disposable electrodes [7]. The resulting screen-printed sensors have been widely used for clinical (enzymatic) testing of various biomolecules [8] and hold great promise for field monitoring of trace metals. We have recently demonstrated that mercury-coated screen-printed carbon-strip electrodes offer reliable quantitation of trace lead, as desired for decentralized lead blood testings [9]. Similarly, in the following sections we will

Correspondence to: J. Wang, Department of Chemistry, New Mexico State University, Las Cruces, NM 88003 (USA).

demonstrate that low-cost gold-coated screen-printed carbon electrodes (on an inert plastic support) can be used for convenient measurements of $\mu g\ l^{-1}$ levels of mercury, without compromising the attractive stripping behavior inherent to significantly more expensive gold electrodes.

EXPERIMENTAL

Apparatus

A TraceLab potentiometric stripping unit (PAU 20, Radiometer), with a SAM sample station (Radiometer) and an IBM Personal System/2 55 SX were used to obtain the stripping potentiograms. Square-wave stripping voltammetry was performed with a BAS-100A electrochemical analyzer [Bioanalytical Systems (BAS)]. Most potentiometric stripping experiments were carried out in 20-ml cells, while stripping voltammetric experiments employed 10-ml cells. The electrodes joined these cells through a hole in the cover.

The screen-printed electrodes (ExacTech blood glucose strips, Medisense) were purchased from a local drugstore. These strips consist of the working and reference electrodes printed on a PVC substrate (with carbon contacts on the opposite side). The gold film was plated on the carbon-strip contact (because of the coverage of the original working electrode with the enzyme/mediator layer). Most experiments employed the conventional Ag/AgCl reference electrode and the platinum wire auxiliary electrode of the TraceLab or the BAS-100 units. Some experiments involved a two-electrode system and 100-μl sample drops. In these experiments the printed Ag/AgCl layer, on the other side of the strip, served as reference electrode. For this purpose, the strip was cut in the center, to allow placing of the carbon-contact working electrode in close proximity to the printed reference electrode (on a microscope slide).

Reagents

All solutions were prepared with doubly distilled water. The mercury, selenium and gold atomic absorption standard solutions (1000 mg l^{-1}) and dimethylmercury were purchased from Aldrich. Human albumin was obtained from Sigma. The supporting electrolyte was a 0.05 M HCl solution.

Procedure

Potentiometric stripping analysis (PSA) was carried out in the following manner. The gold film was preplated from a non-deaerated and stirred 50 mg l^{-1} gold solution (in 0.05 M HCl) by holding the carbon strip at −0.40 V for 20 min. The electrode potential was then switched to +0.75 V and was held there for a 2-min "cleaning" period. Mercury measurements were subsequently performed by imposing the deposition potential (−0.10 V) for a short (1–4 min) period while stirring the solution. The stripping was then initiated by applying a constant current of +2.0 μA; the electrode was conditioned for 15 s at +0.75 V before the next deposition–stripping cycle. Analogous stripping voltammograms were obtained after a 4-min deposition (at −0.10 V), and a 10-s equilibration, using a rapid square-wave scan to +0.9 V.

RESULTS AND DISCUSSION

Figure 1 displays stripping potentiograms, obtained under identical conditions, at the gold-coated glassy carbon (A) and carbon-strip (B) electrodes for mercury solutions of increasing concentration (10–50 $\mu g\ l^{-1}$, a–e). Despite the very low concentration and short (2 min) deposition period, the screen-printed electrode exhibits well-defined and sharp peaks ($E_p = +0.53$ V, $b_{1/2} = 63$ mV). Hence, a convenient quantitation of $\mu g\ l^{-1}$ concentrations is possible. Comparison to the traditional glassy-carbon-based electrode indicates that the analytical performance is not compromised by the use of the significantly cheaper screen-printed surface.

The effect of various experimental variables upon the stripping response of the gold-coated screen-printed electrode was explored. Figure 2 shows stripping potentiograms for 25 $\mu g\ l^{-1}$ mercury after different preconcentration periods (0–5 min, a–f). The well-defined peak increases linearly with increasing preconcentration time, re-

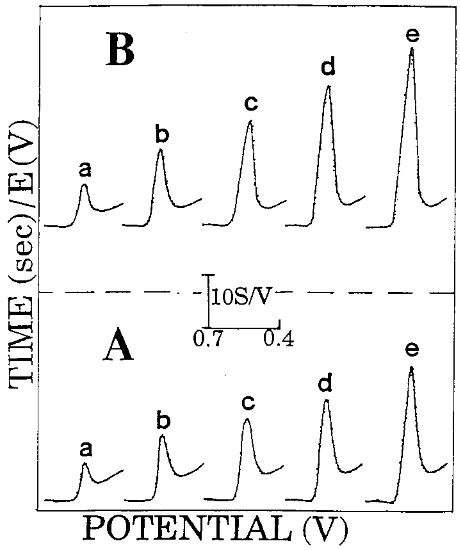

Fig. 1. Stripping potentiograms obtained at the gold-coated glassy carbon disk (A) and carbon-strip (B) electrodes, for increasing mercury concentration in 10 μg l^{-1} steps (a–e). Preconcentration for 2 min at −0.10 V, from a stirred, non-deaerated solution. Constant stripping current, +2 μA; electrolyte, 0.05 M HCl.

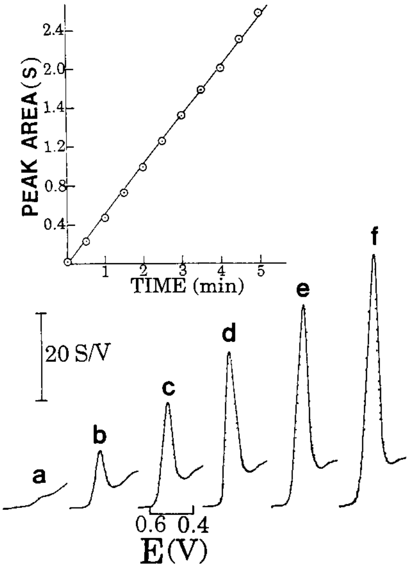

Fig. 2. Potentiometric stripping response to 25 μg l^{-1} mercury after different preconcentration times: (a) 0, (b) 1, (c) 2, (d) 3, (e) 4, and (f) 5 min. Other conditions as in Fig. 1. Also shown (as inset) is the resulting plot of peak area vs. time.

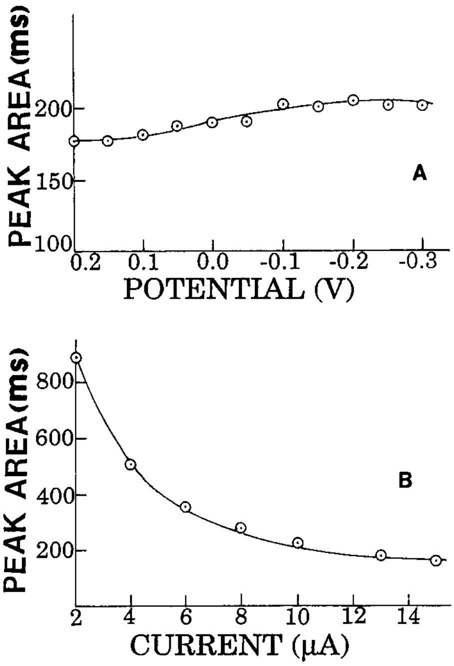

Fig. 3. Effect of deposition potential (A) and stripping current (B) upon the stripping response to 25 μg l^{-1} mercury. Preconcentration time, 2 min; stripping current (A), +10 μA. Other conditions as in Fig. 1.

flecting the enhancement of the mercury concentration in the gold film. The peak sharpness is maintained upon increasing the preconcentration period. In contrast, quantitation is not possible without accumulation (a). The highly linear relationship between response and preconcentration time is indicated also by the resulting plot (shown on top).

Figure 3 shows the effect of the deposition potential (A) and stripping current (B) upon the 25 μg l^{-1} mercury peak. Only a slight increase in the response is observed upon changing the deposition potential between +0.2 V and −0.1 V. No further change in the peak area is observed at more negative potentials. The stripping current has a profound effect upon the mercury response. A nearly exponential decrease in the peak area is observed upon increasing the stripping current between 2 and 14 μA. Such profile reflects the faster oxidation (i.e., shorter stripping) at larger currents. All subsequent work employed deposition at −0.1 V, followed by stripping with a current of 2 μA.

In order for the gold-coated carbon-strip electrode to possess significant analytical utility, it must exhibit a well-defined and reproducible concentration dependence. Figure 4 shows the potentiometric stripping response for mercury over the 5–30 $\mu g\ l^{-1}$ range. Well-defined stripping peaks are observed following 4 min preconcentration. A detection limit of 0.5 $\mu g\ l^{-1}$ can be estimated based on the signal-to-noise characteristics of peak (a). [A lower detection limit of 0.10 $\mu g\ l^{-1}$ was achieved from measurements of 0.25 $\mu g\ l^{-1}$ following 15 min accumulation (not shown).] The six peaks of Fig. 4 are part of twelve concentration increments from 2.5 to 30 $\mu g\ l^{-1}$. The resulting calibration plot (also shown, top) is highly linear. A least-squares treatment of these data yielded a slope of 81 ms l μg^{-1} (standard deviation of slope = 0.45 ms l μg^{-1}; intercept = 7 ms; correlation coefficient = 0.999). Highly linear calibration plots were obtained also following a 2-min deposition (slope 35.9 ms l μg^{-1}, over the 10–100 $\mu g\ l^{-1}$ range) and using an unstirred solution (slope 3.51 ms l μg^{-1} over the 50–300 $\mu g\ l^{-1}$ range; 4 min deposition).

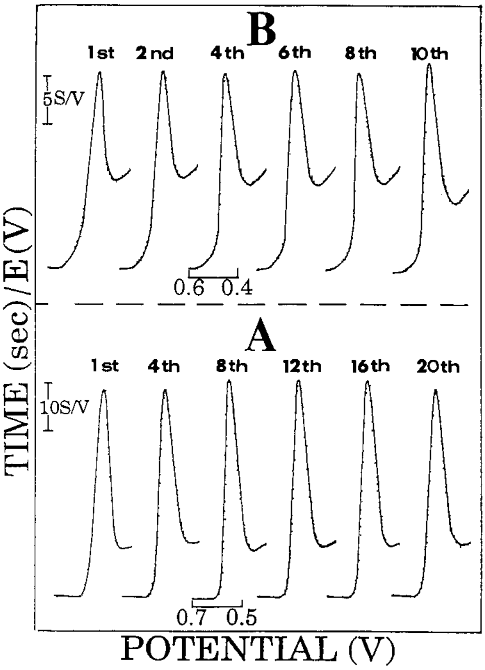

Fig. 5. Potentiograms for repetitive stripping runs in a 20-ml solution (A) and using different 100-μl sample drops (B). Mercury concentration, (A) 25 and (B) 300 $\mu g\ l^{-1}$; preconcentration time, (A) 4 and (B) 3 min. Other conditions as in Fig. 1, except that a quiescent solution was used in B.

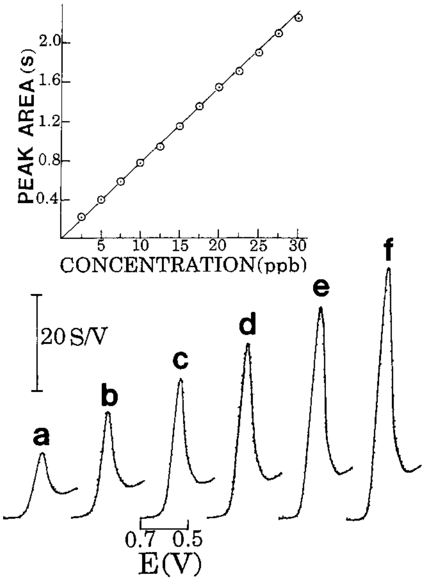

Fig. 4. Stripping potentiograms for increasing mercury concentration in 5 $\mu g\ l^{-1}$ steps (a–f). Preconcentration for 4 min. Other conditions as in Fig. 1. Also shown (top) is the resulting calibration plot over the 0–30 $\mu g\ l^{-1}$ range.

The stripping response of the gold-coated carbon-strip is also very reproducible. For example, the stripping potentiograms for 25 $\mu g\ l^{-1}$ mercury (displayed in Fig. 5A) are part of a prolonged series of 20 repetitive measurements that yielded a highly stable response (R.S.D. = 2.5%). Similarly, the 10 stripping peaks of Fig. 5B were obtained with different 100-μl samples containing 300 $\mu g\ l^{-1}$ mercury. (This was accomplished by covering the two-electrode strip with the sample drop.) An R.S.D. of 2.2% was calculated for this series.

High selectivity is another attractive feature of the screen-printed sensors for mercury. The following metal ions were tested at the 100 $\mu g\ l^{-1}$ level and found not to interfere with the measurements of 10 $\mu g\ l^{-1}$ mercury: Pb(II), Cd(II), Ni(II), Cu(II), Fe(III), Bi(III), Sb(III), Mn(II), Co(II), Cr(III), V(V), Sn(II), Se(IV), In(III), Tl(I), Ga(III), Ti(IV), Mo(VI), and Al(III) (4 min deposition). In contrast, Rh(III) and Pd(II) at 100 $\mu g\ l^{-1}$ resulted in 25% and 45% depressions, respectively, of the 10 $\mu g\ l^{-1}$ mercury peak. Additional

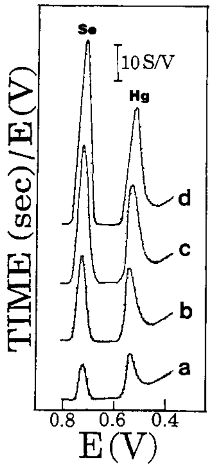

Fig. 6. Stripping potentiograms for mixtures of mercury and selenium. Mercury concentration increased in 20 μg l^{-1} steps with the selenium level in 10 μg l^{-1} steps (a–d). Deposition time, 1 min; "cleaning" at +0.85 V for 30 s. Other conditions as in Fig. 1.

peaks, observed at +0.280 V and +0.712 V in the presence of Cu(II) and Se(IV), respectively, did not affect the quantitation of mercury. Indeed, the sharp and well-defined selenium and mercury peaks permit convenient quantitation of mixtures of these metals. For example, Fig. 6 shows stripping potentiograms for mercury and selenium mixtures of increasing concentration (a–d). Surface-active organic materials have a negligible effect upon the potentiometric stripping response to mercury. For example, human albumin at 10 mg l^{-1} caused only a 4% depression of the 20 μg l^{-1} mercury peak (4 min deposition).

The screen-printed potentiometric stripping electrodes respond not only to inorganic mercury, but also to trace levels of organomercurial species. Figure 7 displays stripping potentiograms for solutions of increasing dimethylmercury concentrations (2.5–15 μg l^{-1}, a–g). The short (4 min) deposition period yielded well-defined stripping peaks, proportional to the organomercurial concentration. The slope of the resulting calibration plot (on top) is 55.6 ms l μg^{-1} (standard devia-

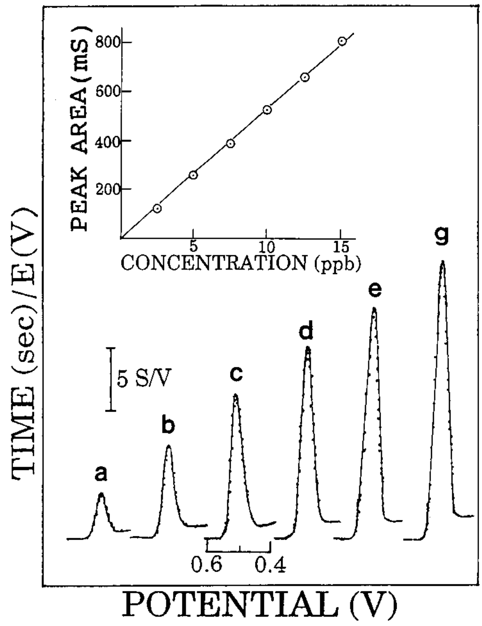

Fig. 7. Stripping potentiograms at the gold-coated carbon-strip electrode for increasing dimethylmercury in 2.5 μg l^{-1} steps (a–g). Preconcentration time, 4 min. Other conditions as in Fig. 1.

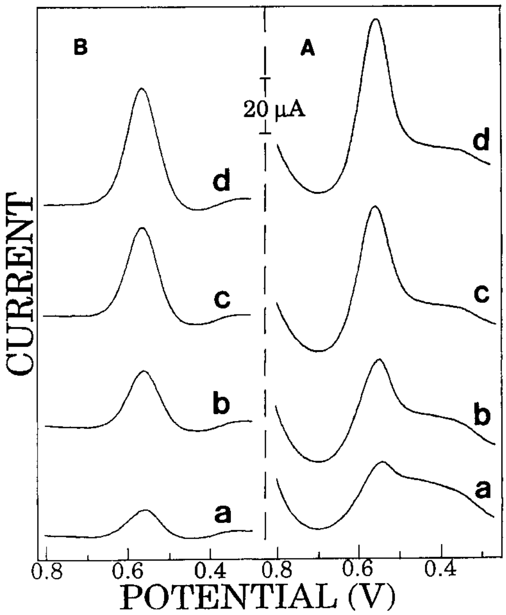

Fig. 8. Conventional (A) and subtractive (B) square-wave stripping voltammetric measurements of mercury solutions of increasing concentrations of 20–80 μg l^{-1} (a–d). The subtractive response was obtained by recording the difference in currents following 240 and 5 s depositions. Deposition time 240 s at −0.10 V; square-wave frequency, 20 Hz; amplitude, 40 mV; step, 6 mV; electrolyte, 0.05 M HCl.

tion of slope = 0.80 ms l μg^{-1}; intercept = 23 ms; correlation coefficient = 0.999). The peak potential (0.521 V) is slightly different from that observed for the inorganic mercury ion (0.528 V). When coupled with an appropriate speciation scheme (e.g., [10]), these disposable electrodes should thus be useful for classifying the chemical forms of mercury.

In addition to potentiometric stripping measurements, it is possible to use voltammetric stripping modes for mercury quantitation with screen-printed electrodes. Rapid square-wave stripping voltammetry is particularly useful for this task. Figure 8A shows stripping voltammograms for mercury solutions of increasing concentration [20–80 μg l^{-1} (a–d)] following a 240-s deposition. The defined stripping peaks are accompanied by a large background current (characteristic of the gold surface). Such background contributions are effectively compensated by employing a subtractive stripping operation, e.g., by recording the difference between the currents following 240 and 5-s depositions (Fig. 8B).

Gold films, plated in situ on the carbon-strip substrate, may offer an attractive alternative to the preplated gold films. Figure 9 compares the response to 5 μg l^{-1} mercury of the carbon-strip with the gold film preplated (A) and codeposited with the mercury (B). The in-situ deposition offers a sharper response, higher sensitivity (peak area, 541 vs. 396 ms) and a low background contribution. Preplating of the gold film may be, however, more practical and economical when mass production and screening are concerned.

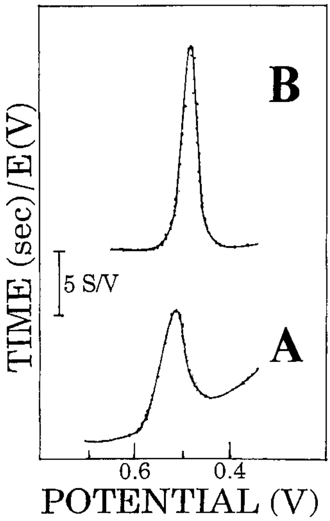

Fig. 9. Potentiometric stripping response to 5 μg l^{-1} mercury using preplated (A) and in-situ plated (B) gold films. Conditions as in Fig. 1, except that the in-situ deposition (B) proceeded in the presence of 1 mg l^{-1} Au(III).

In conclusion, the growing needs for "one-shot" field testings for trace mercury have led to the coupling of screen-printing technology and potentiometric stripping analysis. The stripping response for mercury at these disposable electrodes is comparable to that common at traditional stripping electrodes. The new mercury sensors thus hold great promise for decentralized (environmental, industrial, clinical) measurements of mercury. The highly reproducible response makes the screen-printed electrodes attractive also to routine (centralized) applications. Research in our laboratory is progressing toward the adaptation of other stripping schemes and procedures with screen-printing technology.

This work was supported by grants from the Department of Health and Human Services (Centers of Disease Control) and the IMS. The authors thank Radiometer America for the gift of the TraceLab system.

REFERENCES

1 J. Wang, Stripping Analysis, VCH, Deerfield Beach, FL, 1985.
2 S. Perone and W.J. Bretbow, Anal. Chem., 37 (1965) 968.
3 P. Kiekens, M. Martens, M. Bogaert and E. Temmerman, Analyst, 109 (1984) 909.
4 R. Andrews, L. Larochelle and D.C. Johnson, Anal. Chem., 48 (1976) 212.
5 D. Jagner and K. Aren, Anal. Chim. Acta, 141 (1982) 157.
6 L. Sipos, P. Valenta, H.W. Nürnberg and M. Branica, J. Electroanal. Chem., 77 (1977) 263.
7 S. Wring and J.P. Hart, Analyst, 117 (1992) 1281.
8 M.J. Green and P.I. Hilditch, Anal. Proc., 28 (1991) 374.
9 J. Wang and B. Tian, Anal. Chem., 64 (1992) 1706.
10 G. Bately and T.M. Florence, Anal. Lett., 9 (1976) 379.

Analytica Chimica Acta, 274 (1993) 7–23
Elsevier Science Publishers B.V., Amsterdam

Modelling of coulometric sensor–actuator systems based on ISFETs with a porous actuator covering the gate

J. Luo, W. Olthuis and P. Bergveld
Mesa Research Institute, Faculty of Electrical Engineering, University of Twente, 7500 AE Enschede (Netherlands)

M. Bos and W.E. van der Linden
Department of Chemical Technology, University of Twente, 7500 AE Enschede (Netherlands)

(Received 16th October 1992)

Abstract

The ion-selective field effect transistor (ISFET)-based coulometric sensor–actuator systems have found applications in acid–base titration and in the construction of a low-drift carbon dioxide and a pH-static enzyme sensor. In this paper a brief review is given of the previously developed ISFET-based sensor–actuator systems and the newly proposed system which employs a porous nobel metal as the actuator deposited at a short distance over the gate. The advantages and disadvantages of the different systems are compared. Furthermore, an analytical model is proposed for the new system with a porous nobel metal as the actuator. Two ways to make the porous gold actuator over the gate of the ISFET are described. The acid–base titration is chosen for the model study. The experimental results are in accordance with the theoretical description. Both the theoretical and experimental results show that devices with a different actuator thickness will behave differently. For a thin porous actuator, an approximately quadratic relationship between the titration time and the concentration of the titrated species is predicted by the model and confirmed by the experiment. For a thick porous actuator, titration of a weak acid shows an approximately linear relationship between the concentration of the titrated species and the titration time, which is predicted by the model. The theoretical calculation of the titration curve of a fully dissociated acid requires the use of a general formula derived from the model. The typical titration times are from 0.5 to 10 s, the corresponding concentrations of the titrated species range from 0.5 mM up to ca. 10 mM.

Keywords: Coulometry; Titrimetry; Acid–base; Ion-selective field effect transistor; Sensor–actuator

The ion-selective field effect transistor (ISFET)-based integrated coulometric sensor–actuator system was introduced in 1985 [1] in order to solve the problem of in situ ISFET calibration and to exploit new applications of the ISFET. Since then a series of developments has been made [2]. The reported applications of the system are typically: the acid–base titration [2,3], construction of a low-drift carbon dioxide sensor [2,4] and the introduction of the pH-static enzyme sensor [5]. Progress in the theoretical description of the system has also been achieved recently [6,7].

Generally, the integration of a coulometric actuator with an ISFET has several advantages. In the first place, it provides the ISFET with an easy and rapid way of regular in situ calibration. This is particularly useful in some specific applications such as, for instance, in vivo pH monitoring. Secondly, for an application of the system to the

Correspondence to: J. Luo, Mesa Research Institute, Faculty of Engineering, University of Twente, 7500 AE Enschede (Netherlands).

acid–base titration, drift is no longer a problem, as the ISFET is used in a dynamic way. In addition, the fast response of the ISFET makes the titration more accurate and rapid. Furthermore, a local pH control in the vicinity of the gate of the ISFET can be achieved, which can lead to new applications of the system as exploited in the pH-static enzyme sensor [5].

The different research projects have shown a promising prospect in the development of coulometric sensor–actuator systems. There are, however, still some disadvantages such as the delay in response existing in the previously developed systems. This is due to the fact that the actuator was a planar electrode closely surrounding the gate, but still at a distance of ca. 15–20 μm. In order to circumvent this problem, a newly designed system has been proposed which employs a porous noble metal as an actuator over the ISFET [8]. In this paper, we will give a brief analysis of the previously developed conventional coulometric sensor–actuator systems and the recently reported new system. The advantages and disadvantages of the different systems are discussed and compared. Afterwards, a model for the recently developed new system is presented and theoretical results are compared with the experimental results.

Closed-cell type microliter coulometric titrator

Figure 1 shows the basic components of the previously developed prototype coulometric sensor–actuator system [1]. The system is made by integrating a large noble metal actuator electrode and a counter electrode on a piece of silicon. A window in the actuator electrode is etched for the gate of the ISFET which functions as a pH indicator. A flow-through cell is constructed by sealing a silicon cover with an etched cavity on the chip. In principle, the operation of the system quite resembles the conventional coulometric titration system. For a titration the sample is first injected into the cavity, the current is then applied to the actuator electrode and the counter electrode. By coulometrically generating protons or hydroxyl ions, an acid or base titration can be performed with high accuracy. The amount of the electrical charge used for a coulometric titration is approximately linearly proportional to the concentration of the sample, because it can roughly be considered as a titration of the whole bulk solution. The main advantage of the system is the exploitation of the fast response of the ISFET as pH sensor for a rapid coulometric titration. Additionally, the system is greatly miniaturized due to the application of the silicon technology and, as a consequence, the required sample volume is sub-

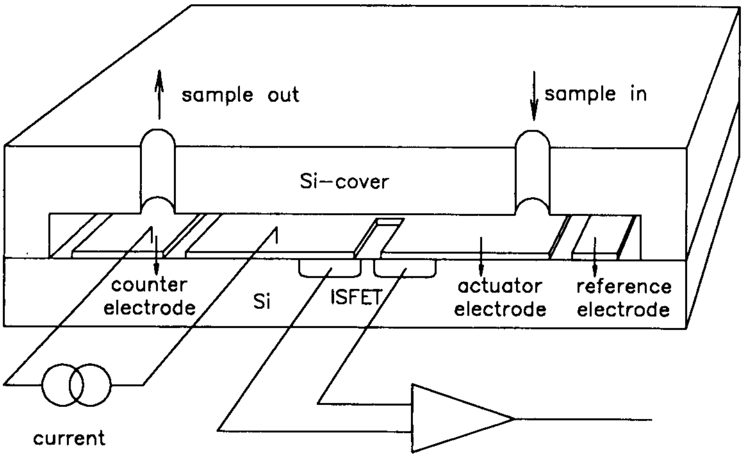

Fig. 1. Schematic representation of the previously developed closed-cell type microliter coulometric titrator.

stantially reduced. The disadvantages of the system are: an injection of the sample by a syringe or micropump is necessary, and after each titration the sample has to be flushed out. It is therefore not suitable for an in situ application.

Diffusion-controlled coulometric sensor–actuator system

In order to facilitate the sensor–actuator for in situ applications, a second system was proposed [2,3] of which the basic elements are shown in Fig. 2. It is a modified system of the aforementioned type. The main difference is that the silicon cover of the first system has been omitted, thus allowing the free diffusion of species between the bulk solution and the actuator electrode. In this case the injection of the sample is not necessary, the whole system can be inserted in the analyte solution. The titration is still performed by applying a constant current to the actuator electrode. In this case the square root of the time needed to reach the end-point is linearly proportional to the concentration of the titrated species. This is expected, because the operation of the system is in principle the same as the classical constant-current chronopotentiometry. Except for the delay in response due to the non-zero distance between the gate of the ISFET and the actuator, the Sand equation [9] can be used to describe the behaviour of the system because the diffusion is regarded as one-dimensional due to the use of a large planar actuator electrode around the gate of the ISFET. The significant improvement in this system with respect to the classical chronopotentiometry is the separation of the signals of the indicating electrode from the generating (working) electrode. The pH in the vicinity of the actuator electrode can be selectively measured by the ISFET. This is advantageous especially for the performance of a titration at low concentration. In chronopotentiometry the generating electrode potential is measured, which is in fact the sum of the double layer charging, electrode polarization and redox couple potential change. At low concentrations, the effect of the double layer charging and the polarization will have a relatively strong influence, making it difficult to extract the pH information from the electrode potentials. A main advantage of the system where an ISFET is used for the pH measurement is that it circumvents the problems mentioned above. In addition, the device can be made in a dipstick fashion, so it can be easily used in a continuous way. Furthermore, it permits a continuous local pH control in the vicinity of the ISFET. A disadvantage is the non-linear relation between the amount of the generated titrant needed for a titration and the concentration of the titrated species. In addition, there is a delay in response because of the non-zero distance between the actuator electrode and the gate of the ISFET. Consequently, the pH in

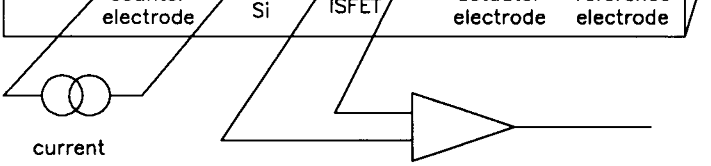

Fig. 2. Schematic representation of the basic components of the dipstick ISFET-based coulometric sensor–actuator system.

the vicinity of the ISFET is not uniformly distributed not only because of the delay time, but also because of the concentration gradient in the diffusion layer.

Another application of the second system worthwhile to mention here is the construction of a pH-static enzyme sensor [5], which utilizes specifically the ability of the local pH control of this system. With a membrane containing an immobilized enzyme mounted on top of the ISFET-based sensor–actuator device, the pH in the membrane can be adjusted to a desired value for an optimal operation of the enzyme. The catalytic products from the enzymatic reaction can be continuously titrated to keep the pH inside the membrane constant by applying a current to the actuator electrode, of which the current is in turn a measure of the concentration of the substrate. However, the aforementioned disadvantages of the second system such as the delay in response and the not uniformly distributed pH inside the membrane will limit the possibilities of this application.

Coulometric sensor–actuator system with a porous noble metal as the actuator

The recently proposed ISFET-based coulometric sensor–actuator system [8] employs a porous noble metal, for instance porous gold, as an actuator closely shaped around and over the gate of the ISFET. The basic components of this system are shown in Fig. 3. This system is expected to keep the advantages of the aforementioned two systems and to get rid of the disadvantages. The preliminary results have shown that the delay in response of the system is considerably reduced because the distance from actuator to the gate of the ISFET is minimized. Since the gate is fully surrounded by the porous actuator, the titration of the internal volume of the porous actuator will give rise to a smaller concentration gradient, which limits the diffusion of the species from the bulk solution to the gate of the ISFET. As a result, the amount of generated titrant needed for a coulometric titration is expected to be approximately linearly proportional to the concentration of the titrated species. Another advantage is that the system is less sensitive to convection. This makes the system more suitable for on-line applications. The other advantages such as ease of operation and possibility for a design of a dipstick device still remain.

The behaviour of the previously developed systems has already been extensively studied [6,7]. A semi-quantitative description of the system delay in response has also been presented [6]. For the new system with a porous noble metal as the actuator, preliminary results have shown that the delay in response is considerably reduced, whilst also the expected approximately linear relation-

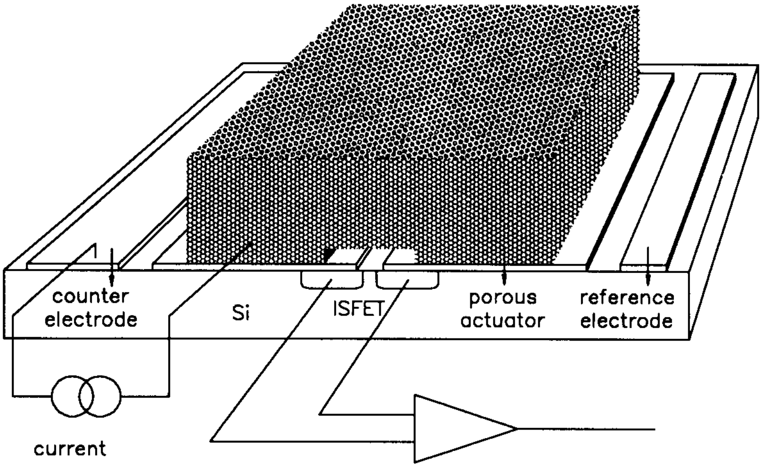

Fig. 3. Schematic representation of the basic components of the coulometric sensor–actuator system based on an ISFET with gate-covered porous gold actuator.

ship between the amount of the generated titrant used for titration and the concentration of the titrated species was found [8]. In the following part of this paper, we will propose an analytical model to describe the behaviour of the new system, combined with improved technologies in making the devices. The model will be verified with corresponding experimental results.

MATHEMATICAL MODEL

General considerations

For a coulometric titration of an acid or base, the titrant generated at the actuator electrode by electrolysis of water depends on the direction of the applied current. The reactions at the electrodes are as follows:

$$\begin{aligned} &\text{Anode:} && 2H_2O \rightarrow 4H^+ + 4e^- + O_2 \\ &\text{Cathode:} && 2H_2O + 2e^- \rightarrow 2OH^- + H_2 \end{aligned} \qquad (1)$$

When a current is applied to the porous actuator, the continuously titrated species inside the pores of the actuator will generate an electrochemical potential gradient between the internal volume of the porous actuator and the bulk solution. Mass transport will then occur. For the system used here, only diffusion is considered in the mass transport. Convection is assumed to be absent for two reasons: firstly, the titration is performed in a stagnant solution and secondly, in the relatively short time of titration convection caused by a change in density or thermal effect is excluded. The effect of migration can be eliminated by adding excess of supporting electrolyte. For the derivation of the model some extra assumptions are made:

(1) The diffusion is considered to be one-dimensional only, because the geometrica area of the actuator is much larger than its thickness. This assumption means that there is only a concentration gradient perpendicular to the ISFET inside the porous layer and in the bulk solution. The concentration profiles of the species can then be divided into two parts as shown in Fig. 4, where x is the distance from the gate to the bulk and l is the thickness of the porous actuator. $C_1(x, t)$ and $C_2(x, t)$ represent the concentration profiles of the species inside and outside the porous actuator, respectively.

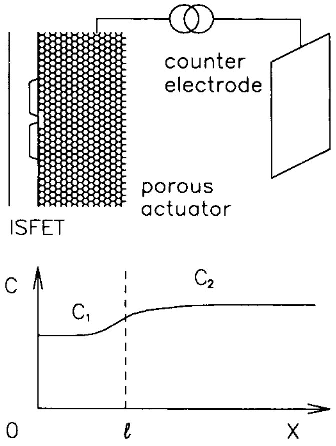

Fig. 4. Illustration of the concentration profiles inside and outside the porous actuator for $t > 0$.

(2) The porosity of the porous actuator is assumed to be homogeneous, and the applied current is assumed to be uniformly distributed at the active surface of the porous actuator, i.e., the current density is assumed to be constant over the whole active surface. As a consequence of this assumption, the titrant is uniformly generated inside the porous actuator.

(3) Since the pH is measured by an ISFET, it is not necessary to determine the current density at the electrode for the calculation of the electrode potential. The internal volume of the actuator to be titrated can then be considered as a homogeneous source or sink. In the following calculations a parameter, ρ, defined as the apparent titrant production rate per unit volume is introduced:

$$\rho = \frac{I}{FV_{\text{act}}} = \frac{I}{FSl} \qquad (2)$$

where I is the applied current and F the Faraday constant, V_{act} is the total volume of the porous actuator, S and l are the geometric area and thickness of the porous actuator, respectively. Owing to a reasonably high porosity of the actuator the volume taken up by the gold itself is ignored. Since only the faradaic portion of the current is significant for the faradaic process, the subscript f will further be used to denote the faradaic portion of the current and the corresponding value of ρ: $\rho_f = I_f/FSl$, representing the real titrant production rate per unit volume. In the case of an applied constant current, the titrant production rate per unit volume is also a constant.

(4) The diffusion coefficients of the species inside the porous actuator are considered to be the same as in the bulk solution because of the relatively large pore size.

With the above assumptions, the equations governing the mass transport inside and outside the porous actuator are then derived as follows.

Derivation of the model

In the bulk solution, i.e., $l < x < \infty$, the change of the concentration of the sample is only caused by diffusion. The diffusion equation for $C_2(x, t)$ is

$$\frac{\partial C_2(x, t)}{\partial t} = D\frac{\partial^2 C_2(x, t)}{\partial x^2} \quad l < x < \infty \tag{3}$$

The change of the concentration of the sample inside the porous actuator is caused by both its diffusion and the reaction with the generated titrant. The change of the concentration of the sample by diffusion can be written immediately as

$$\frac{\partial C_1^{\mathrm{d}}(x, t)}{\partial t} = D\frac{\partial^2 C_1(x, t)}{\partial x^2} \quad 0 < x < l \tag{4}$$

where the superscript d denotes the change of concentration by diffusion. If the rate of charge transfer, i.e., the electrolysis of water as described by Eqn. 1, and the related dissociation kinetics are not taken into account, the change of the concentration of the sample by the reaction with the generated titrant is

$$\frac{\partial C_1^{\mathrm{f}}(x, t)}{\partial t} = -\rho_{\mathrm{f}} \quad 0 < x < l \tag{5}$$

Combining the two processes, the diffusion equation for $C_1(x, t)$ is expressed as

$$\begin{aligned}\frac{\partial C_1(x, t)}{\partial t} &= \frac{\partial C_1^{\mathrm{f}}(x, t)}{\partial t} + \frac{\partial C_1^{\mathrm{d}}(x, t)}{\partial t} \\ &= D\frac{\partial^2 C_1(x, t)}{\partial x^2} - \rho_{\mathrm{f}} \quad 0 < x < l\end{aligned} \tag{6}$$

Eqns. 3 and 6 govern the mass transport inside and outside the porous actuator. The initial and boundary conditions are

$$t = 0,\ C_1(x, 0) = C_2(x, 0) = C_0 \tag{7}$$

$$x = 0,\ \frac{\partial C_1(0, t)}{\partial x} = 0 \tag{8}$$

$$x = l,\ \begin{cases}\dfrac{\partial C_1(l, t)}{\partial x} = \dfrac{\partial C_2(l, t)}{\partial x} \\ C_1(l, t) = C_2(l, t)\end{cases} \tag{9}$$

$$x \to \infty,\ C_2(x, t) = C_0 \tag{10}$$

where C_0 is the initial bulk concentration of the species. Equation 8 is based on the fact that there is no flux flowing through the ISFET which is positioned at the edge of the actuator ($x = 0$). Equation 9 reflects the conservation and continuation of matter. Applying the initial condition (Eqn. 7) and boundary condition (Eqns. 8, 9 and 10) to Eqns. 6 and 3, expressions for $C_1(x, t)$ and $C_2(x, t)$ can be obtained (cf. appendix A):

$$\begin{aligned}C_1(x, t) = C_0 - \rho_{\mathrm{f}}t + \frac{\rho_{\mathrm{f}}}{2}\Bigg\{&\left[t + \frac{(l+x)^2}{2D}\right] \\ &\times \operatorname{erfc}\frac{l+x}{2\sqrt{Dt}} - (l+x)\sqrt{\frac{t}{\pi D}} \\ &\times \exp\left[-\frac{(l+x)^2}{4Dt}\right] \\ &+ \left[t + \frac{(l-x)^2}{2D}\right]\operatorname{erfc}\frac{l-x}{2\sqrt{Dt}} - (l-x) \\ &\times \sqrt{\frac{t}{\pi D}}\exp\left[-\frac{(l-x)^2}{4Dt}\right]\Bigg\}\end{aligned} \tag{11}$$

$$\begin{aligned}C_2(x, t) = C_0 - \frac{\rho_{\mathrm{f}}}{2}\Bigg\{&\left[t + \frac{(x-l)^2}{2D}\right]\operatorname{erfc}\frac{x-l}{2\sqrt{Dt}} \\ &- (x-l)\sqrt{\frac{t}{\pi D}}\exp\left[-\frac{(x-l)^2}{4Dt}\right] \\ &- \left[t + \frac{(x+l)^2}{2D}\right]\operatorname{erfc}\frac{x+l}{2\sqrt{Dt}} + (x+l) \\ &\times \sqrt{\frac{t}{\pi D}}\exp\left[-\frac{(x+l)^2}{4Dt}\right]\Bigg\}\end{aligned} \tag{12}$$

The end-point is detected by the gate of the ISFET, and because the gate is closely surrounded by the porous actuator, the position of the gate is considered to be located at $x = 0$. This assumption is acceptable for two reasons. One is that the real distance from the gate to the actuator is only 3 μm which is much smaller than the thickness of the actuator. The other reason is that the space volume around the gate is negligible compared to the volume of the porous actuator. The concentration at $x = 0$ is

$$C_1(0, t) = C_0 - \rho_f t + \rho_f \left[\left(t + \frac{l^2}{2D} \right) \operatorname{erfc} \frac{l}{2\sqrt{Dt}} - l\sqrt{\frac{t}{\pi D}} \exp\left(-\frac{l^2}{4Dt} \right) \right] \tag{13}$$

For the sake of clarity an auxiliary variable θ is introduced: $\theta = l/2(Dt)^{1/2}$. Then Eqn. 13 becomes

$$\begin{aligned} C_1 &= C_0 - \rho_f t + \rho_f t \times \left[(1 + 2\theta^2) \operatorname{erfc}\theta - \frac{2\theta}{\sqrt{\pi}} \exp(-\theta^2) \right] \\ &= C_0 - \rho_f t + \rho_f t * 4 i^2 \operatorname{erfc}\theta \\ &= C_0 - \rho_f t * [1 - 4 i^2 \operatorname{erfc}\theta] \end{aligned} \tag{14}$$

where

$$i^2 \operatorname{erfc}\theta = \tfrac{1}{4}(1 + 2\theta^2) \operatorname{erfc}\theta - \frac{2\theta}{\sqrt{\pi}} \exp(-\theta^2) \tag{15}$$

At the time the end-point is reached, $C_1(0, t)$ equals zero. The titration time τ can be obtained from Eqn. 14 by letting $C_1(0, \tau) = 0$:

$$\tau = \frac{C_0}{\rho_f [1 - 4 i^2 \operatorname{erfc}\theta]} \tag{16}$$

Equation 16 is the formula to calculate the time to reach the end-point for an acid or base titration. From Eqn. 16 it can be seen that the titration time is proportional to the initial bulk concentration of the titrated species, but it must be pointed out that in a general case $i^2\operatorname{erfc}\theta$ may also be a function of τ, resulting in a titration time that is not a linear function of the initial bulk concentration. The situation can, however, be simplified in some specific circumstances which will be discussed later.

Consideration of the double layer charging

As the porous actuator has an enormously large active surface area, the charging of the double layer capacitance cannot be neglected. On the other hand, for the calculation of τ by Eqn. 16 the faradaic portion of the current has to be known. In practice, only the applied current is known. If both faraday and double layer charging effects play a role the applied current to the actuator has to be separated into two parts: the faradaic current, I_f, and the current used to charge the double layer, I_d. Generally, these currents are not constant during the titration. At the beginning of the titration and at the time around the end-point, the actuator potential changes rapidly and the current for the charging of the double layer capacitance is significant, so most of the current is used to charge the double layer. After the double layer is charged to the redox couple potential and before the end-point is reached, the applied current is nearly faradaic. The exact expression for the double layer charging current is difficult to obtain, so that an approximation is often made by means of a simplified calculation or estimation in practical situations. Here we will apply the constant double layer charging current approximation [9]. In this case the current for the charging of the double layer is assumed to be constant during the whole titration and therefore the total applied current is simply expressed as

$$I = I_f + I_d \tag{17}$$

where I_f is the faradaic current, I_d is the current used to charge the double layer. Substitution of Eqn. 17 into Eqn. 16 yields

$$\tau = \frac{C_0}{\rho [1 - 4 i^2 \operatorname{erfc}\theta]} + \frac{I_d \tau}{I} \tag{18}$$

where $I_d\tau$ is the total number of coulombs needed to charge the double layer capacitance. Note that now the apparent titrant production rate per volume ρ appears in Eqn. 18 instead of ρ_f. This means that the calculation of τ can now be easily performed. According to the assumption, $I_d\tau \approx C_{dl}\Delta E$, where C_{dl} is the average double layer capacitance and ΔE the actuator potential difference during titration, Eqn. 18 can be written as

$$\tau = \frac{C_0}{\rho[1 - 4i^2\mathrm{erfc}\theta]} + \frac{C_{dl}\Delta E}{I} \tag{19}$$

Comparing Eqn. 19 with Eqn. 16, the second term of the right-hand side of Eqn. 19 represents the contribution of the double layer charging to the titration time.

Applicability of the model to practical systems

Equation 19 expresses the relation of the time needed to reach the end-point at the gate of the ISFET as a function of the initial bulk concentration of the species for an acid or base titration. The first term of Eqn. 19 represents the contribution of the faradaic process. As is already mentioned before, the titration time is not a linear function of the initial bulk concentration in a general case, because $i^2\mathrm{erfc}\theta$ is also a function of the titration time. Thus Eqn. 19 is not convenient for practical use. However, the parameter θ and the function $i^2\mathrm{erfc}\theta$ have their real physical meanings, so that in some specific circumstances, the function $i^2\mathrm{erfc}\theta$ can be approximated by a linear function of θ. Equation 19 can then be simplified. This is done by evaluating the value of $i^2\mathrm{erfc}\theta$ as a function of θ as follows.

The expression $(2Dt)^{1/2}$ is conventionally used as a measure of the average displacement of the species due to diffusion after a time t. By its definition, θ ($= l/2\sqrt{Dt}$) divided by a factor of $\sqrt{2}$ is the ratio of the thickness of the actuator to the diffusion distance of the species from the bulk solution into the porous actuator. It can thus be reasoned that before the diffusing species reach the gate of the ISFET, the change of the concentration of the species in the vicinity of the gate is caused only by the generated titrant. The titration can then be considered as a volumetric titration inside the porous actuator. When the diffusing species reaches the gate of the ISFET ($x = 0$) after time t, the change of the concentration of the species at this point will of course be influenced by the diffusion in addition to the generated titrant. After this moment the diffusion process will also determine the titration time τ. Therefore, θ can be considered as a parameter to evaluate the time for the species to reach the gate of the ISFET by diffusion and consequently the value of $i^2\mathrm{erfc}\theta$ can be used as a measure of the contribution of the diffusion to the time of titration. In other words, the value of θ and $i^2\mathrm{erfc}\theta$ are expected to be suitable criteria to distinguish whether the titration is a diffusion-controlled titration or a volumetric titration inside the porous actuator. Based on this consideration, the function $1 - 4i^2\mathrm{erfc}\theta$ is evaluated as a function of θ as shown in Fig. 5. From this figure it can be seen that if θ approaches zero or infinity, $1 - 4i^2\mathrm{erfc}\theta$ will approximate two asymptotic lines. If one of these two extreme cases applies, $i^2\mathrm{erfc}\theta$ can be replaced by a simple linear expression of θ, which is independent of τ or is only a simple function of τ. Hence, the applications of Eqn. 19 to an acid or base titration can be generally classified into the following three cases.

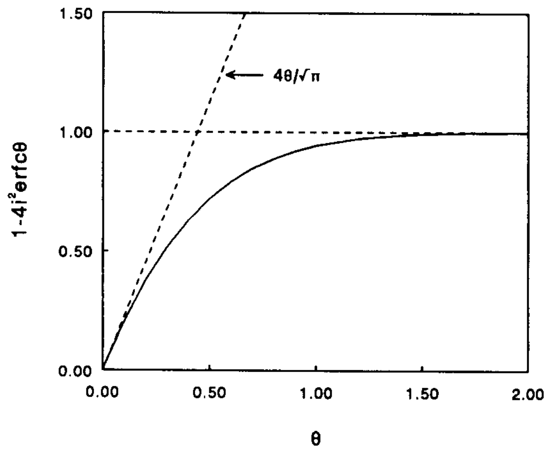

Fig. 5. Plot of $1 - 4i^2\mathrm{erfc}\theta$ as a function of θ.

Case 1. If the actuator is very thick and the time for a titration is short, i.e., $l > 2(Dt)^{1/2}$ or $\theta > 1$, the value of $i^2\mathrm{erfc}\theta$ will be very small. If $\theta \to \infty$, $i^2\mathrm{erfc}\theta$ will ultimately approach zero. In this case the diffusion can be ignored and the titration can be regarded as a bulk titration inside the porous actuator. Then, Eqn. 19 becomes

$$\tau = \frac{C_0}{\rho[1 - 4i^2\mathrm{erfc}\theta]} + \frac{C_{dl}\Delta E}{I} \cong \frac{C_0}{\rho} + \frac{C_{dl}\Delta E}{I} \tag{20}$$

It can be seen that τ is now linearly proportional to the initial bulk concentration of the species. The limit to neglect the $i^2\text{erfc}\theta$ depends on the required precision. For instance if $\theta = 1$, then $4i^2\text{erfc}\theta = 0.06$. It means that if the titration is treated as a titration of the internal volume of the porous actuator only, the diffusion caused deviation of the calculated titration time is ca. 6%.

Case 2. If the porous actuator is very thin and the time for a titration is long, i.e., $l \ll 2(Dt)^{1/2}$ or $\theta \ll 1$, $1 - 4i^2\text{erfc}\theta$ will approach $4\theta/\sqrt{\pi}$. After substitution of $1 - 4i^2\text{erfc}\theta$ by $4\theta/\sqrt{\pi}$, Eqn. 19 becomes

$$\tau = \frac{C_0}{\rho[1 - 4i^2\text{erfc}\theta]} + \frac{C_d \Delta E}{I}$$

$$\cong \frac{FSl\sqrt{\pi}}{4\theta I} C_0 + \frac{C_d \Delta E}{I}$$

$$\cong \frac{FS\sqrt{\pi D \tau}}{2I} C_0 + \frac{C_d \Delta E}{I} \qquad (21)$$

or

$$\sqrt{\tau} \cong \frac{FS\sqrt{\pi D}}{2I} C_0 + \frac{C_d \Delta E}{I\sqrt{\tau}} \qquad (22)$$

The titration can now thus be regarded as a diffusion-controlled titration. In fact, the first term of the right-hand side of Eqn. 22 is exactly the same as the Sand equation which was derived in the classic chronopotentiometry [9]. The square root of the titration time is linearly proportional to the bulk concentration of the titrated species if the double layer charging is omitted. The precision for the approximation can also be calculated. As an example, for $\theta = 0.05$, $[1 - 4i^2\text{erfc}\theta - 4\theta/\sqrt{\pi}]/[1 - 4i^2\text{erfc}\theta] = -0.045$. This indicates that $1 - 4i^2\text{erfc}\theta$ can be replaced by $4\theta/\sqrt{\pi}$ for the calculation if an error of 4.5% is allowed in this example.

Case 3. If the above two extremes do not apply, Eqn. 19 has to be used to calculate the titration time as a function of the concentration of the titrated species. The calculation can be done by means of a computer or by consulting tabulated values of the error function.

EXPERIMENTAL

Technology to make the device

The procedure to make the sensor–actuator devices is comparable to the previously reported one [8] and as shown in Fig. 6. There are two improvements. First, the structure of the ISFET was modified in order to enhance the ability of

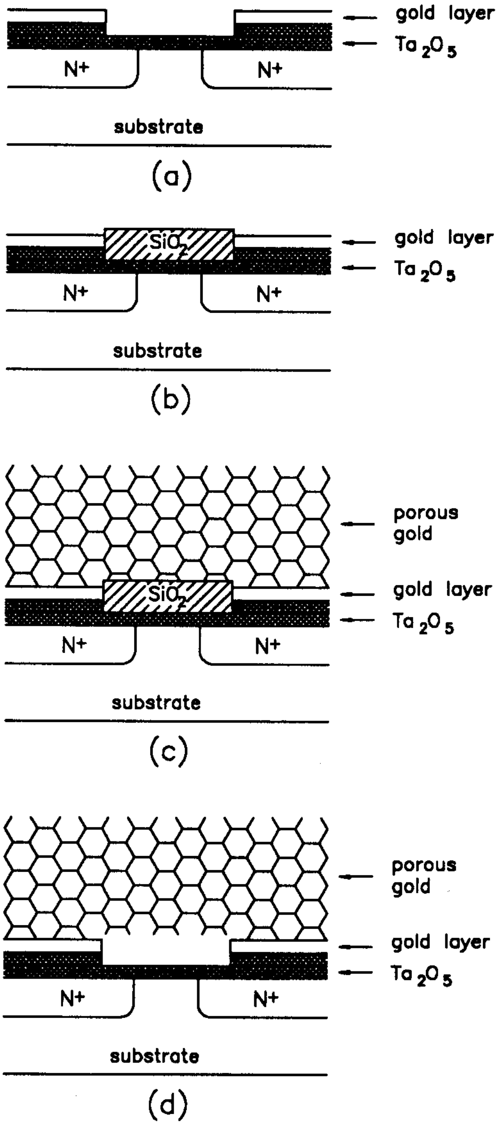

Fig. 6. Procedure to make the device. (a) Flat ISFET with a thin layer of evaporated gold around the gate; (b) deposition of a sacrificial layer of SiO_2 by PECVD; (c) deposition of a layer of porous gold; (d) etching of the sacrificial layer.

the ISFET to withstand the hydrofluoric acid etching, because the etching of the sacrificial layer by hydrofluoric acid is very aggressive and the etching usually takes a rather long time to guarantee a complete removal of both the sacrificial layer and the glass compounds in the thick-film paste, which is used for the fabrication of the porous actuator electrode. During the manufacture micro cracks in the upper-layer of tantalum pentoxide have been found at the edge of the field silicon dioxide [10]. The cracks result from the volume expansion of the tantalum during oxidation to become tantalum pentoxide. The etchant can slowly penetrate from the crack part into the field silicon dioxide and consequently cause a damage of the ISFET. The ISFET will finally have an abnormally large leakage current. The new type of ISFET has a completely flat surface, so that the cracking in the top layer of tantalum pentoxide is avoided. The flat structure

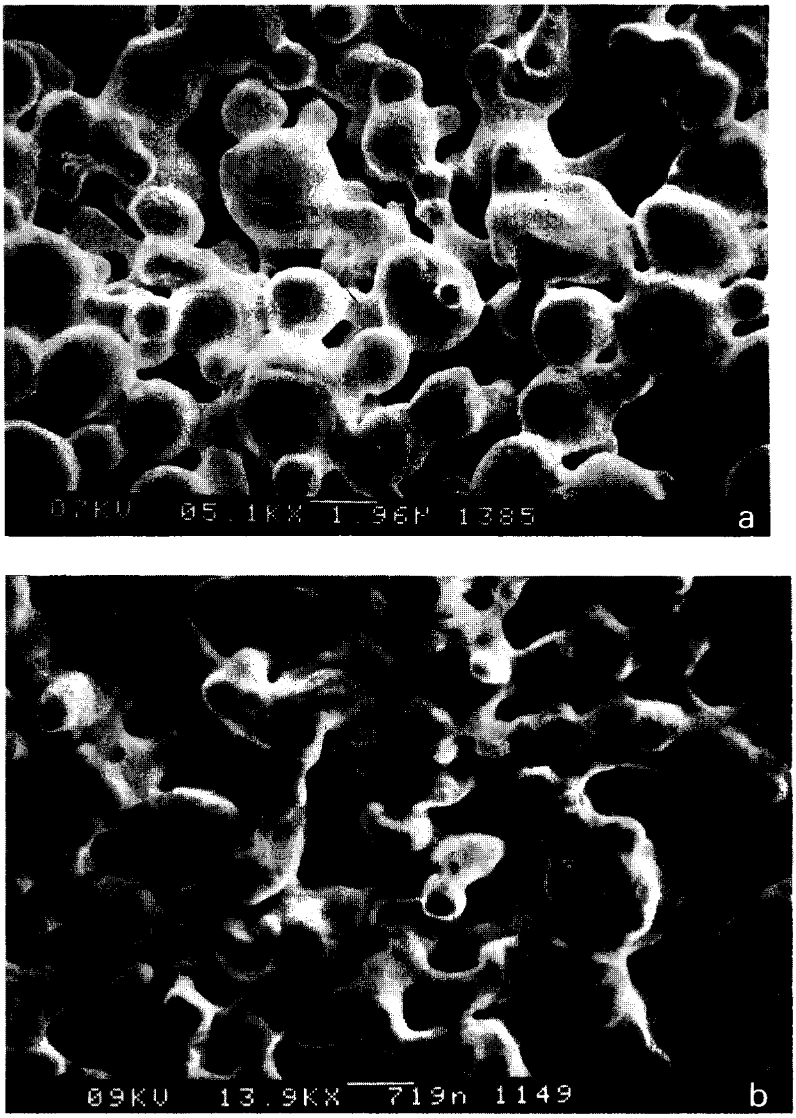

Fig. 7. Microstructure of the porous gold made by (a) sintering of thick-film paste at 600°C and (b) sintering of black gold at 550°C.

is achieved by etching of the whole field silicon dioxide layer after finishing the diffusion process [10]. An extra thick layer of tantalum pentoxide with an open window for the gate area is made after the first tantalum pentoxide is formed. It functions as a protection layer to prevent migration of gold into the silicon. The second improvement is the simplification of the sacrificial layer. Since the flat structured ISFET can withstand a long time of hydrofluoric acid etching without damage, a single silicon dioxide layer as the sacrificial layer, made by plasma enhanced chemical vapour deposition (PECVD), was applied instead of a sandwich layer of $SiO_2/Si/SiO_2$ that has been used before [8]. The thickness of the sacrificial layer is 3 μm.

Gold was chosen as the material for the porous actuator. The porous gold was made in two ways. The first way was by sintering of thick-film paste (DuPont 9910) at 600°C, which has previously been reported [8]. The second way was by sintering of black gold. The black gold was made by vapour deposition of gold onto a substrate at a certain pressure in a nitrogen atmosphere. The pressure used for deposition was ca. 0.5 Torr, the distance from the source of gold evaporation to the substrate is ca. 5 cm. The obtained black gold was sintered at 550°C also in a nitrogen atmosphere. The microstructure of the porous actuators made by sintering of thick-film paste and sintering of black gold is shown in Fig. 7a, b by means of scanning electron microscopy (SEM) photographs. Due to a low efficiency of the vapour deposition at high pressure, the thickness of the porous gold actuator made by sintering of black gold is usually thinner than that made by sintering of gold thick-film paste. The thickness of the porous actuator made by sintering of black gold is in the range of 10–30 μm, while a porous actuator made by sintering of thick-film paste is 100–200 μm.

Determination of the geometric parameters and estimation of the total double layer capacitance

For the theoretical calculation of the titration times for an acid or base titration, the apparent titrant production rate per unit volume ρ and the total double layer capacitance should be known first. These two parameters are related to the dimension of the actuator. The calculation of ρ requires the determination of the geometric area and the thickness of the porous actuator. The total double layer capacitance of the actuator is dependent on the total active area of the actuator and the specific capacitance. Unfortunately, these parameters are difficult to determine exactly. This is because the dimension of the actuator is not always well defined to the difficulty in applying photolithography. The difficulty in packaging the devices gives rise to an imprecisely defined area, too. Thus the geometric area, S, and the thickness of the porous actuator, l, for each device are measured individually by an optical microscope. The production rate per unit volume is then calculated by its definition (see Eqn. 2). Another geometric parameter that is difficult to determine is the total active area of the actuator. Its value is related to the grid size and the pore size of the porous gold, both of which are dependent on the way of preparing the actuator and are also not well defined. In fact, exact determination of the total surface area of the actuator is insignificant in this case, because the specific double layer capacitance is actually a function of the electrode potential and the ionic strength [11]. However, estimation is often adequate for the application of the derived model as long as the accuracy for calculation is within the experimental error and the correctness of Eqn. 19 still holds. Normally, these conditions are fulfilled. The estimation for the total double layer capacitance is made as follows. The specific double layer capacitance is estimated as 20 $\mu F\ cm^{-2}$ as ordinarily accepted [12]. The total surface area of the actuator was estimated according to the measured grid size and thickness of the porous actuator from the SEM photograph. The porous gold actuator is considered as a composition of laminated layers of gold with layer thicknesses of average grid size. Since the actuator is rather porous, i.e., the gold particles are not tightly packed, each layer of gold is assumed to have the same area as the geometric area. The number of layers is determined by dividing the total actuator thickness by the grid size of the gold. The total active area is assumed to be equal to the geometric area times the

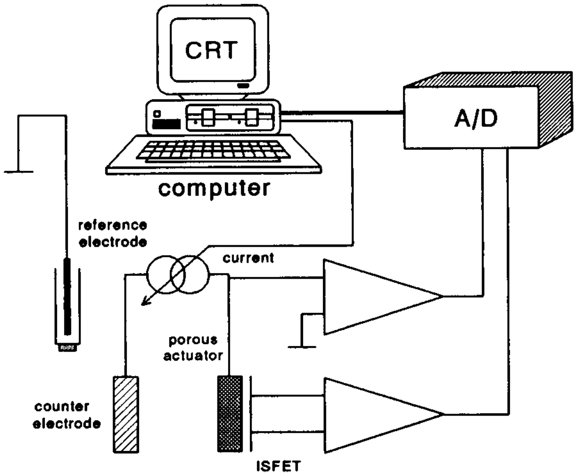

Fig. 8. Measuring set-up for an acid–base titration.

number of layers. The total double layer capacitance is then calculated as

$$C_{\mathrm{dl}} = SNC_{\mathrm{dl}}^{*} \tag{23}$$

where S and N are the geometric area and the number of layers of the gold particles, respectively and C_{dl}^{*} is the specific capacitance of the double layer, being 20 μF cm^{-2}.

Acid to base titration

A nitric and an acetic acid titration were chosen for a model study of the system. The set-up for the titration is shown in Fig. 8. The output of the ISFET amplifier as well as the actuator potential are registered by the computer. The titration was performed in a 25-ml plastic container. After each titration, a reversed current was applied and the solution was stirred for homogenizing the solution inside and in the vicinity of the actuator. There was ca. one minute pause after stirring and before the start of each titration in order to get rid of convection effects.

RESULTS AND DISCUSSIONS

In order to examine the reduction of the delay time, the titration with a previously developed sensor–actuator device with planar actuator is performed first as a comparison. Because the porous actuator made in different ways has different thicknesses, the titration with various devices will, according to the model, show different behaviour. Therefore, the titration with various devices, of which the porous actuator is made in different ways, will be discussed separately.

Titration with a planar type sensor–actuator device

Titration of nitric acid using the previously developed prototype device with a planar structure of the actuator was carried out. Figure 9 shows the typical registration curves of the ISFET amplifier output voltage as well as the actuator potential and the corresponding first derivatives. The times to reach the end-points at the ISFET and the actuator are determined by the minima of the corresponding first derivatives. This method applied to the actuator is in fact the classic chronopotentiometry. From the upper curves of Fig. 9, the time to reach the end-point at the ISFET can be found at $t = 1.72$ s. From the lower curves of the actuator potential and the first derivative, the time to reach the end-point at the actuator is at $t = 1.02$ s. The delay time can be calculated by a simple subtraction, which results for this example in 0.7 s.

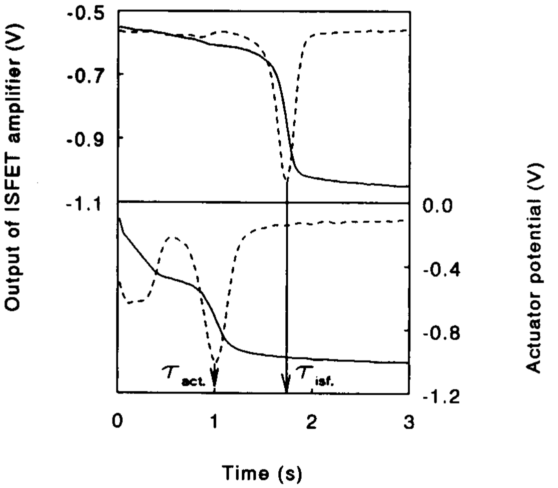

Fig. 9. Registration curves and the first derivatives (dashed lines) for a nitric acid titration. The actuator is a planar structure. [KNO$_3$] = 0.1 M, [HNO$_3$] = 2.0 mM, applied current density is 20 μA mm^{-2}.

Titration using a device with a porous actuator made by sintering of black gold

A series of titration of nitric acid was also carried out using a device with a porous gold actuator made by sintering of black gold. Figure 10 shows the registration curves and the first derivatives recorded from the titration. From Fig. 10 it can be seen that the times to reach the end-points at the ISFET and the actuator are about the same. Compared to Fig. 9, it can be concluded that the delay time is considerably reduced.

The dimension of the porous gold actuator made by sintering of black gold was measured. The geometric area is ca. 0.5 mm^2 and thickness is ca. 30 μm. The average grid size of the porous is roughly estimated to be in the order of 1 μm from Fig. 6b. The number of layers for calculation is then 30. The total double layer capacitance is calculated to be ca. 3 μF. The titration times are typically from 0.5 to 10 s. The corresponding θ can be calculated to have a value from 0.2 to 0.05 for this device. According to the model and calculated values of θ, the device with such a thin porous actuator should show a quadratic relation between the titration time and the initial bulk concentration of the titrated species. The titration can be regarded in this case as diffusion controlled, and consequently Eqn. 21 can be applied for a simplified calculation. Figure 11 shows the theoretical and experimental results. For the sake of accuracy, the theoretical values were calculated by Eqn. 19. The experimental results show a good agreement with the theoretical calculation. The concentration of the titrated nitric acid is ca. 0.5–3 mM, and the applied current was 20 μA.

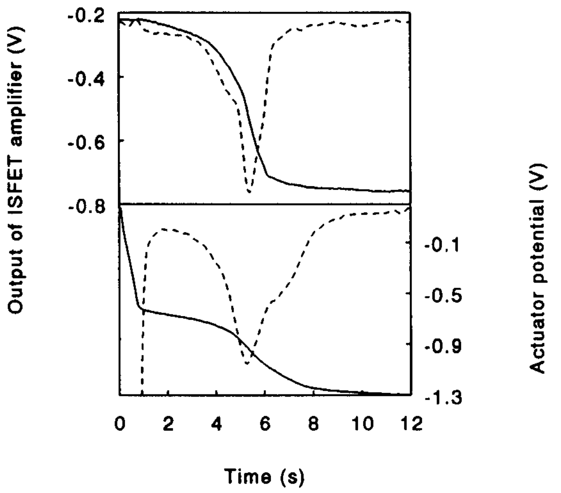

Fig. 10. Registration curves and the first derivatives (dashed lines) for a nitric acid titration. The porous actuator was made by sintering of black gold. The applied current is 30 μA, [KNO$_3$] = 0.1 M, [HNO$_3$] = 2.7 mM.

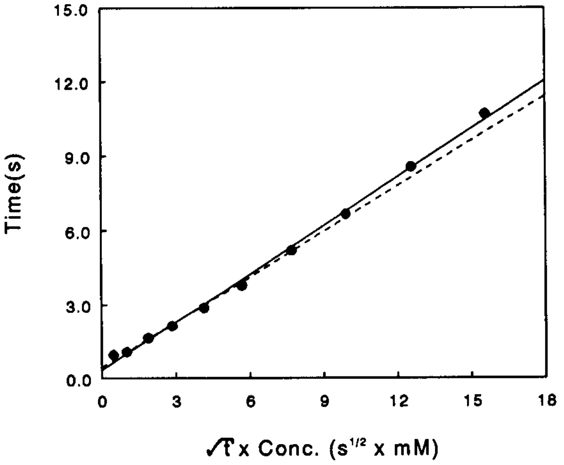

Fig. 11. Relation of the titration time and the concentration of titrated nitric acid. Dashed line is theoretically calculated, marks and solid line are experimental results with linear fitting. The applied current is 20 μA. The porous actuator was made by sintering of black gold.

Titration using devices with porous actuator made by sintering of thick-film paste

The titration of both nitric acid and acetic acid was performed using the devices with a porous gold actuator made by sintering of thick-film paste. Because the porous actuator made in this way is very thick, the time for the diffusion of the species to reach the gate of the ISFET will be long. The behaviour of this device will therefore be quite different from that of the devices described in the previous section. It can be expected that the diffusion starts at the interface between the actuator and the bulk electrolyte, so the depletion of the titrated species can be assumed to take place gradually from inside the actuator towards the boundary. Theoretical calculation of

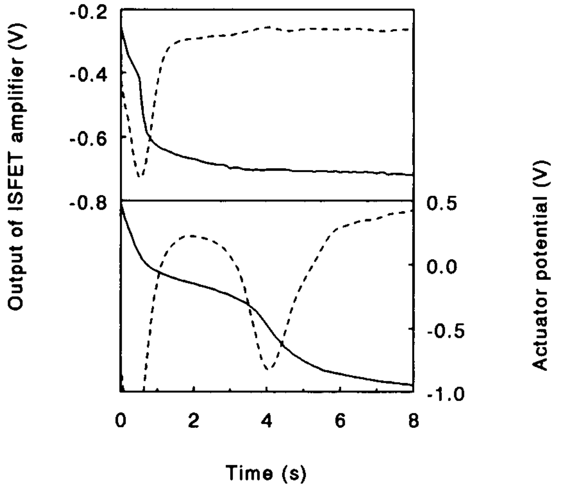

Fig. 12. Registration curves and the first derivatives for a nitric acid titration. The porous actuator was made by sintering of thick-film paste. The applied current is 30 μA, $[KNO_3] = 0.1$ M, $[HNO_3] = 0.5$ mM.

the concentration profile can be based on Eqn. 11. Figure 12 shows the registration curves using this device for a nitric acid titration. It can be seen that the time to reach the end-point at the actuator is later than at the gate of ISFET, implying that the species are gradually titrated and depleted at different locations inside the actuator and that the depletion of the species in the vicinity of the gate is always prior to the depletion of the whole volume of the actuator.

The thickness of the actuator made by sintering of thick-film paste is between 100 and 200 μm. The average grid size of the porous gold is estimated to be 2 μm from Fig. 6a. The number of layers for calculation is then 50–100. The geometric area was designed to be ca. 0.5–1 mm^2. The total double layer capacitance can then be calculated to be ca. 5–20 μF.

The typical titration times of the system are from 0.5 to 10 s. For a titration of acetic acid, the dominant diffusion species is the acetic acid molecule, of which the value of θ is calculated to be 2.2–0.58 (100 μm) and 4.3–0.96 (200 μm). For a titration of nitric acid, the dominant diffusion species being the protons, the value of θ is calculated to be 0.17–0.34 (100 μm) and 0.33–0.68 (200 μm). The smaller values of θ for a nitric acid titration with respect to the acetic acid titration are due to the fact that a proton has a much higher mobility than an acetic molecule. According to the model and calculated values of θ, the titration of the weak acid or base permits the use of Eqn. 20 for simplified calculation, while titration of a fully dissociated acid or base requires the use of Eqn. 19. Figures 13 and 14 show the results of the titration of acetic acid and nitric acid. The titration times are presented as function of the concentration of the acids. The concentration of the titrated species is from 0.5 up to ca. 10 mM. The dashed lines in Figs. 13 and 14 are calculated from Eqn. 19. The geometric area and thickness of the actuator are measured to be 0.68 mm^2 and 100 μm for the result of Fig. 13, and 0.6 mm^2 and 200 μm for the result of Fig. 14. The corresponding total double layer capacitances are calculated, according to Eqn. 23, to be 6.8 and 12 μF.

From the experimental results shown in Fig. 13, a linear relation between the titration times and the concentration of the titrated species can be seen for the acetic acid titration, which is in agreement with the model prediction. In that case, Eqn. 20 can be applied for simplified calculation. The slopes of the curves from the theoreti-

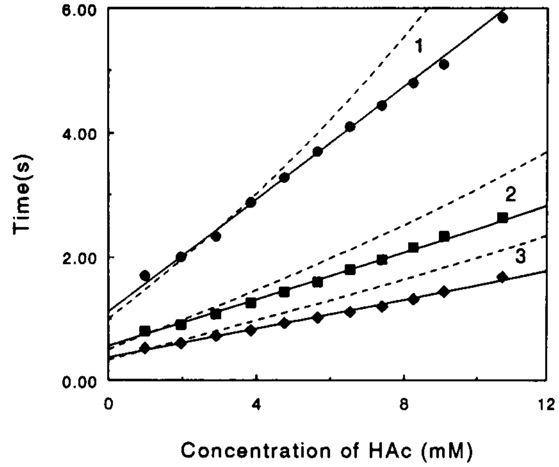

Fig. 13. Titration time as a function of the concentration of acetic acid. Dashed lines are theoretically calculated, marks and solid lines are experimental results with linear fitting. The applied currents are: (●) 10 μA; (■) 20 μA; (◆) 30 μA. The porous actuator was made by sintering of thick-film paste.

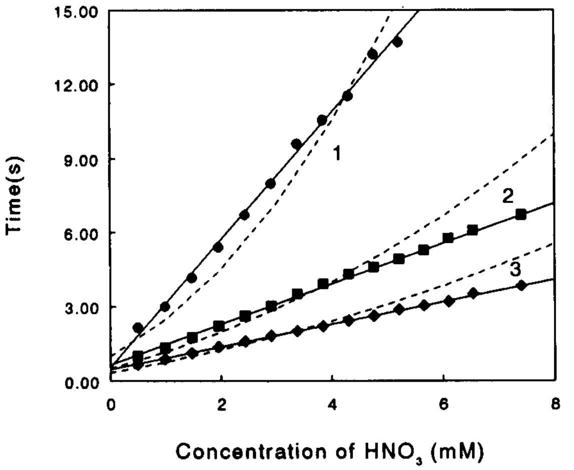

Fig. 14. Titration time as a function of the concentration of nitric acid. Dashed lines are theoretically calculated, marks and solid lines are experimental results and linear fitting. The applied currents are: (●) 10 μA; (■) 20 μA; (◆) 30 μA. The porous actuator was made by sintering of thick-film paste.

cal calculation (dashed lines) are larger than the experimental ones. One direct reason is the negligence of the volume of the gold. In a real situation, the volume of the electrolyte inside the actuator is smaller than the total volume of the actuator. This means that the experimental titration of the species will actually be faster than theoretically predicted. The actual slope can be determined before application by calibration in a well-defined acid. For practical applications, this is always necessary because the pore size of the actuator cannot be accurately determined. Also due to the technological difficulties the thickness and the geometric area of the porous actuator are not precisely controlled. These geometric parameters will ultimately determine the slope of the calibration curves.

The calibration curves in Fig. 14 from the experimental results are found to be more linear than theoretical ones in Fig. 14. A possible reason is that the concentration gradient of C_2 is in practice less than C_1 at the boundary of the actuator because the internal solution-filled volume of the actuator is less than its total volume, through which the flux of the diffusing species into the porous actuator will be less than assumed. Another reason may be the different effective diffusion coefficients (normally smaller values) of the species inside the pores [13]. In addition, the gases originating from the electrolysis of water may form a diffusion barrier for mass transport. These effects will limit the diffusion process, which means that more linear calibration curves will be obtained in practice. An experimental support for these explanation is that the system is found not to be very sensitive to stirring during titration. This diffusion-limiting process is in fact an advantage and will improve the applications of the coulometric sensor–actuator system, for instance, the application to the pH-static enzyme sensor. If an enzyme is immobilized in the pores of the actuator, the controlled pH inside the porous actuator will be more uniformly distributed due to a smaller concentration gradient.

It should be noted that in both Fig. 13 and Fig. 14, none of the extrapolations of the linear fitting curves intersects the origin of the axis. This shift of the curves along the time axis is mainly due to the existence of a large total double layer capacitance resulting from a very large active surface area of the porous actuator. Apart from the double layer charging, if the generated titrant is not uniformly distributed inside the porous actuator, it will probably also cause partly a shift of the calibration curves. For instance if the current density gradually decreases from the outside of the actuator to the inside of the actuator [14], and consequently the species near the gate of the ISFET will be titrated slower than expected, this will result in a longer titration time and a subsequent shift of the calibration curves along the time axis. As with the delay time of the previous system [6], this effect will also cause a difficult in the application.

Conclusions

In this paper, we have described and compared the previously developed two ISFET-based coulometric sensor–actuator systems and the newly designed coulometric sensor–actuator system which is based on an ISFET with a gate-covering porous nobel metal as the actuator electrode. The porous gold actuator has been successfully made in two ways: sintering of the applied gold thick-film paste and sintering of the vapour deposited black gold. From the point of technological consideration, the advantage of the former is the ease of making a thick porous gold actuator, a disadvantage is the incompatibility with integrated circuit (IC) technology. The latter production method is more compatible with IC technology, but the disadvantage is the very low efficiency for vapour deposition of gold.

A model characterizing the system has been proposed, which quantitatively describes the behaviour of the system. For a very thin porous actuator, the titration time is proportional to the squared concentration of titrated species. This is predicted by the model and confirmed by the experimental results. For a thick porous actuator, the titration time is linearly proportional to the titrated species in the case of a weak acid titration; in the case of a fully dissociated acid titration, the behaviour is also described by the model. However, the measured calibration curve is found to be more linear than expected from theory. Meanwhile, a deviation in slopes of the calibration curves exists. This deviation is ascribed to the poor reproducibility of the geometric parameters, e.g., the thickness, geometric area and the active surface area of the porous actuator during processing of the devices.

Experimental results have also shown that the delay of the system response, which existed due to the distance between the gate of the ISFET and planar actuator, has been considerably reduced after introduction of a porous actuator closely surrounding the gate of the ISFET. Another advantage is that the system is less sensitive to the convection, which makes the system more suitable for on-line application. The disadvantage of the new system is a more significant double layer charging effect, which will result in a shift of the calibration curves along the time axis and will cause an error for some specific applications of the new systems.

The authors would like to thank J.G. Bomer for technical assistance. This project is financially supported by Foundation for Fundamental Research on Matter (FOM).

APPENDIX

Solution of the diffusion Eqns. 6 and 3

Applying the Laplace transform to Eqns 6, 3, and 7, we obtain

$$C_1(x, s) = A_2 \exp\left(-\sqrt{s/D}\,x\right) + A_2 \times \exp\left(\sqrt{s/D}\,x\right) + C_0/s - \rho_f/s^2 \tag{A.1}$$

$$C_2(x, s) = B_1 \exp\left(-\sqrt{s/D}\,x\right) + B_2 \times \exp\left(\sqrt{s/D}\,x\right) + C_0/s \tag{A.2}$$

where s is the Laplace plane variable. If boundary Eqn. 8 is substituted into Eqn. A.1, we obtain $A_1 = A_2$. It can be inferred from Eqn. 10 that $B_2 = 0$. Let $A_1 = A_2 = A$, $B_1 = B$, then Eqns. A.1 and A.2 become

$$C_1(x, s) = A\left[\exp\left(-\sqrt{s/D}\,x\right) + \exp\left(\sqrt{s/D}\,x\right)\right] + C_0/s - \rho_f/s^2 \tag{A.3}$$

$$C_2(x, s) = B \exp\left(-\sqrt{s/D}\,x\right) + C_0/s \tag{A.4}$$

Applying the boundary condition Eqn. 9 to the Eqns. A.3, A.4 and their derivatives, the coefficients A and B are obtained:

$$B = -\frac{\rho_f}{2s^2}\left[\exp\left(\sqrt{s/D}\,l\right) - \exp\left(-\sqrt{s/D}\,l\right)\right] \tag{A.5}$$

$$A = \frac{\rho_f}{2s^2}\exp\left(-\sqrt{s/D}\,l\right) \tag{A.6}$$

Substituting A and B into Eqns. A.3 and A.4 yields

$$C_1(x, s) = \frac{C_0}{s} - \frac{\rho_f}{s^2} + \frac{\rho_f}{2s^2}\exp\left(-\sqrt{s/D}\,l\right) \times \left[\exp\left(\sqrt{s/D}\,x\right) + \exp\left(-\sqrt{s/D}\,x\right)\right] \tag{A.7}$$

$$C_2(x, s) = \frac{C_0}{s} - \frac{\rho_f}{2s^2} + \left[\exp\left(\sqrt{s/D}\,l\right) - \exp\left(-\sqrt{s/D}\,l\right)\right]\exp\left(-\sqrt{s/D}\,x\right) \tag{A.8}$$

By inverting the Laplace transforms [15], the solutions are obtained:

$$\begin{aligned} C_1(x,t) = C_0 - \rho_f t + \frac{\rho_f}{2}\Bigg\{ & \left[t + \frac{(l+x)^2}{2D}\right] \\ & \times \operatorname{erfc}\frac{l+x}{2\sqrt{Dt}} - (l+x)\sqrt{\frac{1}{\pi D}} \\ & \times \exp\left[-\frac{(l+x)^2}{4Dt}\right] \\ & + \left[t + \frac{(l-x)^2}{2D}\right]\operatorname{erfc}\frac{l-x}{2\sqrt{Dt}} - (l-x) \\ & \times \sqrt{\frac{t}{\pi D}}\exp\left[-\frac{(l-x)^2}{4Dt}\right]\Bigg\} \end{aligned} \quad (A.9)$$

$$\begin{aligned} C_2(x,t) = C_0 - \frac{\rho_f}{2}\Bigg\{ & \left[t + \frac{(x-l)^2}{2D}\right]\operatorname{erfc}\frac{x-l}{2\sqrt{Dt}} \\ & -(x-l)\sqrt{\frac{t}{\pi D}}\exp\left[-\frac{(x-l)^2}{4Dt}\right] \\ & - \left[t + \frac{(x+l)^2}{2D}\right]\operatorname{erfc}\frac{x+l}{2\sqrt{Dt}} + (x+l) \\ & \times \sqrt{\frac{t}{\pi D}}\exp\left[-\frac{(x+l)^2}{4Dt}\right]\Bigg\} \end{aligned} \quad (A.10)$$

or

$$\begin{aligned} C_1(x,t) &= C_0 - \rho_f t + 2\rho_f t \\ & \times \left(i^2\operatorname{erfc}\frac{l+x}{2Dt} + i^2\operatorname{erfc}\frac{l-x}{2Dt}\right) \end{aligned} \quad (A.11)$$

$$C_2(x,t) = C_0 - 2\rho_f t\left(i^2\operatorname{erfc}\frac{x-l}{2Dt} + i^2\operatorname{erfc}\frac{x+l}{2Dt}\right) \quad (A.12)$$

REFERENCES

1 B.H. v.d. Schoot and P. Bergveld, Sensors Actuators, 8 (1985) 11.

2 B.H. v.d. Schoot and P. Bergveld, in Proc. Transducers'87, The Fourth International Conference on Solid-State Sensors and Actuators, Tokyo, June 2–5, 1988, Institute of Electrical Engineering Japan, Tokyo, p. 719.

3 W. Olthuis, B.H. v.d. Schoot, F. Chavez and P. Bergveld, Sensors Actuators, 17 (1989) 279.

4 B.H. v.d. Schoot and P. Bergveld, Sensors Actuators, 13 (1988) 251.

5 B.H. v.d. Schoot and P. Bergveld, Anal. Chim. Acta, 199 (1987) 157.

6 W. Olthuis, J. Luo, B.H. v.d. Schoot, P. Bergveld, M. Bos and W.E. v.d. Linden, Anal. Chim. Acta, 229 (1990) 71.

7 J. Luo, W. Olthuis, B.H. v.d. Schoot, P. Bergveld, M. Bos and W.E. v.d. Linden, Anal. Chim. Acta, 237 (1990) 71.

8 J. Luo, W. Olthuis, B.H. v.d. Schoot, P. Bergveld, M. Bos and W.E. v.d. Linden, in S. Middelhoek (Ed.), Proc. Transducers'91, The Sixth International Conference on Solid-State Sensors and Actuators, San Francisco, September, 1991, Elsevier, Amsterdam, Lausanne, p. 229.

9 A.J. Bard and L.R. Faulkner, Electrochemical Methods, Fundamentals and Applications, Wiley, New York, 1980, p. 249.

10 J. Luo, Adaptation of ISFET technology: a flat ISFET, Thesis, University of Twente, 1993.

11 G. Prentice, Electrochemical Engineering Principles, Prentice-Hall, Englewood Cliffs, NJ, 1991, p. 101.

12 Z. Galus, Fundamentals of Electrochemical Analysis, Wiley, London, 1976, p. 2.

13 E.L. Cussler, Diffusion, Mass Transfer in Fluid Systems, Cambridge University Press, Cambridge, 1984, p. 185.

14 R. de Levie, Electrochim. Acta, 9 (1964) 1231.

15 J. Crank, The Mathematics of Diffusion, Oxford University Press, London, 1975, p. 377.

Analytica Chimica Acta, 274 (1993) 25–35
Elsevier Science Publishers B.V., Amsterdam

Crayfish walking leg neuronal biosensor for the detection of pyrazinamide and selected local anesthetics

Donal Leech and Garry A. Rechnitz
Hawaii Biosensor Laboratory, Department of Chemistry, University of Hawaii at Manoa, 2545 The Mall, Honolulu, HI 96822 (USA)

(Received 6th October 1992)

Abstract

Neuronal biosensors based on the use of crayfish *Procambarus clarkii* walking legs are reported for the first time and possible analytical applications are explored. The neuronal biosensor is shown to respond selectively to the antitubercular drug and potent food marker, pyrazinamide. The sensor is characterized with respect to selectivity, dose-response relationship, reproducibility and operating lifetime. The detection of local anesthetics is accomplished by monitoring the decrease in pyrazinamide-induced nerve firing in the crayfish walking leg. This decrease is a result of the local anesthetic block of the axonal sodium channels in the nerves. Applicability of this novel procedure to analytical measurements is demonstrated by the construction of dose-response curves for several local anesthetics. Problems associated with the current sensor configuration are presented and future research directions that may improve the neuronal-based biosensor are discussed.

Keywords: Biosensors; Crayfish; Pyrazinamide

In recent years researchers have recognised the analytical applicability of the unique binding properties of neuronal receptors. Recent advances using isolated neuronal receptors, such as the nicotinic acetylcholine receptor (nAchR), include non-isotopic binding assays and the development of receptor-based biosensors. Biosensors have been designed using the nAchR that detect ligand binding as a change in capacitance [1], impedance [2] or fluorescence [3,4]. The difficulties associated with the isolation, purification, immobilization and stabilization of these receptors, however, has led to the investigation of intact receptors for biosensing applications. A neuronal biosensor has been reported which utilizes the visceral ganglia of the pond snail for the detection of the neurotransmitter serotonin [5].

Our approach has been to use intact chemoreceptor structures from the decapod crustacea for the detection of receptor stimulants. This approach allows the sensing cells to remain in their, presumably optimized, native environment. The chemoreceptors function by converting binding energy into electrical impulses (action potential spikes) that can be recorded by conventional electrophysiological microelectrode techniques. Our earlier papers reported the application of antennules from the blue crab *Callinectus sapidus* to neuronal biosensing [6–8]. All of our studies with the antennular chemoreceptor-based biosensors have recently been reviewed [9,10]. These studies demonstrated the extreme sensitivity, high selectivity and broad response range that could be achieved using this approach. Recently we reported the use of antennules from the freshwater crayfish *Procambarus clarkii* for the selective detection of the antitubercular drug pyrazinamide [11]. The freshwater crayfish offers better thermal

Correspondence to: G.A. Rechnitz, Hawaii Biosensor Laboratory, Department of Chemistry, University of Hawaii at Manoa, 2545 The Mall, Honolulu, HI 96822 (USA).

and time stability than the salt water crabs used in previous studies thus leading to longer viable sensor lifetimes and obviating the need for rigid control of the temperature.

Electophysiological investigations of the pyridine receptors located in the walking leg of the crayfish *Austropotamobius torrentium* have shown pyrazinamide to be the most effective stimulant of action potential firing among the 79 pyridine analogs tested [12]. In this communication we report on the first use of the the crayfish walking leg for the development of a chemoreceptor-based biosensor for the detection of pyrazinamide. This paper also reports on a novel use of the intact-chemoreceptor biosensor for the detection of local anesthetics. Local anesthetics (LAs) can be detected based on their ability to block the axonal sodium channel and thus their ability to decrease the excitability of nerve upon stimulation with the potent stimulant pyrazinamide.

Electrophysiological and behavioral studies have revealed the presence of chemoreceptors on the antennules and both first and second walking leg (pereiopod) of the crayfish [13]. Crayfish pereiopods are comprised of a two part protopod, the coxa and basis. The endopod (the walking leg lacks an exopod) rises from the protopod and consists of five articles: ischium, merus, carpus, propodus and dactylus. In the first and second pereiopod the propopodite and dactylopodite form a pincers. Chemosensory sensilla (aesthetascs) are located on the crayfish antennules and the first and second pereiopods. A schematic depicting the structure of the crayfish first pereiopod is shown in Fig. 1. Morphological investigation by Altner et al. [14] has shown that each sensillum of the crayfish *A. torrentium* consists of eight dendrites, six of which are chemosensitive, lying within a central canal. The pore of the canal is plugged with electron dense material suggested to be mucopolysaccharides through which all stimulus molecules must diffuse to reach the dendrites. The physiology of chemoreception has been presented in detail previously [6–11] and will not be discussed further here.

The structure and pK_a of the LAs investigated in this report are depicted in Fig. 2. Extensive electrophysiological studies have shown that the mode of action of the LAs is to block the voltage-dependent sodium channel in nerve membranes resulting in a depression in the excitability of the nerve fibers [15]. Several mechanisms have been proposed to describe the action of the LAs. The simplest of these, the one-site model, proposes that both charged and uncharged LAs bind at a single site in the channel, leading to channel block. A "modulated receptor hypothesis" has been proposed by several researchers [15–17] to account for the use-depen-

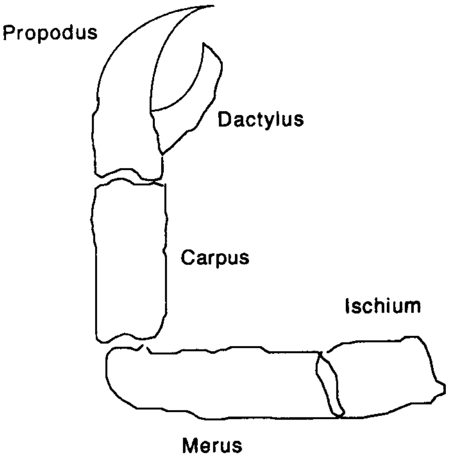

Fig. 1. Schematic diagram of the structure of the crayfish first periopod.

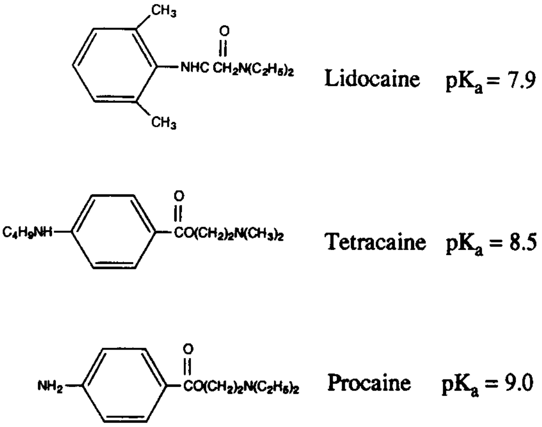

Fig. 2. The structure and pK_a of the local anesthetics investigated in this report.

dent blocking properties and the wide variety in the potency and duration of action of the LAs. This model postulates that each channel state (i.e., open, resting or inactivated) can have different kinetics of interaction with the LAs. The most rapid interaction of the LAs is for open channel block but their highest affinity is for inactivated forms of the channel. Studies have shown the molecular size, lipophilicity and charge of the LAs to be important determinants of potency of sodium channel block [15–18].

Many methods, including polarography [19] and spectrophotometry [20] have been reported for the detection of LAs. A recent paper reported the use of PVC-coated wire electrodes for the potentiometric determination of the cationic forms of the LAs [21]. A rapid assay procedure for LA activity has been reported based on the competitive inhibition of [^{3}H]batrachotoxinin A 20α-benzoate binding to voltage-dependent sodium channels in a vesicular preparation from the guinea pig cerebral cortex [22]. A non-isotopic assay procedure for the screening of LA activity and the quantitative detection of LAs is presented in this report. This report introduces the novel application of the intact-chemoreceptor

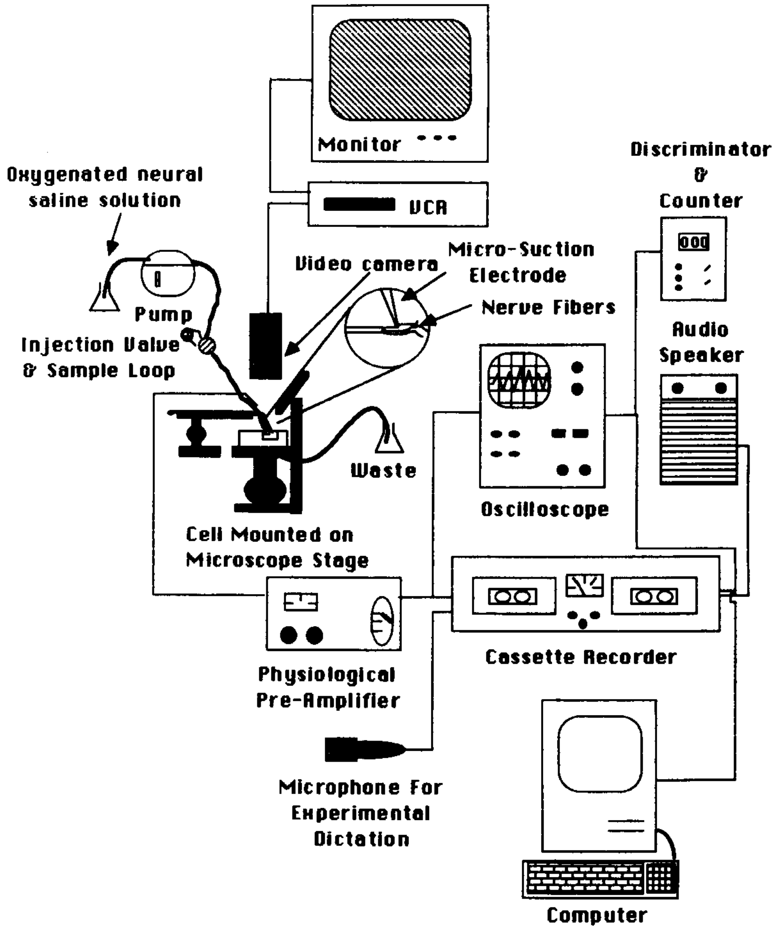

Fig. 3. Schematic of the experimental set-up used to record the action potential firing of the nerves.

biosensor for LA detection based on LA blockage of axonal sodium channels.

EXPERIMENTAL

Reagents

The neural bathing solution and carrier was prepared according to a modified Van Harreveld formula and consisted of 205 mM NaCl, 5.4 mM KCl, 13.5 mM $CaCl_2$, 2.6 mM $MgCl_2$ and 10 mM Tris–malate buffer adjusted to pH 7.5. Stock solutions of the local anesthetics, procaine hydrochloride, lidocaine hydrochloride and tetracaine hydrochloride (Sigma), the pyridine analogues, pyrazinamide, 3-acetyl pyridine and nicotinamide (Sigma), and all other possible stimulants were prepared daily or as required in the neural bathing media. Tracer studies were performed with a 2,6-dichlorophenolindophenol sodium salt (DCPIP, Sigma) dye solution in deionized water.

Apparatus

A schematic diagram of the experimental setup is shown in Fig. 3. The specially designed plexiglass cell was constructed to fit on the mechanical stage of a BioStar 1820 (Reichert-Jung) inverted biological microscope. The microscope was capable of a maximum magnification of 450 ×. A video unit attached to the microscope consisting of a Hitachi VK150 colour video camera connected to a Sony Trinitron color video monitor extended the maximum magnification capability to 1700 ×, thus allowing visualization of the sensory aesthetascs and nerve fibers. The video images were stored on video tape using a JVC HR-D660U video cassette recorder for subsequent photography with a Chinon CM-7 35-mm camera.

The cell consisted of a circular chamber of 2 cm diameter, surrounded by a water jacket for temperature control. The bottom of the cell was lined with a Sylgard 184 (Dow Corning) elastomer for the pinning of the preparations. The flow into and out of the cell was controlled by the same peristaltic pump (Rainin). The bathing solution was introduced and removed through two ports located approximately 2 mm from the top of the chamber (total depth of 12 mm) and 45° to each other. The outlet tubing was of a larger diameter than the inlet in order to maintain a constant operating volume in the cell. Test solutions were introduced via a four-way valve (Rheodyne) equipped with a 0.25-ml sample injection loop located 20 cm from the inlet port. Reference and ground wires were inserted into the cell and connected to a Grass P-15 physiological preamplifier. Glass micropipettes were pulled to approximately 25 μm taper (Narishige PP-83 glass microelectrode puller) and flame polished by rapidly passing through the flame. An Ag/AgCl electrode was inserted into the micropipette and positioned in the holder (E.W. Wright) and then placed in the micromanipulator (Narishige) and connected to the preamplifier. The amplifier output was monitored on a Sony Tektronix 314 storage oscilloscope and also fed into one channel of a Yamaha KX-W900U stereo cassette deck for storage on audio tape. A microphone enabled an oral account of the experiment to be recorded on the other channel of the audio tape and speakers attached to the stereo cassette recorder allowed aural monitoring of action potential firing. Data analysis was accomplished by feeding the stored data into a window discriminator and digital event counter (Newark Electronics) for frequency counting. Stored data was also fed into a Macintosh SE computer via a MacInstruments data acquisition package (G.W. Instruments) allowing the computer to function as a storage oscilloscope.

Procedures

The freshwater crayfish *P. clarkii* could be conveniently captured in the Manoa stream located on the university campus. The first pereiopod of the crayfish was excised at the ischium-merus joint, placed on a microscope slide and submerged in a drop of neural solution. The hard carapace and connective muscle were removed from the merus and carpus portions of the walking leg to reveal approximately 1 cm of nerve fibers. The whole preparation consisting of the propopodite and dactylopodite pincers and the nerve bundle was pinned into the cell, mounted on the microscope mechanical stage and connected to the flow lines. Oxygenated neural saline solution was circulated through the cell at all times in an effort to increase the viable lifetime of the sensing system. The Ag/AgCl pickup electrode was positioned with the micromanipulator to gently contact the nerve fibers and mild suction was applied to the back of the micropipette to fill the electrode with electrolytic fluid and establish good electrical contact with the nerve fibers. Spontaneous action potential firing of the nerves was then monitored on the oscilloscope (and over the speakers) to ensure good electrical contact and to check the viability of the nerves. The injection of the various analytes was carried out and the frequency of action potential firing monitored. If no response was observed the electrode was repositioned and the process repeated.

Frequency of action potential firing (spike frequency) was monitored by counting the number of events falling in a set time period, usually 8 s, with the window discriminator and event counter. Background (spontaneous) firing frequencies were also counted and subtracted from the response frequency. Dose-response curves for pyrazinamide were obtained by injection of serially diluted stock solutions always commencing with the least concentrated to minimize receptor saturation, adaptational effects and nerve damage by this toxic stimulant. The dose-response curves for pyrazinamide were constructed by plotting the maximum firing frequency versus concentration. Inhibition curves for the LAs were obtained by injection of mixed solutions consisting of a constant pyrazinamide concentration, to elicit action potential firing, and variable LA concentrations. The inhibition curves were constructed by plotting the decrease in the maximum pyrazinamide-induced firing frequency, or the decrease in action potential amplitude, versus concentration.

Tracer studies were performed by injection of 1 mM of DCPIP into the chamber using deionized water as the carrier. Samples of 50 μl were taken at intervals after the injection of DCPIP from the centre of the chamber and at the side of the chamber where the walking leg pincers were normally pinned. The samples were diluted to 0.5 ml with deionized water and their absorbance measured at 600 nm on a Milton Roy Spectronics 1201 spectrophotometer. The concentration was expressed as a percentage of the maximum concentration attained in the center of the chamber and related to the injected concentration by linear extrapolation. Standard solutions of DCPIP were also prepared and their absorbance measured to ensure that the Beer–Lambert law was obeyed over the concentration range used.

RESULTS AND DISCUSSION

Tracer studies

Tracer studies of the bathing cell using the dye DCPIP were performed in order to investigate the mixing process in the chamber and the relationship between the injected concentration and the maximum concentration reached in the chamber. Tracer studies are also helpful in determining the washout time of the stimulant. At the λ_{max} for DCPIP (600 nm) an ϵ_{600} of 16000 M^{-1} cm^{-1} was calculated from the linear absorbance–concentration curve for DCPIP concentrations up to 0.1 mM ($n = 6$, $r^2 = 0.9999$). Sampling of the tracer solution was from a point in the center of the chamber where the nerve fibers were pinned and electrode contact with the nerve fibers was normally achieved and also from a position at the side of the chamber 90° from the inlet where the crayfish pincers that contain the chemosensory aesthetascs were normally pinned.

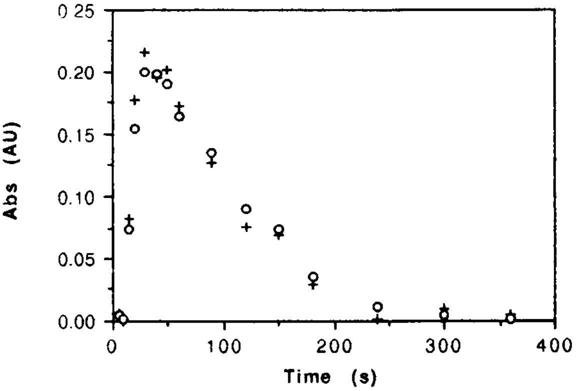

Fig. 4. Time course of injected DCPIP in the cell at sampling positions in the center of the cell (+) and 90° from the inlet (o).

The time course of the injected dye solution at both sampling positions in the chamber is shown in Fig. 4. The zero time indicates the time at which the sample injection loop was opened, thus explaining the 14-s time lag between injection and increase in response. This figure shows that little variation is seen in the time profile of the dye solution between the two different sampling positions, demonstrating the good mixing achieved in the chamber. The maximum in the response profile is attained approximately 35 s after injection of the tracer dye. The actual maximum concentration achieved in the cell was calculated, by linear approximation, to correspond to 13% of the injected dye concentration. All subsequent concentration values for pyrazinamide and the LAs refer to the injected concentration unless otherwise specified. From Fig. 4 the washout time required to remove all traces of the dye from the chamber was determined to be 4 min.

Pyrazinamide detection

Action potential firing can be induced in response to a depolarizing stimulus. This stimulus may be electrical (a depolarizing voltage or current pulse) or chemical (injection of a receptor agonist). in this study we utilize the potent stimu-

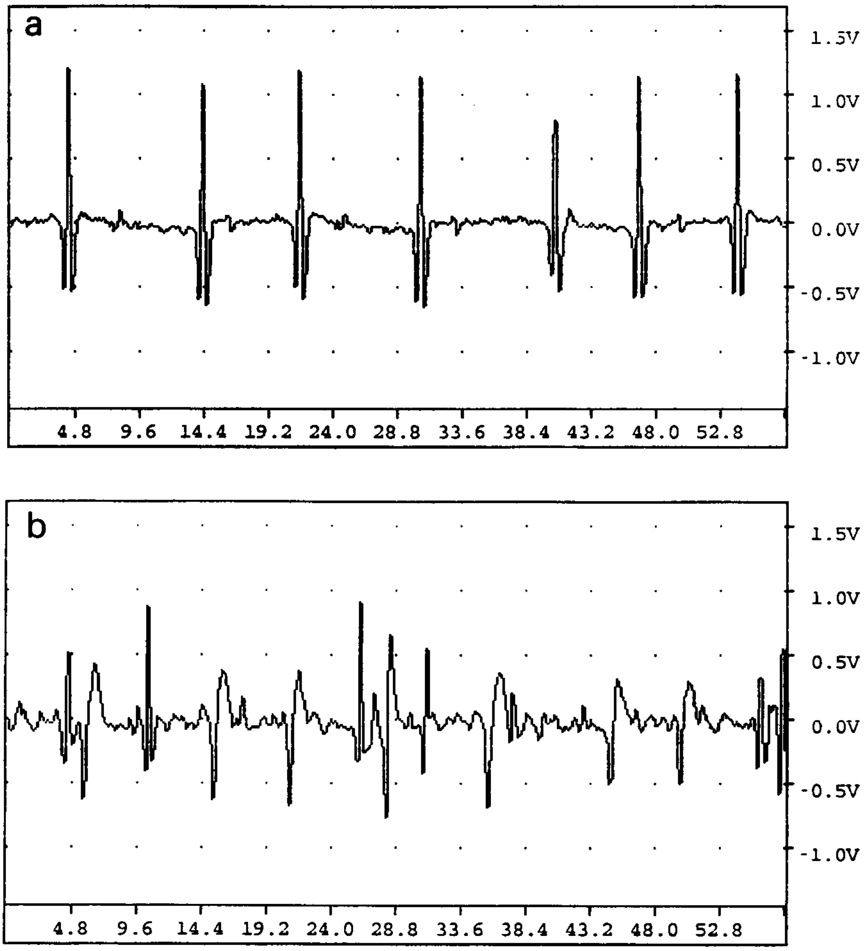

Fig. 5. Single-unit (a) and multi-unit (b) response data recorded at different crayfish walking leg nerve fibers in response to the injection of 5×10^{-4} M pyrazinamide. The data are shown as viewed with the MacInstruments data acquisition software after amplification and digitization.

lant pyrazinamide to elicit action potential firing in the nerves for the detection of nerve block by the LAs. The response of the crayfish antennular receptrode to this stimulant has been well characterized by our group [11]. The application of the chemoreceptors located in the first pereiopod of the crayfish to the detection of pyrazinamide is investigated in the following section. Properties of this pyridine chemoreceptor agonist which are favorable to its use as a stimulus for the detection of the LAs are also investigated.

As previously reported [6–11] there are two types of response patterns that can be obtained with the extracellular recording techniques used in this study, the so-called multi-unit and single-unit response patterns. These two response patterns are illustrated in Fig. 5, which depicts the response (after amplification and digitization) obtained at the crayfish walking leg upon injection of 5×10^{-4} M pyrazinamide. Multi-unit data consists of action potentials firing at various amplitudes in response to the stimulant. This is because the pickup microelectrode is normally in contact with several nerve fibers and the action potential amplitude detected is dependent on the seal between the micropipette and the nerve fiber. If only one nerve fires in response to injection of stimulant then a single-unit response pattern is observed, as shown in Fig. 5a. The analysis of single-unit data is simple, relying on the window discriminator to eliminate noise and the event counter to count the frequency of firing in response to stimulation application. Multi-unit responses are more difficult to analyze, requiring careful consideration of the window for discrimination of unwanted signals.

As discussed previously, an increase in the action potential firing frequency results from an injection of a chemoreceptor agonist. A typical lag time between injection of pyrazinamide and the onset of increase in action potential firing of 45–60 s was seen, with the firing frequency reaching a maximum approximately 15–30 s later. The lag time between maximum cell concentration (determined to be approximately 35 s after injection, from tracer studies above) and maximum firing frequency attainment may be attributed to the diffusion of the stimulant through the aesthetasc pore to reach the chemoreceptive dendrites; this lag has been reported previously for the detection of pyridine analogues at the crayfish *A. torrentium* walking leg [12]. The maximum firing frequency has been shown to be related to the concentration of applied agonist [6], allowing a dose-response curve of maximum firing frequency versus agonist concentration to be constructed for pyrazinamide detection at the crayfish walking leg. A typical dose-response curve is shown in Fig. 6. This curve indicates that an increase in firing frequency over background firing is observed for injections of pyrazinamide concentrations above 1×10^{-5} M. The dose-response curves show linear responses for concentrations ranging from 1×10^{-4} M up to 5×10^{-4} M. A response plateau is reached at concentrations above 5×10^{-4} M, possibly indicating receptor saturation. The dose-response curves obtained at the crayfish walking leg are similar to those reportedly obtained at the crayfish antennule [11]. In that study a different cell configuration was used which involved a flow injection type system with minimal dilution of injected agonist. If the walking leg dose-response curves are corrected for stimulant dilution in the cell system utilized in this study (vide supra) an ED_{50} value (concentration of half-maximal response) of approximately 2.8×10^{-5} M is obtained. This ED_{50} value is close to that obtained at the antennular receptrode [11] indicating the homogeneity of this

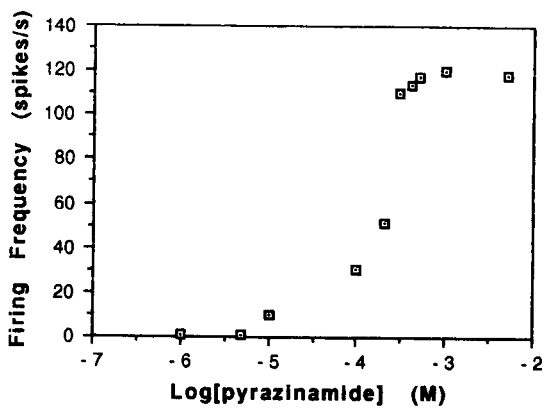

Fig. 6. Dose-response curve obtained at the crayfish walking leg for pyrazinamide.

chemoreceptor response from structure to structure.

The crayfish pyridine-sensitive units also respond to other pyridine analogues and a detailed study of the structure–activity relationship of this receptor in the walking legs of the *A. torrentium* crayfish has been reported [12]. The order of potency for the three pyridine based stimulants, pyrazinamide > 3-acetylpyridine > nicotinamide, tested in this study at the *P. clarkii* walking leg was similar to that at the *A. torrentium* walking leg. The selectivity of the pyridine-sensitive units in the walking leg of *P. clarkii* for pyridine analogues was investigated by injecting solutions of other possible stimulants. This included injections of neurotransmitters, excitatory amino acids, hormones, essential amino acids and other possible food markers. No response at the pyridine-sensitive units for any of these solutions was observed indicating the high selectivity that can be achieved with the chemoreceptor-based biosensor.

From the dose-response behaviour of pyrazinamide at the walking leg chemoreceptor, a pyrazinamide concentration of 5×10^{-4} M was selected to elicit axonal action potential firing in order to detect channel block by the local anesthetics. This concentration stimulates the maximum firing frequency response while minimizing the nerve poisoning that can result from injections of this toxic drug. The reproducibility of repeated injections of this concentration of pyrazinamide was investigated to ensure ample time was allowed for recovery of the nerves between injections and to assess the working lifetime of the sensor for the detection of the LAs. The time profile resulting from repeated injections of 5×10^{-4} M pyrazinamide is shown in Fig. 7. In this study a 10-min rinse time between injections was utilized as shorter rinse times resulted in a rapid desensitization leading to a decrease in firing frequency maxima with each successive injection. Figure 7 demonstrates the reproducibility of the biosensor for repeated pyrazinamide injections. Slight variations in the firing frequency maximum occur over the first 9 injections, yielding a mean firing frequency maximum value of 71 spikes s^{-1} (relative standard deviation of 10%). The decrease in the maximum firing frequency with subsequent injections may be attributed to nerve damage caused by the repeated injections of the toxic pyrazinamide and/or by nerve damage resulting from the stress associated with the suction microelectrodes. Adaptational events also contribute to the observed decrease as seen in Fig. 7 from the resulting slight recovery in the firing frequency maximum upon increasing the rinse time to 20 min. The operating lifetime of the biosensor can thus be assessed to be limited to approximately 2 h. An improvement in the viable lifetime of the dissected nerves by incubation in oxygenated saline solution, to approximately two days has been achieved [23]. However, extension of the operating lifetime of the system using the current invasive microelectrode detection procedures has not been achieved.

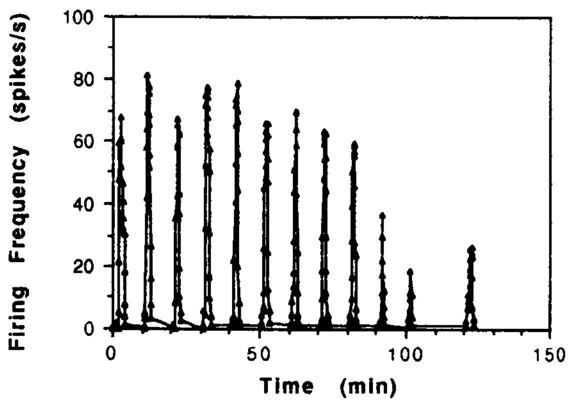

Fig. 7. Time profile of the neuronal firing frequency in response to repeated injections of 5×10^{-4} M pyrazinamide.

Local anesthetic detection

The detection of the LAs can be achieved by monitoring the decrease in elicited excitability of the nerves upon injection of increasing LA concentrations. Monitoring the decrease in spontaneous background firing of the nerves upon injection of the LAs proved unfeasible because of the low rate of spontaneous firing and the variability in firing frequency within and between nerve populations. Response curves were generated by monitoring the decrease in neuronal activity, as described below, upon injection of mixed solutions of the stimulant, 5×10^{-4} M pyrazinamide, and the LA. Rinse times of 10 min were normally allowed for the recovery from block by the nerves except for concentrations of LA higher than 1×10^{-4} M, when longer rinse times were required.

Two data analysis procedures were adopted for the construction of inhibition curves for the LAs at the crayfish walking leg, depending on the type of response elicited by injection of pyrazinamide. For the single-unit data response patterns, inhibition curves could be constructed from the decrease in the detected compound action potential amplitude with increasing LA concentration. This decrease is a result of the increasing block of axonal sodium channels with increasing LA concentration. Inhibition curves for the local anesthetics lidocaine and tetracaine constructed in this manner are shown in Fig. 8. For the multi-unit response patterns it was difficult to resolve the responding nerve action potential spikes from each other and the background, thus a different data analysis approach was devised. Using the window discriminator, a cut-off action potential amplitude was selected and all of the action potential spikes falling within the window were counted. Upon injection of increasing concentrations of the LAs an increasing proportion of the action potential spikes fail to reach the minimum amplitude required to be counted. Thus inhibition curves, similar to those obtained from the single-unit response data, can be constructed from the decrease in the firing frequency maximum with injection of increasing LA concentrations. Inhibition curves for procaine, lidocaine and tetracaine analyzed in this manner are presented in Fig. 9. The response curves are affected by the choice of the discrimination window and this is reflected in the variability of the results from preparation to preparation. Other factors, such as differences in nerve fiber diameters [24] and the use-dependent blocking properties of the LAs [15–18] may also contribute to the variability in inhibition curves from nerve to nerve.

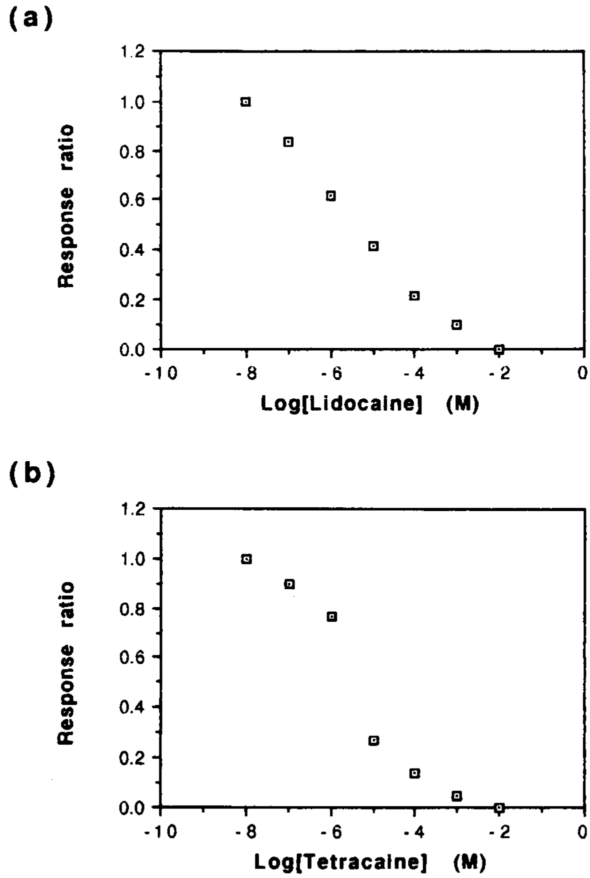

Fig. 8. Inhibition curves constructed from the decrease in action potential amplitude upon injection of increasing concentrations of the local anesthetics lidocaine (a) and tetracaine (b). The response ratio is the ratio between action potential amplitude obtained upon injection of pyrazinamide/local anesthetic mixed solutions and the action potential amplitude obtained for injections of pyrazinamide alone. See text for further details.

From Figs. 8 and 9 IC_{50} values of approximately 2×10^{-6} M for both lidocaine and tetracaine and 5×10^{-5} M for procaine can be determined. The relative blocking potency of the LAs has been shown to be related to the pH of the bathing solution and also to the relative hydrophobicity of the LAs [15–18]. Because both lidocaine and tetracaine have lower pK_a values than procaine, a higher proportion of these drugs will exist in the more potent neutral form thus explaining their relative potencies. The similar potency of action between tetracaine and lidocaine even with the differences in pK_a values can be attributed to the more hydrophobic nature of tetracaine thus allowing this LA to interact with the channel to the same extent as lidocaine. In fact other workers have reported on the higher potency of tetracaine with respect to lidocaine,

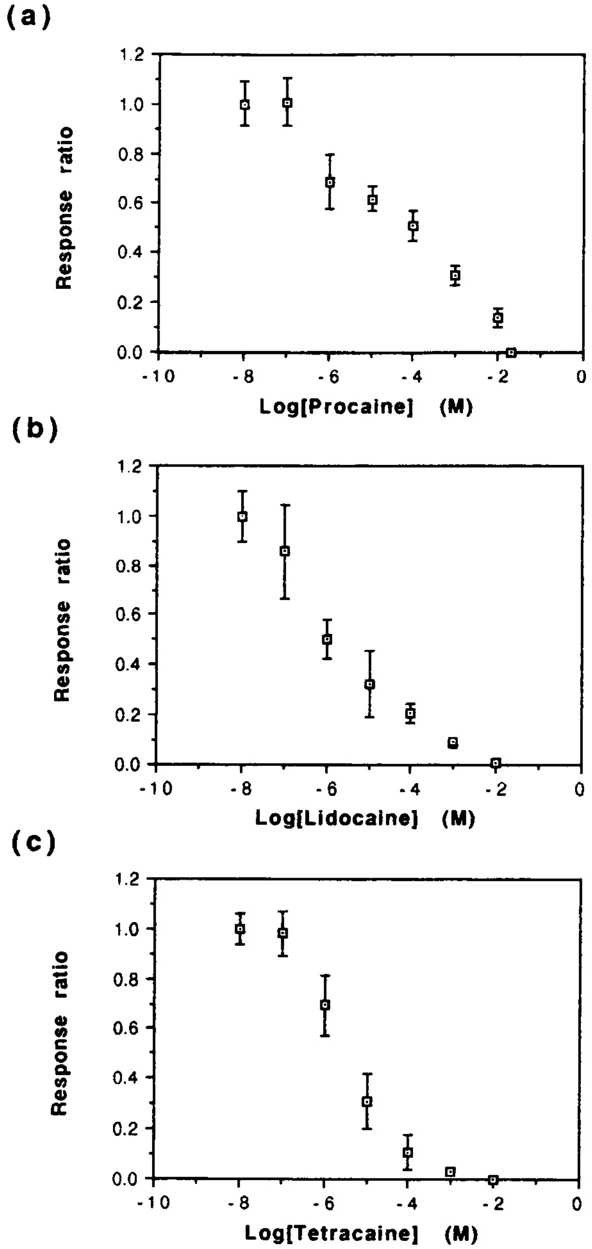

Fig. 9. Inhibition curves constructed from the decrease in the firing frequency in response to stimulant injection upon injection of increasing concentrations of the local anesthetics procaine (a), lidocaine (b) and tetracaine (c). The response ratio is the ratio between the firing frequency obtained upon injection of 5×10^{-4} M pyrazinamide/local anesthetic (variable concentration) mixed solutions and that obtained upon injection of 5×10^{-4} M pyrazinamide alone. See text for further details.

with the relative potency of the three local anesthetics investigated in these studies, based on voltage-clamped frog nerve preparations [18] and competitive binding of the LAs with radio-labelled batrachotoxin at sodium channels in a vesicular preparation from guinea pig cerebral cortex [22], determined to be tetracaine > lidocaine > procaine. The discrepancies between the previously reported potencies and those reported here may be attributed to the above mentioned variables and also to the different detection methods and preparations utilized in these studies. Future research into the application of intact receptors for the detection and activity assay of channel blockage in order to improve the procedure is discussed below.

Conclusion

This report demonstrates the utility of the chemoreceptors based in the walking leg of the crayfish for the detection of the antitubercular drug pyrazinamide. This drug has been shown to elicit a potent reponse at the walking legs of the crayfish. The properties of the response for pyrazinamide have been utilized for the development of a novel detection procedure at the walking legs. This procedure demonstrates the utility of the chemoreceptor-based sensing system for the novel application of the detection of local anesthetic induced channel blockage. As the nerve blocking properties of the LAs is related to their pharmacological activity this procedure has an added application in the possible screening of new local anesthetics. Although there are several problems with the current procedure, such as limited lifetimes, variability of results and the tedious experimental procedures, future directions in this research could lead to a viable sensor for the LAs and a simple non-isotopic screening assay for the channel blocking activity of drugs. Future work in this laboratory will focus on the use of electrical stimulation of the nerve fibers for detection of nerve block and on further possible procedures for the extension of the operating lifetimes of the chemoreceptor-based biosensors. Promising possibilities in this direction include the use of alternative detection methods to the invasive microelectrode techniques, such as voltage-sensitive dyes and the detection of the biomagnetic field surrounding the nerve fibers upon stimulation of action potential firing.

The assistance of D. Wijesuriya is acknowledged. Financial support from the National Science Foundation is gratefully acknowledged.

REFERENCES

1 M.E. Eldefrawi, S.M. Sherby, A.G. Andreou, N.A. Mansour, Z. Annau, N.A. Blum and J.J. Valdes, Anal. Lett., 21 (1988) 1665.
2 R.F. Taylor, I.G. Marenchic and E.J. Cook, Anal. Chim. Acta, 213 (1988) 131.
3 K.R. Rogers, J.J. Valdes and M.E. Eldefrawi, Anal. Biochem., 182 (1989) 353.
4 K.R. Rogers and M.E. Eldefrawi, Biosensors Bioelectronics, 6 (1991) 507.
5 R.S. Skeen, W.S. Kisaalita, B.J. Van Wie, S.J. Fung and C.D. Barnes, Biosensors Bioelectronics 5 (1990) 491.
6 S.L. Belli and G.A. Rechnitz, Anal. Lett., 19 (1986) 403.
7 S.L. Belli and G.A. Rechnitz, Fresenius' Z. Anal. Chem., 331 (1988) 439.
8 R.M. Buch and G.A. Rechnitz, Anal. Lett., 22 (1989) 2685.
9 R.M. Buch and G.A. Rechnitz, Anal. Chem., 61 (1989) 533A.
10 D. Leech and G.A. Rechnitz, Electroanalysis, in press.
11 D. Wijesuriya and G.A. Rechnitz, Anal. Chim. Acta, 256 (1992) 39.
12 H. Hatt and I. Schmiedel-Jakob, J. Comp. Physiol. A, 154 (1984) 855.
13 M.S. Laverack, in M.A. Ali (Ed.), Nervous System in Invertebrates, Plenum Press, New York, 1987, pp. 323–352.
14 I. Altner, H. Hatt and H. Altner, Cell Tissue Res., 228 (1983) 357.
15 B. Hille (Ed.), Ionic Channels of Excitable Membranes, Sinauer, Sunderland, MA, 1984.
16 B. Hille, J. Gen. Physiol., 69 (1977) 497.
17 L.M. Hondeghem and B.G. Katzung, Ann. Rev. Pharmacol. Toxicol., 24 (1984) 387.
18 K.R. Courtney, J. Pharmacol. Exp. Therapeutics, 213 (1980) 114.
19 V.V. Ogutsov and L.P. Yavors'ka, Farm. Zh., (1986) 62.
20 M.E. El-Kommos and K.M. Emara, Analyst, 112 (1987) 1253.
21 H. Satake, T. Miyata and S. Kaneshina, Bull. Chem. Soc. Jpn., 64 (1991) 3034.
22 E.T. McNeal, G.A. Lewandowski, J.W. Daly and C.R. Creveling, J. Med. Chem., 28 (1985) 381.
23 D. Wijesuriya and G.A. Rechnitz, Anal. Chim. Acta, 264 (1992) 189.
24 A. Staiman and P. Seeman, Can. J. Physiol. Pharmacol., 52 (1974) 535.

Analytica Chimica Acta, 274 (1993) 37–46
Elsevier Science Publishers B.V., Amsterdam

Potentiometric ion- and bioselective electrodes based on asymmetric polyurethane membranes

Dong Liu and Mark E. Meyerhoff
Department of Chemistry, University of Michigan, Ann Arbor, MI 48109 (USA)

Howard D. Goldberg and Richard B. Brown
Department of Electrical Engineering and Computer Science, University of Michigan, Ann Arbor, MI 48109 (USA)

(Received 13th May 1992; revised manuscript received 14th September 1992)

Abstract

The potentiometric ion responses of ammonium- and proton-selective electrodes prepared by incorporating appropriate neutral carriers within novel asymmetric polyurethane membranes are reported. The membranes are formed by first casting a plasticized polyurethane(PU)/terpoly(vinyl chloride/vinyl acetate/vinyl alcohol) (PVA)-based ion-selective membrane and then applying a thin second layer of a more hydrophilic polyurethane (HPU) containing polylysine. The resulting asymmetric membranes function equivalently to normal PU/PVA membranes and conventional poly(vinyl chloride) type membranes in terms of potentiometric ion selectivity and dynamic response properties. The large amount of amine functional groups from the polylysine within the outer hydrophilic layer can be further activated for direct enzyme immobilization. As examples, adenosine deaminase and urease are immobilized on ammonium- and proton-selective membranes, respectively, to yield adenosine and urea electrodes with good dynamic responses and sensitivities. Advantageous use of this new membrane system for preparation of solid-state microfabricated enzyme-based sensors is also described.

Keywords: Biosensors; Ion-selective electrodes; Potentiometry; Asymmetric membranes; Polyurethane membranes; Solid-state electrodes

Over the last three decades, a variety of bioselective electrodes have been developed using potentiometric gas- and ion-selective membranes as transduction elements [1–4]. Appropriate bioreagents (such as enzymes, antibodies, bioreceptors, cells and tissues) are immobilized on such transducers in a manner that enables the detection of the product of the corresponding biological reaction in a thin layer of solution adjacent to the electrode's surface. Immobilization methods used include entrapment within a crosslinked polymer matrix, physical adsorption and covalent attachment through bifunctional crosslinking reagents [5]. Use of simple polymer membrane type ion-selective electrodes [6–10] (e.g., ammonium, carbonate, pH) as the base sensing elements has the advantage of providing biosensors that are easy to fabricate and exhibit rapid response times. In principle, potentiometric biodetection schemes based on these transducers can also be combined with the modern silicon technology to make small, multisensing and disposable solid-state biosensors [11–15] that could serve as flow-through biodetectors, or single-use biosensing devices. While lack of selectivity over endogenous ions in real

Correspondence to: M. E. Meyerhoff, Department of Chemistry, University of Michigan, Ann Arbor, MI 48109 (USA).

samples has been a problem with ion-selective electrode-based biosensors [7], a variety of new approaches to eliminate these interferences, particularly in flow-through detection systems, have been introduced recently with considerable success [16–18].

Traditionally, enzymes have been deposited on conventional poly(vinyl chloride) (PVC) type ion-selective membranes via glutaraldehyde crosslinking reactions, etc. [2,5]. Such immobilized protein layers, however, generally have poor adhesion to the very hydrophobic surface of the plasticized PVC membrane. While modification of the membranes such as using functionalized polymers (e.g., aminated or carboxylated PVC) has been attempted to covalently attach or adsorb the bioreagents to the hydrophobic PVC membranes [10,19,20], the number of available functional groups for such purposes is often quite low, yielding biosensors with poor bioreagent loading factors.

The problem of efficiently attaching enzymes and other bioreagents to polymer membrane electrode surfaces has been addressed previously by Cha and Meyerhoff [9], who developed novel asymmetric cellulose acetate type ion-selective membranes for such purposes. These membranes, while useful for preparing conventional electrodes in which the membrane is mounted between the sample and inner reference electrolyte solutions, are not suitable for preparation of solid-state (or solid-contact) type probes. This is because the more hydrophilic outer cellulose acetate film used for enzyme immobilization must be coated from the back side with appropriate plasticizer/ionophore/cellulose acetate cocktail to render the resulting dual layer films ion responsive. Although Gotoh et al. [12] have suggested the use of poly(vinyl butyral) (PVB) membranes to prepare micro-field effect transistor based solid-state biosensors, such PVB films served only as a matrix for the immobilized enzymes and did not need to exhibit electrochemical response and selectivity toward given ions. This is because the underlying metal oxide gate of the FET was used as an effective pH transducer to monitor pH changes arising from the enzyme reactions within the PVB layer.

In this paper a new type of asymmetric ion-selective membrane is described which is potentially more useful for fabrication of solid-state type potentiometric biosensors. The proposed membrane system consists of a very thin hydrophilic polyurethane (HPU) membrane possessing a high density of amine functional groups (in the form of polylysine) that is coated and fused to an underlying more hydrophobic plasticized polyurethane (PU)/poly(vinyl chloride/vinyl acetate/vinyl alcohol) (PVA) membrane containing the appropriate ion carrier. The potentiometric response of the asymmetric polyurethane membranes is shown to be essentially the same as the base ion-selective membrane (PU/PVA) and the large amount of functional groups within the outer hydrophilic film can be used for the covalent attachment of bioreagents to the membrane's surface. Since the underlying PU/PVA ion-selective film has been shown previously to adhere very tightly to silicon dioxide and silicon nitride surfaces [21], the new asymmetric membrane system is well suited for fabrication of solid-state biosensor devices. Indeed, the performance of both conventional and solid-state potentiometric enzyme electrodes prepared with this asymmetric membrane system is presented below using urea and adenosine as model analytes. It should be noted that although polyurethane matrices have been used previously as solid-phases for enzyme and protein immobilization [22,23], in such systems, the polyurethanes were never an integral part of a signal transducer, as is reported herein.

EXPERIMENTAL

Apparatus

For preparation and testing of conventional sensor designs, the asymmetric membranes with and without immobilized enzymes were mounted in Philips electrode bodies (IS-561) (Glasblaserei Möller, Zürich). The external reference electrode was a double-junction Ag/AgCl Fisher electrode. The potentiometric measurements of the ion-selective electrodes were monitored through a high impedance amplifier to a Zenith Z-100 PC computer equipped with a Data Translation A/D converter system (DT2801).

Gel permeation chromatography (GPC) on a Waters ALC 200 system (Milford, MA) was used to determine the molecular weight of the hydrophilic polyurethane. The effluent (in THF) was monitored by a differential refractometer (R401) and the retention time of the sample through a series of three μStyragel columns of pore size 500, 10^3 and 10^4 Å was used for the calculation of molecular weight based on prior calibration with narrow molecular weight polystyrene standards.

Reagents

Tecoflex polyurethane (PU) (SG-80A) was obtained from Thermedics (Woburn, MA). The terpolymer, poly(vinyl chloride/vinyl acetate/vinyl alcohol) (80:5:15 wt.%, MW 40000) was a product of Scientific Polymer Products (Ontario, NY). Nonactin, bis(2-ethylhexyl) sebacate (DOS), bis(2-ethylhexyl) adipate (DOA) and potassium tetrakis(4-chlorophenyl) borate (KTpClPB) were purchased from Fluka (Ronkonkoma, NY). Adenosine, adenosine deaminase (ADA, Type VII, from calf intestinal mucosa), urease (type VII, from Jack Beans), glutaraldehyde and polylysine (PLS) (hydrobromide, MW 30000–70000) were obtained from Sigma (St. Louis, MO). Tridodecylamine (TDDA) was obtained from Eastman Kodak (Rochester, NY) and silicon(IV) tetrachloride ($SiCl_4$; 1.0 M solution in dichloromethane) was from Aldrich (Milwaukee, WI). The hydrophilic PU (HPU) (40% water uptake) was a gift from Mr. Peter Burleigh, Mallinckrodt Sensor Systems (Ann Arbor, MI). It was prepared according to the procedure outlined in Ref. 24.

All other chemicals were of analytical-reagent grade. All standard solutions and buffers were prepared with reverse osmosis/deionized water.

Preparation of asymmetric ion-selective membranes

Figure 1 shows a schematic diagram of the asymmetric polyurethane membrane, depicted in this case with an enzyme layer attached to the polylysine incorporated within the outer HPU film.

The basic underlying ion-selective membrane was composed of 33 wt.% of PU/PVA (80 wt.% of PU and 20 wt.% of PVA), 66 wt.% of plasticizer and 1 wt.% of ionophore. For ammonium ion-selective membranes, DOA was used as plasticizer and nonactin as the ionophore. For proton-selective membranes, DOS and TDDA served as the plasticizer and pH ionophore [25], respectively, and KTpClPB at 1 wt.% was also added to the membrane casting solution. All of the membrane components (total mass = 200 mg) were dissolved in THF and cast into a 22 mm (i.d.) glass ring placed on a glass plate. The THF solvent was allowed to evaporate overnight before further coating with the outer HPU/PLS layer.

The second layer of the asymmetric membrane was prepared by first treating the surface of the

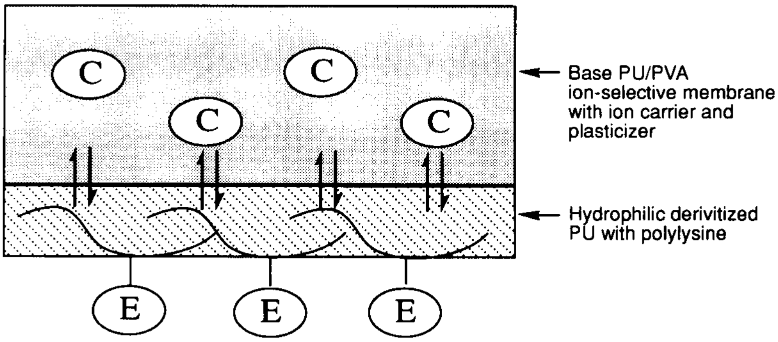

Fig. 1. Schematic diagram of the asymmetric polyurethane-based ion-selective membrane configured with immobilized enzyme layer: C, ion carrier; E, enzyme.

base PU/PVA ion-selective membrane with 150 μl of 0.02 M $SiCl_4$ (in CH_2Cl_2) for 2–3 min. Then, 1 mg of PLS with 10 mg of HPU in a mixed solvent (250 μl of methyl alcohol and 50 μl of THF) was applied on top of the base PU/PVA membrane. Several hours were required for the outer film to cure. In the case of proton-selective asymmetric membranes, only 1 mg of PLS and 5 mg of HPU in the same amount of mixed solvent were applied to the surface of the base PU/PVA membrane.

Electrodes were prepared by punching small disks from the above membranes and mounting them in the Philips electrode body with HPU/PLS layer facing out toward the sample side. The internal reference electrolyte was 0.1 M of NH_4Cl for NH_4^+-selective electrodes and 0.02 M NaH_2PO_4–0.03 M Na_2HPO_4–0.015 M NaCl, pH 7.0, for the proton-selective electrodes. All potentiometric measurements were made at room temperature with a sample volume of 100 ml.

Immobilization of adenosine deaminase / urease on the asymmetric ion-selective membranes

Adenosine deaminase and urease were attached to the surface of the asymmetric membranes using the glutaraldehyde crosslinking method described in Ref. 9 with minor modifications. For the two-step glutaraldehyde method, the asymmetric ion-selective membrane mounted in the electrode body was immersed in 2.5% of glutaraldehyde solution for 5 min. After brief washing of the membrane with cold water, 10 μl of ADA (19 units) or urease (286 units) (prepared by dissolving 0.5 mg ADA/urease in 10 μl of 0.05 M phosphate buffer, pH 7.0) was applied onto the outer surface of the membrane (surface area of 12.6 mm^2).

For the one-step glutaraldehyde method, 3.5 μl of glutaraldehyde and 10 μl of enzyme solution were sequentially applied on the surface of the asymmetric membrane mounted within the electrode body. The coupling reaction was allowed to proceed for 12 h at 4°C. The membrane was then washed with Tris–HCl buffer (0.05 M, pH 7.2) and stored in buffer at 4°C before use.

Evaluating potentiometric responses of conventional ion- and bioselective electrodes

The potentiometric responses of NH_4^+/H^+-selective electrodes and the corresponding ADA/urease enzyme electrodes were evaluated by addition of standard solutions of inorganic salt or adenosine/urea into 100 ml of well stirred buffer solution at room temperature. The background electrolyte used depended on the ions and substrates being examined (0.05 M Tris–HCl, pH 7.2, for NH_4^+, adenosine, and urea response with NH_4^+-selective membrane electrodes; 11.4 mM boric acid–6.7 mM citric acid–10 mM NaH_2PO_4 for pH response, and 0.001 M Tris–HCl–0.1 M NaCl, pH 7.0, for urea response with H^+-selective membrane). For evaluating the pH response of the TDDA-doped membranes, the pH of the boric acid/citric acid/phosphate universal buffer was varied by addition of either NaOH or HCl while simultaneously measuring the pH of the solution with a calibrated glass electrode. For the ammonium-selective membranes, ion selectivity coefficient data were obtained by the separate solution method [26].

Preparation of solid-state enzyme electrodes

The solid-state biosensor design examined in these studies is illustrated in Fig. 2. Aluminum conductor leads were patterned on silicon wafers, and insulated (except at the sensing site) with silicon nitride using standard microelectronic fabrication procedures. A layer of silver epoxy was

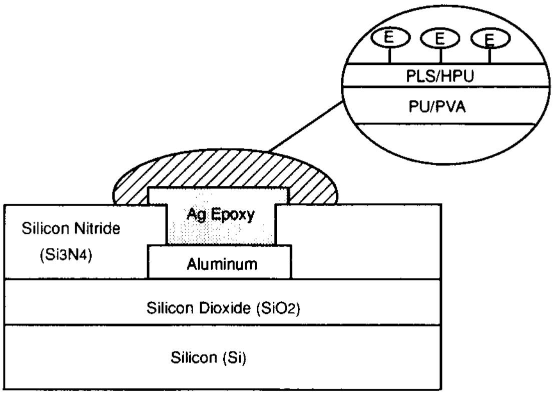

Fig. 2. Side view of the solid-state biosensor fabricated with asymmetric polyurethane membrane.

then screen printed over the exposed aluminum at the sensing site. A thin (100–300 μm) layer of the plasticized PU/PVA polymer casting solution containing either TDDA or nonactin was then cast onto the silver epoxy layer. This membrane adhered tightly to the silver epoxy and the surrounding silicon nitride coating of the wafer. A very thin layer of HPU containing polylysine was then coated over the ion-selective layer using a $SiCl_4$ pretreatment step as described above for the regular asymmetric membranes. Urease and adenosine deaminase were then immobilized by the one- or two-step glutaraldehyde procedures outlined above.

RESULTS AND DISCUSSION

Characterization of asymmetric membranes

A key component of the asymmetric ion-selective membrane system is the outer hydrophilic polyurethane (HPU) material which can be loaded with polylysine for subsequent bioreagent immobilization. This membrane must be hydrophilic enough to readily pass ions liberated from any biocatalytic reaction occurring at the surface. Preliminary characterization of the HPU film consisted of measuring its water uptake as well as determining its elemental composition (C, H and N analysis) and molecular weight (by GPC), and comparing these values to the supposedly more hydrophobic Tecoflex material which comprises 80 wt.% of the polymer material used to formulate the underlying ion-selective layer. The average molecular weight of the HPU material was found to be 45 000, which is much lower than that found for the hydrophobic polyurethane (MW 190 000). Water uptake experiments indicated that the HPU material absorbs water to a far greater extent than the hydrophobic Tecoflex material (40 wt.% vs. 1 wt.%). Elemental analysis of the two polymers yielded the following results: C 66.48%, H 11.13%, N 2.29% for the hydrophobic Tecoflex polyurethane; C 61.30%, H 9.99%, N 3.70% for the HPU. This elemental analysis data correlates with the fact that more diisocyanate reagent, and thus more urethane linkages are present within the HPU polymer and this leads to a more hydrophilic polymer with enhanced water uptake [24].

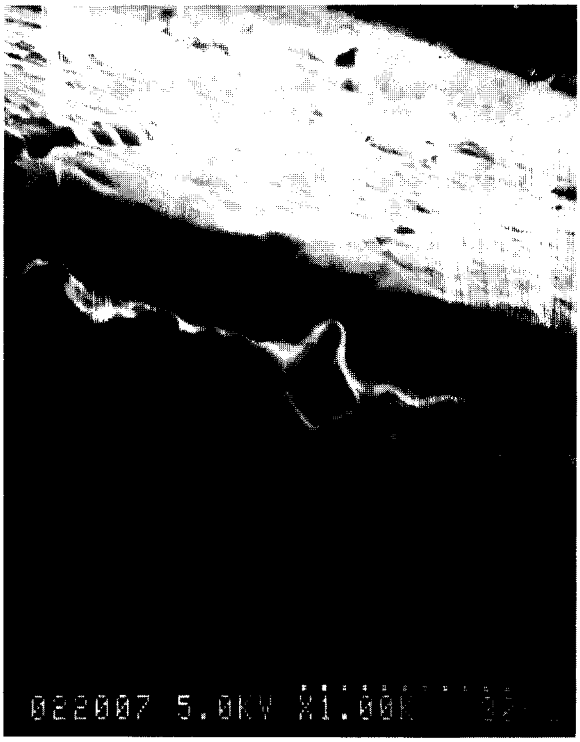

Fig. 3. Scanning electron micrograph of the cross-section of an asymmetric ion-selective polyurethane membrane.

A scanning electron micrograph of the cross-section of a dry asymmetric ion-selective polyurethane membrane is shown in Fig. 3. The thicker layer is the plasticized PU/PVA ion-selective membrane (approximately 300 μm in thickness), while the upper thin layer is formed from the HPU mixed with polylysine (HPU/PLS) (approximately 9 μm in thickness). It can be seen that the textures of two layers are quite different. The hydrophobic plasticized bulk layer is more dense while the upper layer appears somewhat porous, apparently due to its more hydrophilic character.

The adhesion of the hydrophilic HPU/PLS layer to the underlying hydrophobic PU/PVA membrane is greatly enhanced by applying 0.02 M of $SiCl_4$ to the surface of the thicker PU/PVA layer containing the ion-selective reagents (e.g., nonactin or TDDA). Indeed, using this procedure, the two layers remain fused for extended periods even when continuously soaked for 30 days in aqueous solution. The addition of the $SiCl_4$ apparently helps crosslink the terminal hydroxyl groups on the HPU with the surface hydroxyl groups from the vinyl alcohol portion of the PVA terpolymer and the terminal hydroxyl groups of the Tecoflex PU. An energy dispersive x-ray spectrum (EDS) of the cross-section of the asymmetric polyurethane membrane suggests that the $SiCl_4$ is mostly distributed at the interface of the two layers and penetrates into the underlying bulk ion-selective membrane to a depth of about 10 μm. Only low intensity Si or Cl bands were observed near the surface of the asymmetric HPU/PLS membrane, suggesting that the amine groups of the polylysine at the surface are not greatly affected by the added $SiCl_4$ and are free to be used for enzyme immobilization.

It is believed that the potentiometric ion response of the asymmetric membrane occurs at the interface of the HPU layer and the plasticized PU/PVA film. That is, the HPU/polylysine layer acts as a thin hydrophilic sponge in which ions readily move up to the hydrophobic PU/PVA/ionophore film where they participate in an equilibrium phase extraction creating the interfacial charge separation or phase boundary potential [27] which changes as a function of ion activities.

The ability of the outer HPU film to retain the added polylysine after prolonged exposure to aqueous solution was also investigated. Since the polylysine is not chemically attached to the outer HPU, it was initially thought that this very hydrophilic cationic material would leach out quickly with time. To investigate this possibility, the outer surface of the asymmetric membranes was treated with trinitrobenzenesulfonate (TNBS), a reagent that reacts rapidly with the primary amine groups of polylysine to yield a color change from yellow to orange-red [28]. This test was carried out both before and after extended soaking and washing sequences. It was found that the degree of color formation did not change appreciably even after repeatedly soaking the membranes in Tris–HCl buffer solution for 7 days, with frequent changes of the buffer each day (5 times per day). Thus, it appears that the polylysine is well entrapped/entangled within the hydrophilic polyurethane membrane and reactive amine groups remain at the surface for extend periods of time. It should be noted that polylysine has been used previously for the non-covalent immobilization of anionic charged biomolecules, such as heparin, by taking advantage of its polycationic character to yield strong charge–charge interaction [29]. However, the amine groups of anchored polylysine can also be used for covalent enzyme immobilization via classical crosslinking agents (e.g., glutaraldehyde). Since the covalent binding is irreversible, more stable immobilization can be achieved.

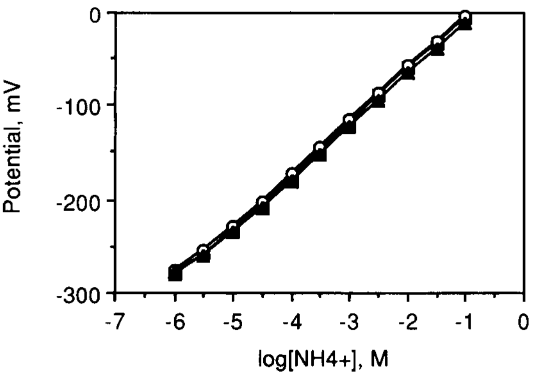

Fig. 4. Potentiometric response of ammonium-selective membranes doped with nonactin: (□) PVC membrane; (○) PU/PVA membrane; (▲) PU/PVA-HPU/PLS asymmetric membrane.

Potentiometric ion response and selectivity of the asymmetric membranes

Before using the asymmetric membranes to prepare biosensors, it is important to document that such membranes do indeed respond potentiometrically to ions, and with response characteristics and selectivities nearly equivalent to conventional polymer membrane ISEs. Figure 4 illustrates the typical equilibrium potentiometric responses observed toward ammonium ions in a Tris–HCl buffer background electrolyte for electrodes fabricated with an asymmetric membrane, a plain PU/PVA membrane (no outer HPU/PLS layer), and a conventional PVC membrane, all containing nonactin as the membrane active ionophore. As shown, the potentiometric re-

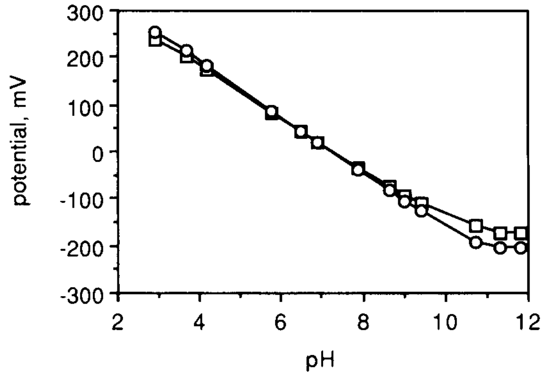

Fig. 5. Potentiometric pH response of TDDA-doped polyurethane membranes. (○) PU/PVA membrane; (□) PU/PVA–HPU/PLS asymmetric membrane.

sponse toward ammonium ions, in terms of slope (typically 56 mV/decade in the range of 10^{-5} to 10^{-1} M of NH_4^+) and detection limits, is essentially equivalent for the three different membranes. Response times were also quite similar (typically within 10 s), indicating that the diffusion of ammonium ions through the outer HPU/PLS thin film is rather rapid, at least relative to ion-extraction reactions at the PU/PVA/ionophore-HPU interface.

Figure 5 shows the potentiometric pH response of TDDA-doped asymmetric and plain PU/PVA membranes. As can be seen, the addition of the HPU/polylysine outer layer does not affect significantly the response to protons. Typically, slopes of 57 mV/pH are observed for the asymmetric membranes in the pH range of 3–10. Again, no noticeable elongation in response time is observed when comparing the dynamic pH response of the asymmetric membranes to plain PU/PVA films doped with TDDA. It should be noted that these equivalent responses can only be achieved by reducing by one-half of the amount of polylysine loaded into the outer HPU layer (compared to the ammonium-selective membrane system).

To determine whether the presence of the outer HPU layer alone, or an outer HPU/PLS layer influences ion selectivities, the selectivity coefficients of the ammonium membranes were determined via the separate solution method. As shown in Table 1, for the most part, little difference in ammonium ion selectivity is observed for the asymmetric ammonium membranes (PU/PVA–HPU/PLS) when compared to plain PU/PVA, PU/PVA coated with HPU (no polylysine) (PU/PVA–HPU) and conventional PVC membranes. Some increased response to protons is observed, although practical selectivity for measurements of ammonium at or near neutral pH values is still quite acceptable.

Conventional biosensors based on the asymmetric ion-selective membranes

Urease and adenosine deaminase served as model enzyme systems to examine the utility of using the asymmetric polyurethane-based membranes for preparation of potentiometric biosensors. These enzymes were coupled to the surfaces of pH and ammonium-selective asymmetric membranes, respectively. Adenosine deaminase catalyzes the following reaction:

Adenosine + $H_2O \rightarrow$ Inosine + NH_4^+

Urease catalyzes the hydrolysis of urea as follows:

$(NH_2)_2CO + 2H_2O + H^+ \rightarrow 2NH_4^+ + HCO_3^-$

TABLE 1

Selectivity coefficients of nonactin-based membranes prepared with various polyurethane matrices

Membrane matrix	Log $K_{NH_4^+,i}^{pot}$ [a]						
	Li^+	Na^+	K^+	Mg^{2+}	Ca^{2+}	Me_4N^+	H^+
PU/PVA	−4.8	−3.2	−1.2	−4.7	−4.7	−4.0	−4.4
HPU–PU/PVA	−4.1	−3.1	−1.2	−4.4	−4.5	−3.9	−3.5
HPU/PLS–PU/PVA	−4.1	−3.1	−1.2	−4.4	−4.5	−3.9	−3.5
PVC [b]	−4.5	−2.9	−0.9	−2.9	−5.0	−3.7	−5.0

[a] Determined by the separate solution method [26]. [b] From Ref. 19.

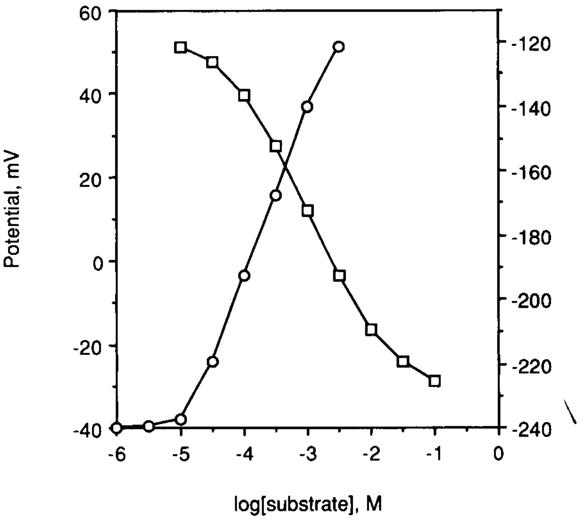

Fig. 6. Calibration curves for (○) adenosine electrode prepared by immobilizing adenosine deaminase through one-step glutaraldehyde method on NH_4^+-selective asymmetric membranes; (□) urea electrode by covalently attaching urease through one-step glutaraldehyde method on proton-selective asymmetric membranes.

In practice, both reactions can be detected by either monitoring pH changes or NH_4^+ ions generated. In the present studies, the use of the proton-selective membrane was restricted to the urea/urease system, while both ADA and urease were immobilized on the ammonium selective asymmetric membranes.

Enzyme immobilization was achieved by covalently attaching the enzymes to the amine groups available on the surface of the membrane through glutaraldehyde crosslinking reactions. With two-step glutaraldehyde method, a monolayer of enzyme is immobilized, while one-step glutaraldehyde method results in multilayers of enzymes due to the crosslinking of enzyme molecules. This usually yields greater enzyme loading [5].

A typical calibration curve for an adenosine electrode prepared by immobilizing ADA on the asymmetric NH_4^+-selective membrane using the one-step glutaraldehyde method is shown in Fig. 6. The linear response range is from 10^{-5} to 3×10^{-2} M of adenosine with a slope of 48 mV per decade. Response times are on the order of 60 s to reach steady-state potential. It should be noted that electrodes in which the asymmetric membrane was treated with enzyme, but no glutaraldehyde, also yield significant adenosine response (not shown). This observed response is due to non-specifically adsorbed ADA, presumably via ion-exchange reactions with protonated amino groups of the polylysine within the outer HPU layer. While the response of these latter electrodes can be eliminated by soaking the electrode in 4 M of $MgCl_2$ (to dissociate the adsorbed enzyme), the response of the glutaraldehyde treated enzyme electrodes remains the same after such treatment. Indeed, adenosine electrodes prepared in this way can last for at least one month, with little loss in response slope or detection limits.

Urea sensors based on pH-selective asymmetric membranes were also tested. For such biosensors, the thickness of the outer HPU layer was found to be critically important with regard to the magnitude of the potentiometric response to urea observed. By decreasing the total amount of the outer HPU/PLS layer (to 5 μm), optimum response in terms of sensitivity is observed. It is believed that the thinner outer membrane keeps the enzyme layer closer to the hydrophobic ion-selective detector layer (inner PU/PVA) so that rapid diffusion of protons into the bulk solution does not diminish surface steady-state pH changes. A typical calibration plot for a urea sensor based on the proton-selective asymmetric membranes is also presented in Fig. 6. The slope is 29.8 mV per decade with the dynamic range of 10^{-4} to 10^{-2} M of urea. Naturally, as with any enzyme electrode based on pH detection, sensitivity is highly dependent on the buffer capacity of the sample medium [30]. The response time to reach 95% of the steady-state potential is about 3 min. Urea sensors based on the NH_4^+-selective asymmetric membranes exhibit much higher response slope (56 mV per decade) and shorter response time (in seconds) when compared to those based on proton-selective membranes (see below).

Response of microfabricated enzyme-electrodes

When urease is immobilized on the surface of the asymmetric ammonium selective membrane cast onto the solid-state device shown in Fig. 2

(using two-step glutaraldehyde), the resulting biosensor responds rapidly and selectively toward urea (see Fig. 7). Typical calibration curves for this device show a linear relation between the e.m.f. and the logarithm of urea concentrations in the range of 10^{-5}–10^{-2} M with slopes of 55–56 mV per decade. This near-Nernstian slope and wide dynamic measuring range suggests that high enzyme loading has been achieved on the surface of the asymmetric membranes [5]. In the case of solid-state adenosine sensors prepared in the same manner (with immobilized ADA), the high slopes and detection limits remain essentially constant during one month of continuous operation. These results support previous claims regarding the very tight adhesion of the plasticized PU/PVA/ionophore membranes to silicon nitride and silver epoxy surfaces [21]. Indeed, had the membrane lifted around the edges, leakage of electrolyte would have shorted the membrane and eliminated any potentiometric ion or substrate response.

It should be noted that each of the films used to construct the solid-state biosensor, starting with the silver epoxy layer, can be screen printed for mass fabrication purposes. In addition, the size and number of sensing regions per unit area of the silicon wafer can be varied. While the above results have been obtained with single sensing sites on relatively large chips (0.8 cm × 1.0 cm, with polymer membrane sensing area of 0.2 cm^2), it is envisioned that an array of biosensing sites on the same size chip can be readily achieved using screen printed asymmetric membranes and site-directed photoimmobilization of enzymes onto to the highly aminated HPU/PLS layers.

In summary, a new asymmetric membrane system with improved surface properties for development of conventional and solid-state type potentiometric biosensors has been described. The potentiometric ion response of this new asymmetric membrane is essentially the same as the base PU/PVA membrane as well as the conventional PVC membranes. At the same time, the amine functional groups on the membrane surface can be used advantageously for covalently attachment of bioreagents. While used here to construct enzyme electrodes for adenosine and urea, it is likely that other bioreagents including intact cells, antibodies, etc., could be incorporated/attached to the outer PU/PLS layer to fabricate a variety of other biosensors (including single use devices). With the advantage of good adhesion to silicon wafer surfaces, this polyurethane asymmetric

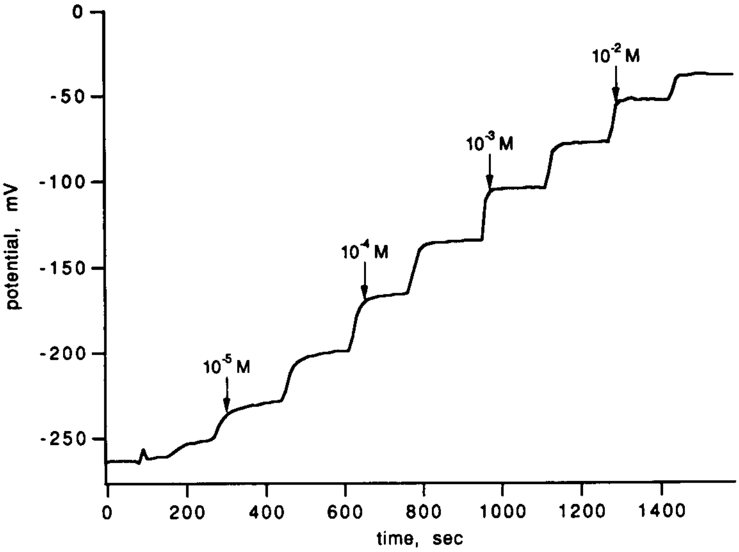

Fig. 7. Dynamic potentiometric response of urea solid-state sensor based on NH_4^+-selective asymmetric membrane.

membrane is a very promising candidate for use in constructing various solid-state biosensing devices.

This work was supported by a grant from the National Science Foundation (ECS-8915497).

REFERENCES

1 M.A. Arnold and M.E. Meyerhoff, CRC Crit. Rev. Anal. Chem., 20 (1988) 149.
2 G.G. Guilbault, Analytical Uses of Immobilized Enzymes, Marcel Dekker, New York, 1984.
3 J. Janata, Principles of Chemical Sensors, Plenum Press, New York, 1989.
4 F.W. Scheller, R. Hintsche, D. Pfeiffer, F. Schubert, K. Riedel and R. Kindervater, Sensors Actuators, B4 (1991) 197.
5 P.W. Carr and L.D. Bowers, Immobilized Enzymes in Analytical and Clinical Chemistry, Wiley-Interscience, New York, 1980, Chap. 5.
6 G.G. Guilbault and G. Nagy, Anal. Chem., 45 (1973) 417.
7 K. Yasuda, H. Miyagi, Y. Hamada and Y. Takata, Analyst, 109 (1984) 61.
8 G.S. Cha and M.E. Meyerhoff, Electroanalysis, 1 (1989) 205.
9 G.S. Cha and M.E. Meyerhoff, Talanta, 36 (1989) 271.
10 J. Anzai, M. Shimada, T. Osa and C. Chen, Bull. Chem. Soc. Jpn., 60 (1987) 4133.
11 I. Karube, in R.D. Schmid, G.G. Guilbault, I. Karube, H.-L. Schmidt and L.B. Wingard (Eds.), Biosensors International Workshop, VCH, Weinheim, 1987, pp. 155-163.
12 M. Gotoh, E. Tamiya and I. Karube, J. Membrane Sci., 41 (1989) 291.
13 F. Gardies, N. Jaffrezic-Renault, C. Martelet, H. Perrot, J.M. Alleton and S. Alegret, Anal. Chim. Acta, 231 (1990) 305.
14 R. Hintsche, B. Möller, I. Dransfeld, U. Wollenberger, F. Scheller and B. Hoffmann, Sensors Actuators, B4 (1991) 287.
15 Y. Hanazato, M. Nakako, S. Shiono and M. Maeda, IEEE Trans. Electron. Dev., 36 (1989) 1303.
16 S.A. Rosario, G.S. Cha, M. Trojanowicz and M.E. Meyerhoff, Anal. Chem., 62 (1990) 2418.
17 W. Matuszewski, S.A. Rosario, M.E. Meyerhoff and M. Trojanowicz, Anal. Chem., 63 (1991) 1906.
18 S.A. Rosario and M.E. Meyerhoff, Anal. Chim. Acta, 258 (1992) 281.
19 S.C. Ma, N.A. Chaniotakis and M.E. Meyerhoff, Anal. Chem., 60 (1988) 2293.
20 S.C. Ma and M.E. Meyerhoff, Mikrochim. Acta, 1 (1990) 197.
21 G.S. Cha, D. Liu, M.E. Meyerhoff, H.C. Cantor, A.R. Midgley, H.D. Goldberg and R.B. Brown, Anal. Chem., 63 (1991) 1666.
22 G. Iorio and G. Catapano, J. Membrane Sci., 22 (1985) 317.
23 K. Mosbach, Methods Enzymol., 135 (1987) 240.
24 W.D. Potter, U.S. Pat., 4,534,355 (1985).
25 P. Schulthess, Y. Shijo, H.V. Pham, E. Pretsch, D. Ammann and W. Simon, Anal. Chim. Acta, 131 (1981) 111.
26 G.G. Guilbault, R.A. Durst, M.S. Frant, H. Freiser, E.H. Hansen, T.S. Light, E. Pungor, G.A. Rechnitz, N.M. Rice, T.J. Rohm, W. Simon and J.D.R. Thomas, Pure Appl. Chem., 48 (1976) 127.
27 W.E. Morf, The Principles of Ion-Selective Electrodes and of Membrane Transport, Elsevier. Amsterdam, 1981.
28 P. Cuatrecasas, J. Biol. Chem., 245 (1970) 3059.
29 X. Ma, S.F. Mohammad and S.W. Kim, J. Colloid Interface Sci., 147 (1991) 251.
30 R.M. Ianniello and A.M. Yacynych, Anal. Chim. Acta, 146 (1983) 249.

Analytica Chimica Acta, 274 (1993) 47–52
Elsevier Science Publishers B.V., Amsterdam

Multiple-indicator fiber-optic sensor for high-resolution pCO_2 sea water measurements

David R. Walt and G. Gabor

Max Tishler Laboratory for Organic Chemistry, Tufts University, Department of Chemistry, Medford, MA 02155 (USA)

Catherine Goyet

Woods Hole Oceanographic Institution, Department of Chemistry, Woods Hole, MA 02543 (USA)

(Received 22nd May 1992; revised manuscript received 14th September 1992)

Abstract

A multiple-indicator fiber-optic sensor was employed to detect low level CO_2 changes in sea water. pK_a values of these indicator systems at high ionic strength were determined, and the bicarbonate concentrations were added as calculated by the Henderson–Hasselbach equation. The 7-hydroxycoumarin-4-acetic acid (HCA)–*meta*-Cresol Purple (MCP) indicator system provides a resolution of 7 $\mu g\ ml^{-1}$ CO_2 in the 200–800 $\mu g\ ml^{-1}$ CO_2 range, the CO_2 range of sea water.

Keywords: Fluorimetry; Spectrophotometry; Fibre-optic sensors; pCO_2; Sea water; Waters

The ocean is an enormous carbon reservoir and is regarded as a major sink for atmospheric CO_2. The ocean is believed to absorb almost half of the anthropogenic CO_2 gas injected into the atmosphere. As a result, the effect of this greenhouse gas is limited and the potential global warming of the planet is reduced. The atmospheric CO_2 gas penetrates into the deep ocean in high latitude areas of deep water formation, and into the surface ocean by continuous CO_2 gas exchanges across the ocean–atmosphere interface. These exchanges are controlled by the gas transfer velocity [1,2] and the difference of CO_2 partial pressure (pCO_2) between the atmosphere and the surface ocean. The spatio-temporal variations of CO_2 in the atmosphere are very well known within ±2 $\mu g\ ml^{-1}$ [3] but those of the surface ocean, which depend on physical and biochemical processes, still need to be determined.

The development of new technology for oceanic pCO_2 measurements is therefore increasingly important to determine the spatio-temporal variations of oceanic pCO_2 and to quantify the CO_2 flux crossing the ocean–atmosphere interface in order to predict the effect of continuous increases of anthropogenic CO_2 in the atmosphere on the earth's climate.

The search for accurate analytical methods to measure the partial pressure of CO_2 goes back to the 1920s when Van Slyke et al. [4] employed manometric measurements for pCO_2 determination. pCO_2 electrodes [5] were adapted in the 1950s for blood gas measurements [6]. Spectrophotometric measurements [7] were employed for several applications, but with the advent of

Correspondence to: D.R. Walt, Max Tishler Laboratory for Organic Chemistry, Tufts University, Department of Chemistry, Medford, MA 02155 (USA).

optical sensors in the last decade a resurgence in spectrophotometric methods for CO_2 determination has occurred [8–14]. Optical sensors consist of reagents attached to the distal tip of an optical fiber that change their optical properties upon exposure to a specific analyte. These sensors are small (approximately 100–600 μm), require no direct electrical connection between the sample and sensor, and are free from electromagnetic interference. These characteristics make optical sensors ideal for measurements at sea. Spectrophotometric methods can be based on changes of absorbance [9,14] or fluorescence [8–13]. Neither of these methods, however, has the requisite sensitivity necessary for measuring the small (approximately 1–10 μg ml^{-1}) changes in CO_2 required in sea water.

The conventional approach to preparing CO_2 sensors is to utilize the equilibrium:

$$CO_2 + H_2O \rightleftarrows H_2CO_3 \rightleftarrows HCO_3^- + H^+$$

In this way the partial pressure of CO_2 can be related to the pH. A pCO_2 sensor based on this principle can be constructed with a gas-permeable membrane that excludes interference from pH changes of the bulk solution. pH and, in turn, pCO_2 can then be related by the Henderson–Hasselbach equation:

$$\mathrm{pH} = \mathrm{p}K_a + \log\frac{[HCO_3^-]}{[CO_2]}$$

This equation shows that the sensitivity of the measurement at a given CO_2 concentration is affected by the pK_a of the indicator and the HCO_3^- concentration of the internal fill solution.

Recently we introduced an approach employing inner-filter effects (IFEs) to enhance the sensitivity of pH sensors [15]. The enhancement is a consequence of screening the excitation energy (primary IFE) and the simultaneous quenching of the emitted fluorescence (secondary IFE) by one or two absorbers with complementary pH profiles and spectral overlap. The enhancement results in a compression of the fluorescence signal change into a small pH range leading to an increase in the slope of the pH response curve in a narrow pH range. In addition to the enhanced sensitivity, one can also vary the pK_a of these systems, by varying the indicators, their concentrations, or the exciting wavelength. In this manner a particularly suitable system for pCO_2 determinations can be obtained with a pK_a affected by the bicarbonate content and by the high ionic strength of sea water. In this paper we present a two-indicator system employing inner filter effects that enables precision measurements in aqueous solutions and in sea water.

Experimental

Materials. 7-Hydroxycoumarin-4-acetic acid (HCA) was purchased from Aldrich (Milwaukee, WI) and Molecular Probes (Eugene, OR), *meta*-Cresol Purple (MCP) from Kodak (Rochester, NY), Neutral Red (NR) from Aldrich and hydroxypyrenetrisulfonic acid (HPTS) from Molecular Probes, and bisphenol A carbonate block copolymer from Petrarch. Tanks of CO_2 gas in nitrogen at concentrations of 200, 500 and 800 μg ml^{-1} were from Cryodyne Technologies (North Haven, CT). All materials were used without further purification.

Solutions. Synthetic sea water was prepared by dissolving NaCl (36 g, 0.67 mol) and Na_2CO_3 (244 mg, 2.31×10^{-3} mol) in 1 l of distilled water. 0.1 M phosphate buffers were prepared by mixing appropriate amounts of 0.1 M Na_2HPO_4 and 0.1 M NaH_2PO_4 stock solutions. Stock solutions of $2–5 \times 10^{-3}$ M indicators were prepared in synthetic sea water. The stock solution of HCA (4.28×10^{-3} M) was prepared in synthetic sea water–ethanol (2:1, v/v). Sea water standards of 200, 500 and 800 μg ml^{-1} CO_2 and indicator–sea water solutions of the same pCO_2 levels are prepared by continuous bubbling of water-vapor-saturated standard CO_2 gas into the respective solutions.

Apparatus. Absorbances of $2–5 \times 10^{-5}$ M indicator solutions were recorded on an IBM 9240 UV–Vis spectrophotometer. Fluorescence measurements were made on a spectrofluorimeter that has been described elsewhere [16]. Basically it is comprised of a 75-W xenon arc lamp light source, two Spex 1680 0.22 M double monochromators (excitation and emission), an RCA photomultiplier tube, and optics designed to couple light to and from an optical fiber. A PC-AT with an AsystW program controlled the movements of the stepping motors as well as enabled the acquisition and display of the experimental data. Data were then analyzed using a datatap program.

The sensors were prepared by inserting a bisphenol A carbonate copolymer membrane sleeve, approximately 1.5–2.5 mm long, filled with the sensing solution, flanged into a threaded male connector with a 1-mm hole. The optical fiber protruded slightly from a ferrule and the entire assembly was sealed by screwing the corresponding female connector onto the male connector with the flange of the membrane acting as a gasket (Fig. 1). The concentrations of the two sensing solutions of HCA–MCP in sea water were 4.5×10^{-4} M/3.5×10^{-4} M and 8.76×10^{-4} M/7.6×10^{-4} M, respectively.

Measurements. Absorption spectra of the indicators were measured in 2–5×10^{-5} M buffered solutions. Fluorescence measurements were carried out both by bare fiber inserted vertically into the mixed dye solutions (4.5×10^{-4} M HCA with 3.5×10^{-4} M MCP) equilibrated with 200, 500 and 800 μg ml^{-1} CO_2 and by the sensor inserted vertically in sea water equilibrated by bubbling with various pCO_2 standard gases.

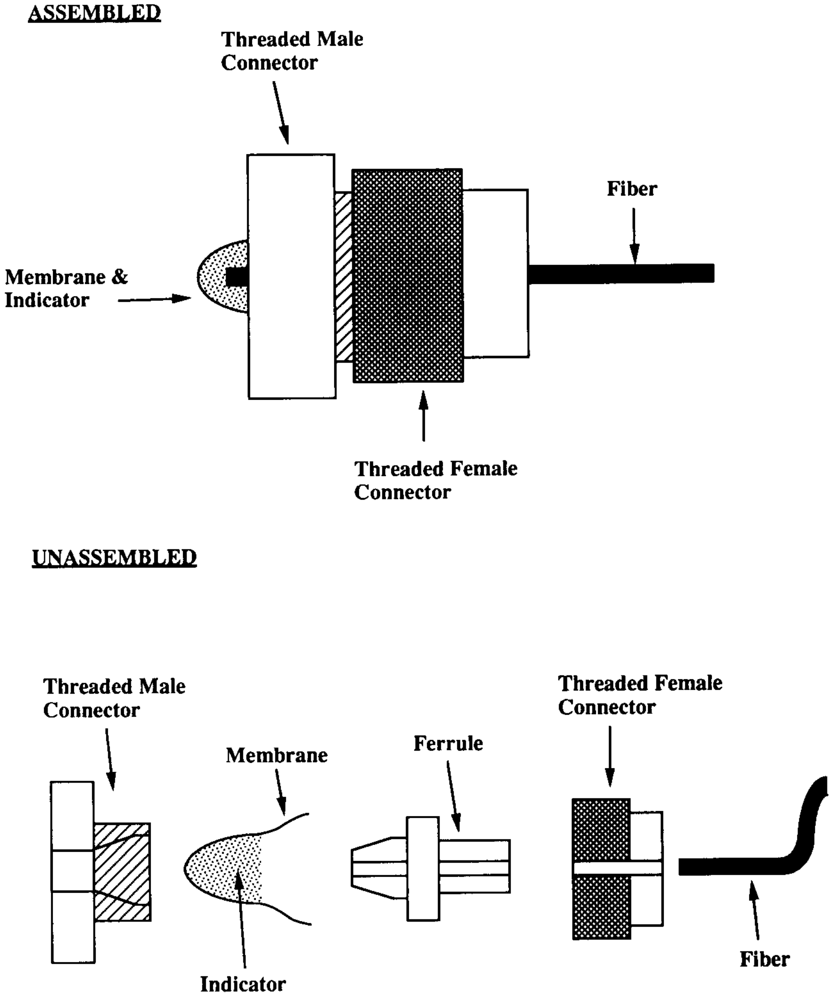

Fig. 1. Design of a CO_2 sensor. Both assembled and unassembled diagrams are depicted.

RESULTS AND DISCUSSION

In previous work [15] we demonstrated the utility of inner-filter effects for enhancing the sensitivity of fluorescence-based pH measurements. The method employs multiple-indicator systems and operates on the basis of inner-filter effects which screen both excitation and emission of the fluorescent indicator at low pH and have negligible effect at high pH. Consequently, the entire fluorescence signal change is compressed into a narrow pH region. In the present system, the HCA–MCP pair was employed to generate steep $\Delta I/\Delta$pH slopes due to the application of this principle. The HCA–MCP system has the advantage of good solubility in sea water. This indicator solution has a pK_a of 8.2, allowing its use in natural sea water ($HCO_3^- = 2.3 \times 10^{-3}$ M) (Table 1). This dye system has a maximum excitation wavelength of 390 nm, a frequency range requiring silica or high-quality glass fibers to minimize attenuation of the excitation light.

A second dye system comprised of hydroxypyrenetrisulfonic acid (HPTS) and Neutral Red (NR) was also examined and was taken to sea [17]. This system has an excitation maximum in the 469–484 nm range which enables the use of lower-quality fibers. Unfortunately NR precipitates at high ionic strength, thereby limiting the utility of this mixture for oceanic measurements. Furthermore, the system is unstable and loses its sensitivity after several weeks. Finally, with this dye combination the bicarbonate solution must be adjusted to 4.55×10^{-5} M to yield the pH range of 6.5–7.1 most appropriate for measurements of 200 to 800 μg ml^{-1} CO_2 with this mixture as shown in Table 1.

TABLE 1

Calculated pH values for various pCO_2 and bicarbonate concentrations

(The bicarbonate concentrations were selected to maximize the sensitivities of HCA–MCP and HPTS–NR.) [a]

pCO_2 (μg ml^{-1})	pH	
	$NaHCO_3$	
	2.31×10^{-3} M	4.55×10^{-5} M
800	7.93	6.51
500	8.16	6.74
200	8.56	7.14

[a] Assumes a solubility coefficient of 1 at such low pCO_2.

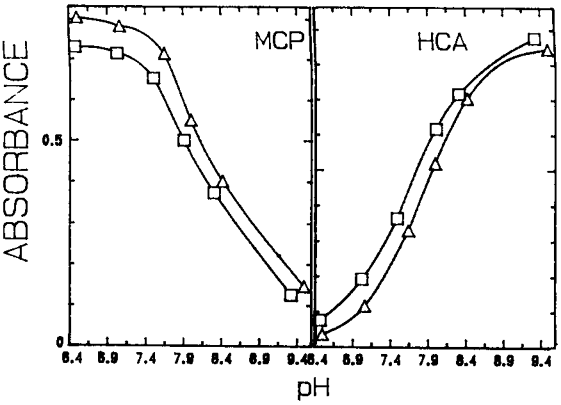

Fig. 2. pH profiles in (△) aqueous and (□) salt solutions. Absorbance readings were measured for HCA at 390 nm and MCP at 400 nm. HCA, 4.28×10^{-5} M; MCP, 4.86×10^{-5} M.

In order to avoid dilution or concentration of the indicator by water vapor transfer, it is important to maintain an identical osmotic potential across the gas-permeable membrane. This adjustment was accomplished by adding 0.67 M NaCl to the indicator bicarbonate fill. Figure 2 shows the pH titration curves of both MCP and HCA in the presence and absence of NaCl. The pK_a values of the four indicators examined all shifted to lower pH by 0.2–0.5 pH units, as shown in Table 2. The values in water are well known reported literature values that were verified by experiments (not shown). The value in NaCl solution was determined by the offset of the water-only titration curves as shown in Fig. 2 for MCP and HCA. With the MCP and HCA mixture, the optimal pH for exhibiting the maximum spectral change per change in CO_2 partial pressure over the range of 200–800 μg ml^{-1} is between 8.1 and 8.2 in 0.67 M NaCl.

TABLE 2

pK_a values of indicators in aqueous solutions and in 0.67 M NaCl

Solvent	HCA	MCP	HPTS	NR
Water	7.75	8.3	7.30	7.25
0.67 M NaCl	7.50	8.1	6.95	6.75

CO_2 gas standards of 200, 500, and 800 μg ml^{-1} were used to saturate identical solutions of the MCP–HCA mixed indicator by bubbling the standards continuously into the solutions. Large volumes of solution were used to prevent artifacts resulting from evaporation of the solvent due to bubbling. An optical fiber was inserted into each of these solutions sequentially to measure the fluorescence emanating from the HCA at the different pCO_2 levels. The response of a bare fiber alternating between two solutions containing 200 and 800 μg ml^{-1} pCO_2 gave fluorescence intensity readings of 830000 cps and 590000 cps, respectively. Previous work [15] with this dye mixture in pH buffers indicate that this change is approximately threefold greater than would be obtained with a single indicator. After verifying the sensitivity of the solution with CO_2 gas bubbling, the same solution was used to fill a sensor with a configuration as depicted in Fig. 1. The same HCA–MCP solution was used to fill a polymer sleeve membrane which was connected to the distal tip of an optical fiber. Dissolved CO_2 gas from the measured solution diffused through the polymer into the indicator fill solution, where the carbonate equilibrium reaction occurred. The resulting pH change of the indicator solution was reflected by a change in its fluorescence intensity as measured by the optical fiber. The results of a sensor measurement made over a 2-h period are shown in Fig. 3. With this configuration a slow response is observed due to the rate of CO_2 gas diffusion through the membrane and into the internal filling solution. The thick (ca. 50 μm) membrane coupled with the large (ca. 5 μl) indicator volume account for the relatively long response time of the sensor. However, this response time is perfectly adequate for most in situ sea water measurements. Furthermore, the large indicator volume mitigates against photobleaching which would be a problem over the long measurement times contemplated for these sensors. The solutions are stable under storage for several months.

Sensitivity can be further increased by well known methods to increase excitation light intensity such as by increasing the excitation slit or by using a larger-diameter optical fiber. Examples for a step change of 200–800 μg ml^{-1} CO_2 are shown in Table 3. Instrumental noise is 2000 cps. Therefore, with a 400-μm fiber, a signal of 4000 cps ($S/N = 2$) provides the sensor with a resolution of approximately 7 μg ml^{-1} CO_2.

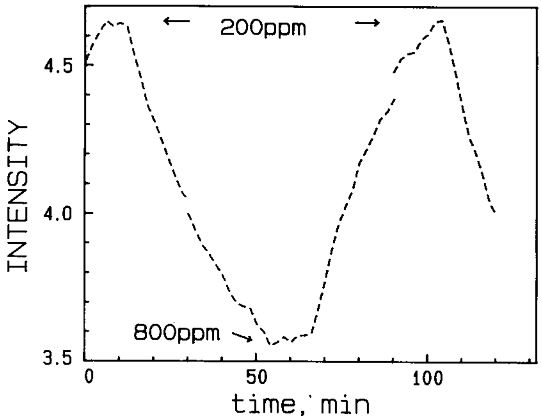

Fig. 3. Performance of CO_2 sensor. HCA, 4.5×10^{-4} M; MCP, 3.5×10^{-4}. Intensity values at CO_2 concentrations of 800 μg ml^{-1} (low I) and 200 μg ml^{-1} (high I).

Fluorescence intensities of the dye solutions at different temperatures are shown in Fig. 4. In the rather narrow range of temperatures in these experiments, the principal contributor to this temperature dependence is the changing acidity of the phenolic residues on the indicators [18]. The temperature coefficient reported by Peterson et al. [19] is 0.0174°C^{-1}. At higher temperatures, phenolic compounds become better bases leading to a greater contribution of the basic (fluorescent) form, and as a result we observe an increase in the fluorescence intensity.

TABLE 3

Influence of slit width and fiber diameter on fluorescence intensity change

Slits ex/em (mm)	Fiber diameter (μm)	ΔI for Δ600 μg ml^{-1} CO_2 ($\times 10^4$ cps)
0.25/1.25	200	9.0
1.25/1.25	200	15.1
5.00/5.00	200	23.8
0.25/0.5	400	36.7

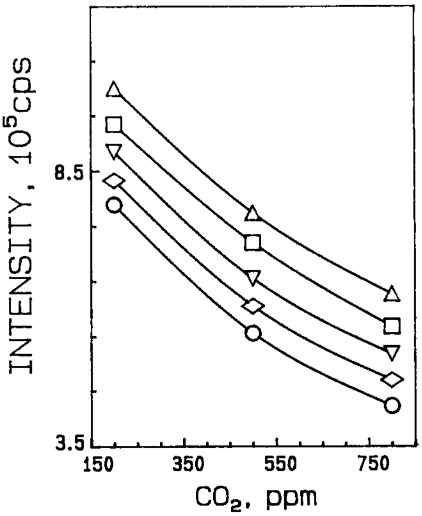

Fig. 4. Temperature dependence of HCA–MCP (8.76×10^{-4} M and 7.6×10^{-4} M, respectively) in sea water fluorescence for CO_2 sensor in the 200–800 μg ml^{-1} range; (△) 19.5°C; (□) 15.0°C, (▼) 10.0°C; (◇) 5.0°C; (○) 0.5°C. Discontinuities are due to sporadic shutter malfunction (e.g., partial opening or sticking).

Conclusions

The present sensor demonstrates the viability of optical sensors for pCO_2 measurements in sea water. The sensor design would enable either continuous shipboard measurements and, when developed further, could be useful for application to deployable buoy systems. Key features of the present sensor are both the use of multiple indicators to increase the slope of the pH versus intensity curve which enhances the sensitivity of the CO_2 measurements, and the use of a semi-permeable membrane which separates the sea water from the internal indicator solution of appropriate osmotic potential.

This work was supported in part by the National Science Foundation under grant OCE-8700808.

REFERENCES

1 P.S. Liss and L. Merlivat, in P. Buat-Menard (Ed.), The Role of Air–Sea Exchange in Geochemical Cycle, NATO ASI Series, Reidel, Dordrecht, 1986, p. 113–127.
2 R.C. Upstiff-Goddard, A.J. Watson, P.S. Liss and M.I. Liddicôat, Tellus, 42 B (1990) 364.
3 W.D. Komhyr, R.H. Gammon, T.B. Harris, L.S. Waterman, T.J. Conway, W.R. Taylor and K.W. Thoning, J. Geophys. Res., 90 (C6) (1985) 5567.
4 D.D. Van Slyke and J.M. Neill, J. Biol. Chem., 61 (1924) 523; 78 (1928) 765.
5 J.W. Severinghaus, Ann. N.Y. Acad. Sci., 148 (1962) 115.
6 (a) J.W. Severinghaus and Bradley A. Freeman, J. Appl. Physiol., 13 (1958) 515.
(b) A.H.J. Maas and P.J. Mertens, Clin. Chim. Acta, 28 (1979) 443.
7 L.L. Claypool and R.M. Keefer, Proc. Am. Soc. Hort. Sci., 40 (1942) 177.
8 N. Opitz and D.W. Lübbers, Adv. Exp. Med. Biol., 180 (1984) 757.
9 G.G. Vurek, P.J. Feustel and J.W. Severinghaus, Ann. Biomed. Eng., 11 (1983) 499.
10 Z. Zhujun and W.R. Seitz, Anal. Chim. Acta, 160 (1984) 47; ibid., p. 305.
11 J.L. Gehrich, D.W. Lübbers, N. Opitz, D.R. Hansmann, W.W. Miller, J.K. Tusa and M. Yafuso, IEEE Trans. Biomed. Eng., BME-33 (1986) 117.
12 O.S. Wolfbeis, L.J. Weis, M.J.P. Leiner and W.E. Zeigler, Anal. Chem., 60 (1988) 2028.
13 C. Munkholm, D.R. Walt and F.P. Milanovich, Talanta, 35 (1988) 109.
14 G. Serra, A. Schirone and R. Boniforti, Anal. Chim. Acta, 232 (1990) 337.
15 G. Gabor and D. Walt, Anal. Chem., 63 (1991) 793.
16 S. Luo and D.R. Walt, Anal. Chem., 61 (1989) 174.
17 C. Goyet, D.R. Walt and P.G. Brewer, Deep-Sea Res., 39 (1992) 1015.
18 A. Albert and E.P. Serjeant, in Ionization Constants of Acids and Bases, Methuen, London, 1962, p. 14.
19 J.I. Peterson, S.R. Goldstein, R.V. Fitzgerald and D.K. Buckhold, Anal. Chem., 52 (1980) 864.

Analytica Chimica Acta, 274 (1993) 53–58
Elsevier Science Publishers B.V., Amsterdam

L-Lactate oxidase electrode based on methylene green and carbon paste

Juozas Kulys, Lizhong Wang [1] and Ausra Maksimoviene

Institute of Biochemistry, Lithuanian Academy of Sciences, Vilnius-MTP (Lithuania)

(Received 19th November 1991; revised manuscript received 4th March 1992)

Abstract

An amperometric L-lactate electrode based on methylene green (MG) and carbon paste chemically modified with L-lactate oxidase is described. The electrode action is based on the effective reduction of oxidized L-lactate oxidase by reduced MG (apparent rate constant = 1.7×10^6 l mol^{-1} s^{-1}) and rapid electrochemical mediator conversion. The enzyme electrode generates an anodic current at 0.05–0.6 V vs. SCE. The pH optimum of the electrode is 7.0. The apparent Michaelis constant depends on the amount of L-lactate, and varies in the range 4.1–9.7 mM. The maximum electrode sensitivity is 50.4 μA l mmol^{-1} cm^{-2} and does not depend on the oxygen concentration in solution. The electrode is insensitive to glucose and ethanol. At 0.15 V the response to L-ascorbic acid (40 μM) is equivalent to 9.8% of the normal physiological L-lactate level in blood. The enzyme electrodes were used for L-lactate determination in goat whole blood. They remained stable on storage in the dry state for at least 2 months.

Keywords: Amperometry; Enzymatic methods; Carbon paste; Enzyme electrodes; Lactate; Methylene green mediator

In blood, the L-lactate level is specific to muscle diseases, critical care, lymphomas and sarcomas, etc. The concentration of L-lactate in the blood of sportsmen can indicate the intensity of physical exercises. In the food industry, L-lactate measurements can be used to monitor the fermentation of wine, beer, fruit juice and milk products, and also for measurements in fodder production, in silo preparation, etc. [1]. Hence L-lactate is an important metabolite for the determination of which a reliable analytical method is required.

Amperometric enzyme electrodes are becoming increasingly popular. Screen-printed, thin- and thick-film sensors and bioelectrodes based on carbon paste are examples of the applications of recent technology in the preparation of sensors [2–17].

L-Lactate-sensitive electrodes based on lactate oxidase [1,18–22], lactate dehydrogenase [23–25], flavocytochrome b_2 [26–29] or yeast [30] have been prepared. Bioelectrodes based on lactate dehydrogenase and cytochrome b_2 even in the immobilized state have only short-term stability, whereas those based on L-lactate oxidase have a disadvantage connected with oxygen fluctuation. L-Lactate oxidase-based electrodes with ferrocene or tetrathiafulvalene as mediator were almost insensitive to oxygen [18]. However, these mediators have a high redox potential (0.27 and 0.35 V vs. SCE, respectively [31,32]). Electrodes including these mediators act at the potential at which other redox compounds available in real biological solutions (ascorbic acid in blood, juice and other food products, paracetamol in blood, etc.) are oxidized.

Correspondence to: J. Kulys, Institute of Biochemistry, Lithuanian Academy of Sciences, Vilnius-MTP (Lithuania).

[1] On leave from Department of Pharmaceutical Analysis, Guangdong Medical and Pharmaceutical College, Guangdong, China.

In this work, methylene green (MG) was used as a mediator for the preparation of a carbon paste–L-lactate oxidase-based electrode. Bennetto et al. [33] proposed methylene green as an indicator for the performance of phenothiazine redox dyes in an *Escherichia coli* system, but this mediator did not find application in bioelectrocatalytic systems. From the present experimental measurements it follows that MG undergoes reversible oxidation–reduction conversion and is suitable for enzyme electrode preparation. The good solubility in water of MG restricts its application when adsorbed on a graphite electrode but this mediator can be used in a carbon paste medium. As far as we know, a carbon paste–L-lactate oxidase-based electrode has not been investigated previously. Recently, carbon paste electrodes sensitive to L-lactate based on yeast and different mediators were prepared in this laboratory [34].

EXPERIMENTAL

Reagents

L-Lactate oxidase was prepared from *Streptococcus* sp. microorganisms. The activity of lyophilized powder of L-lactate oxidase, which was expressed as the amount in μmoles of assumed oxygen per minute at 5 mM L-lactate, pH 7.0 and 25°C, was 87 U g^{-1}.

Graphite powder (Fluka), paraffin oil (Merck) and lithium L-(+)-lactate (Sigma) were used as received. Potassium chloride, disodium hydrogenphosphate and sodium dihydrogenphosphate were of the highest purity (Reachim, USSR). Methylene green (MG) was obtained from Aldrich and methylene blue (MB) from (Reachim, USSR). For electrochemical measurements MG was purified by reversed-phase liquid chromatography [35].

In voltammetric measurements (0.1 M sodium phosphate buffer solution containing 0.1 M potassium chloride was used.

Preparation of chemically modified carbon paste

Chemically modified carbon paste (CMCP) was prepared from graphite powder and paraffin oil. Amounts of 50–100 mg of graphite powder, 50 mg of paraffin oil, 10 or 35 mg of mediator and 2–60 mg of L-lactate oxidase were thoroughly mixed in a mortar. Pentane (two volumes) was added to prepare a uniform paste.

Electrode construction

The electrodes were prepared as follows: a 2–3-cm long PTFE tube (1.5 mm o.d. and 0.6 mm i.d.) was packed with CMCP, and electrical contact was achieved by inserting a platinum wire into the CMCP. The end of the tube was rubbed gently with a scalpel to produce a flat electrode with a surface area about 0.28 mm^2.

Electrode operation

Electrode currents were measured in a thermostated glass cell with a common three-electrode system. The current of the electrode was measured using a newly rubbed (renovated) surface each time. No special surface pretreatment was necessary. The electrode was dipped into the thoroughly stirred and thermostated buffer solution (9 ml) and connected to a potentiostat. Successive additions of 10–200 μl of L-lactate solution in buffer were made after the residual current had become constant. The increase in the anodic current was registered by a recorder. The electrode response conformed to the difference between total and residual current. Measurements in oxygen-free media were done by debubbling buffer solution with highly purified argon (for longer than 15 min).

For measurements on undiluted blood samples, a special cell consisting of a Plexiglas holder and auxiliary and reference electrodes (Fig. 1) was used. A drop of blood (ca. 0.03 ml) was dripped on the central part of the cell and the maximum current value was indicated at the end of the first minute.

Between measurements the electrodes were kept in a dry state in a refrigerator.

The cyclic voltammograms of MB and MG were obtained using a glassy carbon electrode (diameter 2 mm) installed in a PTFE holder in 50% (v/v) methanol and 0.1 M phosphate buffer solution (pH 7.0) at a scan rate of 10–100 mV s^{-1} and a mediator concentration of 0.5 mM.

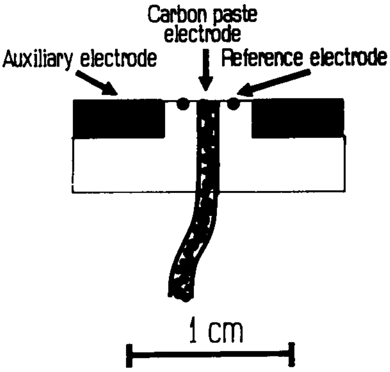

Fig. 1. Scheme of electrochemical cell for investigation of whole blood samples.

The electrode current was registered by an OH-105 polarograph (Radelkis, Budapest). The potentials for electrochemical measurements were determined in the thermostated cell vs. SCE, except that the potential of the enzyme electrode amounted in the electrochemical cell (Fig. 1) was determined vs. an Ag/AgCl electrode in 0.1 M phosphate buffer (pH 7.0) containing 0.1 M potassium chloride.

Determination of methylene green reactivity

The reaction of MG with reduced L-lactate oxidase was evaluated spectrophotometrically in anaerobic phosphate buffer solution using 5 mM L-lactate at pH 7.0. MG reduction was monitored by the absorbance (A) change at 650 nm. The oxidation rate constant calculations were done following a cyclic scheme of enzyme action. The concentration of enzyme was calculated from the enzyme reaction with oxygen assuming that the oxidation rate constant for L-lactate oxidase is the same as for glucose oxidase and reduced FAD, i.e. 1.95×10^6 l mol^{-1} s^{-1} [36]. The final calculations were done using the equation

$$k_{MG} = k_{OX} V_{MG} [E]_{OX} / V_{OX} [E]_{MG}$$

where k, V and [E] are oxidation rate constant, initial reaction rate and enzyme concentration, respectively, and the subscripts MG and OX indicate reaction with methylene green and oxygen, respectively; $V_{MG} = (\Delta A / \Delta t)_{t=0} / A$, $V_{OX} = (\Delta[O_2]/\Delta t)_{t=0}/[O_2]$.

RESULTS AND DISCUSSION

Oxidation–reduction properties of methylene green

The cyclic voltammogram of the purified MG in methanol–buffer solution shows a single oxidation–reduction peak with a formal redox potential $[(E_a + E_P)/2]$ of −0.12 V. The difference between the oxidation and reduction peak potentials (ΔE_P) was 42 mV at a scan rate 10 mV s^{-1}. $I_P/v^{1/2}$ was constant at potential scan rates in the range 5–200 mV s^{-1}. In the pH range 4.9–10 the slope of the anodic and cathodic peak potential dependence on solution pH is 30 mV per pH unit; at lower pH the slope increases to 60 mV per pH unit. With methylene blue the difference between the peak potentials was similar, and the slope of the pH dependence was also 30 mV per pH unit in the pH range 5.7–10 and 61 mV per pH unit in the pH range 3.4–5.7. The presented voltammetric data of MG conversion are consistent with quasi-reversible phenothiazinium ion–phenothiazine two electron–proton or two electron–two proton conversion, as investigated previously using MB [37]. The formal pK_a of MG at which the electron transfer mechanism changes is 4.9. The shift of the pK_a of MG to more acidic values in comparison with MB can be explained by the electron-accepting character of the additional nitro group. The increase in the redox potential of MG can be explained similarly.

MG is reduced after L-lactate oxidase and L-lactate have been introduced into the buffer solution. The oxidation rate constant is $(1.7 \pm 0.2) \times 10^6$ l mol^{-1} s^{-1}.

Parameters of the enzyme electrodes

For an enzyme electrode containing 6.2% of L-lactate oxidase a stable residual current was established 30 s after a potential (0.15 V) was applied. An increase in MG to 19% increased the anodic current, and the lowest residual current was established at 0.2 V. Even at the lowest potential a reduction of MG took place and the cathodic current increased.

At 0.15 V the enzyme electrode current in 1 mM L-lactate solution increased within 1 min and remained constant for 2–3 min. The enzyme electrode response was virtually constant in the electrode potential range 0.05–0.6 V.

The electrode stationary-state current dependence was linear up to 4–8 mM L-lactate and reached a saturated state at higher substrate concentration (Fig. 2). Over the whole concentration range the calibration graph is like a Michaelis–Menten dependence, and apparent kinetic parameters (I_{max} and $K_{M app}$) can be calculated.

The electrode sensitivity ($I_{max}/K_{M app}$) and the linear calibration range depend on the amount of enzyme (Fig. 2). On increasing the amount of L-lactate oxidase from 1.2 to 20% an increase in $K_{M app}$ from 4.1 to 9.7 mM was observed. At higher amounts of enzyme this constant fell to 6.3 mM. In the range 1.2–20% of enzyme the electrode sensitivity increased from 1.2 to 50.4 μA l mmol^{-1} cm^{-2} and in the presence of 32% of enzyme it decreased to 24.9 μA l mmol^{-1} cm^{-2}. If 20% L-lactate oxidase was used the electrode sensitivity and apparent Michaelis constant were the same as in oxygen-free solution.

Under the operating conditions, the enzyme electrode response increased with increase in temperature from 17 to 30°C. At higher temperatures the electrode response decreased. In buffer solution at 25°C the enzyme electrode response was constant for 2–3 min and after 8 min of operation it fell by 30%.

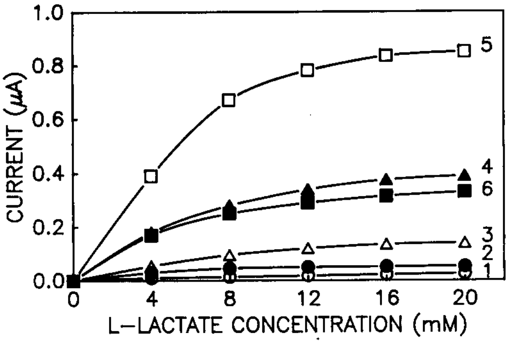

Fig. 2. Dependence of enzyme electrode current on L-lactate concentration at electrode potential 0.15 V, pH 7.0 and 25°C. Compositions of chemically modified carbon paste: (1) 61.3%, (2) 59.5%, (3) 56.6%, (4) 51.4%, (5) 42.5% and (6) 30.5% graphite, (1) 1.2%, (2) 3.0%, (3) 5.9%, (4) 11.1%, (5) 20.0% and (6) 32.0% enzyme, (1–6) 6.5% methylene green and (1–6) 31% paraffin oil.

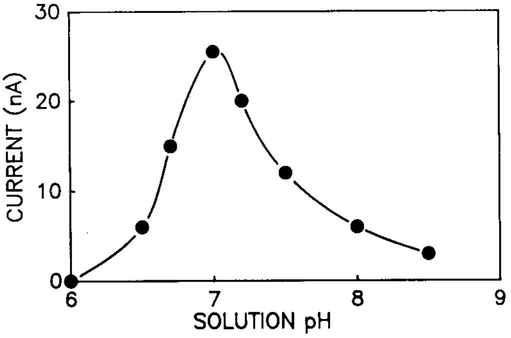

Fig. 3. Dependence of electrode sensitivity on solution pH at 0.15 V, 25°C, at 0.25 mM lactate. Electrode composition as in Fig. 2, (5).

When the enzyme electrode was kept in a dry state at 4°C its response retained more than 95% of the initial value after 2 months of storage.

The enzyme electrode exhibited the highest sensitivity at pH 7.0. The sensitivity decreased sharply in acidic or alkaline media (Fig. 3).

Explanation of enzyme electrode action

As follows from the kinetic investigations in phosphate solution, L-lactate oxidase effectively catalyses MG reduction by L-lactate. Reduced MG undergoes rapid oxidation at the carbon electrode. The enzyme electrode action can be explained on the assumption that a substrate (S) reduces L-lactate oxidase (E) adsorbed on graphite, oxidized MG diffuses from the carbon paste, dissolves in the reactive layer near the electrode surface and interacts with the reduced enzyme:

$$E(ox) + S \rightarrow E(red) + P$$

$$E(red) + MG(ox) \rightarrow E(ox) + MG(red)$$

Reduced mediator is oxidized electrochemically on the graphite electrode:

$$MG(red) \rightarrow M(ox) + 2e + H^+$$

The suggested scheme differs from the action of enzyme electrodes based on reduced mediators [18]. When ferrocenes or tetrathiafulvalene are used, the formation of oxidized mediators which interact with reduced enzyme takes place in situ, and the accumulation of a high mediator concentration in the reactive layer is hampered because of the high background. In the present system, when the oxidized mediators are used the background can be easily depressed by changing the electrode potential.

Two possible parallel reactions must be taken into account when considering the action of MG-based enzyme electrodes: the electrochemical reduction of oxidized mediator:

$$\mathrm{MG(ox)} + 2e + \mathrm{H}^+ \rightarrow \mathrm{MG(red)}$$

which takes place at potentials below zero residual current potential, and the oxidation of reduced enzyme by oxygen:

$$\mathrm{E(red)} + \mathrm{O_2} + \mathrm{H}^+ \rightarrow \mathrm{E(ox)} + \mathrm{H_2O_2}$$

A high concentration of the mediator used in CMCP promotes a shift of the enzyme electrode action potential per 0.2–0.3 V into the anodic range. This potential can be decreased by lowering the mediator concentration in CMCP. However, for a high concentration of mediator in CMCP and a high rate of electron transfer from reduced L-lactate oxidase to the mediator, the rate of reaction with oxygen was low. For this reason, even if the enzyme electrode action potential was low, its response was insensitive to oxygen.

As follows from Fig. 2, the enzyme electrode sensitivity increases on increasing the amount of enzyme in CMCP (a decrease in the sensitivity at higher enzyme concentrations can be caused by the alterations to the electrical parameters resulting from a low graphite content in CMCP). Consequently, the prepared enzyme electrodes operate in a non-diffusion regime. In turn, the apparent Michaelis constant depends on the amount of enzyme (Fig. 2). This means that the enzyme electrode acts in the kinetic regime with some diffusion limitations [38]. To increase the sensitivity and linear calibration range an enzyme of higher specific activity can be used.

The dependence of the enzyme electrode response on pH has a pronounced maximum, as was observed with other native enzymes. The pH optimum for L-lactate oxidase action when MG is used as the acceptor has not been investigated before and it is complicated to draw conclusions about the effect of immobilization on the enzyme properties.

The long-term stability of the enzyme electrode depends mainly on the stability of L-lactate oxidase. In a paraffin matrix the stability of CMCP is high and the enzyme electrode retains its sensitivity for more than 2 months when stored in a refrigerator. The low stability of the enzyme electrode under the operating conditions is presumably caused by the loss of the mediator and enzyme. However, this problem was solved by using a renovated electrode surface and short-term electrode exposure in the solution.

Enzyme electrode selectivity

The selectivity of the enzyme electrode was tested using α-D-glucose, ethanol and L-ascorbic acid. The first two compounds were chosen for the well known possibility of detecting them in blood using enzyme electrodes. Ascorbic acid is an electrochemically active compound, the presence of which could interfere with glucose, L-lactate and other metabolite determinations using enzyme electrodes [21].

At 0.15 V the electrode containing 20% of enzyme responds to ascorbic acid but not to glucose (10 mM) and ethanol (10 mM). The sensitivity of the biosensor was 5.4 times higher as compared with L-lactate up to an ascorbic acid concentration of 0.21 mM. At the normal physiological levels of ascorbic acid (40 μM) and L-lactate (2.2 mM) in blood [39] the response of the enzyme electrode to ascorbic acid was 9.8%. The electrode selectivity to ascorbic acid can be improved by decreasing the electrode action potential and increasing the specific activity of the enzyme.

Determination of L-lactate in whole blood

The enzyme electrode containing 5.9% of enzyme was used for the determination of L-lactate in goat whole blood. Goat whole blood was chosen as it contains a high physiological level of L-lactate. For comparison, an L-lactate oxidase-based rapid analyser (Eksan-L) was used [1]. The L-lactate concentration in undiluted blood was estimated to be 9.4 mM. To decrease the L-lactate concentration during the determination the blood was diluted 1.5–8-fold with buffer solution (pH 7.0). The rapid analyser was calibrated against 10 mM L-lactate in buffer solution, whereas for L-lactate determination with the enzyme electrode the calibration graph was used in the range 1–10 mM L-lactate.

There was an excellent correlation ($r = 0.9979$, $n = 18$) between L-lactate concentration determined in blood with the enzyme electrode and using the reference method. The slope of the correlation line was 0.94 and the intercept was 0.28 mM. The small positive intercept on the y-axis can be explained by the non-linear characteristic of enzyme electrode calibration. The coefficient of variation of three parallel L-lactate determinations with the enzyme electrode was $\leqslant$ 9.2%.

In conclusion, it has been illustrated that graphite chemically modified with MG can be applied to the preparation of an enzyme electrode that is suitable for the determination of L-lactate in whole blood. Such modified graphite electrodes containing other oxidoreductases could find a wide application as inexpensive enzyme electrodes.

The authors thank G. Gleixner (Technical University of Munich) for the purification of MG, Dr. J. Marcinkeviciene for the determination of MG reactivity, Dr. V. Miliukiene for supplying blood samples and Dr. J. Piksilingaite for comments on the manuscript.

REFERENCES

1 J.J. Kulys, V.-S.A. Laurinavicius, S.-H.A. Firantas and B.S. Kurtinaitiene, Zh. Anal. Khim., 43 (1988) 1878.
2 D.R. Matthews, E. Bown, A. Watson, R.R. Holman, J. Steemson, S. Hughes and D. Scott, Lancet, iv (1987) 778.
3 E. Mann-Buxbaum, F. Pittner, T. Schalkhammer, A. Jachimowicz, G. Jobst, F. Olcaytug and G. Urban, Sensors Actuators, B1 (1990) 518.
4 U. Bilitewski, P. Ruger and R.D. Schmid, Biosensors Bioelectron., 6 (1991) 369.
5 J. Scholze, N. Hampp and C. Brauchle, Sensors Actuators, B4 (1991) 211.
6 J. Kulys and E.J. D.'Costa, Anal. Chim. Acta, 243 (1991) 173.
7 J. Kulys and E.J. D.'Costa, Biosensors Bioelectron., 6 (1991) 109.
8 T. Ikeda, H. Hamada, K. Miki and M. Senda, Agric. Biol. Chem., 49 (1985) 541.
9 J. Wang and M.S. Lin, Anal. Chem., 60 (1988) 1545.
10 M. Bonakdar, J.L. Vilchez and H.A. Mottola, J. Electroanal. Chem., 266 (1989) 47.
11 P.D. Hale, T. Inagaki, H.I. Karan, Y. Okamoto and T.A. Skotheim, J. Am. Chem. Soc., 111 (1989) 3482.
12 W.W. Kubiak and J. Wang, Anal. Chim. Acta, 221 (1989) 43.
13 L. Gorton, H.I. Karan, P.D. Hale, T. Inagaki, Y. Okamoto and T.A. Skotheim, Anal. Chim. Acta, 228 (1990) 23.
14 P.D. Hale, T. Inagaki, H.S. Lee, H.I. Karan, Y. Okamoto and T.A. Skotheim, Anal. Chim. Acta, 228 (1990) 23.
15 J. Wang and K. Varughese, Anal. Chem., 62 (1990) 318.
16 J. Wang, L.-H. Wu, Z. Lu, R. Li and J. Sanchez, Anal. Chim. Acta, 228 (1990) 251.
17 G. Bremle, B. Persson and L. Gorton, Electroanalysis, 3 (1991) 77.
18 G. Palleschi and A.P.F. Turner, Anal. Chim. Acta, 234 (1990) 459.
19 M. Mascini, S. Fortunati, D. Moscone, G. Palleschi, M.M. Benedetti and P. Fabietti, Clin. Chem., 31 (1985) 451.
20 C.M. Battersby and P. Vadgama, Diab. Nutr. Metab., 1 (1988) 43.
21 V.A. Laurinavicius, J.J. Kulys, V.V. Gureviciene and K.J. Simonavicius, Biomed. Biochim. Acta, 48 (1989) 905.
22 J. Kulys, V. Laurinavicius, M. Pesliakiene and V. Gureviciene, Biotechnol. Appl. Biochem., 11 (1989) 149.
23 W.J. Blaedel and R.A. Jenkins, Anal. Chem., 48 (1976) 1240.
24 J.J. Kulys, N.K. Cenas and J.J. Kanapieniene, Stud. Biophys., 119 (1987) 175.
25 L. Gorton and A. Hedlund, Anal. Chim. Acta, 213 (1988) 91.
26 D.L. Williams, A.R. Doig and A. Korosi, Anal. Chem., 42 (1970) 118.
27 H. Durliat, M. Comtat and A. Baudras, Clin. Chem., 22 (1976) 1802.
28 J.J. Kulys and G.-J.S. Svirmickas, Anal. Chim. Acta, 117 (1980) 115.
29 S.L. Staskeviciene, N.K. Cenas and J.J. Kulys, Anal. Chim. Acta, 243 (1991) 167.
30 J.J. Kulys and K.V. Kadzjauskene, Dokl. Akad. Nauk SSSR, 239 (1978) 636.
31 M.J. Carney, J.S. Lesniak, M.D. Likar and J.R. Pladziewicz, J. Am. Chem. Soc., 106 (1984) 2565.
32 V. Khodorkovsky, A. Edzifna and O. Neilands, J. Mol. Electron., 5 (1989) 33.
33 H.P. Bennetto, M.E. Dew, J.L. Stirling and K. Tanaka, Chem. Ind. (London), (1981) 776.
34 J. Kulys, L. Wang and V. Razumas, Electroanalysis, 4 (1992) 527.
35 J. Kulys, G. Gleixner, W. Schuhmann and H.-L. Schmidt, Electroanalysis, in press.
36 M.K. Weibel and H.J. Bright, J. Biol. Chem., 246 (1971) 2734; Biochem. J., 124 (1971) 801.
37 V. Zutic, V. Svetlicic, M. Lovric, I. Ruzic and J. Chevalet, J. Electroanal. Chem., 177 (1984) 253.
38 J. Kulys, Fresenius' Z. Anal. Chem., 335 (1989) 86.
39 K. Diem and C. Lentner (Eds.), Scientific Tables, Ciba-Geigy, Basle, 7th edn., 1975, pp. 607 and 611.

Analytica Chimica Acta, 274 (1993) 59–63
Elsevier Science Publishers B.V., Amsterdam

Determination of methamphetamine in urine in situ using a methamphetamine-sensitive membrane electrode

Kiyoyuki Watanabe and Kunio Okada
Criminal Investigation Laboratory, Okayama Prefectural Police Headquarters, Tonda-cho, Okayama 700 (Japan)

Takashi Katsu
Faculty of Pharmaceutical Sciences, Okayama University, Tsushima-naka, Okayama 700 (Japan)

(Received 5th September 1992; revised manuscript received 23rd October 1992)

Abstract

A method for the determination of methamphetamine in urine using a methamphetamine-sensitive membrane electrode was developed. No pretreatment of urine samples was required, which enabled methamphetamine excreted in the urine of drug addicts to be assayed sensitively and selectively. The electrode was constructed by incorporating sodium tetrakis[3,5-bis(trifluoromethyl)phenyl]borate as the ion exchanger and tricresyl phosphate as the membrane solvent in a poly(vinyl chloride) membrane matrix. The detection limit for methamphetamine in urine was 10 μM. The response characteristics were affected considerably by changing the membrane solvent and tricresyl phosphate was found to be the most suitable for the determination of methamphetamine in urine.

Keywords: Ion selective electrodes; Potentiometry; Membrane electrodes; Methamphetamine; Urine

Methamphetamine is known to stimulate central nervous system activity, it has a significant potential for abuse and tolerance and its dependence-producing property leads to psychological disintegration [1]. In Japan, the use of this drug is regulated by the Stimulant Drugs Control Act passed in 1951. Nevertheless, methamphetamine abuse is still endemic in Japan. Therefore, the detection of methamphetamine in the urine of offenders, which is analysed most commonly by gas chromatography–mass spectrometry or infrared spectrometry after extraction of methamphetamine from the urine with an organic solvent, followed by purification by thin-layer chromatography [1], forms a large part of the workload of the Japanese Criminal Investigation Laboratory in each prefecture. A great deal of effort has been devoted to developing and improving techniques used to determine methamphetamine [1,2]. The methods reported hitherto include spectrophotometry, spectrofluorimetry, chromatography, mass fragmentometry and immunoassay [1,2].

We were interested in using an ion-selective electrode, which is attractive for routine analyses, as compounds can be determined easily with no associated sample colour or turbidity problems and hence the samples require no pretreatment. Considerable attention has been paid to the development and application of drug-sensitive electrodes [3,4]. The initial methamphetamine-sensitive electrode developed was a coated-wire type and dinonylnaphthalenesulphonic acid was used as the ion exchanger [5]. Selectivity data have

Correspondence to: T. Katsu, Faculty of Pharmaceutical Sciences, Okayama University, Tsushima-naka, Okayama 700 (Japan).

been evaluated for a few basic amino compounds, but not for inorganic cations (such as Na^+ and K^+) which are important when analysing biological samples. More recently, Hassan and Elnemma [6] succeeded in constructing an amphetamine-selective liquid-membrane electrode, based on the use of a neutral carrier, dibenzo-18-crown-6 or dibenzo-24-crown-8. The electrode showed a highly sensitive and selective response to amphetamine, which lacks the *N*-methyl group of methamphetamine. Although the response of this electrode to methamphetamine has not been determined, it would be expected to be weak, because the specific interaction between the host crown ether and guest amphetamine was the basis of the electrode response [6].

In this study, a methamphetamine-sensitive electrode was constructed by incorporating sodium tetrakis[3,5-bis(trifluoromethyl)phenyl]-borate (NaTFPB) as the ion exchanger and tricresyl phosphate (TCP) as the membrane solvent into a poly(vinyl chloride) (PVC) membrane matrix. NaTFPB was chosen because of its highly lipophilic character and high stability [7] and TCP, which suffered no serious interference from amines with high lipophilicities, was found to be the most suitable for the determination of methamphetamine in urine. This electrode enabled methamphetamine excreted in the urine of drug addicts to be determined in situ. This appears to be the first attempt to determine a biologically active drug excreted in urine directly using an ion-selective electrode.

EXPERIMENTAL

Electrode system

The methamphetamine-sensitive membrane electrode was based on a PVC membrane [8,9] and its components were 0.5 mg of NaTFPB (Dojindo), 60 μl of TCP (Tokyo Kasei) and 30 mg of PVC (degree of polymerization 1020) (Nacalai Tesque). The materials were dissolved in tetrahydrofuran, poured into a flat Petri dish (30 mm diameter) and the solvent was allowed to evaporate at room temperature. The resulting membrane was cut out and stuck to a PVC tube (4 mm o.d., 3 mm i.d.) using tetrahydrofuran as an adhesive. Two other PVC membranes containing 2-fluoro-2′-nitrodiphenyl ether (FNDPE) (Dojindo) and di(*n*-octyl) phthalate (DOP) (Tokyo Kasei) membrane solvents were prepared similarly. Each PVC tube was filled with an internal solution of 10 mM methamphetamine hydrochloride and the sensor membrane was conditioned overnight. The electrochemical cell arrangement was Ag, AgCl/ internal solution/sensor membrane/sample solution/1 M NH_4NO_3 (salt bridge)/10 mM KCl/Ag, AgCl. The e.m.f. between the silver/ silver chloride electrodes was measured with an appropriate field-effect transistor operational amplifier (input resistance $> 10^{12}$ Ω) and recorded. The volume of sample solution was 1 ml. The selectivity coefficients of the electrodes were evaluated by the fixed-interference method [8,9]. The detection limit was defined as the intersection point of the extrapolated linear regions of the calibration graph [8,9].

Methamphetamine hydrochloride and ephedrine hydrochloride were purchased from Dainippon Seiyaku and all the other chemicals were of analytical-reagent grade, unless stated otherwise.

Gas chromatography

Methamphetamine in urine was extracted with hexane, as described below, for determination by conventional gas chromatography. Urine (5 ml) was pipetted into a test tube (10 ml), followed by addition of hexane (2 ml), in which a known amount of the required internal standard compound had been dissolved, then one drop of 5 M NaOH was added to this mixture to lead the methamphetamine into the hexane layer. The tube was capped, shaken and centrifuged at low speed and about 1 μl of the hexane layer was injected directly into a gas chromatograph (Hewlett-Packard Model 5890) equipped with a DB-1 capillary column (J&W Scientific). The carrier gas was helium, the splitting ratio was ca. 40:1, the flow-rate was 1.5 ml/min and the injection temperature was set at 300°C. The column temperature was increased from 100 to 250°C at 10°C/min and then held at 250°C for 5 min. The effluent passed into a flame ionization detector. The identification and quantification of methamphetamine were based on the retention time and peak area relative to those of the appropriate internal standard. Two internal standards were used, hexadecane for the higher methamphetamine concentration range ($\gtrsim 5 \times 10^{-5}$ M) and tridecane for the lower range ($\lesssim 5 \times 10^{-5}$ M).

RESULTS AND DISCUSSION

The effect of membrane solvents on the response of the electrode to methamphetamine in urine was studied first using NaTFPB as the ion exchanger. Calibration graphs were obtained by measuring known amounts of methamphetamine added to a urine sample from a normal donor and plotting the concentrations against the corresponding e.m.f. values obtained. Typical results obtained with the three membrane solvents used, TCP, FNDPE and DOP, are shown in Fig. 1. Of these, a wide range of linear responses and the lowest detection limit (10 μM) were obtained with TCP. Calibration graphs for these electrodes were also obtained for methamphetamine in blood serum and in a solution containing 0.5 M $MgCl_2$. In the latter instance, a high concentration of $MgCl_2$ was added to adjust the ionic strength of the solution [9]. The $MgCl_2$ salt was chosen because the response to magnesium is negligible, which is apparent from the selectivity coefficient of the electrode discussed later.

The detection limit and the slope of the calibration graph of each electrode under these three different conditions are summarized in Table 1. The FNDPE-containing electrode showed a wide range of responses to methamphetamine in serum with the lowest detection limit (5 μM), in contrast to the urine results, whereas DOP was inferior to FNDPE and TCP for methamphetamine determination in both serum and urine, although all the electrodes afforded comparable detection limits in 0.5 M $MgCl_2$ solution (1–2 μM). These results demonstrate that the choice of membrane solvent is important to ensure the lowest possible detection limit for each type of sample obtained. From the results of this study, the use of TCP is

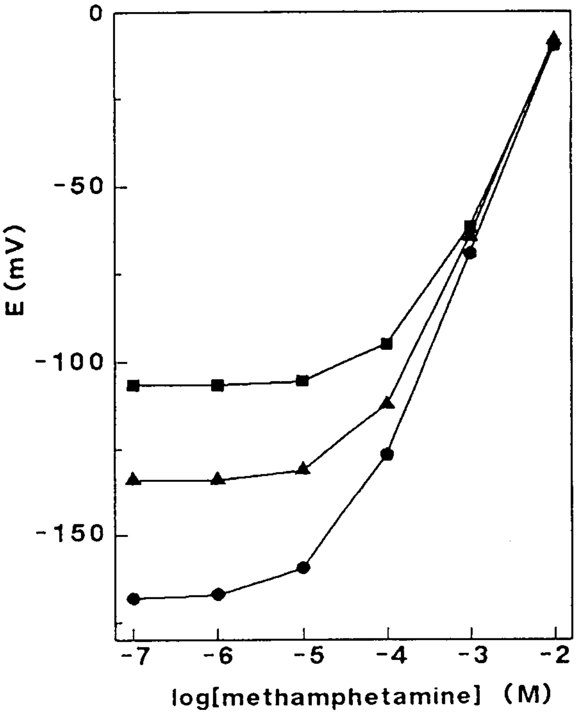

Fig. 1. Effect of membrane solvents on the electrode-response to methamphetamine in urine. ● = TCP, ▲ = DOP, ■ = FNDPE.

TABLE 1

Electrode parameters

Sample	TCP		FNDPE		DOP	
	Slope (mV per decade)	Detection limit (μM)	Slope (mV per decade)	Detection limit (μM)	Slope (mV per decade)	Detection limit (μM)
Urine	56	10	52	200	56	60
Serum	57	20	55	5	57	30
0.5 M $MgCl_2$ [a]	56	2	56	1	56	2

[a] Added to adjust the ionic strength of the solution.

TABLE 2

Selectivity coefficients, log $K_{i,j}^{\mathrm{Pot}}$ [a]

Membrane solvent	Interfering ion (j)	Concentration (M)	Log $K_{i,j}^{\mathrm{Pot}}$
TCP	Mg^{2+}	0.5	−5.5
	Ca^{2+}	0.5	−5.2
	Na^+	0.5	−4.3
	K^+	0.5	−4.4
	H^+	0.5	−3.1
	$CH_3NH_3^+$	0.5	−3.3
	$(CH_3)_4N^+$	0.05	−2.7
	$(C_2H_5)_4N^+$	0.005	−1.4
	Ephedrine	0.0005	−1.9
FNDPE	Mg^{2+}	0.5	−5.7
	Ca^{2+}	0.5	−5.1
	Na^+	0.5	−5.1
	K^+	0.5	−4.2
	H^+	0.5	−4.9
	$CH_3NH_3^+$	0.5	−3.7
	$(CH_3)_4N^+$	0.0005	−0.9
	$(C_2H_5)_4N^+$	0.00005	0.7
	Ephedrine	0.0005	−1.1

[a] i = Methamphetamine and j = interfering ion.

recommended for the determination of methamphetamine in urine, whereas FNDPE is the most suitable for its determination in blood serum.

In order to establish the response characteristics of TCP and FNDPE in more detail, the selectivity coefficients of both electrodes were also measured using the fixed-interference method. The results, together with the concentrations of interfering ions used, are summarized in Table 2. The electrode made with TCP suffered no serious interference from quaternary amines with high lipophilicities and also showed a significantly high selectivity for ephedrine, which is structurally similar to methamphetamine. Such a capacity of TCP to discriminate methamphetamine from various amines is important, because electrode-sensitive amines and their metabolites, other than methamphetamine, may be excreted in urine simultaneously. A previous study [8] has also demonstrated that a TCP-containing membrane tends to respond to specific amines, independently of the sequence of lipophilicities of amines. Although TCP was superior to FNDPE for the recognition of methamphetamine, it showed a higher response to Na^+ than FNDPE. This appears to be the reason why FNDPE afforded the lowest detection limit for methamphetamine in blood serum, in which a high concentration of Na^+ alone is noticeable.

TCP was used thereafter, as the primary aim of this study was to determine the concentration of methamphetamine in the urine of drug addicts. The response time of this electrode was less than 10 s when the concentration of methamphetamine was changed from 10 to 100 μM. The pH dependence of the electrode with three different methamphetamine concentration levels is shown in Fig. 2. The pH of the solution was changed by adding an appropriate amount of dilute hydrochloric acid or sodium hydroxide solution. The ionic strength of the solution was adjusted by adding 0.5 M $CaCl_2$, instead of 0.5 M $MgCl_2$, because $Mg(OH)_2$ is deposited at high pH values (pH > 9) [9]. The electrode response was independent of pH over the pH range 3–8. The significant increase in the potential observed below pH 3 with the lowest concentration of methamphetamine used (1×10^{-5} M) was due to

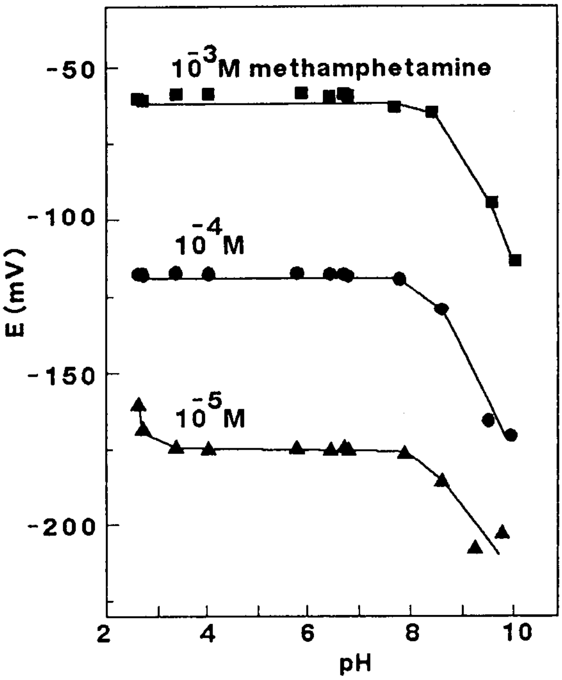

Fig. 2. Effect of pH on the response of the TCP-containing electrode to methamphetamine.

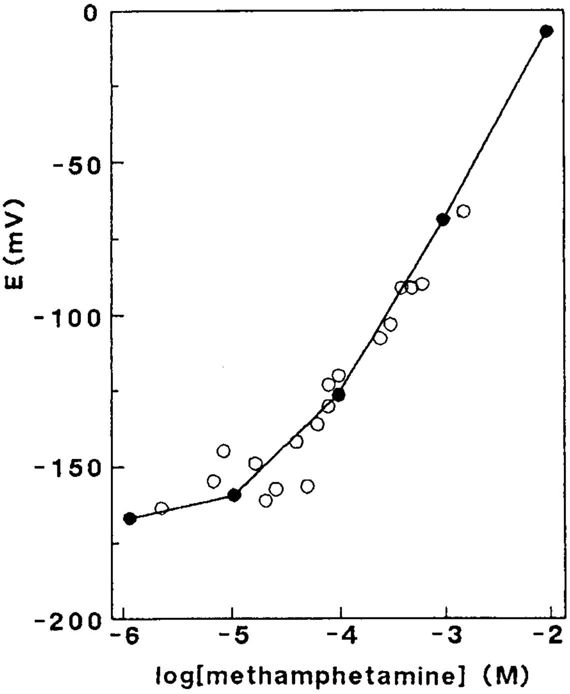

Fig. 3. Plots of the methamphetamine concentration determined by gas chromatography vs. the electrical potential measured using the methamphetamine-sensitive electrode. Results for urine sample from 18 methamphetamine addicts (○) and the calibration graph (●) of the electrode are shown.

interference from H^+ and the potential decrease above pH 8 was attributable to an increase in the concentration of unprotonated amines, as the pK_a of methamphetamine has been reported to be about 9.5 [10]. The pH independence in the range 4–9 was suitable for the determination of methamphetamine in urine, the normal pH range of which is 4.7–7.8 [11].

Next, the electrode was used to determine the methamphetamine concentration in the urine of drug addicts. It is known that a relatively large amount of methamphetamine is excreted in urine without being metabolized [1]. Urine samples from eighteen users arrested in Okayama prefecture were analysed using the TCP-containing methamphetamine-sensitive electrode and simultaneously by gas chromatography (Fig. 3). The methamphetamine concentrations determined by gas chromatography are shown on the abscissa and the corresponding electrical potentials determined with the electrode are shown on the ordinate. The plots were virtually superimposable on the calibration graph obtained with the TCP-containing electrode, which is also shown. This close correlation demonstrated clearly that methamphetamine in urine can be determined using this electrode. No pretreatment of the urine samples is required and, therefore, the determination can be carried out in situ, offering a simple practical assay of methamphetamine excreted in urine. This advantage should make a valuable contribution not only in forensic chemistry but in various other fields requiring methamphetamine determination.

This work was supported by a Grant-in-Aid from the Shimadzu Science Foundation.

REFERENCES

1 T. Niwase, Eisei Kagaku, 25 (1979) 1.
2 T.A. Brettell and R. Saferstein, Anal. Chem., 63 (1991) 148R.
3 V.V. Cosofret and R.P. Buck, Ion-Sel. Electrode Rev., 6 (1984) 59.
4 Z. Zhang and V.V. Cosofret, Sel. Electrode Rev., 12 (1990) 35.
5 L. Cunningham and H. Freiser, Anal. Chim. Acta, 139 (1982) 97.
6 S.S.M. Hassan and E.M. Elnemma, Anal. Chem., 61 (1989) 2189.
7 H. Nishida, N. Takada, M. Yoshimura, T. Sonoda and H. Kobayashi, Bull. Chem. Soc. Jpn., 57 (1984) 2600.
8 T. Katsu, T. Kayamoto and Y. Fujita, Anal. Chim. Acta, 239 (1990) 23.
9 K. Watanabe, K. Okada and T. Katsu, Eisei Kagaku, 38 (1992) 142.
10 S. Borodkin and M.H. Yunker, J. Pharm. Sci., 59 (1970) 481.
11 G.B. Schumann, in L.A. Kaplan and A.J. Pesce (Eds.), Clinical Chemistry: Theory, Analysis, and Correlation, Mosby, St. Louis, 1984, p. 996.

Analytica Chimica Acta, 274 (1993) 65–70
Elsevier Science Publishers B.V., Amsterdam

Adsorption voltammetry of the gallium–morin system

Lianjia Qu

Department of Applied Chemistry, Shandong Institute of Building Materials Industry, Jinan 250022, Shandong (China)

Wenrui Jin

Department of Chemistry, Shandong University, Jinan 250100, Shandong (China)

(Received 18th June 1992; revised manuscript received 28th September 1992)

Abstract

The behaviour of the gallium (III) complex with morin in HOAc–NaOAc at a mercury electrode was investigated. The adsorption phenomena were observed by linear-sweep voltammetry and drop-time curves. The electrode reaction was found to be the irreversible reduction of the centre ion Ga(III) in the complex adsorbed on the surface of the electrode. Under optimum conditions, the limit of detection and the linear range of the 1.5th-order derivative linear-sweep adsorption voltammetry were 4×10^{-10} mol l^{-1} and 1×10^{-9}–1×10^{-7} mol l^{-1}, respectively. The method can be applied to the determination of gallium in food samples.

Keywords: Voltammetry; Foods; Gallium; Morin

Although the mechanism of gallium uptake by tumours has not been fully elucidated, the antitumour activity of gallium has been demonstrated. Methods capable of measuring trace gallium in foods are required for studying the physiological distribution of gallium in biological systems. The electrochemical determination of ultratrace gallium appears to be a useful approach. For the polarography and voltammetry of gallium, complexing media are the most suitable. The detection limits of anodic stripping voltammetry based on the formation of its amalgam are 4×10^{-9}–8×10^{-8} mol l^{-1} in a solution containing either thiocyanate or salicylic acid [1–3]. When pulse polarography was used, 7×10^{-7} mol l^{-1} gallium could be determined in the presence of alizarins [4]. Using single-sweep polarography, 10^{-7}–10^{-8} mol l^{-1} gallium can be measured in the presence of ligands such as bromopyrogallol red [5,6], *p*-dimethylaminophenylfluorone [7], cupferron [8], alizarin complexone [9], cupferron–diphenylguanidine [10], salicylfluorone [11] and pyrocatechol [12]. The adsorptivity of metal ion complexes on the surface of an electrode can be used for the accumulation of the substance to be determined. The adsorption voltammetry of the gallium complex with phenylfluorone based on this principle has been reported [13]. The method allows 3×10^{-9} mol l^{-1} of gallium to be detected.

In this work the adsorption voltammetric determination of gallium in the presence of morin was investigated. The adsorptive and voltammetric characteristics and the electrode process of the system at a hanging mercury drop electrode (HMDE) were studied. With this method, 4×10^{-10} mol l^{-1} of gallium can be detected when the 1.5th-order derivative technique is used.

Correspondence to: Wenrui Jin, Department of Chemistry, Shandong University, Jinan 250100, Shandong (China).

EXPERIMENTAL

Apparatus

A Model SDP-1, 0.5th-order derivative polarograph (Jintan Analytical Instrument Factory) modified according to [14] (in order to add the 1.5th-order derivative technique mode) was used. It was coupled with a Model LZ_3-104 *X-Y* recorder (Shanghai Dahua Instrument Factory). The three-electrode system consisted of a Model SH-84 HMDE (Department of Chemistry, Shandong University) as the working electrode, a platinum plate as the counter electrode and an Ag/AgCl electrode as the reference electrode connected to the analyte via a salt bridge filled with 0.4 mol l^{-1} HOAc + 0.4 mol l^{-1} NaOAc (pH 4.15). A Model UV 3000 UV-visible spectrophotometer (Shimadzu) was used for spectrophotometry. Electrolysis was performed using a mercury-pool electrode with an area of 3 cm^2.

Reagents and solutions

A 1×10^{-3} mol l^{-1} stock solution of Ga(III) was prepared by dissolving an appropriate amount of Ga_2O_3 (spectrally pure) in a small amount of hydrochloric acid (analytical-reagent grade) in a water-bath and diluting with water. Standard solutions were obtained by diluting the stock solution with water. A 1×10^{-3} mol l^{-1} stock solution of morin was prepared by dissolving an appropriate amount of morin in ethanol. HOAc and NaOAc were of analytical-reagent grade. All solutions were prepared using doubly distilled water.

Procedure

The supporting electrolyte was 0.4 mol l^{-1} HOAc-0.4 mol l^{-1} NaOAc. The solution containing Ga(III) and morin was deaerated for 15 min with pure nitrogen. The measurements were carried out after a preconcentration step, in which the solution was usually stirred during a preconcentration time, t_a, of 2 min at a preconcentration potential E_a. After a rest period of 30 s, the response curve was recorded by scanning the potential in the negative direction either in the conventional mode or with the 1.5th-order derivative technique. Each measurement was performed with a fresh drop with an area of the HMDE of 1.41 mm^2. All potentials were measured against the Ag/AgCl electrode.

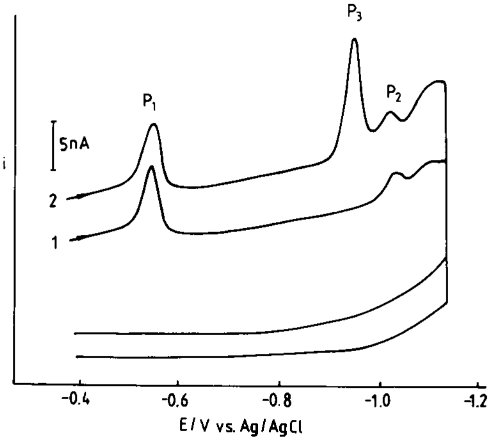

Fig. 1. Cyclic adsorption voltammograms of morin and its complex with Ga(III): (1) 1×10^{-6} mol l^{-1} morin; (2) (1)+1 $\times 10^{-6}$ mol l^{-1} Ga(III). 0.4 mol l^{-1} HOAc-0.4 mol l^{-1} NaOAc; $E_a = -0.20$ V; $t_a = 2$ min; $t_r = 30$ s; $v = 100$ mV s^{-1}.

RESULTS AND DISCUSSION

Adsorptive and voltammetric characteristics of the Ga(III) complex with morin

Two peaks (P_1 and P_2) appeared in the linear-sweep voltammogram of morin in HOAc-NaOAc for $E_a = -0.20$ V at $t_a = 2$ min (Fig. 1, curve 1). The peak potentials E_{p_1} and E_{p_2} are -0.53 and -1.03 V, respectively. When a micro amount of Ga(III) is added to the solution, a new peak (P_3) appears at a position between E_{p_1} and E_{p_2}. In a solution of pH 4.15, the peak potential of P_3 is -0.95 V for a scan rate of 100 mV s^{-1}. It seems logical to assume that the new peak results from the Ga(III) complex with morin.

Figure 2 shows a typical plot of the 1.5th-order derivative of the current with respect to time for the reduction of Ga(III) complexes with morin. The peak-to-peak value of the 1.5th-order derivative plot, e'_{pp}, is more sensitive than the peak current on the voltammogram of the reduction of the Ga(III) complex, i_p; e'_{pp} increases on extending t_a. Over a relatively long t_a, adsorption equilibria between the complex on the surface of the

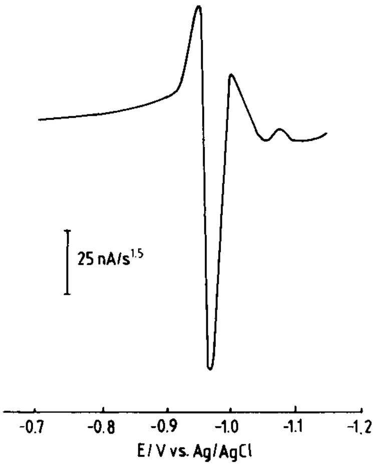

Fig. 2. Typical 1.5th-order derivative plot of current versus time for the Ga(III) complex with morin. $E_a = -0.65$ V; $v = 69$ mV s^{-1}; other conditions as in Fig. 1.

electrode and that in the solution are established (Fig. 3); i_p and e'_{pp} are proportional to the potential scan rate, v, and $v^{2.5}$, respectively. These results are characteristic of the reaction of adsorbed reactants on the electrode [15–19].

The drop-time curves of the supporting electrolyte and that of solutions of morin and its complex with Ga(III) are shown in Fig. 4. When morin is added to the supporting electrolyte, the drop time decreases in the potential range from 0 to −0.60 V. In the presence of both morin and Ga(III), the shape of the drop-time curve is the same as that for morin alone. However, the drop-time is lower in the potential range between 0.0 and −1.20 V, demonstrating the adsorptivity of the Ga(III) complex with morin. The adsorption of the complex on the surface of the mercury electrode is dependent on the potential. The adsorption is stronger between −0.60 and −0.70 V.

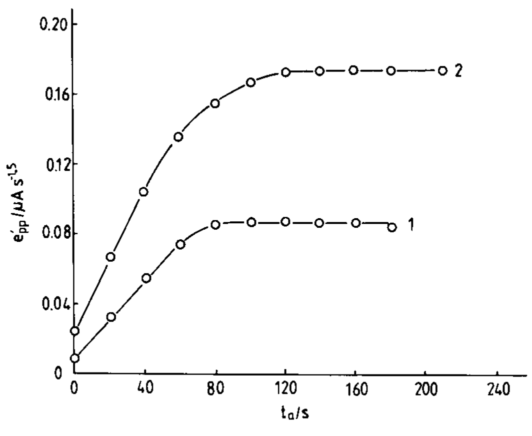

Fig. 3. Dependence of e'_{pp} of the Ga(III) complex with morin on the preconcentration time at different concentrations of Ga(III). Ga(III) concentration: (1) 5×10^{-8} mol l^{-1}; (2) 1×10^{-7} mol l^{-1}. Conditions as in Fig. 1.

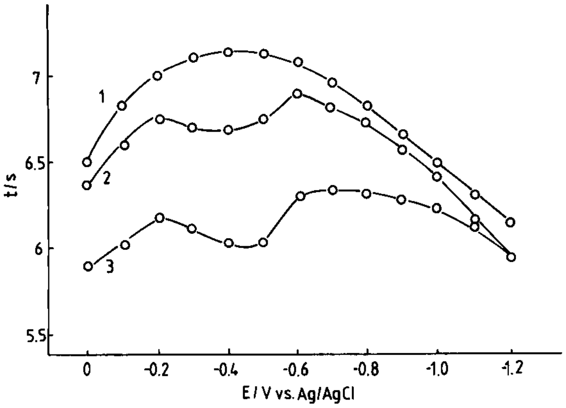

Fig. 4. Drop-time curves: (1) 0.4 mol l^{-1} HOAc–0.4 mol l^{-1}NaOAc; (2) (1) + 1×10^{-4} mol l^{-1} morin; (3) (2) + 1×10^{-4} mol l^{-1} Ga(III).

Electrode process

The absorbance maxima of morin are located at 255 and 345 nm for absorption spectra in 0.4 mol l^{-1} HOAc–0.4 mol l^{-1} NaOAc. When Ga(III) is added to the solution, a new absorbance peak at 432 nm appears. This means that a Ga(III) complex with morin is formed in the solution. The absorbance peak at 432 nm increases with increasing concentration of Ga(III) until a maximum absorbance value is observed at a ratio of Ga(III) to morin (L) of 1 : 3. This is evidence for the formation of a complex of 1 : 3 composition, viz., GaL$_3$. Therefore, the most important reaction in the bulk of the solution involves the following equilibrium:

$$\text{Ga(III)} + 3\text{L} \rightleftharpoons \text{GaL}_3 \qquad (1)$$

The value of e'_{pp} for the reduction of the complex adsorbed has also a maximum, when the ratio of the concentration of Ga(III) to that of morin is 1 : 3. This means that the complex in the bulk of the solution and the complex adsorbed on the surface of the electrode have the same composition. Thus, the adsorption process can be expressed as follows:

$$GaL_3 + Hg \rightleftharpoons GaL_3(ads)(Hg) \qquad (2)$$

In order to obtain some information on the reactants and products, electrolysis was used. The working electrode was a mercury-pool electrode. An electrolysis potential of -1.00 V (more negative than the peak potential of reduction of the complex) was used. With increasing electrolysis time, the peak current of reduction of the complex decreased to zero. The mercury-pool electrode was removed from the solution and washed with doubly distilled water. The mercury was poured into a cell without Ga(III), then a small amount of HCl and water were added. If gallium was produced in the mercury during electrolysis, it would be dissolved into the HCl solution in the cell. After a few minutes (with stirring), definite amounts of HOAc, NaOAc and morin were added to the cell, giving concentrations of 0.4, 0.4 and 1×10^{-6} mol l^{-1}, respectively. In this solution and using linear-sweep adsorption voltammetry with the HMDE, a peak at $E_p = -0.95$ V was obtained. Obviously, this peak is produced by the complex of Ga(III) with morin adsorbed on the surface of the electrode. Also, the gallium was originally a component present in the mercury pool electrode produced during electrolysis. Hence it is reasonable to propose that the product of the reduction of the complex is metallic gallium and it can be inferred that Ga(III) in the complex GaL_3 is discharged in the interfacial reaction. When a definite amount of morin was added to the cell after the electrolysis, no peak due to reduction of GaL_3 appeared. This indicates that Ga(III) in the complex has been reduced and was taken up in the mercury electrode, which was removed from the cell. Let us choose an electrolysis potential of -0.85 V (more positive than the peak potential of reduction of the complex). After the peak current of reduction of morin at $E_p = -0.53$ V had dropped to zero (which means that the morin has been reduced and is absent), a definite amount of Ga(III) was added to the cell. By using linear-sweep adsorption voltammetry, the peak P_3 corresponding to the reduction of the Ga(III) complex was not obtained. If a definite amount of morin was added to the cell, the peak corresponding to the reduction of Ga(III) complex was obtained again. This indicates that P_3 corresponds to the reduction of the Ga(III)–morin complex and not to a complex of gallium(III) with the product of reduction of morin, which is produced at a potential more negative than -0.53 V. The peak potential P_3 does not change with pH, suggesting that protons do not take part in this interfacial reaction of the complex. This means that the reactant cannot be morin, because if morin is the reactant protons will be consumed.

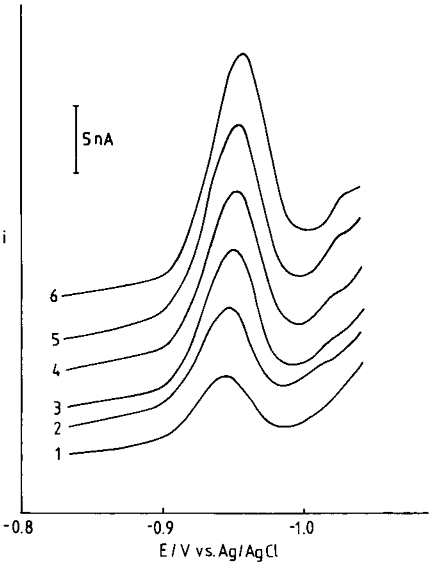

Fig. 5. Linear-sweep adsorption voltammograms of the Ga(III) complex at different scan rates, v: (1) 30; (2) 50; (3) 74; (4) 86; (5) 100; (6) 120 mV s^{-1}. Conditions as in Fig. 2.

From the above experiments, it can be suggested that the reactant is Ga(III) in GaL_3 adsorbed on the surface of the mercury electrode and the products are Ga amalgam and morin, which is also adsorbed on the surface of the electrode based on the drop-time curves shown in Fig. 4.

Figure 5 shows the linear-sweep adsorption voltammograms of the Ga(III) complex at different scan rates. From the asymmetric shape of the peak and the facts that the position of the peak on the potential axis shifts in the negative direction with increasing scan rate and that no peak corresponding to the oxidation of the product of the reduction of the complex on the cyclic adsorption voltammograms of the Ga(III) complex appears, it may by concluded that the interfacial electrochemical reduction of the complex is an irreversible process [16]. The apparent transfer coefficient of the interfacial reaction, αn, can be taken from the peak half-width, $W_{1/2,\mathrm{ir}}$, according to the following equation [16]:

$$\alpha n = 62.5/W_{1/2,\mathrm{ir}} \qquad (3)$$

The peak half-width is 40 mV. From this value, an α value of 0.52 and an n value of 3 can be calculated; αn can also be obtained using the relationship between $E_{\mathrm{p,ir}}$ and log v according to the following equation [16]:

$$E_{\mathrm{p,ir}} = K - (2.303RT/\alpha nF) \log v \qquad (4)$$

where v is the scan rate. From the slope of linear plot of $E_{\mathrm{p,ir}}$ vs. log v, $\alpha = 0.5$ and $n = 3$ are obtained. Both values are in agreement with those obtained from the peak half-width.

Hence the interfacial reaction can be expressed as follows:

$$\mathrm{GaL_3(ads)(Hg)} + 3\mathrm{e}^- \rightarrow \mathrm{Ga(0)(Hg)} + 3\mathrm{L(ads)} \qquad (5)$$

Analytical application

It was found experimentally that the optimum composition of the supporting electrolyte is 0.4 mol $\mathrm{l^{-1}}$ HOAc–0.4 mol $\mathrm{l^{-1}}$ NaOAc; the optimum concentration of morin is 1×10^{-6} mol $\mathrm{l^{-1}}$ and the optimum preconcentration potential is −0.65 V. Under these conditions, the linear range and the detection limit of 1.5th-order derivative linear-sweep adsorption voltammetry are 1×10^{-9}–1×10^{-7} mol $\mathrm{l^{-1}}$ and 4×10^{-10} mol $\mathrm{l^{-1}}$, respectively. Experimental results showed that a 1000-fold excess of Ca(II) and Mg(II), a 500-fold excess of Ni(II), Cd(II) and Pb(II), a 200-fold excess of Fe(III) and Al(III), a 100-fold excess of Cu(II) and Zn(II) and a 40-fold excess of Cr(III) do not interfere in the determination of Ga(III). The interference of metal ions can be overcome by extraction.

TABLE 1

Results of the determination of gallium in samples of food and recoveries of Ga(III) added to the samples

Sample	Content determined (μg $\mathrm{g^{-1}}$)	Average recovery (%)
Wheat flour	0.130, 0.121, 0.130	96
Millet	0.156, 0.160	103
Rice	0.182, 0.191	111
Maize flour	0.062, 0.069	92

Samples of food (ca. 0.5 g) were digested with a mixture of 3 ml of $\mathrm{HNO_3}$ and 3 ml of $\mathrm{HClO_4}$ in a beaker [20]. The small amount of white residue was dissolved with a small volume of water. After adding 2 ml of 10% ascorbic acid solution, the mixture was left for 5 min, then 22 ml of 7 mol $\mathrm{l^{-1}}$ HCl were added into the beaker, and the solution and 30 ml of a mixture of benzene and ethyl acetate (1 + 1) were transferred into a separating funnel. The solution was vibrated for 1 min. The aqueous phase in the funnel was discarded. The organic phase was washed with 30 ml of 7 mol $\mathrm{l^{-1}}$ HCl and the aqueous phase was discarded. Then the organic phase was extracted twice with 20-ml volumes of water. The 40-ml extract (aqueous phase) was removed from the separating funnel and boiled for 10 min. After cooling, the solution was diluted to 50 ml in a 50-ml volumetric flask. A 10-ml volume was taken from the flask and transferred into a cell and the 1.5th-order derivative plot of current was recorded. The 1.5th-order derivative plots of current were also recorded for the solution after adding a standard solution of Ga(III) to the sample solution under the same conditions. The amount of gallium in the sample solution can thus be determined from the resulting standard addition plot. Typical results obtained are summarized in Table 1.

REFERENCES

1 L.N. Vasileva and E.N. Vinogradova, Zh. Anal. Khim., 18 (1963) 454.
2 M.S. Zakharov, Zh. Anal. Khim., 18 (1963) 450.
3 E.D. Moorhead and P.H. Davis, Anal. Chem., 47 (1975) 622.

4 H.D. Sommer and F. Umland, Fresenius', Z. Anal. Chem., 301 (1980) 203.
5 S.-Z. Lu, Metall. Anal. (China), No. 3 (1982) 7.
6 Z.-Z. Tan, Fenxi Huaxue, 10 (1982) 525.
7 J.-Y. Chen and Y.-H. Deng, Fenxi Huaxue, 10 (1982) 459.
8 S.-Y. Zhang and K.-L. Xu, Chem. J. Chin. Univ., 4 (1983) 449.
9 N.-Q. Li and J.-K. Zhang, Chem. J. Chin. Univ., 6 (1985) 217.
10 Z.-F. Zhao, G.-Z. Cao and Y.-H. Shao, Fenxi Shiyanshi, 4, No. 3 (1985) 1.
11 X.-Y. Tao, Metall. Anal. (China), 6, No. 6 (1986) 25.
12 Q.-L. Li, H. Liu and T. Hu, Fenxi Shiyanshi, 6, No. 9 (1987) 6.
13 S.-Q. Wen, R.-L. Chen, W.-R. Jin and H. Zhai, Metall. Anal. (China), 6, No. 2 (1986) 38.
14 G.-J. Lin and W.-R. Jin, Fenxi Shiyanshi, 9, No. 2 (1990) 56.
15 R. Kalvoda, W. Anstine and M. Heyrovsky, Anal. Chim. Acta, 50 (1970) 93.
16 E. Laviron, J. Electroanal. Chem., 52 (1974) 355.
17 A.P. Brown and F.C. Anson, Anal. Chem., 49 (1977) 1589.
18 W.-R. Jin, H. Cui, L.-X. Zhu and S.-R. Wang, J. Electroanal. Chem., 309 (1991) 37.
19 W.-R. Jin and X.-X. Li, Anal. Chim. Acta, 236 (1990) 453.
20 W.-R. Jin, S.-Q. Wen, H.-T. You and Y. Li, Fenxi Huaxue, 13 (1985) 296.

Analytica Chimica Acta, 274 (1993) 71–85
Elsevier Science Publishers B.V., Amsterdam

Evaluation and correction of signal model errors in a matched filter for the quantification of chromatographic data

B. van den Bogaert, H.F.M. Boelens and H.C. Smit

Laboratory for Analytical Chemistry, University of Amsterdam, Nieuwe Achtergracht 166, 1018 WV Amsterdam (Netherlands)

(Received 26th February 1992)

Abstract

The effect of errors in the signal model in a matched filter for use in the quantification of chromatographic data and the influence of the noise type on this effect are evaluated. The errors are modelled as incorrect parameter values in an otherwise correct model, and their effect is monitored in the signal-to-noise ratio in the output of the matched filter. Normalization of the matched filter on the variance of the noise in the output makes the matched filter output a direct measure of this signal-to-noise ratio. The normalized matched filter output as a function of the signal model parameters is derived mathematically for a Gaussian signal and first order band-limited white noise. This function has a maximum for the correct signal model, suggesting the use of the maximum in the output of the normalized matched filter as the criterion in a Simplex optimization of the signal model as a means of correcting for signal model errors. Computer simulations confirm the feasibility of this approach. The signal-to-noise ratio improvement of the Simplex optimized matched filter as a function of signal-to-noise ratio in the input and the time constant of the noise is discussed, both on the basis of the mathematically derived formulae and the results of the computer simulations.

Keywords: Chromatography; Coloured noise; Matched filtering; Noise; Noise model; Quantification; Robustness; Signal model errors; Signal/noise enhancement

The work described here fits in with the pursuit of optimal procedures for data processing in analytical chemistry, and for the field of chromatography in particular (as described in e.g. [1–3]). An optimal procedure extracts the highest amount of information from the data. The information content of a result depends on its reliability, i.e. its accuracy and precision. This publication is concerned with the precision aspect of quantitative analytical information, and, in particular, with the application of a procedure known as the matched filter (MF), or matched linear system.

The MF was introduced in analytical chemistry in the early 1970s [4], but it has not become a widely applied technique. Therefore, we will start by developing the argument in favour of its use in quantitative chromatography. After that, we will give a mathematical description of the MF. The major topic covered in this work is the robustness of the MF with respect to signal model errors. We will evaluate this effect mathematically for a specific situation for which the mathematics can be solved relatively easily. Following this evaluation, the results of computer experiments with a method to correct the signal model errors will be presented.

Correspondence to: H.C. Smit, Laboratory for Analytical Chemistry, University of Amsterdam, Nieuwe Achtergracht 166, 1018 WV Amsterdam (Netherlands).

INTRODUCTION OF THE MATCHED FILTER

Signal intensity estimation

The term chromatography is used here to indicate a system that consists of injection, column, and single-channel detection. The detector data are modelled as consisting of transient signals, corresponding to components, and additive noise. Both signals and noise are defined with respect to a base level, whose value is taken to be zero throughout the current work, thus excluding the aspect of base-level estimation from the considerations. A chromatographic signal will be described as a shape multiplied by a scale factor, located on a specific position in the data. In quantitative chromatography, the signal property to be estimated from the data is the signal intensity, which is not necessarily identical to the signal scale factor. It will be shown that signal intensity can be defined and estimated in various ways, each estimator having its own merits. The choice of an estimator crucially affects the quality of the overall quantification. The current work is dedicated to finding an optimal estimator, i.e. an estimator with minimal systematic and random error.

We recognize two error sources in the estimation of signal intensities from detector data: signal overlap and detector noise. Signal overlap is a deterministic phenomenon. It will lead to a systematic error when the intensities of overlapping signals cannot be determined individually, and the concentrations of the components differ between samples or between sample and standards. Signal overlap poses a complication of the application of the MF that will not be treated in this publication. Only completely separated signals are studied, modelled as the chromatograms of a pure compound. Detector noise is a stochastic phenomenon and therefore a source of random error. It is assumed here that the noise is additive, normally distributed with zero mean, that it is (weakly) stationary and ergodic. Noise will be described by its power spectral density (PSD).

Peak height

The amplitude in any point of the signal can be used as the measure of signal intensity in quantification. It is estimated as the value in a point that is fixed for all standards and samples. The obvious point to use is the signal maximum, the peak top, since it has the lowest relative standard deviation of all points in the signal and since it is the easiest point to recognize. Thus, the estimator is equal to the signal scale factor, multiplied by the maximum of the signal shape. This estimator, peak-height measurement, is the simplest signal intensity estimator conceivable. Its main problem is the estimation of the position of the maximum of the signal component in the data. The larger the variance of the noise additive to some signal, the more likely the true signal maximum will be obscured by the noise.

Peak integration

Signal intensity can also be defined as the integrated signal, which is equal to the integral of the signal shape, multiplied by the signal scale factor. The practical advantage of this definition over the previous one is that, under specific circumstances, it can be estimated with less random error. This will be illustrated with a simple example with discrete data.

When the data consists of a signal that is a constant and noise that is white, i.e., the noise contributions in the individual points are uncorrelated, the relative standard deviation of the sum over n points will be less than that of an individual point by a factor equal to the square root of n.

In the chromatographic reality, a signal is peak-shaped and an increase in n will not give a constant decrease in the relative standard deviation, since points far from the maximum will contribute only little to the sum. Therefore it may be expected that there is an optimal value for n. For asymmetric peaks and for coloured noise, the optimal value will be different. For several signal shapes and noise types the optimal value has been derived mathematically [5]. The derivations show that for some situations, the optimal value is so low that integration reduces to peak-height measurement, indicating that the intuitive advantage of integration has a limited validity.

In practice, integration is not equal to taking the integral over the optimum interval on the correct position, but to taking the sum of the values for the points measured between the estimated begin and end of the signal. The uncertainty associated with these estimations makes the comparison of practical integration with practical peak-height measurement more complicated than the comparison described above. We will not discuss this any further.

Moving average

The intuitive argument in favour of integration is based on a description of the data in their original form, i.e., in the time domain. In order to extend the argument to other signal intensity definitions, and ultimately to the MF, it is useful to turn to the Fourier or frequency domain. For this purpose, integration can be described as measuring the maximum of the signal component in the output of a moving-average filter, analogous to peak-height measurement in the original, unfiltered data [6]. The filter in this description takes the average over the number of points that is summed in integration. The operation of this filter can be described mathematically as a cross-correlation of the detector data with a block-shape, or, in the Fourier domain, as the multiplication of the Fourier transform (FT) of the data with the complex conjugate of the FT of the block-shape, which is a sinc function.

The block-shape is the impulse response, the corresponding sinc function the transfer function of the moving-average filter. The transfer function of a linear filter can be considered a frequency weight function, acting upon the FT of the data being filtered. Because of the linearity of both filter and FT, the weight function operates on the FTs of the signal and the noise component in the data separately. However, FTs are essentially complex functions, which complicates the evaluation of the weight function. Furthermore, noise is not defined by its FT, but by its power spectral density, which is the FT of its auto-correlation function (ACF). Fortunately, a linear filter can also be described as acting on the PSD of the data, taking the square of the norm of the filter transfer function as the weight function. For the moving average this is a sinc^2. Note that the PSD of the data is the sum of the PSDs of signal and noise and two cross-power spectral densities. These cross terms are in fact cross-correlations between signal and noise and their expected value is zero.

The Fourier argument in favour of the moving average, and therefore integration, is based on observation of the ratio of the signal power to the noise power in each frequency. A realistic peak-shaped signal, e.g., a Gaussian, consists primarily of relatively low frequencies. Assuming white noise, one can imagine that there will be high frequencies whose power originates from the noise rather than from the signal. By giving these frequencies little weight, the total noise power is reduced, whereas the total signal power is hardly affected. This is what the moving average does, with its sinc^2-shaped weight function, a function that can be tuned to resemble the signal PSD. In fact, the moving average acts as a low-pass filter.

The period of the sinc^2 function is inversely proportional to the width of the block-shape in the time domain. A narrow block will have little effect on the noise, and a wide block will not only affect the noise, but also the signal. Just like in the time-domain argument for integration, it can be expected that there is an optimum value for the width of the block-shape.

When integration would indeed be implemented as peak-height measurement after moving-average filtering, it would face the same problem as normal peak-height measurement: finding in the data the position of the maximum in the signal component. Because of the signal-to-noise ratio (S/N) improvement brought about by the filter, the detection is expected to be more successful with filtering than without. In other words, the random error introduced by the detection will be less, or, for a specific error level, the input noise level at which the maximum can be detected will be higher.

Cross-correlation

The intuitively optimal filter performs a weighing in the frequency domain that is consistent with the signal-to-noise power ratio per frequency. Following this intuition, the moving average is not optimal. It has side lobes, that, although rapidly decreasing in amplitude, will give weight to frequencies primarily describing noise. Furthermore, the PSD of the signal will usually have a shape that is different from the shape of the main lobe of the sinc^2.

Assuming white noise, the intuitively optimal filter would use the PSD of the signal itself as the frequency weight function. This operation is known as cross-correlation. The working of its weighing principle can also be compared to that of integration in the time domain. The maximum of the signal component in the output of the cross-correlation is formed by taking the sum over the signal, but, in contrast to integration, weighing each point according to its relative standard deviation.

The maximum of the signal component in the output of the moving-average filter can be used as signal intensity estimator in conjunction with a definition of signal intensity in terms of total power. In the absence of noise, cross-correlation of the data with the signal is equal to calculating the auto-correlation of the signal. The maximum of the auto-correlation is equal to the total power of the signal. In practice, the data may be cross-correlated, not with the signal itself, but with the signal shape, in which case the maximum will be equal to the scale factor of the signal that is present in the data, multiplied by the total power of the signal shape.

Peak-height measurement after cross-correlation faces the same signal maximum detection problem as the previously described signal intensity estimators. Extending on the argument for the moving average, the detection after cross-correlation can be expected to be the most successful.

Matched filter

Summarizing the intuitive argument: using a filter that weighs all frequencies in the data according to the ratio of signal power to noise power per frequency and taking the maximum in the output of this filter, constitutes an optimal estimator of the intensity of the signal component in the data, i.e., an estimator with minimal relative standard deviation.

In case of white noise, the filter consists of a cross-correlation of the data with the signal, or signal shape. This is often called matched filter (MF), being matched to the shape of the signal. We prefer to use the term MF for the general case in which the noise is not necessarily white. This MF can also be described as a cross-correlation, but not a cross-correlation of the original data with the signal shape, but of the prewhitened data with a likewise prewhitened signal shape.

Prewhitening refers to the operation of a filter that transforms the PSD of the noise component of the data into a constant for all frequencies. Note that this transformation is designed for the ensemble average of the noise PSD, not for the PSDs of the individual noise realizations. Of course, a prewhitening filter also affects the signal, but the change is deterministic and known and the result is what is referred to above as the prewhitened signal.

When the maximum of the signal component in the filter output is used as signal intensity estimator, this intensity is defined, analogous to the estimator based on cross-correlation, as the total power of the prewhitened signal shape.

MF PRINCIPLE

Mathematically, the MF can be derived as the linear system that minimizes the squared relative standard deviation in the maximum of the signal component in the output of the system, or, equivalently, as the linear system that maximizes the squared instantaneous S/N in that maximum [7,8]. The square in the quantity to be optimized arises from mathematical convenience, similar to least-squares regression. The S/N optimization is the more common derivation. Its aim can be expressed, using a frequency-domain description, as the system transfer function $H(jf)$ that optimizes:

$$(S/N)^2_{\text{out}} = \frac{y(\mu)^2}{\sigma^2_{\text{out}}} = \frac{\left| \int_{-\infty}^{+\infty} H(jf) k X(jf) \exp(j2\pi f \mu)\, \mathrm{d}f \right|^2}{\int_{-\infty}^{+\infty} | H(jf) |^2 S(f)\, \mathrm{d}f} \qquad (1)$$

where $y(t)$ is the signal component in the output, μ the position of the maximum of $y(t)$, σ_{out} the standard deviation of the noise in the output, $S(f)$ the power spectral density of the noise component in the input, $X(jf)$ the FT of the shape of the signal component in the input and k the scale factor of the signal component in the input.

The optimizing filter transfer function is based on models of both the signal component and the noise component in the input, i.e., models for $X(jf)$ and $S(f)$. The scale factor is not included in the filter. Since it multiplies both signal and noise, it has no influence on the optimality of the filter. The filter is defined by:

$$H(jf) = \frac{X^*(jf)}{S(f)} \exp(-j2\pi f\mu) \tag{2}$$

where the asterisk denotes the complex conjugate. The prewhitening aspect of the MF can be found in the denominator: dividing the FT of a signal by the square root of the PSD of the noise has the effect of prewhitening the noise. The PSD in the denominator of Eqn. 2 whitens both the signal $X(jf)$ and its complex conjugate.

The role of the term μ deserves some attention. Note that the filter that optimizes the S/N at position μ in its output turns out to be a function of that same position. The exponential term containing μ is the Fourier domain equivalent of a time shift over μ. This means that the filter can optimize the S/N at any position in its output by adjusting this time shift, i.e., by moving the maximum to the required position. Vice versa, an arbitrary value for μ in the filter transfer function will only cause a time shift of the output, without affecting the optimality of the S/N in the maximum of the signal component. In practice, an additional time shift may be introduced by the signal model, since the exact position of the signal maximum is usually unknown.

Using the maximum of the signal component in the output of the MF as signal intensity estimator, implies the definition of this intensity as being proportional to the total power of the prewhitened signal shape, the proportionality constant being the signal scale factor. This is expressed mathematically by substitution of Eqn. 2 into the expression for the signal component in the MF output, found in the numerator of Eqn. 1:

$$y(\mu) = k\int_{-\infty}^{+\infty} \frac{|X(jf)|^2}{S(f)}\,\mathrm{d}f \tag{3}$$

By substitution of Eqn. 2 into the denominator of Eqn. 1 a remarkable property of the MF is found. The variance of the noise in the output is equal to the prewhitened signal shape power:

$$\sigma_{\text{out}}^2 = \int_{-\infty}^{+\infty} \frac{|X(jf)|^2}{S(f)}\,\mathrm{d}f \tag{4}$$

Therefore the signal intensity is proportional to the squared maximum instantaneous S/N:

$$(S/N)_{\text{out}}^2 = \frac{y(\mu)^2}{\sigma_{\text{out}}^2} = k^2 y(\mu) \tag{5}$$

Furthermore, the mathematical optimality of the MF is valid only on the true position of the maximum in the signal component in the MF output. The uncertainty inherent to the detection of this position prohibits the practical realization of the predicted S/N. In the current work, the statistics of the detection are not included in the mathematics, but the role of the detection in the estimation procedure at low S/N will be investigated in computer simulation experiments.

The last general remark we wish to make on the MF is that it has been designed for the detection of signals in situations where signals convey information by their presence instead of their intensity, such as the pulses in the transmission of digital data. It has not been designed for the quantification of signals and, not surprisingly, the literature on this use is sparse [9,10].

SIGNAL MODEL ERRORS

Introduction

The MF can, of course, be optimal only if the models that are used are correct. When using the MF for chromatographic data, the signal model is the shape of the peak. Since this shape is not a constant throughout a chromatogram, using one filter for all the peaks in the chromatogram means the use of incorrect models and therefore suboptimality. Furthermore, especially at low S/N, the shape of one particular peak may differ over replicates of the chromatogram, further complicating the use of the MF.

Therefore, the current work is focused on the robustness of the MF with respect to errors in the signal model. The aim is to evaluate the sensitivity of the S/N in the MF output to these errors. The theory of the MF implies that an incorrect model will result in a suboptimal filter, but it does not directly tell us the shape of the optimum. Is it flat or sharp? The influence of the type of noise present, i.e., the noise model in the MF (since the correct model is used), on this shape will also be investigated. Furthermore, on the basis of these evaluations, we will propose a procedure for correcting signal errors, and we will test this procedure using computer simulations. In the computer experiments we will also investigate the role of the signal maximum detection.

Modelling of errors

The signal model in the MF may be an empirically obtained shape, measured with high S/N, or a mathematical model based on theory. For the evaluation of signal model errors, we focus on parameterized theoretical signal models. By doing this, the model errors themselves can be modelled by incorrect values for the parameters in an otherwise correct model.

Furthermore, empirical shapes are by definition rigid. In chromatography, for the reasons outlined above, they will often result in suboptimality. A parameterized model offers flexibility, suggesting that the MF based on such a model may be adapted to give truly optimal results.

Measuring the effect of errors

The performance of the MF as a function of the signal model can be related to the maximum S/N in the output. When the correct model is used, the square of this ratio is proportional to the maximum of the signal component in the output. This suggests that the performance of the MF can be measured directly from the MF output. However, because a filter affects both the signal and the noise component, the absolute value of the MF output is not sufficient to measure the filter performance and another approach is required.

A practical and a theoretical approach can be distinguished. The practical one is to identify signal and noise by statistical processing, i.e., calculation of mean and standard deviation. The theoretical one is to calculate the output variance on the basis of the filter transfer function and the PSD of the input noise.

We propose a further elaboration of the theoretical approach: normalization of the filter transfer function on the output noise variance. In other words, we introduce a normalized filter described by the transfer function:

$$H_n(jf) = \frac{H(jf)}{N} \qquad (6)$$

The factor N is determined by demanding that the variance of the noise in the output of this filter equals one:

$$\begin{aligned}\sigma_{\text{out,n}}^2 &= \int_{-\infty}^{+\infty} |H_n(jf)|^2 S(f)\,\mathrm{d}f \\ &= \frac{1}{N^2}\int_{-\infty}^{+\infty} |H(jf)|^2 S(f)\,\mathrm{d}f = 1\end{aligned} \qquad (7)$$

It follows that the factor N equals σ_{out}, i.e.:

$$\begin{aligned}N = \sigma_{\text{out}} &= \sqrt{\int_{-\infty}^{+\infty} |H(jf)|^2 S(f)\,\mathrm{d}f} \\ &= \sqrt{\int_{-\infty}^{+\infty} \frac{|X(jf)|^2}{S(f)}\,\mathrm{d}f}\end{aligned} \qquad (8)$$

Using the normalized filter transfer function, the output becomes a direct measure of the instantaneous S/N, irrespective of the signal model in the MF and the noise present:

$$\begin{aligned}y_n(\mu) &= \int_{-\infty}^{+\infty} H_n(jf) kX(jf)\exp(j2\pi f\mu)\,\mathrm{d}f \\ &= \frac{1}{\sigma_{\text{out}}}\int_{-\infty}^{+\infty} H(jf) kX(jf)\exp(j2\pi f\mu)\,\mathrm{d}f \\ &= \frac{y(\mu)}{\sigma_{\text{out}}} = (S/N)_{\text{out}}\end{aligned} \qquad (9)$$

Note that the normalization is not designed to evaluate noise model errors, since it is based on the assumption that the output noise variance can be calculated using just the noise model. When a deviation between actual noise and modelled noise should be accommodated, the formula for the output variance should be:

$$\sigma_{\text{out}}^2 = \int_{-\infty}^{+\infty} \frac{|X(jf)|^2 S(f)}{S_m(f)^2}\,\mathrm{d}f \tag{10}$$

where the subscript m denotes the model power spectral density. In earlier work [11] the MF was normalized on the total power of the filter transfer function. When this normalization is used, the maximum of the signal component in the output of the MF is not a direct measure of the squared output S/N. This may be the reason why in the earlier work a maximum in the output was not found when the correct model was used.

Mathematical derivation

General principle. The goal of the mathematical derivation is a formula describing the performance of the MF as a function of signal model errors. We assume a priori knowledge of the signal position, thereby excluding signal maximum detection from the mathematical description of filter performance. Thus the desired performance formula will give the value of the maximum of the signal component in the output of the normalized MF as a function of the deviation between the values of the parameters in the signal and those in the signal model in the MF.

For this derivation, mathematical models of both signal and noise are required. As mentioned earlier, the signal model should be parameterized, to allow signal model errors to be modelled as incorrect values of the parameters in an otherwise correct model. Using a parameterized noise model as well simplifies the investigation of the influence of the type of noise on the signal model error curve.

The first step in the derivation is to write out the signal component in the output as a function of time. Of course, the result will also be a function of the parameters of the signal, the signal model and the noise model. Secondly, the maximum of this function with respect to time, being the quantity to be optimized by the MF, is found by taking the derivative with respect to time and checking the sign change.

The resulting function should have a maximum when the values of the parameters in signal and signal model are identical. This can be checked by taking the derivative of the function with respect to these parameters and checking the sign changes. Ideally, each pair of parameters can be replaced by a single difference or ratio parameter, so that the derivative with respect to these combined parameters can be taken and a maximum should be found where these parameters are zero or one, respectively.

The derivation will be performed here on a specific example: the signal and the signal model will be described as Gaussians and the noise will be described by the first order band-limited white noise model.

Gaussian signal model. The Gaussian shape has been chosen as the signal model, because of its mathematical simplicity compared to other models, such as the exponentially modified Gaussian (EMG) or the Gamma distribution. The Gaussian is simple because it is symmetrical and takes only three parameters to describe a signal, using the formula:

$$x(t) = A_x \exp\left[-\tfrac{1}{2}\left(\frac{t-t_x}{\sigma_x}\right)^2\right] \tag{11}$$

where $x(t)$ is the signal model in the time domain, A_x the signal scale factor, t_x the position of the signal maximum and σ_x the width of the signal. The shape of the Gaussian is defined by only one parameter, the width. When used as the signal model in the MF this shape is the only property of interest, since the position will merely cause a time shift in the filter output and the scale factor amplifies both signal and noise and leaves their ratio unchanged. Therefore, the signal width parameter is used to model errors in the signal model.

First order band-limited white noise. The first order band-limited white noise model requires only one parameter, the cut-off frequency, to define the shape of the PSD. This parameter can be varied continuously over a broad range of values, allowing the description and generation of both virtually white noise and highly correlated noise with the same model. Furthermore, the interpretation of the cut-off frequency is rather straightforward; a high value corresponds to white noise, a low value to correlated noise. Note that the terms white and correlated are used here with a relative rather than an absolute meaning.

The PSD of first order band-limited white noise is defined as:

$$S(f)=\frac{k_{\mathrm{BL}}}{1+\left(\dfrac{f}{f_{\mathrm{c}}}\right)^{2}} \tag{12}$$

where f_{c} is the cut-off frequency of the filter and k_{BL} the power normalization factor, which can be calculated to be:

$$k_{\mathrm{BL}}=\frac{\sigma_{\mathrm{in}}^{2}}{\pi f_{\mathrm{c}}} \tag{13}$$

Mathematical results

The derivation of the signal model error curve is given in detail in the Appendix. Here we will work only with the resulting formula, which is:

$$y_{\mathrm{n}}(\mu)=\frac{A_{x}\sigma_{m}^{3/2}\sigma_{x}\left[4\pi^{2}f_{\mathrm{c}}^{2}\left(\sigma_{m}^{2}+\sigma_{x}^{2}\right)+1\right]}{\sigma_{\mathrm{in}}\pi^{1/4}f_{\mathrm{c}}^{1/2}\left(\sigma_{m}^{2}+\sigma_{x}^{2}\right)^{3/2}\left(8\pi^{2}f_{\mathrm{c}}^{2}\sigma_{m}^{2}+1\right)^{1/2}} \tag{14}$$

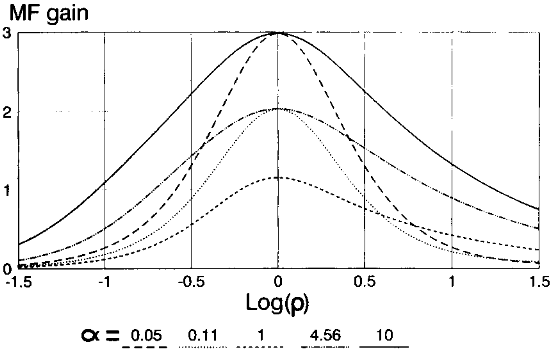

Fig. 1. Theoretical S/N improvement by the MF, as a function of the signal model error parameter, for several values of the relative noise correlation parameter.

Equation 14 is not very transparent and we use the following substitutions to render it more manageable:

$$\rho=\frac{\sigma_{m}}{\sigma_{x}} \tag{15}$$

$$\alpha=2\pi f_{\mathrm{c}}\sigma_{x}=\frac{\sigma_{x}}{\tau_{\mathrm{c}}}$$

These substitutions constitute relative measures for the width of the signal model and the correlation of the noise respectively. When ρ is small, the signal model is too narrow, when ρ is large, the signal model is too wide. Similarly, when α is small, the noise is correlated, when α is large, the noise tends towards white. The term τ_{c} is the time constant of the noise. It can be considered the time domain equivalent of the cut-off frequency.

Yet another substitution can be made:

$$(S/N)_{\mathrm{in}}=\frac{A_{x}}{\sigma_{\mathrm{in}}} \tag{16}$$

Using the Eqns. 14, 15 and 16 an expression is derived for the factor by which the MF improves the S/N, i.e., the factor by which it reduces the relative standard deviation in signal quantification:

$$\mathrm{MF}_{\mathrm{gain}}=\frac{(S/N)_{\mathrm{out}}}{(S/N)_{\mathrm{in}}}=\frac{\sqrt{2}\,\pi^{1/4}\rho^{3/2}\left(1+\alpha^{2}+\alpha^{2}\rho^{2}\right)}{\left(1+\rho^{2}\right)^{3/2}\sqrt{\alpha+2\alpha^{3}\rho^{2}}} \tag{17}$$

The MF gain factor of Eqn. 17 has been plotted as a function of log ρ, for several values of α, in Fig. 1. The log has been taken to ease the inspection of symmetry in the operation of the filter. Several observations can be made on the basis of this figure. The most obvious one is that the gain curves have a single maximum at position $\rho=1$, showing that, as expected, the MF is optimal when the correct model is used. It can be verified mathematically that $\rho=1$ is the only real positive maximum of Eqn. 17 for all values of α. In contrast to the position of the maximum along the ρ-axis, both the height and the shape of the maximum depend on the noise type, i.e., they are functions of α.

Let us consider the height first. It has been plotted as a function of log α in Fig. 2. It is the line marked "theory", the other lines in the figure are part of the discussion of the experimental results. The function is symmetrical with respect to a minimum that can be calculated from Eqn. 17 to have coordinates $\alpha = 2^{-0.5}$ and $\mathrm{MF}_{\mathrm{gain}} = (0.5\pi)^{0.25}$. The noise corresponding with this minimum will be called worst case noise. For the noise types in and around the worst case there is little to be gained by using the MF. Yet, given the optimality of the MF, that is all there is to be gained under those circumstances.

These circumstances are so problematic because of the similarity between the PSDs of noise and signal, as illustrated in Fig. 3. This figure also shows what is going on away from the worst case noise, on both the white and correlated side. In case of white noise, the total noise power is spread out and only little noise power remains in the signal frequencies. In case of correlated noise, the noise power concentrates into the lowest frequencies, again leaving little noise power in the majority of the frequencies in which the signal power resides. Note that when the MF is implemented as a digital filter working on digitized data, very white noise is not likely to be present in the data, since an anti-aliasing low-pass filter, placed before the analog-to-digital convertor (ADC), will have removed all frequencies higher than half the sample frequency of the ADC.

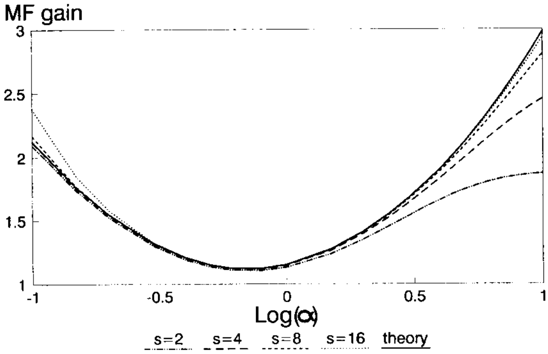

Fig. 2. Theoretical curve and practical curves for several relative sample frequencies (s: points per sigma of the peak) of the S/N improvement by the MF using the correct signal model, as a function of the relative noise correlation parameter.

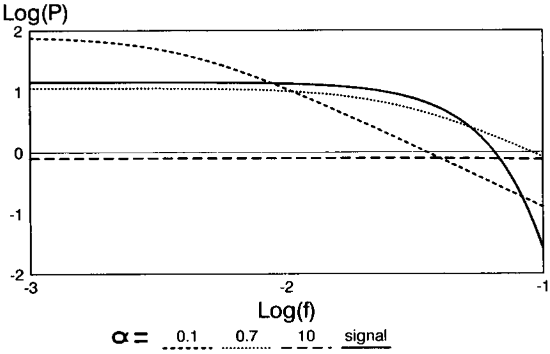

Fig. 3. Power spectral densities (total power normalized to 1) of Gaussian signal and first order band-limited white noise for several values of the relative noise correlation parameter α.

In contrast to its height, the shape of the maximum in the MF gain curves as a function of signal model error cannot be quantified directly as a function of the noise type. Therefore, the discussion of the shape will be more qualitative. It can be seen in Fig. 1 that for a certain maximum height, the curve for white noise is wider than the one for correlated noise. From this it is concluded that the MF is more robust in case of white noises. It is also observed that the curves differ in symmetry.

Both effects are illustrated in Fig. 4. Here the ratio of the height of the maximum in the gain curve to the height in points at both sides of the maximum is plotted as a function of log α. The points chosen are $\rho = 0.2$ and $\rho = 5$, i.e., the signal model in the MF is taken five times to narrow and five times too wide, respectively. Both for small and large α, the ratios at both sides are identical, indicating a symmetrical curve. Following the curves in Fig. 4 from small to large α, it is observed that at first the sensitivity for too wide models decreases faster than that for narrow models, with a maximum difference for a value of α just below 1, beyond which the tables are turned. The difference, also plotted in Fig. 4, is a measure of the asymmetry in the MF performance versus error curves. It shows that for a range of noise types, the MF is more sensitive

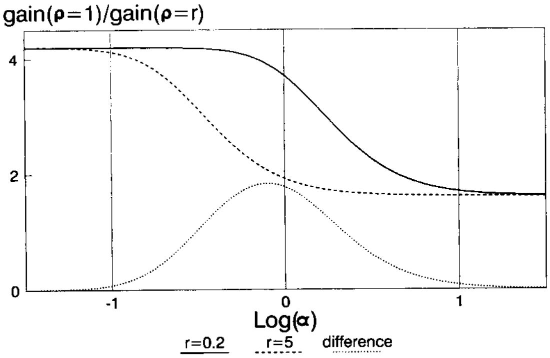

Fig. 4. Ratio of the S/N improvement by the MF using an incorrect signal model to the gain resulting from using the correct model, as a function of the relative noise correlation, for two values of the signal model error (ρ), and the difference between the two curves.

towards too wide models than it is towards too narrow ones, though the effect is rather small.

In Fig. 5 the values of the signal model error parameter ρ for which the gain brought about by the MF equals one have been plotted as a function of the noise type parameter. No analytical solution for these contours of the gain surface has been found and therefore they have been approximated numerically. For points in the area between the contours the MF enhances S/N. Outside the contours, application of the MF causes a reduction of S/N.

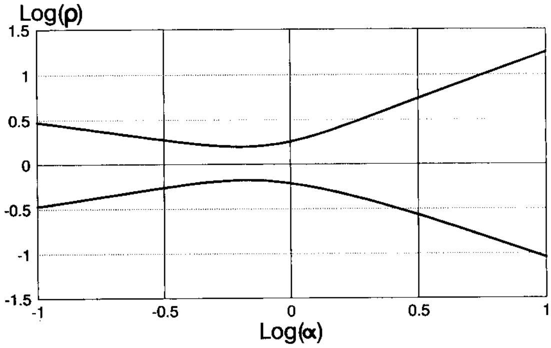

Fig. 5. Contourplot of the S/N improvement by the MF as a function of both the noise correlation (x-axis) and the signal model error. Contours for improvement = 1.

EXPERIMENTAL

Introduction

The mathematical treatment of the MF performance in case of a signal model error, as presented in the previous section, shows that the MF can be regarded as quite sensitive to this error. Instead of accepting this sensitivity, or lack of robustness, as a shortcoming of the MF, we suggest that it can also be considered an advantage. Our suggestion is to correct signal model errors by optimization of the maximum of the signal component in the output of the normalized MF. To investigate the practical feasibility of this idea an experiment has been set up on the basis of simulated data, using the same model system as in the mathematical section.

There are several differences between theory and practice that may be expected to show their effects in the experiments. Our theoretical treatment of the MF works with signals that are continuous and infinitely long, whereas in practice the data will usually be discrete and will always have a finite length. The effect of this fundamental difference can in general be reduced to negligible size by proper selection of the sample frequency and the number of points that is used in the calculations. The subject will not be discussed here. Many textbooks on signal processing or, more specifically, discrete Fourier transformation cover this topic. A discussion in relation to MF can be found in [12].

Another aspect of the experiments is the detection of the maximum in the signal component in the MF output. In the theoretical derivation we were able to observe the MF output on the correct position, but in practice the exact position is usually unknown and has to be estimated. To investigate the influence of this estimation on the overall performance of the proposed procedure, the experiment has been carried out with detection and with preknowledge of the true position, for a range of input S/N values. The position of the maximum is a constant with respect to the signal model error, since both signal and signal model are symmetrical (see also Appendix; the derivation of the maximum). The detection principle used is purposely kept as simple as possible;

it always takes the maximum of the output data. The height of the maximum that is found using this principle may be expected to have a positive bias that will be visible particularly at low input S/N values, because the detection will tend to find a noise maximum instead of the true signal maximum.

Set-up

For a range of S/N values and several time constants of the noise, the maximum of the signal component in the output of the normalized MF is optimized using a modified Simplex procedure. The experiment is performed with and without detection of the maximum and repeated 1000 times. The *C*-source of the MF routine used is available from the authors. The modified Simplex has been used for the sake of simplicity and generality, though the adaptation of only one parameter is a somewhat degenerated form of the Simplex principle.

The simulated data input records contain 1024 points, with the Gaussian peak, having a width (σ) of 4 points, positioned in the centre. Record length and peak width allow the filter operation to be performed as a linear convolution in the time domain, with a filter impulse response consisting of 256 points. The filter length has been chosen to accommodate signal models that are much wider than the true signal, to give the Simplex the space to walk about.

The S/N values for which the procedure is tested are quite low, ranging from 2 to 30, in order to focus on the circumstances under which the gain of the MF is most visible and most desirable. The values are created using a fixed peak height of 1 and a variable noise variance.

TABLE 1

Results of application of the Simplex optimized normalized matched filter (with and without detection) applied to simulated data [Three noises have been tested, characterized by the parameter α, over a range of S/N values. Tabulated are the mean and standard deviation (of individual results) over 1000 simulations of the S/N gain, the signal model parameter estimate and the detected position.]

α	S/N	True position				Estimated position					
		Gain	S.D.	Parameter	S.D.	Gain	S.D.	Parameter	S.D.	Position	S.D.
0.7	2	1.2	0.5	5	3	1.8	0.2	3	2	630	190
	4	1.2	0.2	4.2	1.2	1.2	0.2	4.0	1.4	640	60
	6	1.12	0.16	4.1	0.6	1.13	0.16	4.0	0.6	639	2
	8	1.12	0.12	4.0	0.4	1.13	0.12	4.0	0.4	639.0	0.5
	10	1.13	0.10	4.0	0.3	1.13	0.10	4.0	0.3	639.0	0.4
	20	1.12	0.05	4.00	0.16	1.12	0.05	4.00	0.16	639.00	0.06
	30	1.11	0.03	4.00	0.11	1.11	0.03	4.00	0.11	639.00	0.00
0.07	2	2.6	0.5	4.0	0.7	2.7	0.5	4.0	0.9	640	40
	4	2.6	0.3	4.0	0.3	2.6	0.3	4.0	0.3	639.0	0.3
	6	2.56	0.17	4.0	0.2	2.56	0.17	4.0	0.2	639.00	0.14
	8	2.56	0.12	4.00	0.17	2.56	0.12	4.00	0.17	639.00	0.05
	10	2.56	0.10	4.00	0.13	2.56	0.10	4.00	0.13	639.00	0.03
	20	2.55	0.05	4.00	0.07	2.55	0.05	4.00	0.07	639.00	0.00
	30	2.55	0.03	4.00	0.05	2.55	0.03	4.00	0.05	639.00	0.00
12.5	2	2.6	0.5	4.2	1.6	2.6	0.5	4.1	1.7	640	30
	4	2.6	0.2	4.0	0.6	2.6	0.2	4.0	0.6	639.0	0.6
	6	2.55	0.17	4.0	0.4	2.55	0.17	4.0	0.4	639.0	0.4
	8	2.55	0.13	4.0	0.3	2.55	0.13	4.0	0.3	639.0	0.2
	10	2.55	0.10	4.0	0.2	2.55	0.10	4.0	0.2	639.01	0.18
	20	2.55	0.05	3.99	0.11	2.55	0.05	3.99	0.11	639.00	0.00
	30	2.55	0.04	4.00	0.08	2.55	0.04	4.00	0.08	639.00	0.00

The additive noise that is used in the computer experiments is generated using a shaping filter and normally distributed pseudo random white noise [13]. The pseudo random generator at the basis of the noise generation uses a linear congruence algorithm with a 48-bit mask, followed by a Box–Muller transformation to create normally distributed noise [14]. The whiteness of the basic noise has been checked by statistical testing of the auto-correlation function [15].

The results of experiments performed with three noise types, i.e., three time constants of the first order band-limited white noise model, will be discussed. The time constants used represent the whitest, the worst and the most correlated noise situation that can be simulated. The whitest noise that can be modelled has a flat PSD up to the highest frequency represented, which is half the sample frequency. To simplify matters, the sample frequency may be considered to be 1 Hz, since in simulations it is not a fact but a matter of interpretation. In that case the white time constant equals π^{-1} and the corresponding α value is 12.5. The worst case time constant is calculated from the signal width and the worst case α ($=0.7$) to be 5.6. The most correlated noise that can be modelled is the noise with the highest time constant for which the PSD still distinctly converges to zero. The largest time constant accepted by the noise generation routine, using a PSD consisting of 512 points, is 58, corresponding with an α of 0.07. The theoretical gain factors for white, worst and correlated are 3.33, 1.12 and 2.55, respectively.

For each experiment, the height of the maximum, the position of the maximum (detection mode only) and the signal model parameter, i.e., the peak width, have been retained. The first item is the one the experiment has been set up for, the others are used to give insight in the interpretation of the data.

RESULTS AND DISCUSSION

The results are collected in Table 1. The following features can be observed in the data:

the use of detection of the signal component maximum in the output instead of preknowledge of the true value makes a difference only for worst case noise at low S/N, where detection causes the gain factor to turn out higher;

the gain factor is higher for low S/N both with and without detection;

for worst case and correlated noise the gain factor for high S/N is as predicted, but for white noise the gain factor is lower than predicted even for high S/N values.

As expected, the detection principle results in a positive bias for low $(S/N)_{\text{in}}$. When the signal becomes obscured by the noise, the detection tends to choose a noise maximum instead of the signal. This image is confirmed by the fact that the standard deviation in the maximum found by the detection-based procedure in case of $(S/N)_{\text{in}} = 2$ is too small by a factor two; the maximum of noise records has a smaller variance than entire noise records. Also, the mean of the position estimate is still about right in that situation, but its standard deviation is quite large. This shows that detection can come up with a maximum just about anywhere in the record. Detection operates on filtered data and the $(S/N)_{\text{out}}$ will be critical for its performance. For worst case noise the $(S/N)_{\text{out}}$ will be smallest, which explains why the effect of detection is largest for this noise.

An unexpected phenomenon is the increase of the gain factor at low S/N even without detection. This can be explained as overfitting, i.e. the Simplex optimized MF is, to some extent, able to accommodate noise. This explanation predicts that the effect will be larger for worst case noise than for white noise, since worst case noise is more similar to the signal. This is confirmed by the data. It may be expected that the procedure is given more opportunity for overfitting when detection is used. Though the effect is very small, overfitting does limit the use of the Simplex optimized MF as signal intensity estimator for very low S/N. It creates a bias of stochastic origin that cannot be eliminated by calibration like a deterministic bias.

The last observation to be discussed here is the fact that the gain for white noise does not come up to the predicted value. The explanation can be found in the finiteness of the experimental data. In short: given a sample frequency, it is not possible to represent noise that is whiter than white. Cut-off frequencies higher than half the sample frequency make no difference. The PSD of the noise is flat and remains flat. Frequencies that cannot be represented are folded back onto the frequencies that can be. Therefore, the total power is locked between zero and half the sample frequency, in contrast to the theory, where the power is spread out as the noise becomes whiter. The problem is the sample frequency, that has not been defined in our experiments in an absolute sense, but rather relative to the signal. A certain value for α can be obtained for every relative sample frequency; in the experiments both the width of the signal and the colour of the noise are defined in points, i.e., points per sigma and points per time constant, respectively. For a certain white α, a higher relative sample frequency means a higher value for the time constant, which in turn means noise that is more correlated and therefore better representable.

We have tested this by recording the gain versus α curve for several relative sample frequencies, using the MF routine on noiseless data, without detection or optimization. The results are plotted in Fig. 2. For white noise, i.e., positive values for log α, the results are as predicted: a high relative sample frequency gives a better approximation of the theory. For lower sample frequencies, the gain as a function of α grows towards a maximum. But there is more in this figure: for correlated noise, we observe that the gain for relatively high sample frequencies becomes larger than the theoretical value. This is an artefact similar to the one observed for white noise. There is a limit to the degree of correlation that can be represented in finite data. For a certain correlated α, a higher relative sample frequency also means a higher value for the time constant, which in turn means noise that is more correlated and less representable. This has been tested by using longer records, thus increasing the resolution in the frequency domain, thereby increasing the capability to represent low frequencies. For longer records, the gains came closer to the theoretical values, as expected.

Conclusions

In the example of a Gaussian signal with first order band-limited white noise, Simplex optimization of the parameter value in the signal model, in casu the peak width, results in the correct value for the parameter and therefore the theoretically predicted optimal S/N. In this optimization, the maximum of the signal component in the output of a matched filter, normalized on the output noise variance, is used as the optimization criterion. In general, estimation of this maximum does not affect the results. The flexibility inherent to the optimization results in some overfitting for very low ($\leqslant 2$) S/N values.

APPENDIX: DERIVATION OF THE MF'S SENSITIVITY TO SIGNAL MODEL ERRORS

The following definition of the Fourier transform will be used:

$$x(t) = \int_{-\infty}^{+\infty} X(jf) \exp(+j2\pi ft) \, \mathrm{d}f$$

$$X(jf) = \int_{-\infty}^{+\infty} x(t) \exp(-j2\pi ft) \, \mathrm{d}t \qquad (18)$$

Equation 11 is used to describe the signal. The FT of this function is:

$$X(jf) = A_x\sqrt{2\pi}\,\sigma_x \exp\left[-2(\pi f\sigma_x)^2\right] \times \exp(-j2\pi f t_x) \qquad (19)$$

For the signal model in the MF a function $m(t)$ will be used that is equivalent to $x(t)$, only the subscripts are changed from x to m. Using a model that differs from the true signal results in a normalized MF having a transfer function:

$$H_\mathrm{n}(jf) = \frac{1}{N}\,\frac{M^*(jf) \exp(-j2\pi f\tau)}{S(f)} \qquad (20)$$

The output of this filter is:

$$y_\mathrm{n}(t) = \int_{-\infty}^{+\infty} H_\mathrm{n}(jf) X(jf) \exp(j2\pi ft) \, \mathrm{d}f \qquad (21)$$

Substitution of the signal and the signal model gives:

$$y_n(t) = \frac{A_m A_x \sigma_m \sigma_x 2\pi}{N} \times \int_{-\infty}^{+\infty} \{\exp[-2\pi^2 f^2(\sigma_m^2 + \sigma_x^2)] \times \exp[-j2\pi f(\tau - t - t_m + t_x)]\} \times \{S(f)\}^{-1}\,\mathrm{d}f \tag{22}$$

This can be simplified using the following substitutions:

$$t^* = \tau - t - t_m + t_x$$
$$k_1 = A_m A_x \sigma_m \sigma_x 2\pi$$
$$k_2 = 2\pi^2(\sigma_m^2 + \sigma_x^2) \tag{23}$$

which gives:

$$y_n(t^*) = \frac{k_1}{N}\int_{-\infty}^{+\infty} \frac{\exp(-k_2 f^2)\exp(-j2\pi f t^*)}{S(f)}\,\mathrm{d}f \tag{24}$$

Because both the PSD of the noise and the first exponential term are even with respect to $f = 0$, the FT reduces to a cosine transform:

$$y_n(t^*) = \frac{k_1}{N}\int_{-\infty}^{+\infty} \frac{\exp(-k_2 f^2)\cos(2\pi f t^*)}{S(f)}\,\mathrm{d}f \tag{25}$$

To find the maximum of this signal component in the output the first derivative for t^* is taken and the result is equated to zero:

$$\frac{\mathrm{d}}{\mathrm{d}t^*} y_n(t^*) = \frac{\mathrm{d}}{\mathrm{d}t^*}\frac{k_1}{N}\int_{-\infty}^{+\infty}\frac{\exp(-k_2 f^2)}{S(f)} \times \cos(2\pi f t^*)\,\mathrm{d}f = \frac{-2\pi k_1}{N}\int_{-\infty}^{+\infty}\frac{f}{S(f)}\exp(-k_2 f^2) \times \sin(2\pi t^* f)\,\mathrm{d}f = 0 \tag{26}$$

At this moment, the noise model (Eqn. 12) has to be substituted:

$$\frac{-2\pi k_1}{N k_{\mathrm{BL}}}\int_{-\infty}^{+\infty} f\left(1 + \frac{f^2}{f_c^2}\right)\exp(-k_2 f^2) \times \sin(2\pi t^* f)\,\mathrm{d}f = 0 \tag{27}$$

The integral can be split into two integrals for which standard solutions are found in literature [16]. Substitution of these standard integrals gives an equation for which three solutions are found, but only one of these is a maximum: $t^* = 0$. The corresponding value of t will be called μ. Substitution of this maximum and the noise PSD into Eqn. 25 gives:

$$y_n(\mu) = \frac{k_1}{N k_{\mathrm{BL}}}\int_{-\infty}^{+\infty}\left(1 + \frac{f^2}{f_c^2}\right)\exp(-k_2 f^2)\,\mathrm{d}f \tag{28}$$

This integral too can be split into two for which standard solutions are available. The overall solution is:

$$y_n(\mu) = \frac{k_1}{N k_{\mathrm{BL}}}\left[\frac{\sqrt{\pi}}{\sqrt{k_2}} + \frac{\sqrt{\pi}}{2 f_c^2 k_2^{3/2}}\right] \tag{29}$$

The remaining unknown in this equation is the normalization constant N, which can be calculated according to Eqn. 8 using the model $M(jf)$ instead of the signal $X(jf)$:

$$N^2 = \frac{A_m^2}{\sigma_{\mathrm{in}}^2}\left[\frac{8\pi^2 f_c^2 \sigma_m^2 + 1}{8\sqrt{\pi} f_c \sigma_m}\right] \tag{30}$$

Substitution of Eqns. 13, 23 and 30 into Eqn. 29 gives the desired function:

$$y_n(\mu) = \frac{A_x \sigma_m^{3/2}\sigma_x[4\pi^2 f_c^2(\sigma_m^2 + \sigma_x^2) + 1]}{\sigma_{\mathrm{in}}\pi^{1/4} f_c^{1/2}(\sigma_m^2 + \sigma_x^2)^{3/2}(8\pi^2 f_c^2 \sigma_m^2 + 1)^{1/2}} \tag{31}$$

REFERENCES

1 H.C. Smit, Chemom. Intell. Lab. Syst., 8 (1990) 15.
2 H.C. Smit, Chemom. Intell. Lab. Syst., 8 (1990) 29.

3 P.A. Bristow, J. Chromatogr., 506 (1990) 265.

4 M.H.J. van Rijswick, Chromatographia, 7 (1974) 491.

5 J.M. Laeven and H.C. Smit, Anal. Chim. Acta, 176 (1985) 77.

6 H.C. Smit and H.L. Walg, Chromatographia, 8 (1975) 311.

7 R. Deutsch, System Analysis Techniques, Prentice-Hall, Englewood Cliffs, NJ, 1969.

8 B.P. Lathi, Modern Digital and Analog Communication Systems, Holt, Rinehart and Winston, New York/London, 1983.

9 E.J. van den Heuvel, K.F. van Malssen and H.C. Smit, Anal. Chim. Acta, 235 (1990) 343.

10 E. Voigtman, Anal. Chim. Acta, 246 (1991) 9.

11 E.J. van den Heuvel, K.F. van Malssen and H.C. Smit, Anal. Chim. Acta, 235 (1990) 355.

12 S.A. Dyer and D.S. Hardin, Appl. Spectrosc., 39 (1985) 655.

13 J.M. Laeven, H.C. Smit and J.V. Lankelma, Anal. Chim. Acta, 157 (1984) 273.

14 W.H. Press, B.P. Flannery, S.A. Teukolsky and W.T. Vetterling, Numerical Recipes, Cambridge University Press, Cambridge, 1986.

15 G.M. Jenkins and D.G. Watts, Spectral Analysis and its Applications, Holden-Day, San Francisco, CA, 1968.

16 I.S. Gradshteyn and I.M. Ryzhik, Table of Integrals, Series and Products, Academic Press, New York, 1980.

Analytica Chimica Acta, 274 (1993) 87–97
Elsevier Science Publishers B.V., Amsterdam

Quantification of chromatographic data using a matched filter: robustness towards noise model errors

B. van den Bogaert, H.F.M. Boelens and H.C. Smit

Laboratory for Analytical Chemistry, University of Amsterdam, Nieuwe Achtergracht 166, 1018 WV Amsterdam, (Netherlands)

(Received 4th August 1992)

Abstract

The robustness towards noise model errors of a matched filter used for the quantification of chromatographic data is investigated mathematically and by using computer simulations. It is shown that the matched filter is robust under the assumption of first order band-limited noise. Two extremes of this model suffice for most situations. For these extremes, i.e., for a very small or a very large value of the noise time constant, the filter reduces to a cross-correlation with the signal model and to the second derivative of the signal model multiplied by -1, respectively. When the matched filter is made part of a procedure in which signal model errors are corrected by optimization of the filter performance, the noise model is critical at low signal-to-noise ratios and the correct model is to be preferred.

Keywords: Chromatography; Coloured noise; Cross-correlation; Matched filter; Noise; Noise model errors; Optimization; Quantification; Robustness; Signal/noise enhancement

The importance of using the correct noise model in a matched filter (MF) for the quantification of chromatographic data is evaluated. In previous articles, the MF has been introduced as a tool for quantification [1,2] and its robustness towards signal model errors has been investigated [3]. For the basic quantification technique in chromatography, integration, the influence of different noise models has been investigated by Laeven [4]. A common factor in these papers is the consideration of noise models in chromatography and the notion of low-frequency noise in particular [5].

The MF by definition uses correct models of the signal component and the noise component in the data in order to accomplish what it has been designed for: an optimal signal-to-noise ratio (S/N) in its output [6–8]. The availability of these models is the basis of the mathematical derivation of the filter, but in practice the correctness of the available models may not be guaranteed. The question that arises from this observation is how robust the matched filter is towards discrepancies between the models and the actual signal and noise. The current paper is focused on answering this question with regard to the noise model.

An important source of noise model error is the uncertainty inherent to the establishment of the noise model. Noise, being a stochastic process, can at best be characterized by its average behaviour, modelled in the time domain by an auto-correlation function (ACF) or in the frequency domain by a power spectral density (PSD), being the Fourier transform (FT) of the ACF. The average behaviour of a particular noise can be established only on the basis of long records of measurement data. The more correlated the

Correspondence to: H.C. Smit, Laboratory for Analytical Chemistry, University of Amsterdam, Nieuwe Achtergracht 166, 1018 WV Amsterdam (Netherlands).

noise, the longer the record required to estimate the behaviour with a given reliability. On the time scale of a single chromatographic peak only noises being quite different from each other will be distinguishable and one might argue that the benefit of employing the correct model cannot be expected to be very large. This argument stresses the importance of this research in the overall evaluation of the MF as a data-processing technique, because it attacks the MF at one of its roots. The use of a non-white noise model is a feature that sets the MF aside from most other data-processing techniques. To quantify the benefit of this feature is a strong motive for the investigations described in this paper.

It was found previously that signal model errors can be corrected by optimization of the performance of the MF [3]. This procedure can be regarded an extension of the normal MF: by building flexibility into the MF it can be kept working when part of the required a priori information is missing. To distinguish between the normal MF and the extended, the latter will be referred to as MFX. The matter of robustness towards noise model errors will be investigated for both the MF and the MFX. For the MF, the investigation will be mathematical, for the MFX, it will be experimental.

MATHEMATICAL INVESTIGATION OF THE MF

Derivation of the signal-to-noise ratio gain of the MF

The research is limited to one completely resolved Gaussian peak, with additional first order band-limited white noise. In this context, complete resolution means simply that there is no other peak in the data. Model errors are themselves modelled as incorrect values for parameters in otherwise correct mathematical models, allowing continuous variation of the errors. The parameters are the sigma of the Gaussian peak and the time constant of the noise. The effect of an error is evaluated in the performance of the filter, i.e., in the gain in S/N. S/N is defined here as the ratio of the maximum of the signal to the standard deviation of the noise. In the following, an expression for the gain as a function of the signal, the signal model, the noise and the noise model will be derived.

The MF is defined by the following complex frequency response [6,7]:

$$H(jf) = \frac{M^*(jf)}{S_m(f)} \exp(-j2\pi f\mu) \qquad (1)$$

where the asterisk denotes the complex conjugate, $j^2 = -1$, f the frequency, $M(jf)$ the signal model in the frequency domain, being the FT of $m(t)$, the signal model in the time domain, $S_m(f)$ the noise model in the frequency domain (power spectral density) and μ the time shift introduced by the filter.

In the time domain, the signal $x(t)$ having a Gaussian shape with a peak height equal to one is defined as:

$$x(t) = \exp\left[-\frac{1}{2}\left(\frac{t-t_x}{\sigma_x}\right)^2\right] \qquad (2)$$

where t_x is the position of the signal maximum and σ_x the width of the signal, the "standard deviation" of the Gaussian.

The signal model $m(t)$ is defined by the same expression, using subscript m instead of x for the parameters. Signal and signal model are transformed to the frequency domain using the following definition of the FT:

$$\begin{aligned} x(t) &= \int_{-\infty}^{+\infty} X(jf) \exp(+j2\pi ft)\,\mathrm{d}f \\ X(jf) &= \int_{-\infty}^{+\infty} x(t) \exp(-j2\pi ft)\,\mathrm{d}t \end{aligned} \qquad (3)$$

The result of applying this transformation to the signal is:

$$X(jf) = \sqrt{2\pi}\,\sigma_x \exp\left[-2(\pi f\sigma_x)^2\right] \exp(-j2\pi f t_x) \qquad (4)$$

But for the subscripts, the expression for the signal model in the frequency domain is identical.

The power spectral density of the first order band-limited white noise is:

$$S_x(f) = \frac{2\tau_x}{1+4\pi^2\tau_x^2 f^2} \qquad (5)$$

where τ_x is the time constant of the noise. For the noise model, the expression is the same, but with subscripts m instead of x. The PSD has been normalized on its total power, i.e., the integral over all frequencies, which is equal to the variance of the noise, equals one. Therefore, the S/N in the input equals one, and the S/N in the output is equal to the gain.

The signal component in the output is described in the time domain as the inverse FT of the product of the signal and the complex frequency response of the filter:

$$\begin{aligned} y(t) &= \int_{-\infty}^{+\infty} H(jf)X(jf)\exp(j2\pi ft)\,\mathrm{d}f \\ &= \int_{-\infty}^{+\infty} \frac{M^*(jf)X(jf)}{S_m(f)}\exp[j2\pi f(t-\mu)]\,\mathrm{d}f \end{aligned} \tag{6}$$

The derivation continues with the substitution of signal, signal model and noise model and solving the integral. The maximum is found by taking the derivative, equating the result to zero, solving this equation and checking the sign change, as published previously [3]. The result is:

$$y_{\max} = \frac{\sqrt{2\pi}\,\sigma_x\sigma_m\left(\sigma_m^2+\sigma_x^2+\tau_m^2\right)}{2\tau_m\left(\sigma_m^2+\sigma_x^2\right)^{3/2}} \tag{7}$$

The variance of the noise component in the output is calculated as:

$$\begin{aligned} \sigma_{\text{out}}^2 &= \int_{-\infty}^{+\infty} |H(jf)|^2 S_x(f)\,\mathrm{d}f \\ &= \int_{-\infty}^{+\infty} |M(jf)|^2 \frac{S_x(f)}{S_m(f)^2}\mathrm{d}f \end{aligned} \tag{8}$$

This is developed further by substitution of the signal model, the noise and the noise model. The integral can be split into three separate integrals for which standard solutions exist [9]. The result is:

$$\begin{aligned} \sigma_{\text{out}}^2 = {} & \frac{\sqrt{\pi}}{4}\left(\frac{4\sigma_m}{\tau_x} - \frac{2\sigma_m\tau_m^2}{\tau_x^3} + \frac{\tau_m^2}{\sigma_m\tau_x}\right) \\ & + \frac{\pi}{2}\left(\frac{\sigma_m\tau_m}{\tau_x^2} - \frac{\sigma_m}{\tau_m}\right)^2 \exp\left[\left(\frac{\sigma_m}{\tau_x}\right)^2\right] \mathrm{Erfc}\left(\frac{\sigma_m}{\tau_x}\right) \end{aligned} \tag{9}$$

Dividing Eqn. 7 by the square root of Eqn. 9 gives the output S/N.

Numerical investigation of the MF

Introduction. Two dimensionless parameters have been introduced previously [3]:

$$\rho = \frac{\sigma_m}{\sigma_x}$$

$$\alpha = \frac{\sigma_x}{\tau_x}$$

where ρ is a measure of the relative error in the signal model and α is a measure of the relative correlation of noise and signal in the input. In the current paper a third dimensionless parameter is introduced:

$$\beta = \frac{\sigma_m}{\tau_m}$$

where β is a measure of the relative correlation of the noise model and the signal model in the MF.

In a numerical investigation of Eqn. 9, problems may arise because the power of e may become very large while the complementary error function (Erfc) becomes very small. By combination of these terms under one integral, the numerical instability of the equation is reduced, though it remains sensitive to errors in the evaluation of that combined term:

$$\begin{aligned} \exp(a^2)\,\mathrm{Erfc}(a) &= \exp(a^2)\int_a^{+\infty}\exp(-t^2)\,\mathrm{d}t \\ &= \int_a^{+\infty}\exp(a^2-t^2)\,\mathrm{d}t \end{aligned}$$

Special attention is required for the practical validity of the values chosen for the arguments. It was shown previously [3] that $\alpha = 10$ indicates virtually white noise in case of realistic sampling frequencies. Due to the aliasing that occurs in the sampling, larger values of α cannot not be represented in practice. A similar limitation exists for correlated noise. In order to represent correlated noise, frequencies close to zero need to be described, i.e., a high resolution in the frequency domain is required. Since the frequency resolution is inversely proportional to the length of the time record, long records are required for a high resolution:

$$\Delta f = \frac{1}{T} = \frac{1}{t_s npts} \tag{10}$$

where Δf is the frequency resolution, t_s the sampling interval and *npts* the number of points in a record of data. The minimum frequency resolution is chosen to be equal to the cut-off frequency of the noise:

$$\Delta f_{\min} = f_x = \frac{1}{2\pi\tau_x} = \frac{\alpha}{2\pi\sigma_x} \tag{11}$$

Combining Eqns. 10 and 11, it follows that the number of points in a record should obey:

$$npts \geqslant \frac{2\pi\sigma_x}{\alpha t_s} \tag{12}$$

When the data are sampled at a rate of two samples per sigma of the Gaussian (see Appendix), $\alpha = 10^{-2}$ would require a record of over 1200 points containing just one peak of about 12 points. The existence of such a chromatogram is not very probable and smaller values of α are even less realistic. Arbitrarily, $\alpha = 10^{-2}$ has been chosen as the lower limit in the theoretical investigations. Figure 1 gives some examples of noisy data.

The terms correlated and white are used as relative measures. The lower the value for the time constant, the whiter the noise and the higher the value for the time constant, the more correlated the noise. When the models in the MF are correct, the gain arrives at a minimum for $\alpha = 2^{-0.5}$. This situation is referred to as worst case noise. The worst case is used as a point of reference. When α is larger than the worst case value, we speak of white noise, when it is smaller, we speak of correlated noise. The same terminology is used for β, where white and correlated refer to the models.

Robustness of the MF towards noise model errors. The robustness of the MF towards noise model errors has been investigated by making plots of the gain as a function of β for different values of α, when $\rho = 1$. Three situations have been distinguished according to the nature of the true noise: correlated (Fig. 2a), white (Fig. 2b) and worst case noise (Fig. 2c). As a reference, the gain for $\alpha = \beta$ has been plotted in each figure.

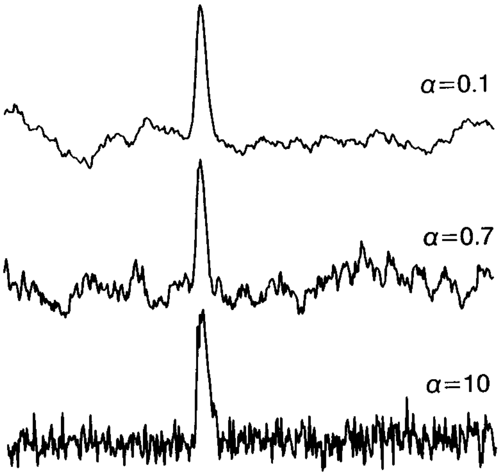

Fig. 1. Some examples of the simulated data for different values of the relative noise correlation parameter α. The S/N value, defined as the peak height divided by the standard deviation of the noise, is 10 in all figures.

The gain curves in Fig. 2a have a large plateau around the correct value of the noise parameter, showing that the MF is very robust towards noise model errors when the noise is correlated. The plateau is limited only to the white side, at roughly the same β for all investigated noises. A β well on the plateau for all noises, e.g., $\beta = 0.01$, describes a filter that can serve as a standard for relatively correlated first order band-limited noise. This is evaluated in the next two sections. For white values of β, the curves cross the optimal line and join on a plateau with a height below gain = 1. The use of a completely white noise model in case of correlated noise worsens S/N.

In Fig. 2b the curves again reach a plateau, indicating their robustness. The plateau is limited at the same value of β for both values of α, suggesting that on the white side too, a single noise model can serve as a standard (in this case, e.g., $\beta = 10$). The use of a correlated noise model in case of white noise gives a worse result than use of the correct model, but the deterioration is not equal for all white noises. Furthermore, the gain of a filter with a correlated model in case of

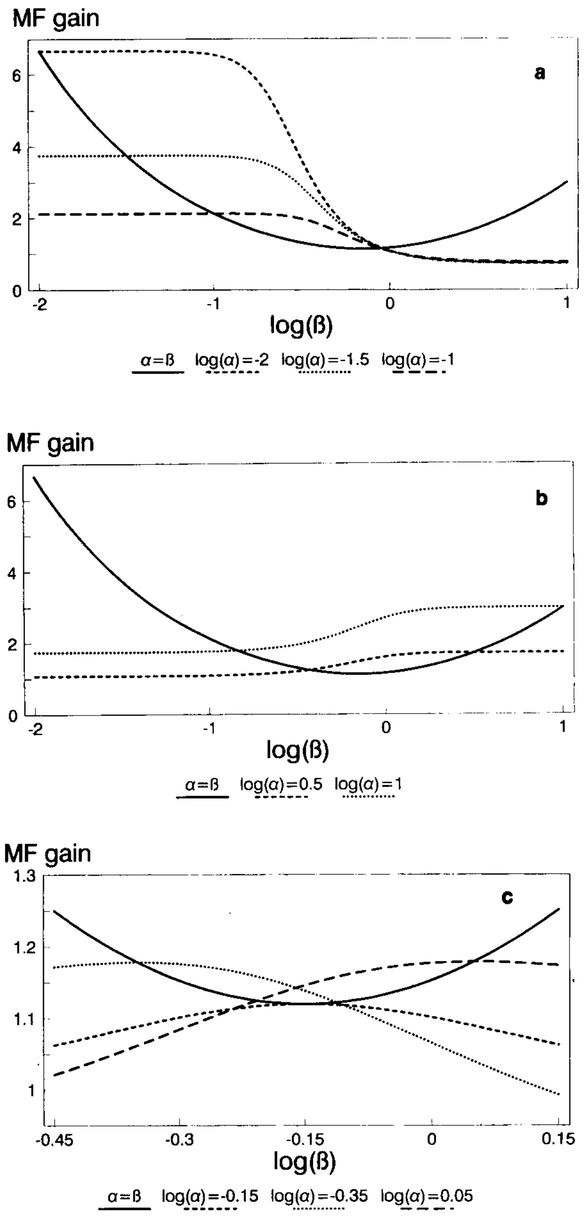

Fig. 2. The gain in S/N effected by the matched filter, as a function of the noise model correlation parameter β, for several values of the true noise correlation parameter α. The signal model is correct in all curves. (a) True noise is correlated; (b) true noise is white; (c) true noise is worst case.

white noise is somewhat larger than vice versa, i.e., wrongly assuming white noise is more destructive than wrongly assuming correlated noise.

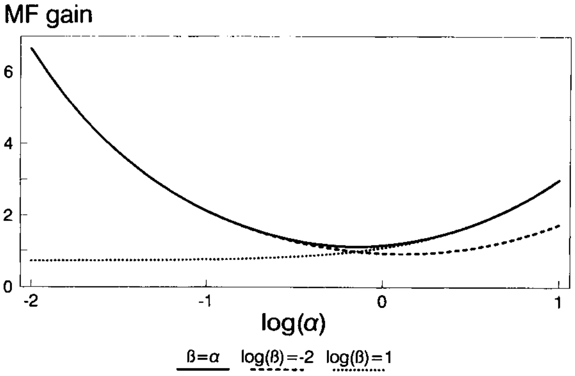

Fig. 3. The gain in S/N effected by the matched filter, as a function of the true noise correlation parameter α, for several values of the noise model correlation parameter β. The signal model is correct in all curves.

In Fig. 2c it is observed that worst case noise is the most critical noise type; the curve merely touches the optimal line and has no plateau like on the white and correlated extremes. Moving away from the worst case to either the white or the correlated side, the development of the plateaus is observed in a flattening of the optimum.

Comparison of correct, fixed correlated and fixed white noise models. In order to investigate the merit of using the correct noise model, the MF gain has been calculated as a function of the true signal correlation α, for the two "standard" values of the noise model correlation β, keeping the signal model correct ($\rho = 1$). The results are plotted in Fig. 3. The curve for $\beta = \alpha$ shows what can be achieved by the truly MF. The curves for $\beta = 10$ and $\beta = 0.01$ correspond to filters that assume white and correlated noise, respectively. When the true noise becomes more correlated than worst case noise, the gain on basis of the white noise assumption distinctly lags behind the optimum. The same holds for the correlated noise model in case of white noise, but the difference does not become as large.

When the gains resulting from the different noise models have to be compared in practice, statistical testing is required. The comparison of gains comes down to a comparison of output S/N values or relative standard deviations. The error in the estimation of the signal will always be much smaller than the error in the estimation of the standard deviation and what remains is a comparison of standard deviations. The square of the ratio between two gains is equal to an F-test criterion. From this criterion, a one-sided confidence limit and the F-distribution, it is possible to calculate the number of observations that is required to conclude if the gain resulting from the use of the correct noise model is bigger than that of another model. This number gives a feeling for the practical relevance of a difference in gains, because it can be related to the number of measurements that is performed in practice. In Fig. 4, it has been plotted as a function of α, for a one-sided confidence limit of 5%. The curves have been cut-off at 25 observations, because they increase so rapidly that a plot of the entire curves, from $\log\ \alpha = -2$ to $\log\ \alpha = 1$, would loose the detail in the more interesting range. For example, when $\log\ \alpha = 0$ and $\log\ \beta = 1$, the required number of observations is about 700.

The following observations are made. In case of a white noise model, the true noise has to be rather correlated to benefit significantly from the use of the true noise model, assuming that the number of replicates in practice is typically far less than 10. It will seldom be worthwhile to use the correct model instead of the correlated model.

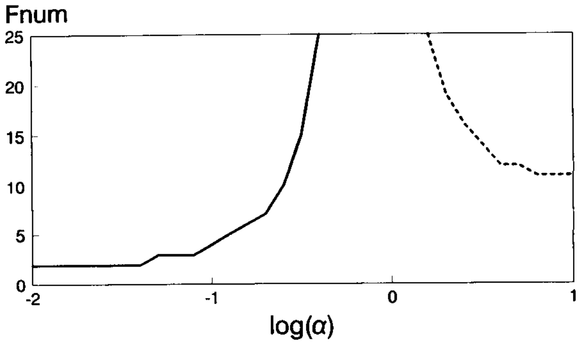

Fig. 4. The number of observations required for the discrimination of the difference between the optimal gain and the gain in case of a fixed white (drawn line, $\beta = 10$) or fixed correlated (dashed line, $\beta = 0.01$) noise model, as a function of the true noise correlation parameter α. The one-sided confidence limit is set to 5%.

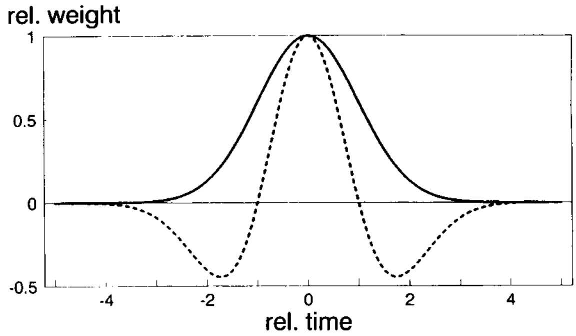

Fig. 5. Impulse response of the matched filter for two extreme values of the relative noise correlation parameter β; $\beta = 0.01$ (dashed line) corresponds to very correlated noise, $\beta = 10$ (drawn line) to white noise. The plots have been scaled on their maximum amplitude. The relative time scale of the x-axis is defined as $(t - t_{\max})/\sigma_m$, where $t_{\max}$ is the position of the maximum of the impulse response.

It is tempting to conclude that the correlated noise model should be used by default when nothing is known about the true nature of the noise. The observations are, however, limited by the scope of the research: Gaussian peaks and first order band-limited noise. The major limitation of the Gaussian model, its symmetry, is quite obvious and its influence may be investigated by using for instance a Gamma distribution or an exponentially modified Gaussian (EMG) as the peak model. At present the limitations of first order noise as chromatographic noise model cannot be evaluated, because there is little information on the types of noises occurring in chromatography. Noise containing a strong low-frequency component was described for a flame ionization detector used in gas chromatography [5], but generalization of that observation would be unwise, given the large array of chromatographic detection techniques.

Nature of the fixed correlated and the fixed white noise model. In Fig. 5, plots have been made of the filter impulse response for the two key types of first order band-limited noise, characterized by $\beta = 10$ for the white and $\beta = 0.01$ for the correlated model. In case of the white noise model, the MF impulse response reduces to the signal model and matched filtering comes down to cross-correlation. This is a well-known fact and the term MF is used commonly to refer to just this operator [6–8]. In case of the correlated noise model, the MF impulse response turns out to be the time-reverse of the second derivative of the signal model multiplied by -1. This effect is also visible in the formula. Correlated noise has a large time constant, which means that the second term in the denominator of Eqn. 5 will dominate and the power spectral density will be inversely proportional to the square of the frequency. In this correlated extreme, the complex frequency response of the MF, assuming a zero time-shift and the correct signal model, will be:

$$H(jf) = 2\pi^2\tau_m f^2 M^*(jf) \qquad (13)$$

Making use of the following properties of the FT

$$m(t) \leftrightarrow M(jf)$$
$$m(-t) \leftrightarrow M^*(jf)$$
$$\frac{\mathrm{d}}{\mathrm{d}t}m(t) \leftrightarrow j2\pi f M(jf) \qquad (14)$$
$$\frac{\mathrm{d}}{\mathrm{d}t^2}m(t) \leftrightarrow -4\pi^2 f^2 M(jf)$$

the filter impulse response, being the inverse FT of $H(jf)$, can be described as being proportional to the second derivative of the time-reverse of the signal model:

$$\begin{aligned} h(t) &= 2\pi^2\tau_m \int_{-\infty}^{+\infty} f^2 M^*(jf)\,\exp(j2\pi ft)\,\mathrm{d}f \\ &= -\tfrac{1}{2}\tau_m \frac{\mathrm{d}^2}{\mathrm{d}t^2} m(-t) \qquad (15) \end{aligned}$$

Consequently, the operation of the MF for very correlated first order band-limited noise can be described as a cross-correlation, not with the signal model, as in case of white noise, but with the second derivative of the signal model multiplied by -1.

Another way of describing the operation of the MF is the cross-correlation of the first derivative of the signal with the first derivative of the signal model. This is shown by elaboration of the signal component in the output of the filter described by Eqn. 13. Yet another property of the FT is used here: the product of two functions is the inverse transform of the convolution of the transforms of these functions. Note that the correlation of two functions $f(t)$ and $g(t)$ is equal to the convolution of $f(t)$ and the time-reverse of $g(t)$. The symbol that is used here to denote a convolution is a multiplication sign surrounded by a circle. The elaboration in formulae is:

$$\begin{aligned} y(t) &= 2\pi^2\tau_m \int_{-\infty}^{+\infty} f^2 M^*(jf) X(jf) \\ &\quad \times \exp(j2\pi ft)\,\mathrm{d}f \\ &= 2\pi^2\tau_m \int_{-\infty}^{+\infty} fM^*(jf) fX(jf) \\ &\quad \times \exp(j2\pi ft)\,\mathrm{d}f \\ &= 2\pi^2\tau_m \left[\frac{1}{j2\pi}\frac{\mathrm{d}}{\mathrm{d}t}m(-t) \otimes \frac{1}{j2\pi}\frac{\mathrm{d}}{\mathrm{d}t}x(t)\right] \\ &= -\tfrac{1}{2}\tau_m \left[\frac{\mathrm{d}}{\mathrm{d}t}m(-t) \otimes \frac{\mathrm{d}}{\mathrm{d}t}x(t)\right] \qquad (16) \end{aligned}$$

It should be stressed that the equivalence of these descriptions of the MF is valid only in the theoretical situation in which the signal is free of noise. The calculation of the first derivative causes an amplification of the high frequencies. For a practical signal, this will usually amount to the amplification of noise. The second-derivative scheme does not suffer from this, since it is the signal model whose second derivative is taken, not the noisy signal itself.

An interesting similarity can be observed here with some publications in which the starting point of the research is different. The basic idea, formulated by Brouwer and Jansen [10], is to get rid of linear background by taking the derivative of the signal. From this, they derive a least-squares procedure that is used for the deconvolution of spectral lines. Their procedure is analogous to the MF for very correlated band-limited noise as derived above. Van Rijswick [11] incorporates the idea of taking the derivative into a MF that itself is based on the assumption of white noise. He uses this modified MF as part of a peak detector in a chromatographic data processing scheme.

EXPERIMENTAL INVESTIGATION OF THE MFX

Introduction

The purpose of the experiments is to investigate the robustness of the MFX, i.e., the influence of noise model errors on the process of correcting signal model errors by Simplex optimization of the maximum in the output of the normalized MF while adapting signal model parameters [3]. The normalization introduced for the MFX consists of dividing the filter by a factor that is proportional to the standard deviation of the output noise. The normalization factor is calculated from the models of signal and noise. An expression can be derived from Eqn. 9, by substitution of the assumption that the noise model is correct, i.e., $\tau_x = \tau_m$, taking the square root and leaving out simple amplification factors:

$$N = \sqrt{2\frac{\sigma_m}{\tau_m} + \frac{\tau_m}{\sigma_m}} \qquad (17)$$

When the noise model is correct, the normalization causes the standard deviation of the noise in the output to remain constant during changes in the signal model. Therefore, the effect of such changes is confined to the signal component in the normalized output. That component has an optimum for the correct signal model. In case of an incorrect noise model, the normalization fails. The signal component will still have an optimum, but the standard deviation of the noise will no longer be constant. This will cause problems for the MFX.

A full theoretical evaluation of the MFX is hindered by the fact that the MFX deals with individual records, whereas the theory used here works with the ensemble average. There is a difference between the ensemble average of the results obtained from applying the operation to individual records and the result of applying the same operation on the ensemble average of the records. Therefore, experiments have been chosen for investigating the MFX.

Set-up

The experiments are performed using simulated data records of 1024 points, containing a Gaussian peak of height one and a width (σ_x) of 4 points and additive noise that is generated using a shaping filter [12]. The width of the Gaussian assures that it is correctly sampled (see Appendix). The S/N in the data is controlled via the variance of the noise. The MFX will be indistinguishable from the MF in case of a high S/N. Since the experiment is focused on the possible failure of the MFX, S/N values of 2, 4, 6, 8 and 10 are investigated.

The signal model error is introduced as an incorrect value for the width parameter of the Gaussian signal model. The starting values for the modified Simplex optimization are $\sigma_m = 3$ and $\sigma_m = 5$. The optimization is allowed to vary σ_m between 1.5 and 15. The lower limit is determined by the sample frequency. Though the model parameter is a continuous variable, it is represented by discrete data. Very small values correspond to peaks that are so narrow they would be undersampled and thus not represented correctly. The upper limit is in principle bounded only by the length of the record, allowing a value of about 50. The value 15 is chosen arbitrarily as about three times the true parameter value, the lower limit being about one third of the true value.

The noise model errors are introduced by using two filters with a fixed noise model, one assuming very correlated noise and one assuming very white noise, and varying the correlation of the noise in the data $\{\log \alpha \in [-1; 0.7]\}$. The filters are coded CL, for the correlated model, and WH, for the white model. The filters operate as cross-correlations; a cross-correlation with the signal model in case of WH and with the second derivative of the signal model multiplied by -1 in case of CL. The normalization factors are derived from Eqn. 17 by making τ_m very large for CL and very small for WH. For WH the factor is the square root of σ_m and for CL the reciprocal of this. Experiments with the correct noise model (code: BW) are performed as a reference.

The MFX optimizes an estimate of the signal amplitude in the output. Two estimation principles are implemented. The signal amplitude is measured at the true position of the maximum of the signal component in the output and at the position of that maximum as estimated by a detector. The detector is kept as simple as possible: it finds the position of the maximum in the entire output record.

For CL, WH and BW, 200 simulations are run for each S/N and each α in both detection

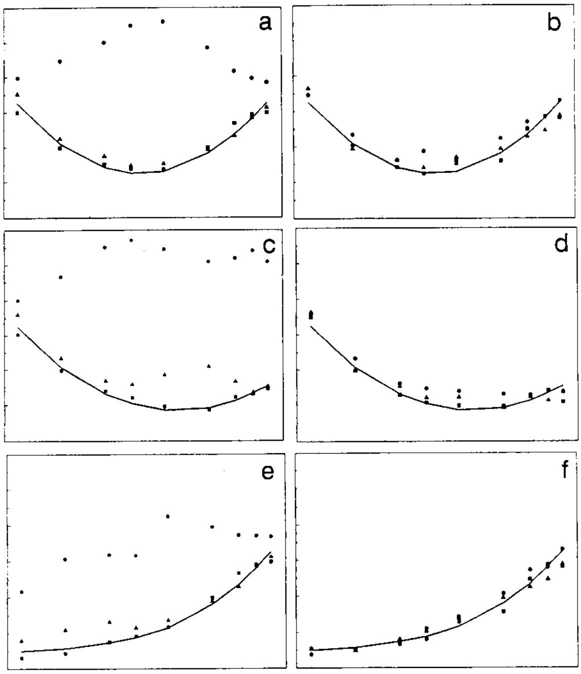

Fig. 6. Gains in S/N as a function of the correlation parameter of the input noise for the MFX using different noise models. (a and b) BW; (c and d) CL; (e and f) WH. Figures a, c and e are experiments with detection; b, d and f with fixed position. The axes are the same for all graphs. $(S/N)_{\text{in}}$: (●) 2; (▲) 4; (■) 8.

modes. The final estimates of the signal amplitude, the signal model parameter and the position of the signal maximum are retained for every simulation. The S/N in the output of the MFX is calculated as the ratio of the mean and the standard deviation of the signal amplitude estimates. Division of the output S/N by the known S/N in the input gives an estimate of the gain. The gain can be related to the theoretical value that can be calculated for the MF assuming $\rho = 1$ and approximating CL by $\beta = 0.01$ and WH by $\beta = 10$.

Results and discussion

In Fig. 6 the experimentally obtained gains have been plotted as a function of the relative noise correlation in the input for several S/N values. The theoretical values have been plotted as reference. BW, CL and WH obviously get into trouble with detection at $(S/N)_{\text{in}} = 2$: the gains are far too high. At $(S/N)_{\text{in}} = 4$, the CL results still clearly deviate from the theoretical values at the white side of the α-range. The same applies to WH at the correlated side. When the true position is used instead of detection the situation is improved visibly for BW, CL and WH.

In case of noise model errors, the estimates of the signal parameter are not normally distributed around the true value. They show a tendency towards too small values for CL and towards too large values for WH. These tendencies have been quantified by determining the relative frequency of the occurrence of the limits of the Simplex optimization as the outcome of the optimization. The results have been collected in Table 1. For $(S/N)_{\text{in}} \geqslant 8$ no encounters with the optimization limits were found for any of the noise models. It has been assured that the trends are not artefacts of the optimization routine by making scans of the signal model parameter. When the optimization ends up at the limit of the allowed interval, the response curve increases monotonically in the direction of one of the limits. Of course the probability of an encounter with one of the limits is determined primarily by the selection of those limits. The more the optimization is closed in, at one side or at both sides, the more encounters with the limit or limits will occur.

The observations made in the gain curves of Fig. 6 are confirmed in Table 1. The MFX degrades with an increase in the noise model error and with a decrease in the input S/N. Detection is responsible for a considerable part of the limit encounters. For noise types around the worst case, even the use of the correct noise model does not prevent the MFX from encountering the lower limit, but both the fixed correlated and the fixed white model have more problems. It is concluded that, when the MFX is used at low S/N values, the use of the fixed correlated model should be restricted to truly correlated noises and the use of the fixed white model to white noises. In general, the use of the correct noise model should be preferred.

In order to explain why CL and WH get of the track in case of white noise and correlated noise, respectively, the standard deviation of the noise in the output of the normalized filter has been plotted in Fig. 7. Because σ_m is changed, β is not

TABLE 1

Relative frequencies of the occurrence of the limits of the allowed parameter range as the outcome of the optimization (The figures are percentages rounded to the nearest smaller integer. Zero values are not displayed.)

Log α		$(S/N)_{\text{in}}$					
		Lower limit			Upper limit		
		2	4	6	2	4	6
		Detected position					
−1.00	BW						
−0.40		4					
0.00		6					
0.48		7					
0.70		3					
−1.00	CL	1					
−0.40		8					
0.00		25	11	1			
0.48		76	31	2			
0.70		83	25	2			
−1.00	WH				77	27	6
−0.40					25	6	
0.00					3	1	
0.48		4			1		
0.70		4					
		True position					
−1.00	BW						
−0.40		3					
0.00		4					
0.48		3					
0.70							
−1.00	CL						
−0.40		4					
0.00		7	1				
0.48		9	3	2			
0.70		9	3	1			
−1.00	WH	1			17	4	3
−0.40		1			6	1	
0.00		1			3		
0.48		2					
0.70							

constant during an optimization. Therefore an extra dimensionless parameter is introduced to describe the relative correlation of the filter:

$$\beta_x = \frac{\sigma_x}{\tau_m}$$

β_x can be interpreted as the β in the last step of the optimization, assuming that the optimization will result in the correct value for the signal model parameter. The MFX will optimize noise instead of the signal for low S/N values. Especially with detection the MFX will zoom in on a noise maximum once it gets hold of one. Figure 7 shows that the MFX should end up with a too small value for the signal parameter in case of CL applied to white noise and a too large value in case of WH applied to correlated noise. This corresponds with the data in Table 1. When the MFX adapts to noise instead of to the signal, the gains calculated on the basis of mean and standard deviation of the output maximum loose their meaning. The magnitude of the output maximum is determined by the limits that have been set to the optimization.

Conclusions

The normal MF with fixed signal model is very robust with regard to noise model errors. In case of first order band-limited noise, two models suffice for the application of the MF: white noise and very correlated noise. The correlated noise model is the more general of the two. The benefit of using more exact noise models is too small to be significant in most practical situations. The MF with signal model correction by Simplex optimization of the output is less robust and the

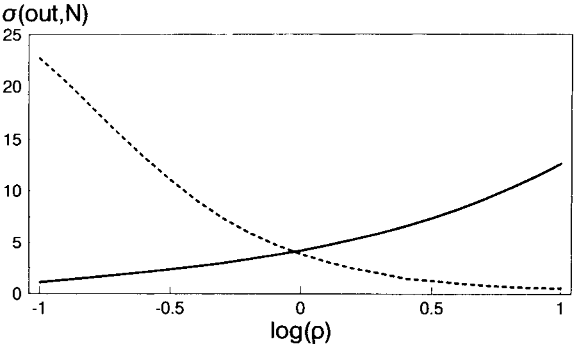

Fig. 7. Standard deviation of the noise in the output of a normalized matched filter as a function of the relative signal model error parameter ρ. The drawn line corresponds to a filter with a fixed white model in the presence of correlated noise ($\alpha = 0.01$. $\beta_x = 10$), the dashed line to a fixed correlated model in the presence of white noise ($\alpha = 10$, $\beta_x = 0.01$).

correct noise model is preferred to the fixed extreme models for small S/N values.

APPENDIX: SAMPLING RATE FOR A GAUSSIAN PEAK

The lowest frequency that can be used for the sampling of a signal should be higher than twice the highest frequency in the signal, the Nyquist or Shannon limit. A Gaussian signal defined in the time domain by Eqn. 2 and, via the FT of Eqn. 3, in the frequency domain by Eqn. 4 does not have an unambiguous highest frequency. When the power spectral density of the signal is observed, it is possible to choose a highest frequency corresponding to a certain percentage of the total signal power that is retained.

The power spectral density of the Gaussian is:

$$\mathrm{PSD} = |X(jf)|^2 = 2\pi\sigma_x^2 \exp(-4\pi^2\sigma_x^2 f^2) \tag{A1}$$

This is again a bell-shape. The width of such a shape is elegantly defined as the distance from the maximum to one of its inflexion points, i.e., the zero-crossings of the second derivative. For the PSD this width is:

$$\sigma_{\mathrm{PSD}} = \frac{\sqrt{2}}{4\pi\sigma_x} \tag{A2}$$

When the PSD of the Gaussian is integrated upto a frequency three times this width, circa 99% of the total power of the signal is found. Therefore this value of $3\sigma_{\mathrm{PSD}}$ is chosen as the highest frequency. The aliasing that occurs when the sampling frequency is chosen accordingly, involves only one percent of the total signal power and will hardly disturb the signal. Consequently, the minimum sampling frequency should follow:

$$f_{\mathrm{s,min}} = 6\sigma_{\mathrm{PSD}} = \frac{3\sqrt{2}}{2\pi\sigma_x} \approx \frac{0.7}{\sigma_x} \tag{A3}$$

In other words, the sampling rate should be at least 0.7 points per σ of the peak.

Note that the sampling frequency is just one of the factors that determine the quality of the digital representation of a signal. Other important factors are the number of bits and the total number of samples.

REFERENCES

1 E.J. van den Heuvel, K.F. van Malssen and H.C. Smit, Anal. Chim. Acta, 235 (1990) 343.
2 E.J. van den Heuvel, K.F. van Malssen and H.C. Smit, Anal. Chim. Acta, 235 (1990) 355.
3 B. van den Bogaert, H.F.M. Boelens and H.C. Smit, 274 (1993) 71.
4 J.M. Laeven and H.C. Smit, Anal. Chim. Acta, 176 (1985) 77.
5 H.C. Smit and H.L. Walg, Chromatographia, 8 (1975) 311.
6 R. Deutsch, System Analysis Techniques, Prentice-Hall, Englewood Cliffs, NJ, 1969.
7 B.P. Lathi, Modern Digital and Analog Communication Systems, Holt, Rinehart and Winston, New York/London, 1983.
8 W.B. Davenport and W.L. Root, An Introduction to the Theory of Random Signals and Noise, McGraw-Hill, New York, 1958.
9 I.S. Gradshteyn and I.M. Ryzhik, Table of Integrals, Series and Products, Academic Press, New York, 1980.
10 G. Brouwer and J.A.J. Jansen, Anal. Chem., 45 (1973) 2239.
11 M.H.J. van Rijswick, Chromatographia, 7 (1974) 491.
12 J.M. Laeven, H.C. Smit and J.V. Lankelma, Anal. Chim. Acta, 157 (1984) 273.

Analytica Chimica Acta, 274 (1993) 99–107
Elsevier Science Publishers B.V., Amsterdam

Approaches to the development of spectrophotometric reaction-rate methods by use of immobilized enzymes in continuous-flow systems

J.M. Fernández-Romero, M.D. Luque de Castro and M. Valcárcel
Department of Analytical Chemistry, Faculty of Sciences, University of Córdoba, 14004 Córdoba (Spain)

(Received 6th July 1992; revised manuscript received 30th September 1992)

Abstract

Three continuous-flow approaches to the development of spectrophotometric reaction-rate methods based on the use of immobilized enzymes are proposed. They are based on the use of an optical biosensor that integrates reaction and detection in the flow cell; or reversing the flow direction and passing the sample plug iteratively through the enzyme reactor and the detector; or a cyclic system that allows the sample plug to be trapped in a circuit that includes the enzyme reactor and the detector. A parameter was defined to compare the features of the methods developed by using these three approaches.

Keywords: Enzymatic methods; Flow system; Kinetic methods; UV–Visible spectrophotometry; Enzyme reactors; Reaction-rate methods

The high selectivity of enzyme reactions is one of their major assets in analytical determinations, further enhanced by the possibility of performing kinetic reaction-rate measurements (reaction half-lives are appropriate for this purpose in most instances). Interferences from the sample matrix are thus avoided because of the differential nature of this type of measurement. An occasional drawback of the use of enzymes in analytical chemistry is the high price of some of them. This can be partly circumvented by immobilizing the biocatalyst [1] in order to use it repeatedly.

Enzymes have been widely used in continuous-flow systems as they offer considerable advantages over other alternatives, the most significant of which is probably that their consumption can be dramatically reduced by using different procedures [2]: by introducing the dissolved biocatalyst through injection; by immobilizing the enzyme on a suitable support to make up a packed reactor and by immobilizing the enzyme in the detection zone (biochemical sensors). Immobilization and packing in reactors is the most frequently used of the three alternatives in continuous-flow systems, yet poses a major problem: making reaction-rate measurements is precluded by the fact that the catalysed reaction stops after the sample plug has passed through the enzyme reactor. The other two alternatives do allow implementation of reaction-rate methods provided that the flow is halted as the injected sample plug reaches the detection zone.

Integration of reaction (retention) and detection is one of the most promising trends in continuous analytical systems on account of the analytical advantages it offers [3]. The use of immobilized enzymes at the detection point is commonplace in electrochemical techniques involving the

Correspondence to: M.D. Luque de Castro, Department of Analytical Chemistry, Faculty of Sciences, University of Córdoba, 14004 Córdoba (Spain).

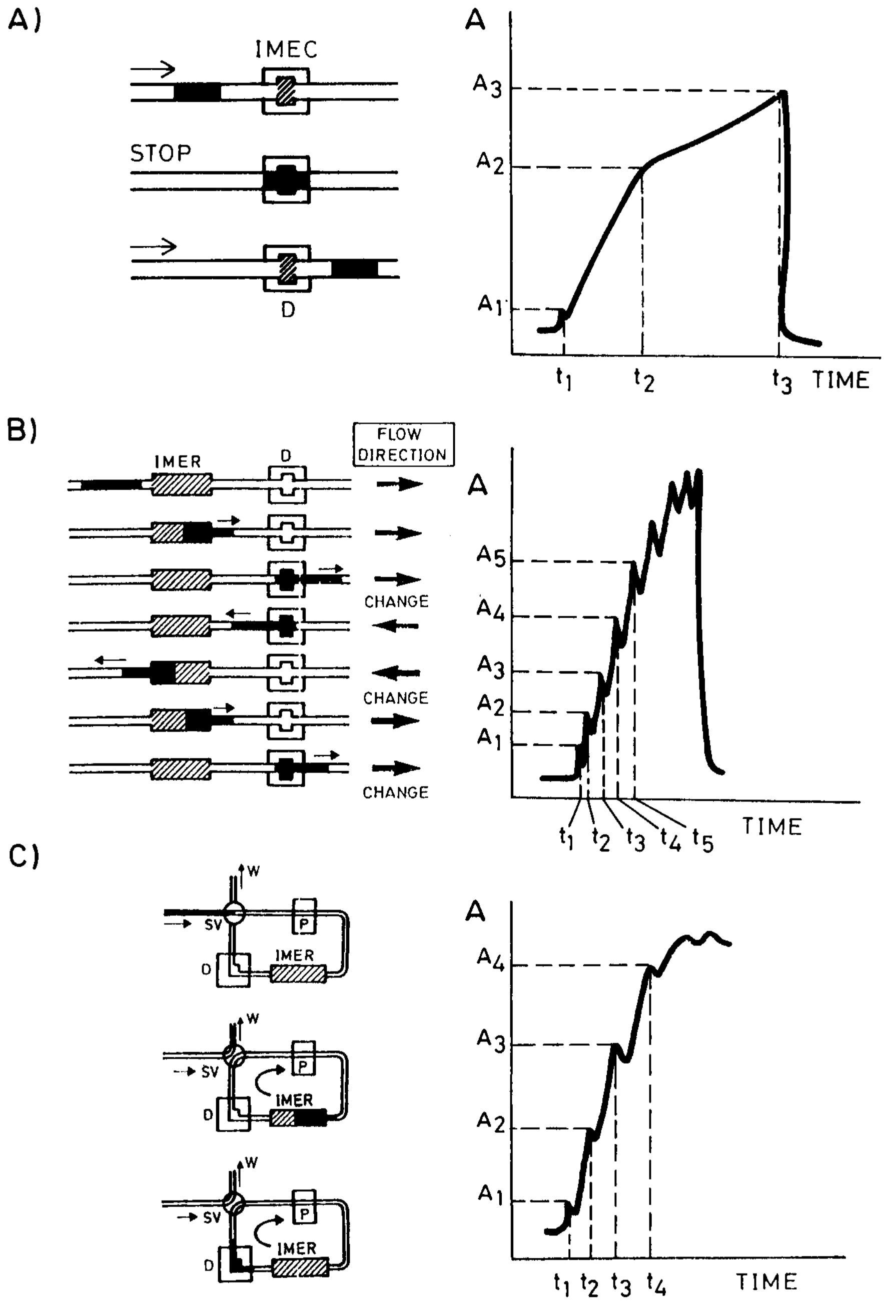

Fig. 1. Principles of the three proposed approaches to the development of reaction-rate methods by using immobilized enzymes, and recordings that they provided, (A) with immobilization of the biocatalyst on the walls of the flow cell and halting of the flow as the samples reach it, (B) with iterative passage of the sample plug through the reactor and detector by changing the flow direction and (C) by trapping the sample plug in a circuit including the reactor and detector and recirculating the plug. IMEC = immobilized enzyme cell; IMER = immobilized enzyme reactor; D = detector; SV = selecting valve; P = peristaltic pump; W = waste; A = absorbance. For further details, see text.

so-called enzyme electrodes (whether potentiometric or amperometric), which can be inserted into flow systems by means of suitable flow cells [4], that occasionally include membranes for interference "filtration" [5]. On the other hand, few flow systems with molecular spectroscopic detection use immobilized enzymes [6].

In this paper a critical comparison is made of three alternatives to the development of methods based on reaction-rate measurements by using immobilized enzymes in continuous-flow systems including a conventional spectrophotometric detector. The first approach involves using a flow-through biosensor in which the enzyme is immobilized on the walls of the flow cell, kinetic measurements being performed after halting the flow as the sample plug reaches the flow cell. The other two approaches rely on an enzymatic reaction in which the biocatalyst is immobilized on controlled-pore glass (CPG), kinetic measurements being based on the iterative passage of the sample plug through the enzymatic reactor and an ordinary flow cell. In turn, such an iterative passage can be achieved by reversing the flow direction at appropriate intervals [7] or by using an "open–closed" cyclic configuration [8]. These approaches have been used previously for a number of purposes, including dispersion studies [8], calculation of stoichiometries [9], speciation analysis [10] and kinetic photochemical determinations [11] in "open–closed" systems, kinetic studies [7], liquid–liquid extraction without phase separation [12,13] and studies on extraction kinetics involving the flow-reversal approach [14]. Neither type of manifold has been used to determine various substrates by using reaction-rate measurements and immobilized enzymes. The aim of this work was to show the advantages of using reaction-rate measurements in continuous systems involving no catalyst consumption and allowing detection with an ordinary spectrophotometer.

The chemical system chosen for developing this study was the hydrolysis of glucuronides catalysed by β-D-glucuronidase. This reaction is of great analytical interest as most pharmaceuticals and drugs of abuse are converted and metabolized by the liver to aid their renal excretion. These reactions take place mostly by conjugation of the active substance with glucuronic acid and excretion as glucuronide derivatives [15]. The determination of these compounds is also of great economic interest because of the impact of their consumption in the clinical, toxicological, forensic and sports areas [16,17].

PRINCIPLES

Three continuous-flow approaches were developed in order to implement reaction-rate measurements by using immobilized enzymes. The principles behind these approaches are as follows.

Immobilization of the enzyme in the flow cell

In 1990, Linares et al. [6] developed the first optical sensor based on the immobilization of an enzyme on the walls of the flow cell of a conventional optical detector. The approach proposed here is based on the same principle, which accomplishes integration of reaction and detection. Figure 1A shows the different steps involved in the process. As the sample plug injected into the flow manifold arrives at the flow cell, the flow is stopped and the course of the enzymatic reaction is monitored. An absorbance–time recording is obtained composed of different linear portions dependent on the monitoring interval. The flow is then resumed and the sample plug is driven to waste.

Iterative change of the flow direction

The principles behind this approach were developed by Ríos et al. [7]. An interface that allows the flow direction to be reversed is connected to the flow-injection manifold, in which the enzyme reactor is placed close to an ordinary spectrophotometric detector. Figure 1B shows the operational scheme of the system. After the sample plug has passed through the enzyme reactor and the flow cell, the interface sends an electrical signal to the peristaltic pump, which responds by changing its direction of rotation. Successive reversal cycles give rise to successive passages of the sample plug through the reactor and detector.

A multi-peak recording is obtained as a result, which reflects the course of the hydrolysis process.

"Open–closed" cyclic system

This approach entails including a switching valve at a special point of the flow manifold, which makes it possible to convert it from an open to a closed circuit and vice versa at programmed intervals. Figure 1C illustrates the basis of this approach. Once the sample plug is in the circuit, the switching valve is turned to its closed position, so the plug is passed iteratively through the enzyme reactor and the detector. The multipeak recording thus obtained reflects the course of the reaction over the monitored interval.

EXPERIMENTAL

Reagents

The stock solutions used included 4-nitrophenyl-β-D-glucuronide (Sigma), which was prepared by dilution with 0.1 M potassium dihydrogenphosphate buffer (pH 6.8) (Merck). More dilute solutions were prepared as required. A stock solution of β-D-glucuronidase from *Escherichia coli*, type IXA (Sigma), was made by dissolving the contents of a vial in 2 ml of the same buffer.

The reagents used for immobilization were: 3-aminopropyltriethoxysilane (Aldrich), glutaraldehyde (Merck) and controlled-pore glass (CPG-240, 120–200 mesh) (Electronucleonics, Fairfield, CT). Stanplast silicone rubber and Superglue-3 (α-cyanoacrylate polymer cement), from Solyplast and Loctite, respectively, were also employed.

Equipment

A Hewlett-Packard Model 8452A diode-array spectrophotometer equipped with an HP 7470A plotter and an HP Vectra ES/12 computer, a Gilson Minipuls-2 peristaltic pump furnished with a laboratory-made interface for controlling the halting and iterative change of the flow direction, two Rheodyne Model 5041 injection valves (one of them modified to act as a switching valve), a Hellma 178.12QS flow cell (inner volume 18 μl) and different types of Hellma 136-OS dismantlable flow cells were used.

Enzyme immobilization

Prior to packing in the reactor, the enzyme was immobilized on CPG by the Masoom and Townshend method [18,19] as modified by Bowers and Johnson [20]. It was then packed in capillary glass tubes (ca. 1 mm i.d., length 2–4 mm), connected to the manifold by using conventional flow-injector connectors, and stored at 4°C.

CPG used for the biosensor was activated as described above and then fixed on the walls of the flow cell according to Linares et al. [6]. A concentrated solution (500 μl) of the enzyme was recirculated through the flow cell for 4 h in order to immobilize the biocatalyst and, after washing, the cell was stored at 4°C.

The enzyme in the packed reactor preserved its activity after storage for 1 month. However, in the flow cell, it lost ca. 40% of its activity after storage for 1 week, perhaps through decomposition of the glue used to fix the activated CPG to the walls of the flow cell (α-cyano derivative groups).

RESULTS AND DISCUSSION

Enzymatic reaction

The enzyme β-D-glucuronidase (β-D-glucuronide glucuronosohydrolase, EC 3.2.1.31) catalyses the hydrolysis of various endogenous glucuronides. The hydrolysis of 4-nitrophenyl-β-D-glucuronide was proposed [21] as an alternative reference method for the determination of the enzymatic activity of β-D-glucuronidase, according to the reaction

$$\text{4-nitrophenyl-}\beta\text{-D-glucuronide} \xrightarrow{\beta\text{-D-glucuronidase}} \text{4-nitrophenol} + \beta\text{-D-glucuronic acid}$$

The species monitored is the 4-nitrophenol formed, which shows maximum absorbance at 405 nm.

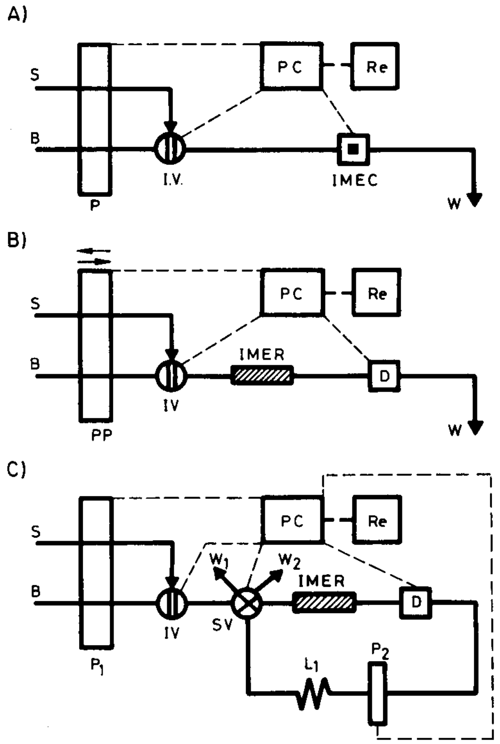

Fig. 2. Flow-injection manifolds for implementation of the principles outlined in Fig. 1 for the selected biochemical system: hydrolysis of glucuronides. (A) Manifold including a biosensor; (B) manifold with iterative change of the flow direction; (C) "open–closed" manifold. PC = denotes personal computer; Re = recorder; B = buffer; S = sample; PP = programmable peristaltic pump; IV = injection valve; L = reactor; (other abbreviations as in Fig. 1).

Continuous-flow configurations

Figure 2 shows the three flow-injection manifolds used. In manifold A the sample plug inserted into the phosphate buffer reaches the flow cell where the biocatalyst is immobilized; the flow is then halted and pairs of absorbance–time data are acquired by the microcomputer over a preset interval.

Figure 2B shows the manifold used to accomplish the iterative reversal of the flow direction. As the sample plug inserted into the phosphate buffer arrives at the flow cell, the direction of the flow is reversed and the plug is passed through the enzyme reactor and the cycle is re-started.

In the "open–closed" manifold shown in Fig. 2C, valve SV is switched to its closed position when the injected sample plug is in the circuit. In this way, the plug is passed iteratively through the enzyme reactor and the detector as many times as required to obtain a multi-peak recording.

Types of measurement

The recordings provided by the three approaches are shown in Fig. 1. Data from these recordings are acquired by the computer through the passive interface.

The optical sensor provides a recording with two linear ranges from the two linear portions provided by the recordings. From these calibration graphs two reaction-rate values can be obtained by using the expression

$$V_i = (A_{i+1} - A_i)/t_{i+1} - t_i) \qquad (1)$$

where A_{i+1} and A_i are the absorbances at the ends of the linear intervals acquired at times t_{i+1} and t_i, respectively. A third value, V_3, was also calculated as the average of the two linear intervals $(A_3 - A_1)/(t_3 - t_1)$.

The other two approaches provide similar multi-peak recordings in which the successive maxima show further development of the hydrolysis reaction compared with previous peaks. The differences between two maxima (whether consecutive or not) allow one to perform different reaction-rate measurements. Thus, four different reaction-rate values were calculated in this way: V_1, V_2 and V_3, given by Eqn. 1, where A_{i+1} and A_i are now consecutive maxima obtained at times t_{i+1} and t_i, respectively; and V_4', by way of example of measurements between non-consecutive peaks, given by $(A_4 - A_1)/(t_4 - t_1)$.

It is significant that the last two manifolds provide multi-peak recordings that differ markedly in shape. This arises from the different intervals between consecutive measurements used and the also different degree of dispersion in each configuration. In the approach involving the iterative reversal of the flow direction, the reaction develops to completion in a shorter time than it does in the "open–closed" manifold, which is a result of more thorough mixing of the reactants and a longer time of contact with the biocatalyst.

Study of variables

The performance of all three approaches is influenced by different variables that can be classified into physical, chemical and flow injection. Some of them are common to all three, whereas others are specific to each. The influence of these variables was studied and their values were optimized by using the univariate method in all instances.

An increase in the temperature of the system also increased the analytical signals obtained. However, above 40°C, the immobilized catalyst was rapidly denatured.

All of the reaction ingredients were prepared in 0.1 M phosphate buffer. The optimum pH for development of the enzymatic reaction was 6.8 (at this pH the enzyme reactor retained its activity at least for 2 months). The maximum absorption of 4-nitrophenol (the monitored product) was obtained at pH 11.0 [20]. Integrated reaction and detection in the manifold in Fig. 2A and the iterative passage of the sample plug through the enzyme reactor and the detector in the manifolds in Fig. 2B and C hindered development of both steps at their optimum pH, so a pH of 6.8 was selected to ensure maximum stability of the immobilized enzyme.

The flow-rate is the most influential of the flow-injection variables and has a different effect on each manifold. In approach A in Figs. 1 and 2, this variable determines the delay time and hence the degree of dispersion of the sample plug in the carrier before the flow is halted. The reaction and detection sequences and hence the type of recording obtained are also determined by the flow-rate in approaches B and C. The flow-rate selected was 1.4 ml min^{-1} for approaches A and B and 1.0 ml min^{-1} for approach C. This was a compromise between sensitivity and sampling frequency.

The volume injected also affects these approaches differently. In the manifold including the biosensor the analytical signal increases with increasing sample volume injected up to 500 μl, at which the dispersion of the sample plug core into the buffer carrier is zero and consequently the concentration of the substrate in contact with the biocatalyst is optimum when the plug zone is halted at the flow cell. Nevertheless, such a large volume entails a long cycle time, which results in a low sampling rate in the manifold with iterative reversal of the flow, and in the rapid attainment of physical equilibrium in the "open–closed" manifold, as the volume in the closed circuit is kept constant, so the carrier volume decreases as the injected volume increases. A sample volume of 250 μl was selected as a compromise for the three approaches for a further comparison of their performance.

There are two variables specific to the biosensor approach, viz., the delay and the stop time, which were studied in the ranges listed in Table 1. Table 1 includes the optimum value found for each.

The obtainment of a multi-peak recording in approach B relies on three variables: time of

TABLE 1

Optimum values of the specific variables

Variable	Flow cell method	Iterative reversal method	"Open–closed" method
Delay time (s)	15	–	–
Stop time (s)	180	–	–
Number of flow reversal cycles	–	10	–
Time at the reverse cycle start (s)	–	3	–
Duration of flow reversal cycles (s)	–	10	–
Length of open reactor (cm)	–	–	50
Switching time (s)	–	–	20
Measurement time (s)	180	60	200

cycle start, cycle duration and number of cycles, which were set to 3 s, 10 s and 10 cycles, respectively, in order to ensure that the plug reached the detector but not beyond it; two passages through the enzyme reactor in each cycle; and an appropriate number of peaks for each sample without reaction completion.

The cycle duration in the "open–closed" manifold was controlled through the flow-rate and the length of reactor L_1, as the remainder of the circuit was reduced to the minimum dimensions required for connections. The optimum length of L_1 (50 cm) provided a cycle time of about 50 s. On the other hand, the time for switching the selecting valve in order to change the open circuit into a closed circuit determined the total, partial or zero trapping of the sample plug in the closed circuit. The optimum value was 20 s, at which the plug was in the centre of the closed circuit.

Features of the proposed methods

Calibration for each method was achieved by using the optimum values given above and injecting standard solutions of 4-nitrophenyl-β-D-glucuronide at concentrations between 3.6×10^{-3} and 5.7 mM in triplicate. Table 2 summarizes the features of the methods (equation, regression coefficient, linear range, reproducibility and α-coefficient, which is defined as the ratio between the upper limit of the linear portion of the calibration graph and the determination limit, and was used to compare the performances of the three methods). The determination limits were calculated as ±10 times the standard deviation of the blank signals. The uncertainty in the linear regression values listed in Table 2 ranged between 2.5 and 4.7%.

The "open–closed" approach provided the best α-coefficient as a result of the highest substrate concentration/enzyme activity ratio achieved in the closed configuration. The reversal flow method yielded the worst α-value, but the largest calibration slope, owing to more efficient substrate–buffer mixing provided by the flow reversal and to the double passage of the sample plug through the enzyme reactor between successive measurements. The intermediate α-value obtained with the biosensor can be ascribed to the smaller amount of biocatalyst present in the flow cell compared with that used in the enzyme reactor.

Similar experiments were carried out by using the three approaches to determine their precision: eleven samples containing two different substrate concentrations at each level (low level, 7.2×10^{-3} and 14.4×10^{-3} mM; high level, 7.2 and 14.4 mM) were assayed in triplicate. The precision, expressed as relative standard deviation (R.S.D.), was acceptable in all instances for the three methods, the highest value corresponding to the biosensor method.

Conclusion

Three alternatives to making spectrophotometric kinetic reaction-rate measurements by using immobilized enzymes implemented in flow-injection systems were developed. All three approaches require simple, inexpensive instrumentation that is usually available in most laboratories. Nevertheless, they involve some modifications to conventional continuous-flow systems such as using an additional valve to open and close the circuit, and automatic control of the functioning of the peristaltic pump is required to halt the flow and reverse the flow direction; none of this poses special problems. The good reproducibility achieved and the wider linear range of the calibration graph compared with conventional approaches [22] demonstrate the usefulness of these approaches, which rely on two major premises of miniaturization in analytical chemistry: modular integration and compaction. The simultaneous development of the enzymatic reaction and spectrophotometric monitoring provides maximum integration. The other two alternatives, however, provide a smaller extent of integration or an approach to integration. There are no significant differences between the analytical features of the proposed methods, at least when applied to the biochemical system dealt with in this work.

The Dirección General de Investigación Científica y Técnica (DGICyT) is thanked for financial support (Grant No. PB90–0925). One of the authors (J.M.F.-R.) expresses his gratitude to

TABLE 2

Features of the proposed methods

Method	Features	Reaction-rate parameter [a]			
		V_1	V_2	V_3	V_4
Flow cell immobilization/ stopped-flow	Equation	$V = 8.42\times10^{-6}C + 4.6\times10^{-4}$	$V = 6.89\times10^{-6}C + 3.7\times10^{-4}$	$V = 5.10\times10^{-6}C + 3.9\times10^{-4}$	–
	Regression coefficient	0.9907	0.9903	0.9952	–
	Linear range (mmol l^{-1}) [b]	7.2×10^{-3}–0.72	7.2×10^{-3}–0.72	7.2×10^{-3}–0.72	–
	R.S.D. (%) range ($n = 11$):				
	Low level	2.31	2.80	2.95	–
	High level	1.56	1.84	1.82	–
	α-Coefficient	667	679	486	–
Iterative flow reversal	Equation	$V = 1.92\times10^{-4}C + 9.6\times10^{-5}$	$V = 1.25\times10^{-4}C - 6.7\times10^{-5}$	$V = 1.78\times10^{-4}C - 3.3\times10^{-4}$	$V = 1.69\times10^{-4}C - 1.4\times10^{-4}$
	Regression coefficient	0.9921	0.9950	0.9951	0.9934
	Linear range (mmol l^{-1}) [b]	3.6×10^{-3}–0.43	3.6×10^{-3}–1.44	3.6×10^{-3}–0.51	3.6×10^{-3}–6.64
	R.S.D. (%) range ($n = 11$):				
	Low level	0.78	1.48	0.76	0.77
	High level	0.20	0.64	1.43	0.88
	α-Coefficient	112	255	129	565
"Open–closed"	Equation	$V = 2.72\times10^{-6}C + 5.5\times10^{-5}$	$V = 1.67\times10^{-6}C + 5.4\times10^{-5}$	$V = 9.77\times10^{-6}C - 2.4\times10^{-5}$	$V = 1.82\times10^{-6}C + 3.8\times10^{-5}$
	Regression coefficient	0.9978	0.9958	0.9938	0.9963
	Linear range (mmol l^{-1}) [b]	3.6×10^{-3}–2.9	3.6×10^{-3}–2.90	3.6×10^{-3}–4.30	3.6×10^{-3}–2.9
	R.S.D. (%) range ($n = 11$):				
	Low level	1.25	1.34	1.59	2.77
	High level	0.64	0.63	0.87	1.09
	α-Coefficient	1349	2071	5443	592

[a] V = reaction rate and C = 4-nitrophenyl-β-D-glucuronide concentration (mM). [b] Features of the chemiluminescence method [18]: $y = 50.2 \pm 0.5$ μA l mol^{-1} [glucuronic acid] $- 0.54 \pm 0.34$ nA ($r = 0.9997$), detection limit = 5 μM, R.S.D. = 2% ($n = 11$).

the Junta de Andalucía for the award of a postdoctoral grant.

REFERENCES

1 G.G. Guilbault, Analytical Uses of Immobilized Enzymes, Dekker, New York, 1984.
2 R.D. Schmid, Flow Injection Analysis (FIA) Based on Enzymes and Antibodies (GBF Monographs, Vol. 14), VCH, New York, 1991.
3 M.D. Luque de Castro and M. Valcárcel, Analyst, 115 (1990) 699.
4 R.L. Solsky, Anal. Chem., 62 (1990) 21R.
5 J. Wang, Anal. Chim. Acta, 234 (1990) 41.
6 P. Linares, M.D. Luque de Castro and M. Valcárcel, Anal. Chim. Acta, 230 (1990) 199.
7 A. Ríos, M.D. Luque de Castro and M. Valcárcel, Anal. Chem., 60 (1988) 1540.
8 A. Ríos, M.D. Luque de Castro and M. Valcárcel, Anal. Chem., 57 (1985) 1803.
9 A. Ríos, M.D. Luque de Castro and M. Valcárcel, J. Chem. Educ., (1986) 552.
10 A. Ríos, M.D. Luque de Castro and M. Valcárcel, Quím. Anal., 6 (1987) 320.
11 M.T. Tena, M.D. Luque de Castro and M. Valcárcel, J. Autom. Chem., 29 (1991) 377.
12 F. Cañete, A. Ríos, M.D. Luque de Castro and M. Valcárcel, Anal. Chem., 60 (1988) 2354.
13 J.A. García-Mesa, P. Linares, M.D. Luque de Castro and M. Valcárcel, Anal. Chim. Acta, 235 (1990) 441.
14 F. Cañete, A. Ríos, M.D. Luque de Castro and M. Valcárcel, Anal. Chim. Acta, 224 (1989) 169.
15 A.C. Moffat, Clarke's Isolation and Identification of Drugs, 2nd edn., Pharmaceutical Press, London, 2nd edn., 1986.
16 A.C. Mehta, Talanta, 34 (1987) 609.
17 E.G. de Jong, R.A.S. Maes and J.M. Van Rossum, Trends Anal. Chem., 7 (1988) 375.
18 M. Masoom and A. Townshend, Anal. Chim. Acta, 174 (1983) 293.
19 M. Masoom and A. Townshend, Anal. Chim. Acta, 166 (1984) 111.
20 D.L. Bowers and P.R. Johnson, Biochim. Biophys. Acta, 661 (1981) 100.
21 H.U. Bergmeyer, Methods of Enzymatic Analysis, Verlag Chemie, Weinheim, 3rd edn., 1983.
22 L.L. Klop and T.A. Nieman, Anal. Chem., 57 (1984) 46.

Analytica Chimica Acta, 274 (1993) 109–116
Elsevier Science Publishers B.V., Amsterdam

Enzymatic determination of alcohol mixtures at the nanogram level by the stopped-flow technique

Eva Förster

Institut für Analytische Chemie, Bergakademie Freiberg, 9200 Freiberg (Germany)

Manuel Silva

Department of Analytical Chemistry, Faculty of Sciences, University of Córdoba, 14004 Córdoba (Spain)

Matthias Otto

Institut für Analytische Chemie, Bergakademie Freiberg, 9200 Freiberg (Germany)

Dolores Pérez-Bendito

Department of Analytical Chemistry, Faculty of Sciences, University of Córdoba, 14004 Córdoba (Spain)

(Received 29th June 1992; revised manuscript received 10th September 1992)

Abstract

A sensitive kinetic enzymatic method for the individual and joint determination of lower straight-chain alcohols is reported. The method is based on reaction of the alcohols with the alcohol dehydrogenase–nicotinamide adenine dinucleotide system, which is monitored by measuring the initial rate of change of the absorbance or fluorescence intensity of the reduced coenzyme formed by using the stopped-flow technique. Methanol, ethanol, propanol and butanol can thus be determined over the range 3.0×10^{-8}–1.0×10^{-6} M with a relative standard deviation of ca. 1.2–3.8%. Spectrofluorimetric measurements are better suited to the individual determinations, whereas spectrophotometric measurements are more useful for resolving alcohol mixtures using the Kalman filter algorithm. Mixtures of methanol–butanol, ethanol–butanol and methanol–propanol at the submicromolar level were successfully resolved with errors of less than 10%.

Keywords: Enzymatic methods; Fluorimetry; UV–Visible spectrophotometry; Alcohols; Kalman filter; Stopped-flow technique

Kinetic methods of analysis based on the catalytic action of enzymes provide reliable, sensitive and selective means of determining enzyme activities and substrate concentrations, so they are of great interest in fields such as clinical, pharmaceutical, food and environmental chemistry [1]. Enzyme-catalysed reactions are often the basis for the determination of carbohydrates (e.g., glucose, maltose), alcohols (e.g., ethanol) and phenolic compounds (e.g., phenol, catechol). Alcohols are usually determined by using either of two enzymes, alcohol dehydrogenase (ADH) in the presence of the coenzyme nicotinamide adenine dinucleotide (β-NAD$^+$) or alcohol oxidase, par-

Correspondence to: D. Pérez-Bendito, Department of Analytical Chemistry, Faculty of Sciences, University of Córdoba, 14004 Córdoba (Spain).

ticularly for methanol and ethanol [2,3]. In the last few years, these determinations have been addressed by using immobilized enzymes in a flow-injection manifold [4–6] and have been mainly concerned with analyses for ethanol in clinical and food samples.

In order to expand the analytical potential of the kinetic determination of substrates by enzyme-catalysed reactions, the β-NAD$^+$–ADH system was used for the determination of lower straight-chain alcohols such as methanol, ethanol, propanol and butanol, both alone and in mixtures, by using the stopped-flow technique for mixing sample and reagents and monitoring reactions, with either spectrophotometric or spectrofluorimetric detection. The methods thus developed permit the determination of these alcohols with a high sensitivity (ng ml^{-1} level) and the Kalman filter algorithm [7] permits the resolution of mixtures.

These alcohols can also be determined individually and jointly by using other analytical techniques, particularly gas chromatography. Thus, mixtures of methanol–ethanol [8–11], methanol–butanol [12], ethanol–butanol [13,14] and ethanol–2-propanol [15] have been resolved in this way, although with lower sensitivity; calibration graphs were linear over the range from about 10^{-6} to 0.1 M. Spectrophotometric methods using oxidants such as silver(II) [16], potassium dichromate [17] and cerium(IV) [18] and conductimetric determinations based on measuring changes in the conductivity of aqueous solutions containing strong electrolytes induced by the presence of alcohols [19,20] have also been reported. Spectrophotometric methods allow the determination of these alcohols at the μg ml^{-1} level, whereas electroanalytical methods are better suited to higher concentrations between 5 and 50% (v/v).

EXPERIMENTAL

Reagents

All reagents were of analytical-reagent grade and solutions were prepared in doubly distilled water. Alcohol solutions (methanol, ethanol, butanol and propanol) were prepared from standards of absolute alcohols (Merck) by appropriate dilution with doubly distilled water. An alcohol dehydrogenase (ADH) (Boehringer, Mannheim) solution of 640 units ml^{-1} was prepared from the lyophilized powdered enzyme (protein activity 400 units mg^{-1}) by dissolving 8 mg in 5 ml of 0.05 M Tris buffer (pH 8.55). A 1.3×10^{-4} M β-nicotinamide adenine dinucleotide (β-NAD$^+$ from yeast, Sigma) solution was prepared by dissolving 8.9 mg in 100 ml of doubly distilled water. The 0.05 M Tris buffer solution (pH 8.55) was prepared by mixing 25.0 ml of a 0.2 M Tris (Merck) solution with the appropriate volume of 0.1 M hydrochloric acid and diluting to 100 ml with doubly distilled water.

Apparatus

Spectrophotometric measurements were made on a Philips PU 8625 UV–visible spectrophotometer and spectrofluorimetric measurements on a Hitachi F-2000 spectrofluorimeter, both of which were furnished with a stopped-flow module [21] supplied by Quimi-Sur Instrumentation, an Ultraterm 383 recirculating water-thermostated bath and a data acquisition system consisting of a Netset PC-AT 16-MHz compatible computer equipped with a PC-Multilab PCL-812PG 12-bit analog-to-digital converter. The software required for application of the initial reaction rate and Kalman filter methods was written by the authors.

Individual determination of alcohols

Two solutions (sample and reagent) were prepared for filling the drive syringes of the stopped-flow module. The sample solution contained 1.0 ml of standard alcohol solution at a final concentration between 3.0×10^{-8} and 1.6×10^{-6} M and 4.0 ml of 0.05 M Tris buffer solution (pH 8.55). The reagent solution contained 1.0 ml of 1.3×10^{-4} M β-NAD$^+$ and 0.5 ml of stock ADH solution. Both solutions were diluted to volume with doubly distilled water in 10-ml volumetric flasks. For each run, equal volumes of both solutions were mixed in the mixing chamber of the stopped-flow module and the variation of the analytical signal [absorbance at 340 nm or fluorescence intensity at λ(ex) = 340 nm and λ(em) = 460 nm] was monitored throughout the reaction. Signal values were acquired at a rate of ca. 1.5 s per point and all measurements were made at 25 ± 0.1°C. The initial rate was measured in about 20–50 s and each solution was assayed in triplicate.

Analysis of alcohol mixtures

One of the two 10-ml reservoir syringes of the stopped-flow module was filled with a solution containing a mixture of alcohols in a given concentration ratio (see Table 3) in 4.0 ml of 0.05 M Tris buffer solution (pH 8.55), and the other with the reagent solution. From this point on, the procedure was identical with that followed for the determination of the each alcohol alone with spectrophotometric detection. The initial concentrations of the two alcohols in each mixture were obtained by using the linear Kalman filter; the input rate constants were calculated by analysing for the individual analytes using the classical logarithmic method of the integrated equation and were improved by applying the extended Kalman filter.

RESULTS AND DISCUSSION

Dilute solutions of lower straight-chain alcohols such as methanol, ethanol, propanol and butanol react with alcohol dehydrogenase in the presence of the coenzyme β-NAD$^+$ to form the corresponding aldehyde and the reduced form of the coenzyme (NADH). Because these reactions are time dependent, alcohols can be determined kinetically by monitoring the reaction rate spectrophotometrically at 340 nm (maximum absorbance of NADH) or spectrofluorimetrically thanks to the native fluorescence of NADH [λ(ex) = 340 nm and λ(em) = 460 nm]. In both instances, the stopped-flow technique was used to ensure rapid and thorough mixing of sample and reagents, and immediate data processing, which makes the kinetic method automatable.

Figure 1 shows the signal vs. time plots obtained with spectrophotometric and spectrofluorimetric detection for ethanol, the most representative of these alcohols under the conditions described under Experimental. The sensitivity was greater when the reaction was monitored spectrofluorimetrically. The maximum signal was reached in about 3 min. It should also be noted that, at fairly long times, the dependence of the signal on time changed from an exponential trend to a slightly increasing trend, for spectrophotometric or spectrofluorimetric detection. This posed no problem in measuring the initial rate; however, it did affect the accuracy with which alcohol mixtures were resolved by using the Kalman filter as shown below.

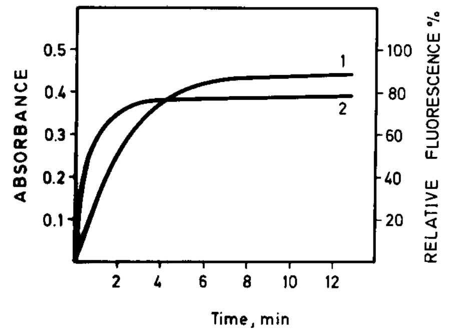

Fig. 1. Typical signal vs. time profiles for the enzymatic determination of ethanol at a concentration of 5.0×10^{-7} M by the stopped-flow technique with (1) spectrophotometric and (2) spectrofluorimetric detection.

At this point, it was also of great interest to test in a general form the performance of the stopped-flow technique in this kinetic enzymatic determination for comparison with its conventional counterpart (batch method). From the results obtained from several experiments, the stopped-flow technique was found to offer several major advantages over the classical batch method: no induction period was observed in the kinetic curve, and the reaction was faster; the precision in the measured initial rates higher; and it required smaller sample and reagent volumes, which is of great interest for homogeneous enzymatic catalytic methods. These features were sufficient for the stopped-flow technique to be adopted for the determination of these alcohols on the basis of the above-mentioned enzymatic reaction.

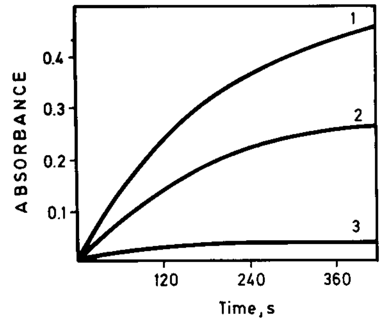

Fig. 2. Effect of the combination of the reagents used to fill the drive syringes of the stopped-flow module: (1) ADH + β-NAD$^+$ and ethanol + Tris; (2) ADH + ethanol and β-NAD$^+$ + Tris; and (3) β-NAD$^+$ + ethanol and ADH + Tris. Ethanol concentration = 5.0×10^{-7} M. For other conditions, see Experimental.

Effect of reaction variables

In order to establish the best reaction conditions, several variables potentially affecting the enzyme-catalysed reaction such as temperature, pH and concentrations of enzyme and coenzyme were investigated. Their influence was studied through plots of initial rate versus concentration. All concentrations quoted are initial concentrations in the drive syringes and kinetic results are the averages of three measurements. This study was carried out by using ethanol as analyte and spectrophotometry for detection.

Before the study proper was started the most appropriate combination of reagents for filling the drive syringes of the stopped-flow unit was determined. Placing solutions of ADH and β-NAD$^+$ in one syringe and alcohol and buffer in the other was found to yield the highest initial rate (Fig. 2). This is consistent with the considerations on the mechanism of this enzymatic reaction, the first step of which involves the formation of the enzyme–coenzyme complex that subsequently reacts with the alcohol [2]. If these ingredients are placed in separate syringes (see Fig. 2), then the product needs a longer time to form and the analytical signal obtained as a result is smaller.

The effect of temperature on the reaction rate was examined between 15 and 45°C. The initial rate increased with increasing temperature up to 22°C, above which it remained constant up to 35°C and then started to decrease owing to denaturation of the enzyme. A temperature of 25°C was chosen for further studies.

The effect of pH on the reaction was investigated on the analyte solution and a pH of 8.55 was chosen as it resulted in the maximum analytical signal (Fig. 3a). The effect of the β-NAD$^+$ and ADH concentrations on the reaction rate at an ethanol concentration of 5.0×10^{-7} M are illustrated in Fig. 3b and c. A 1.3×10^{-5} M β-NAD$^+$ concentration (which allows for a higher [β-NAD$^+$]/[ethanol] ratio, viz., a ca. 25-fold excess) and an alcohol dehydrogenase concentration of 32 U ml^{-1} were used in order to achieve the maximum sensitivity.

Individual determination of each alcohol

Under the selected working conditions, methanol, ethanol, propanol and butanol were

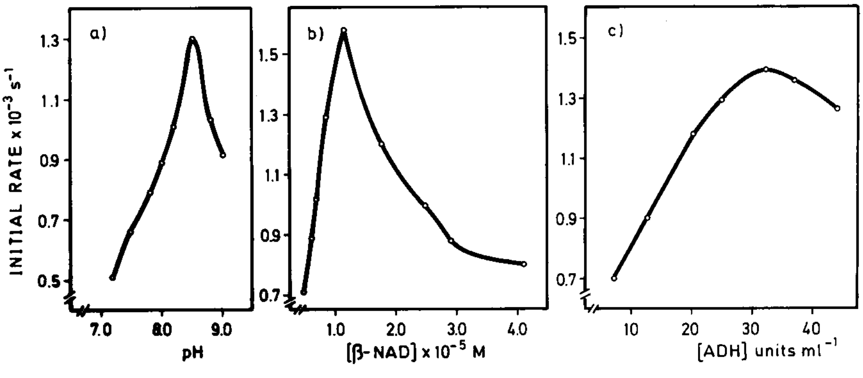

Fig. 3. Effect of chemical variables on the enzymatic determination of 5.0×10^{-7} M ethanol: (a) pH; (b) β-NAD$^+$; and (c) ADH. For other reaction conditions, see Experimental.

determined at the nanogram level by using the proposed kinetic enzymatic method with spectrophotometric and spectrofluorimetric detection. Data relevant to the calibration graphs for these alcohols are summarized in Table 1. The precision was checked on eleven samples containing 4.0×10^{-7} M alcohol when the reaction was monitored spectrophotometrically and 7.0×10^{-8} or 5.0×10^{-7} M with spectrofluorimetric detection. The sampling rate, calculated from the time corresponding to three replicates of the same sample, was about 30 and 20 h^{-1} for spectrofluorimetric and spectrophotometric detection, respectively. As can be seen, the stopped-flow technique performed well (wide dynamic range, high precision and a relatively high sampling rate for the type of the reaction involved) in the individual determinations of these alcohols.

Several conclusions can be drawn from the results obtained. The relative sensitivities (slopes of the respective calibration graphs) decreased in the sequence methanol > ethanol > propanol > butanol when spectrophotometric detection was used, whereas they were all similar for spectrofluorimetric detection. Spectrofluorimetric measurements provided higher sensitivities and wider dynamic ranges in the kinetic enzymatic determination of these alcohols; however, the analytical signal (initial reaction rate) was less reproducible. From the above considerations, one can conclude that spectrofluorimetric measurements are more useful for the individual determination of these alcohols on account of the higher sensitivity, whereas spectrophotometric measurements are more appropriate for the resolution of mixtures of these alcohols on account of the greater discrimination ability.

The proposed stopped-flow method surpasses other kinetic enzymatic methods based on the same reaction in terms of sensitivity and features a similar sampling frequency, particularly in relation to the determination of ethanol by using immobilized enzymes [5,6] or otherwise [22] in a flow-injection manifold. The reported detection limit for ethanol is ca. 0.1 μg ml^{-1} and the sampling frequency is 25–30 h^{-1}. On the other hand, the low cost and high stability of ADH solutions, in addition to the above advantages, make the proposed stopped-flow method an excellent alternative to the individual determination of these alcohols on the basis of this homogeneous enzymatic reaction.

Kinetic enzymatic analysis of alcohol mixtures by use of the Kalman filter

There are various graphical and other mathematical methods for the differential kinetic resolution of mixtures. The choice of the most appro-

TABLE 1

Features of the calibration graphs and precision achieved in the enzymatic determination of alcohols by the stopped-flow technique

Detection method	Alcohol	Linear range		Linear regression equation [a]	Correlation coefficient ($n = 8$)	R.S.D. (%) [b]
		mol l^{-1}	ng ml^{-1}			
Spectrophotometric	Methanol	1.4×10^{-7}–1.3×10^{-6}	4.5–41.6	$IR = 7.3 \times 10^{-5} + 7.8 \times 10^{2}\ C$	0.9992	1.61
	Ethanol	1.3×10^{-7}–1.5×10^{-6}	6.0–69.1	$IR = 3.3 \times 10^{-5} + 6.4 \times 10^{2}\ C$	0.9994	1.30
	Propanol	1.6×10^{-7}–1.1×10^{-6}	9.6–66.1	$IR = -8.2 \times 10^{-7} + 6.1 \times 10^{2}\ C$	0.9997	1.24
	Butanol	1.2×10^{-7}–1.6×10^{-6}	8.9–118.6	$IR = -2.7 \times 10^{-5} + 5.4 \times 10^{2}\ C$	0.9987	1.20
Spectrofluorimetric	Methanol	3.0×10^{-8}–1.0×10^{-7}	1.0–3.2	$IR = 1.5 \times 10^{-4} + 1.8 \times 10^{5}\ C$	0.9997	3.85
		4.0×10^{-7}–1.0×10^{-6}	12.8–32.1	$IR = 1.3 \times 10^{-3} + 4.3 \times 10^{2}\ C$	0.9996	5.03
	Ethanol	3.0×10^{-8}–1.0×10^{-7}	1.4–4.6	$IR = 6.8 \times 10^{-4} + 1.9 \times 10^{5} C$	0.9996	3.63
		4.0×10^{-7}–1.0×10^{-6}	18.5–46.1	$IR = 4.5 \times 10^{-3} + 3.9 \times 10^{3}\ C$	0.9996	3.81
	Propanol	3.0×10^{-8}–1.0×10^{-7}	1.8–6.0	$IR = 1.0 \times 10^{-2} + 1.9 \times 10^{5}\ C$	0.9997	3.64
		4.0×10^{-7}–1.0×10^{-6}	24.0–60.1	$IR = 1.9 \times 10^{-2} + 4.3 \times 10^{3}\ C$	0.9999	2.39
	Butanol	3.0×10^{-8}–1.0×10^{-7}	2.2–7.4	$IR = 1.1 \times 10^{-2} + 2.0 \times 10^{5}\ C$	0.9995	3.25
		4.0×10^{-7}–1.0×10^{-6}	29.6–74.1	$IR = 2.2 \times 10^{-2} + 5.0 \times 10^{3}\ C$	0.9998	2.81

[a] IR = initial rate [absorbance s^{-1} or relative fluorescence intensity (V) s^{-1}]; C = molar concentration. [b] $n = 11$, at mid-range concentration.

TABLE 2

Determination of rate constants [a]

Compound	Logarithmic method	Extended Kalman filter
Methanol	0.0105 (4.02)	0.0110 (2.37)
Ethanol	0.0076 (6.52)	0.0080 (3.51)
Propanol	0.0046 (7.85)	0.0051 (4.16)
Butanol	0.0034 (4.85)	0.0033 (2.55)

[a] All rate constants, expressed in s^{-1}, are averages of five determinations and R.S.D. (%) values are given in parentheses.

priate method is dependent on the relative values of rate constants involved [23], so the simultaneous determination of two or more species in a mixture is relatively easy provided that such a ratio is fairly large or small. Therefore, the first step in this process was to determine the respective rate constants of the mixture components.

The rate constants were determined by using the integrated form of the rate equation for pseudo-first-order kinetics, which can be written as

$$\log(A_\infty - A_t) = \log A_0 - kt/2.303$$

where A_∞ is the final absorbance, A_t the absorbance at time t and A_0 the initial absorbance; from the slope of the plot of $\log(A_\infty - A_t)$ vs. time, the pseudo-first-order rate constant, k, was determined. The rate constant values found for the four alcohols are given in Table 2. As can be seen, the maximum rate constant ratio between two alcohols (methanol and butanol) was ca. 3.

As regards the simultaneous determination of these alcohols, traditional differential reaction-rate methods are of no use as they require larger rate constant ratios for application. We therefore chose to use the linear Kalman filter, a mathematical approach that is currently gaining interest for the resolution of mixtures based on kinetic methodology [24–27].

The enzymatic kinetic determination of these alcohols can be assumed to rely on the following oversimplified kinetic equation:

$$-\left(\frac{d[\mathrm{ROH}]}{dt}\right)_0 = \left(\frac{d[\mathrm{NADH}]}{dt}\right)_0 = \frac{k_r[\mathrm{ADH}]_0[\mathrm{ROH}]}{K_M + [\mathrm{ROH}]} \quad (1)$$

where k_r and K_M are constants derived from a Michaelis–Menten rate equation. As $K_m \gg$ [ROH] for all alcohols, this rate law simplifies to

$$-\left(\frac{d[\mathrm{ROH}]}{dt}\right)_0 = \left(\frac{d[\mathrm{NADH}]}{dt}\right)_0 = k[\mathrm{ROH}] \quad (2)$$

where k is directly proportional to the enzyme activity. Based on Eqn. 2, the extended Kalman filter [7] permits the reliable estimation of the reaction rate constant, k, the net change in absorbance, A_0 (which is directly proportional to the alcohol concentration) and the background contribution, B, based on the following model:

$$A_t = A_0[1 - \exp(-kt)] + B \quad (3)$$

where A_t is the absorbance at time t. In the extended Kalman filter program used, data were obtained by using 1×10^{-6} as the measurement noise variance and 0.5 as the variance on the initial guesses for the parameters, the initial values of which were 0.5 for A_0 and the values obtained from the classical logarithmic methods for the rate constants. This program requires several iterations in order to obtain the best estimate of the parameters (only three iterations are sufficient to achieve the highest precision and accuracy in the results). The rate constant values found for the four alcohols are given in Table 2. As can be seen, the extended Kalman filter is more precise in the determination of these rate constants.

The implementation of the linear Kalman filter for the resolution of alcohol mixtures requires the definition of a measurement model. For the analysis of binary mixtures, such a model can be written according to the terminology used in the Kalman filter [7] as

$$Z(k) = \boldsymbol{H}^{\mathrm{T}}(k)\boldsymbol{X}(k) + v(k) \quad (4)$$

where $Z(k)$ denotes the UV absorbance measurements of the mixture sample, $\boldsymbol{H}^{\mathrm{T}}(k)$ is the observation matrix, $\boldsymbol{X}(k)$ the state vector, which is what ones wishes to determine, and $v(k)$ the measurement noise. In the present instance, for a mixture of two alcohols in which A_1 and A_2 are the maximum absorbance values (directly proportional to the concentration of each alcohol), k_1 and k_2 are their respective rate constants and B is a constant background absorbance, the measurement model equation can be written as

$$A_t = \left[1-\exp(-k_1 t)\; 1-\exp(-k_2 t)\; 1\right]\begin{bmatrix} A_1 \\ A_2 \\ B \end{bmatrix} + v_t \tag{5}$$

The system model equation is also required to apply the linear Kalman filter [7]; however, the state transition matrix is the identity matrix as state variables remain constant in this analysis. The initial guesses and all other conditions used were as described above in connection with the use of the extended Kalman filter.

A typical plot of estimated absorbances against time as the filter moves along the kinetic curve for a methanol–butanol mixture, and a simulated kinetic curve plotted from data obtained by using the linear Kalman filter, are shown in Fig. 4. As can be seen, there is good agreement between the experimental and simulated kinetic curves, which shows the good convergence of the filtering process.

Based on the respective rate constant ratios between the different alcohols, various synthetic mixtures containing different amounts of alcohols were analysed by the linear Kalman filter. For these mixtures, the maximum mole ratio tested between the two components was that which yielded an error of ca. ±10%. The results ob-

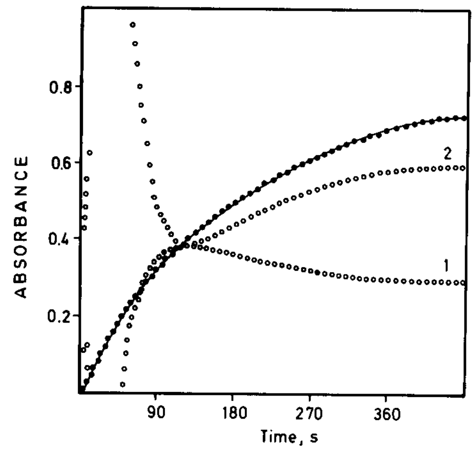

Fig. 4. Absorbance versus time plots obtained in the resolution of a mixture of 4.0×10^{-7} M methanol and 3.8×10^{-7} M butanol by using the linear Kalman filter. (●) Experimental kinetic curve; (1) and (2) estimated absorbances for methanol and butanol, respectively; and (–) simulated kinetic curve constructed from the data obtained in the filtering process. Reaction conditions as described under Experimental.

TABLE 3

Analysis of synthetic alcohol mixtures by use of the linear Kalman filter

Mixture taken		Results found		
Compound	Concentration (10^{-7} M)	Estimated signal [a]	Measured signal	Error (%)
Methanol	4.0	0.2831 (0.0018)	0.2745	3.13
Butanol	3.8	0.6083 (0.0027)	0.6319	−3.73
Methanol	4.0	0.3079 (0.0018)	0.2811	9.53
Butanol	2.0	0.3861 (0.0023)	0.4005	−3.59
Methanol	2.2	0.2407 (0.0017)	0.2515	−4.48
Butanol	3.8	0.4930 (0.0025)	0.5208	−5.34
Ethanol	4.0	0.3623 (0.0031)	0.3521	2.84
Butanol	4.0	0.6375 (0.0044)	0.6953	−8.34
Ethanol	4.0	0.3803 (0.0030)	0.3524	7.95
Butanol	2.0	0.4576 (0.0042)	0.4207	8.55
Methanol	4.0	0.3887 (0.0035)	0.3623	7.28
Propanol	4.0	0.2821 (0.0045)	0.2984	−5.46

[a] For a pure component. Standard deviations ($n = 3$) are given in parentheses.

tained under these conditions are summarized in Table 3. As can be seen, several alcohol mixtures were successfully resolved, which testifies to the good performance of the multi-component Kalman filter in the kinetic enzymatic determination of these alcohols.

The authors gratefully acknowledge financial support from the DIGICyT Project No. PB91-0840 (Spain) and from the Deutscher Akademischer Austauschdienst in Bonn and the Institut für Analytische Chemie of the Bergakademie Freiberg.

REFERENCES

1 H.A. Mottola, Analyst, 112 (1987) 719.
2 E. Bernt and I. Gutmann, in H.U. Bergmeyer (Ed.), Methods of Enzymatic Analysis, Vol. 3, Verlag Chemie, Weinheim, and Academic, New York, 2nd edn., 1974.
3 G.G. Guilbault, Handbook of Enzymatic Methods of Analysis, Dekker, New York, 1976.
4 F. Lázaro, M.D. Luque de Castro and M. Valcárcel, Anal. Chem., 59 (1987) 1859.
5 J. Ruz, M.D. Luque de Castro and M. Valcárcel, Analyst, 112 (1987) 259.
6 A. Maqueira, M.D. Luque de Castro and M. Valcárcel, Microchem. J., 36 (1987) 309.
7 S.D. Brown, Anal. Chim. Acta, 186 (1986) 1.
8 H. Tanner and H. Limacher, Flüss. Obst., 35 (1984) 182.
9 S.T. Cheung and W.N. Lin, J. Chromatogr., 58 (1987) 248.
10 J.P. Camelbeeck, D.M. Comberbach, J. Goossens and P. Roelants, Biotechnol. Tech., 2 (1988) 183.
11 D. Ge, J. Wang, J. Guo and B. He, Sepu, 7 (1989) 384.
12 A. Horna, J. Chromatogr., 457 (1988) 372.
13 D.M. Comberbach, J.M. Scharer and M. Moo-Young, Enzyme-Microb. Technol., 7 (1985) 543.
14 E.F. D'yachkova, T.A. Lovchinovskaya and G.A. Chikin, Gig. Sanit., 4 (1987) 55.
15 M.L. Williams, Chromatogr. Int., 19 (1986) 12.
16 E. Mentasti and C. Baiocchi, Anal. Chim. Acta, 119 (1980) 91.
17 R.T. Sane, S.S. Kamat and A.D. Pandit, J. Assoc. Off. Anal. Chem., 64 (1981) 1145.
18 M. Ignaczak and J. Dziegiec, Chem. Anal. (Warsaw), 27 (1982) 505.
19 E. Chromiak and I. Morawski, Chem. Anal. (Warsaw), 29 (1984) 441.
20 A. Takahashi, N. Tanaka, H. Tanno, A. Kashima and N. Mikami, Bunseki Kagaku, 36 (1987) 473.
21 A. Loriguillo, M. Silva and D. Pérez-Bendito, Anal. Chim. Acta, 199 (1987) 29.
22 F. Lázaro, M.D. Luque de Castro and M. Valcárcel, Anal. Chim. Acta, 185 (1986) 57.
23 D. Pérez-Bendito and M. Silva, Kinetic Methods in Analytical Chemistry, Horwood, Chichester, 1988, Chap. 7.
24 P.D. Wentzell, M.I. Karayannis and S.R. Crouch, Anal. Chim. Acta, 224 (1989) 263.
25 C.A. Corcoran and S.C. Rutan, Anal. Chim. Acta, 224 (1989) 315.
26 R. Xiong, A. Velasco, M. Silva and D. Pérez-Bendito, Anal. Chim. Acta, 251 (1991) 313.
27 W.H. Lewis, Jr., and S.C. Rutan, Anal. Chem., 63 (1991) 627.

Analytica Chimica Acta, 274 (1993) 117–123
Elsevier Science Publishers B.V., Amsterdam

Flow-injection analysis for the measurement of penicillin V in fermentation media

Morten Carlsen, Lars H. Christensen and Jens Nielsen
Department of Biotechnology, Technical University of Denmark, DK-2800 Lyngby (Denmark)

(Received 30th June 1992; revised manuscript received 12th October 1992)

Abstract

Three different flow-injection analysis systems for measuring penicillins in complex fermentation media were tested: a molybdenum blue, an iodimetric and a potentiometric method. All the methods are based on enzymatic hydrolysis of the penicillin to the corresponding penicilloic acid using β-lactamase, followed by detection of penicilloic acid. The β-lactamase is immobilized in a packed-bed reactor in which there is 100% conversion of penicillin to penicilloic acid, and all the methods therefore measure the sum of penicilloic acid and penicillin in the sample. The iodimetric method was found to be the best method for measurement in fermentation media. By replacing the enzyme reactor with an enzyme-free dummy reactor, it is possible to measure the concentration of penicilloic acid alone, and thence the penicillin concentration can be determined by subtraction of the penicilloic acid concentration from the total response in the analyser with the enzyme reactor inserted. The application of the analyser was tested by monitoring a fed-batch penicillin fermentation and the correlation between measurements by the FIA system and a liquid chromatographic method was very good.

Keywords: Enzymatic methods; Flow injection; UV–Visible spectrophotometry; Antibiotics; Enzyme reactors; Fermentation; Iodimetry; Penicillin

Fast and robust measurement techniques for monitoring the most important process variables are needed both in an industrial environmental and for in-depth theoretical analysis, e.g., of fermentation kinetics [1]. Flow-injection analysis (FIA) has been successfully applied for the monitoring of several fermentation variables [2–4]. In this study, a fast, robust and reliable FIA system was developed for monitoring penicillin V and related by-products from a penicillin fermentation. The performance of the FIA system was evaluated during fed-batch fermentations on a complex medium containing corn-steep liquor.

Several methods for measuring penicillins have been reported [5–13], but only a few have been tested for monitoring of penicillin fermentation with a complex medium. Many of these methods utilize the reducing properties of the penicilloic acid, which is produced by the β-lactamase (penicillinase)-catalysed hydrolysis of penicillin (see Fig. 1). The penicilloic acid formed is determined spectrophotometrically using the reduction of the yellow molybdoarsenic acid to molybdenum blue [5] or the decolorization of an iodine–starch complex when iodine is reduced to iodide ions [6]. Alternatively, one may determine the pH change caused by the hydrolysis of penicillin to penicilloic acid [7–11] or the hydrolysis of penicillin V to 6-aminopenicillanic acid using penicillin amidase. Changes in pH can be detected

Correspondence to: J. Nielsen, Department of Biotechnology, Technical University of Denmark, DK-2800 Lyngby (Denmark).

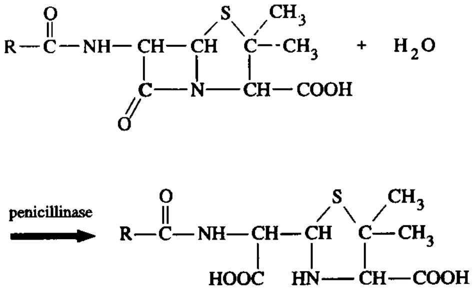

Fig. 1. Enzymatic hydrolysis of penicillin using penicillinase.

with a pH electrode or a hydrogen ion-sensitive field effect transistor (pH-FET) [12]. All these methods are easy to implement, but as a complex medium contains many different reducing substances and may have a varying buffer capacity, one should always check carefully for the presence of interfering components or changes in the sample matrix. Finally, it is possible to measure the change in enthalpy during the hydrolysis of penicillin to penicilloic acid using an enzyme thermistor [13], but this detection device requires careful maintenance.

This paper describes a FIA method that can be used for monitoring the concentrations of both penicillin and penicilloic acid in complex media. The analyser is based on the iodimetric method [6] and its performance is compared with systems based on molybdenum blue and potentiometric methods.

EXPERIMENTAL

Enzyme reactor

All three methods tested start with enzymatic hydrolysis of the penicillin to the corresponding penicilloic acid using immobilized β-lactamase (EC 3.5.2.6). Two kinds of enzyme reactors were tested: a packed-bed reactor (PBR) with the enzyme immobilized on controlled-pore glass (CPG) beads and a wall-coated tubular reactor (WCTR) with the enzyme immobilized to the inner surface of a nylon tube. For the PBR the β-lactamase was immobilized on aminopropyl-CPG beads of 120–200 mesh (mean pore diameter 170 Å), which were packed in a column with a total volume of 60 μl. The WCTR was made of a 1 m × 1.0 mm i.d. nylon tube (volume 800 μl) coiled in a figure-of-eight shape.

With the small pores in the CPG beads it is assumed that the enzyme immobilization is restricted to the outer surface of the beads, and with this assumption the available surface area for immobilization is approximately the same for the two type of reactors [14] (1.8×10^{-3} m^2 for the PBR and 3.1×10^{-3} m^2 for the WCTR). Despite the lower surface area in the PBR, a much higher conversion was found in this type of reactor. This observation could be explained by mass-transfer effects in the WCTR reactor, where the penicillin has to diffuse to the tube wall. The analyser was applied to fermentation media where both penicillin and penicilloic acid will be present at the same time. The penicilloic acid is formed by a non-enzymatic degradation of the penicillin secreted by the cells. It is therefore convenient to have a 100% conversion of penicillin to penicilloic acid in the enzyme reactor. This cannot be achieved with the WCTR, even at very low flow-rates, i.e., a high residence time in the reactor, and the PBR was therefore preferred as there is total conversion [checked by liquid chromatography (LC)] in this type of reactor at the flow-rates which are of interest. For both reactors the stability of the immobilized enzyme is very good, i.e., there is no decrease in the enzyme activity over a period of months.

Molybdenum blue method

In the presence of mercury(II) chloride, penicilloic acid reduces molybdoarsenic acid to molybdenum blue, which can be measured spectrophotometrically in the range 650–700 nm. The FIA manifold is shown in Fig. 2. The injection volume was 40 μl and the reaction coil was a 1 m × 0.5 mm i.d. tube coiled in a figure-of-eight shape. The flow-rates for the carrier stream, molybdoarsenic reagent and mercury(II) chloride solution were all set at 0.6 ml min^{-1}. The linear working range was 10–100 mg l^{-1} K-penicillin V.

The appearance of a molybdenum blue precipitate in the tubes and especially in the detector results in a severe baseline drift, i.e., the baseline signal increases. Attempts to prevent precipita-

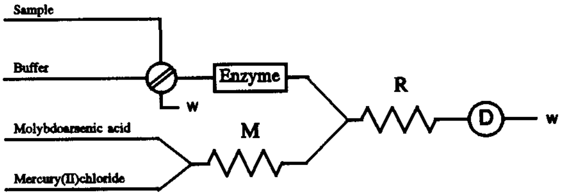

Fig. 2. FIA manifold for detection of penicillin by the molybdenum blue method. M = mixing coil; R = reaction coil; Enzyme = enzyme reactor; D = detector (650 nm); W = waste.

tion in the detector by using different buffers at various pH values as the carrier stream proved unsuccessful. However, thermostating the reagent stream at 45°C is reported to give a better stability of the analyser, i.e., no baseline drift [5].

Iodimetric method

This method is based on measuring the amount of penicilloic acid by the classical iodimetric method in which iodine is reduced to iodide ions [15]. The iodine consumption is detected spectrophotometrically by measuring the decrease in the absorbance of an iodine–starch complex. The exact stoichiometry of the reaction between penicilloic acid and iodine is not known, but it is reported that 1 mol of penicilloic acid reduces 3.5–4.5 mol of I_2 [16,17]. In Fig. 3 absorbance measurements reported by Sykes and Nordström [15] are plotted as $\ln[(A_0 - A_\infty)/(A - A_\infty)]$ versus the reaction time for three initial concentrations of penicilloic acid, where A_0, A and A_∞ are the absorbance at time $t = 0$, $t = t$ and at $t = \infty$, respectively. A linear relationship between $\ln[(A_0 - A_\infty)/(A - A_\infty)]$ and the reaction time is observed in all three experiments. The correlation coefficient is 0.984 and the slope and intercept are 0.155 ± 0.002 and −0.04 ± 0.06, respectively, for 95% confidence limits. Hence the reaction between iodine and penicilloic acid can be considered as first order in penicilloic acid concentration. This is an advantage for application of the reaction in an FIA system as a first-order reaction will give a linear calibration graph.

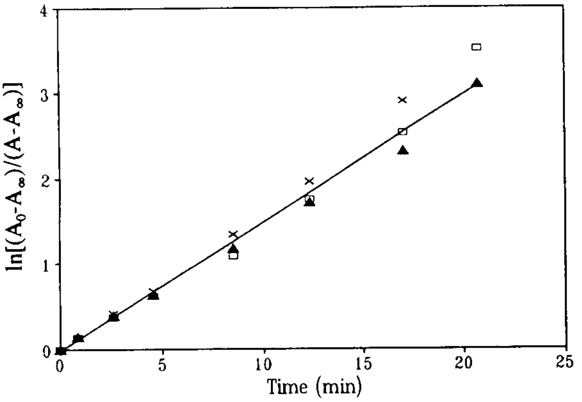

Fig. 3. Decolorization of the iodine–starch complex by three different initial concentrations of penicilloic acid: ▲ = 10.00; □ = 6.67; × = 3.33 μM. Data from [15].

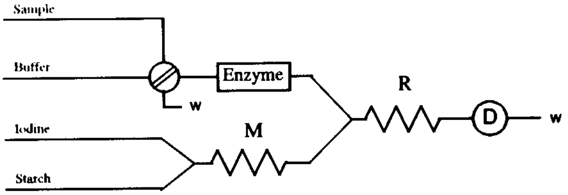

Fig. 4. FIA manifold for detection of penicillin by the iodimetric method. M = mixing coil; R = reaction coil; Enzyme = enzyme reactor; D = detector (650 nm); W = waste.

The FIA manifold is shown in Fig. 4. The injection volume was 10 μl and the reaction coil was a 1 m × 0.8 mm i.d. tube coiled in a figure-of-eight shape. The flow-rate of the carrier stream was 1.2 ml min^{-1} and the iodine and starch solutions were pumped at a flow-rate of 0.7 ml min^{-1}. With these conditions the linear working range was from 2.5 to 150 mg l^{-1} K-penicillin V.

Potentiometric method

The potentiometric method is based on measuring the pH change caused by the hydrolysis of penicillin to penicilloic acid. To obtain a linear correlation between the penicillin concentration and the pH change, the buffer capacity of the carrier stream has to be independent of pH [8], within the experimental range. It was observed that both the PBR and the WCTR have a strong chromatographic effect on H^+ ions, which results in very broad peaks. Therefore, the concept of an immobilized enzyme reactor was abandoned and β-lactamase was continuously fed to the reactor,

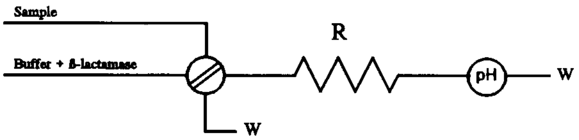

Fig. 5. FIA manifold for detection of penicillin by the potentiometric method. The β-lactamase is dissolved in the carrier stream; R = reaction coil; pH = pH electrode; W = waste.

dissolved in the carrier stream. The buffer capacity of the carrier stream is an important parameter in this system, and the final capacity selected was a compromise between ensuring a sufficient response on injection and preventing interference from varying buffer capacity and pH of the sample.

The manifold is shown in Fig. 5. The injection volume was 10 μl and the reaction coil was a 0.5 m × 0.5 mm i.d. tube coiled in a figure-of-eight shape. The carrier stream was 1.0 mM phosphate buffer (pH 6.5) containing 5 mg l^{-1} β-lactamase at a flow-rate of 1.0 ml min^{-1}. The linear working range of the analyser was from 100 to 800 mg l^{-1} K-penicillin V.

Procedures

The fed-batch penicillin fermentations were carried out in a 41-l Chemap bioreactor with an industrial, high-yielding strain of *P. chrysogenum* obtained from Novo Nordisk. The medium contained 100 g l^{-1} corn steep liquor, 3 g l^{-1} sucrose, 6.0 g l^{-1} phenoxyacetic acid and inorganic salts [$(NH_4)_2SO_4$, KH_2PO_4 and $CaCl_2$]. The size of the inoculum was 10% (w/w) and the inoculum was prepared by a batch fermentation in a 7-l Chemap bioreactor. The feed contained a mixture of glucose, $(NH_4)_2SO_4$ and phenoxyacetic acid. The gas flow-rate to the bioreactor was 1 volume air/volume fermentation broth/min and the temperature and pH were kept constant at 25°C and 6.5, respectively. The fermentation conditions have been described previously [18].

The FIA system consisted of peristaltic pumps (Watson-Marlow, Falmouth, UK) and pneumatically driven injection valves (Rheodyne, Cotati, CA). The spectrophotometer was an in-house design containing a light-emitting diode (650 nm) and a photodiode as detector. The pH combination electrode (Phoenix, Houston, TX) was placed in a 50-μl flow-through cell. All tubes were made of PTFE (0.5 mm i.d. for the molybdenum blue and potentiometric methods, and 0.8 mm i.d. for the iodimetric method).

Reagents in the FIA systems. All reagents for the flow-injection analysers were of analytical-reagent grade. All solutions were degassed before they were used in the FIA systems to avoid air bubbles in the enzyme reactor and detector.

Iodimetric method. A stock solution of starch was prepared by adding a suspension of 13.7 g of soluble starch (Merck) in 100 ml of water to 900 ml of boiling water. Portions of 100 ml of the solution were dispensed into small bottles and sterilized for 20 min at 121°C. The stock solution was diluted 20-fold in distilled water and KI was added to a concentration of 0.72 g l^{-1} before use.

A 70 μM I_2 solution was freshly prepared every day from a stock solution of 0.1 M I_2. The buffer was 25 mM Tris buffer (pH 6.0) [3.03 g of tris(hydroxymethyl)aminomethane, 2.9 g of malic acid and 65 ml of 0.2 M NaOH in 1 l of distilled water].

Molybdenum blue method. The molybdoarsenic acid reagent was prepared as follows: 30 g of $(NH_4)_6Mo_7O_{24} \cdot 4H_2O$ were dissolved in 400 ml of distilled water and 25.2 ml of concentrated sulphuric acid were added while cooling. Then 3.6 g $Na_2HAsO_4 \cdot 7H_2O$ dissolved in 25 ml of water were added and the solution was diluted to 1 l with distilled water. The solution was kept in a dark bottle and stored at 37°C for 24 h before use. Mercury(II) chloride solution was made by dissolving 0.175 g of $HgCl_2$ in 1 l of distilled water. The buffer was citrate–phosphate buffer (pH 6.2) (7.02 g of citric acid and 23.55 g of disodium hydrogenphosphate in 1 l of water).

Potentiometric method. A 1 mM phosphate buffer (pH 6.5) was used.

Enzyme. β-Lactamase (Penase) was obtained from Leo Pharmaceutical Products (Ballerup, Denmark).

Immobilization of enzymes on CPG. The glutardialdehyde procedure [19] was used with aminopropyl-CPG (120–200 mesh) (Fluka) and an enzyme loading of 25 mg of enzyme per gram of CPG beads.

Immobilization of enzymes on nylon tubes. The procedure used was based on *O*-alkylation of the nylon tube [20] (i.d. 1.0 mm and o.d 1.78 mm) (Portex, Hythe, UK) with triethyloxonium tetrafluoroborate (Aldrich) and successive coupling of hexanediamine (Merck), glutardialdehyde and enzyme (5 mg ml^{-1}).

LC method. The LC method applied was a reversed-phase method with gradient elution using Na_2SO_4–H_3PO_4–CH_3CN [0.2 M : 0.04 M : 3.7% (w/w)] and CH_3CN [46.9% (w/w)]. The reversed-phase column was a Waters Nova-Pak C_{18} (30 cm × 3.9 mm i.d., 4-μm packing material). The injection volume was 10 μl and the temperature was 40°C. The peaks were detected at 228 nm using a Waters Model 481 UV–visible detector. Further details are given in [21].

RESULTS AND DISCUSSION

All three methods were tested by measuring penicillin in fermentation samples. The results were compared with measurements of penicillin using the LC method described above. Large deviations between the potentiometric and the LC methods appeared when penicillin in fermentation samples was measured. This deviation did not disappear on changing the buffer capacity and the pH of the carrier stream, probably because of the large inherent buffer capacity of the fermentation medium. The standards could be prepared in a sterile fermentation medium, but as the buffer capacity of the fermentation medium changes throughout the fermentation, this will not solve the problem. Based on these experiments and also because a continuous supply of dissolved enzyme has to be maintained, it was concluded that the potentiometric method is unsuitable for measuring penicillin in fermentation samples, at least with the industrial-type medium used in this study.

The molybdenum blue and iodimetric methods both gave results in good agreement with those of the LC method, but the molybdenum blue method has some drawbacks compared with the iodimetric method. The iodimetric method can run for weeks without washing the tubes and the detector, whereas rinsing of all the tubes and detectors is required every few hours when using the molybdenum blue method. Further, the molybdoarsenic reagent and mercury(II) chloride are toxic, whereas the iodine and the starch solutions are much less harmful. Finally, the iodine and starch reagents are cheap and available in most laboratories, whereas the molybdoarsenic reagent and mercury(II) chloride are more expensive.

The iodimetric method was therefore chosen for routine measurement of penicillin in complex fermentation media. Degradation of penicillin to penicilloic acid occurs throughout the fermentation (5–20% of the penicillin may be degraded) and the manifold in Fig. 4 is not completely suitable. The FIA analyser was therefore modified by inserting an extra valve, which made it possible to inject the sample through either the enzyme reactor or a "dummy reactor". The dummy reactor has exactly the same sample dispersion as the enzyme reactor, but no β-lactamase is immobilized on the beads in this reactor. By injection of a sample through the enzyme reactor the sum of the concentration of penicillin and penicilloic acid is measured, whereas injection through the dummy reactor gives the concentration of penicilloic acid alone. The difference between the two signals is used to calculate the penicillin concentration. Penicillin cannot reduce iodine to iodide [22] and penicillin will therefore not interfere with the measurement of penicilloic acid. Obviously a 100% conversion of penicillin in the enzyme reactor is required if the analyser is to be calibrated with standard penicillin solutions alone. The modified FIA manifold is shown in Fig. 6.

The linear concentration range of the analyser is approximately two decades, and in aqueous solution the limit of determination is 2.5 mg l^{-1} K-penicillin V with the flow-rates and injection volume described above. Linear regression on the logarithmic values gives

$$\log[\text{peak heights (mV)}] = 0.9996 \log[\text{K-Pen V (mg l}^{-1})] + 2.82 \qquad (1)$$

The regression is based on ten different concentrations, and the relative standard deviation

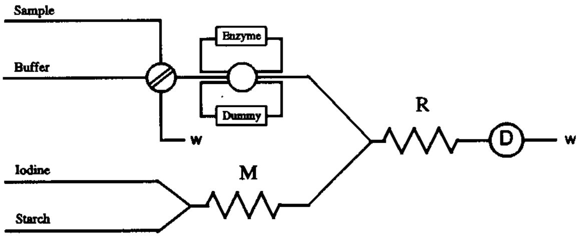

Fig. 6. Modified FIA manifold for detection of penicillin by the iodimetric method. M = mixing coil; R = reaction coil; Enzyme = enzyme reactor; Dummy = dummy reactor; D = detector (650 nm); W = waste.

(R.S.D.) of the slope and the intercept are 1.0% and 0.2%, respectively. The deviation of the slope from 1.000 is less than the R.S.D of the slope and the calibration graph is consequently linear in the range 2.5–150 mg l^{-1} K-penicillin V. The maximum sample injection frequency is 60 h^{-1}, corresponding to the measurement of both penicillin V and penicilloic acid in 30 samples h^{-1}.

When measuring samples from the fermentation medium it is important to consider interferences from components in the medium, e.g., glucose and corn steep liquor (CSL). The influence of glucose, phenoxyacetic acid (PAA) and CSL on the analytical response was examined. For glucose and PAA no interference was found, even for concentrations of 10 g l^{-1} glucose and 40 g l^{-1} PAA, which are higher than those typically present in fermentation media. CSL interferes with the analysis owing to the presence of one or more reducing compounds. The interference of CSL was examined and it was found that the interference (in mV) is almost independent of the penicillin concentration and that there is a linear correlation between the CSL concentration and the signal (at least for CSL concentrations below 200 g l^{-1}). For a sterile medium containing 100 g l^{-1} CSL an interference corresponding to 4 mg l^{-1} K-penicillin V is registered if the sample is diluted 80-fold before being analysed. This corresponds to the measurement of 0.33 g l^{-1} K-penicillin V in the undiluted sample, i.e., the medium containing 100 g l^{-1} CSL. By measuring a sample just before the start of the fermentation (at $t = 0$ where no penicillin V is present), it is therefore possible to determine the CSL interference initially, and this value is subtracted from the signal for both the enzyme and the dummy reactor at the beginning of the fermentation. Later in the fermentation when the concentration of penicillin is much higher (up to 30 g l^{-1} K-penicillin V) the samples are diluted 250-fold, and the interference from the CSL can be ignored.

The application of the analyser was tested during several fed-batch penicillin fermentations where the samples were withdrawn by means of an in situ membrane module (ABC Module, Advanced Biotechnology Corporation, Munich) [21]. During the fermentation a small part of the precursor phenoxyacetic acid is oxidized to *p*-hy-

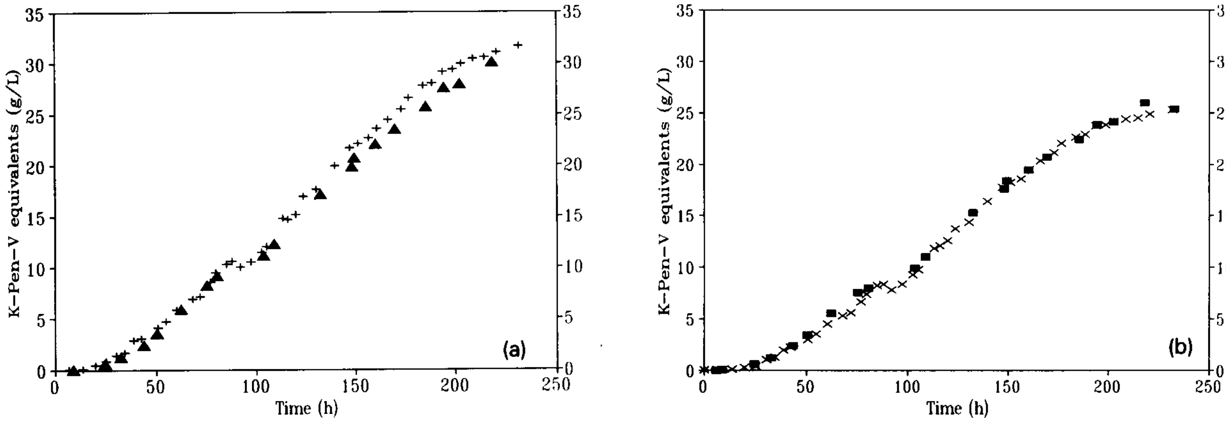

Fig. 7. (a) Measurement of the concentration of the sum of the penicillin and penicilloic acid. + = FIA (iodimetric method); ▲ = LC. (b) Measurement of the concentration of penicillin. × = FIA (iodimetric method); ■ = LC.

droxyphenoxyacetic acid, and this is incorporated into the penicillin molecule to form the by-product *p*-hydroxypenicillin V. This by-product may represent up to 10% of the total β-lactam activity in the medium at the end of the fermentation. The penicillin concentration measured by the FIA system is consequently the sum of penicillin V and *p*-hydroxypenicillin V (determined as K-penicillin V equivalents). For comparison with the LC method the sum of penicillin V and *p*-hydroxypenicillin V is used. In Fig. 7a the concentration profile of the sum of penicillin V, *p*-hydroxypenicillin V and penicilloic acid is shown for a fed-batch fermentation measured by injecting the samples through the enzyme reactor. From Fig. 7a it is possible to calculate the volumetric penicillin production rate, which is a variable for modelling and control of the fermentation process. By subtracting the dummy signal from the enzyme signal one obtains measurements of the concentration of the sum of penicillin V and *p*-hydroxypenicillin V, i.e., the total β-lactam activity in the medium (see Fig. 7b). After approximately 90 h when most of the amino acids of the CSL had been consumed, 2 l of an amino acid mixture were added to the bioreactor to see whether this had any effect on the penicillin production. The response of the culture to the pulse of amino acids is well observed by the FIA system but it seems to have little influence on the volumetric penicillin production.

Conclusion

An FIA system for the measurement of the sum of penicillin and penicilloic acid and the penicillin concentration was developed and applied to the monitoring of a fed-batch penicillin fermentation. The method was compared with two other FIA systems, and was found to be superior, especially for application to fermentation monitoring. The described FIA system is a good alternative to LC owing to the higher analysis frequency, which makes it suitable for on-line monitoring of the fermentation process.

REFERENCES

1 J. Nielsen and J. Villadsen, Chem. Eng. Sci., 47 (1992) 4225.
2 M. Garn, M. Gisin and C. Thommen, Biotechnol. Bioeng. 34 (1989) 423.
3 S. Benthin, J. Nielsen and J. Villadsen, Anal. Chim. Acta, 247 (1991) 45.
4 K. Schügerl, Anal. Chim. Acta, 213 (1988) 1.
5 I. Schneider, Anal. Chim. Acta, 166 (1984) 293.
6 M.A.J. van Opstal, R. Wolters, J.S. Blauw, P.C van Krimpen, W.P. Bennekom and A. Bult, J. Pharm. Biomed. Anal., 8 (1990) 49.
7 R. Gnanasekaran and H.A. Mottola, Anal. Chem., 57 (1985) 1005.
8 B. Olsson, Anal. Chim. Acta, 209 (1988) 123.
9 H. Meier and C. Tran-Minh, Anal. Chim. Acta, 264 (1992) 13.
10 M.S. Fuh, L.W. Burgess and G.D. Christian, Anal. Chem., 60 (1988) 433.
11 S.O. Enfors and H. Nilsson, Enzyme Microb. Technol., 1 (1979) 260.
12 U. Brand, T. Scheper and K. Schügerl, Anal. Chim. Acta, 226 (1989) 87.
13 G. Decristoforo and B. Danielsson, Anal. Chem., 56 (1984) 263.
14 J. Nielsen, Proc. Control Qual., 2 (1992) 371.
15 R.B. Sykes and K. Nordström, Antimicrob. Ag. Chemother., 1 (1972) 94.
16 C.J. Perret, Nature (London), 174 (1954) 1012.
17 T. Sawai, I. Takahashi and S. Yamagishi, Antimicrob. Ag. Chemother., 13 (1978) 910.
18 L.H. Christensen, J. Nielsen and J. Villadsen, Anal. Chim. Acta, 249 (1991) 123.
19 H.H. Weetall, Methods Enzymol., 44 (1976) 134.
20 W.E. Hornby and L. Goldstein, Methods Enzymol., 44 (1976) 118.
21 L.H. Christensen PhD Thesis, Technical University of Denmark, Lyngby, 1992.
22 H.T. Clarke, J.R. Johnson and R. Robinson, The Chemistry of Penicillin, Princeton University Press, Princeton, NJ, 1949.

Analytica Chimica Acta, 274 (1993) 125–128
Elsevier Science Publishers B.V., Amsterdam

Segmental flow injection with ion-selective electrodes for the determination of fluoride in water

J.A. Borzitsky and A.V. Dvinin
Sillamae Chemical–Metallurgical Enterprise, Sillamae 202010 (Estonia)

O.M. Petrukhin and Yu.I. Urusov
D.I. Mendeleev Moscow Chemical Technology Institute, Miusskaya pl 9, Moscow 125820 (Russia)

(Received 8th May 1992; revised manuscript received 24th September 1992)

Abstract

A flow analyser with enhanced sampling frequency combining the features of flow-injection and continuous-flow analysis is described. Parameters of the analyser were optimized to ensure the highest rate of analysis allowed by the bubble-through flow cell with fluoride-selective electrodes. Fluoride was determined in 0.1-ml water samples with a sampling rate as high as 720 h^{-1} and a relative standard deviation better than 1%.

Keywords: Flow injection; Ion selective electrodes; Fluoride; Water

There are two widely used techniques which are commonly regarded as flow analysis: continuous-flow analysis (CFA) and flow-injection analysis (FIA) [1,2]. There have been disputes about the names and definitions of CFA and FIA [3]. One of the definitions of FIA regards the use of a non-segmented stream and the method of injection as less important and emphasizes only the controlled dispersion of samples [4]. The latter definition, however, can be applied to both FIA and CFA, as any kind of flow analysis is meaningful only if dispersion is kept under control in one way or another, otherwise the results would not be reproducible [3]. Recent reports describing the novel segmental flow-injection technique completely eliminate the borderlines between CFA and FIA [5–7]. Flow systems with an injector introducing air segments at the beginning and at the end of each sample slug allow the longitudinal dispersion of solute taking place in different parts of the flow conduit to be substantially reduced, thus solving the most crucial problem of FIA. The need for debubbling the stream before detection prevented, however, complete utilization of the advantages connected with the air-segmentation technique.

Previously a wall-jet flow cell arrangement was reported with minimum hold-up and fast response, particularly suitable for potentiometric measurements in air-segmented streams without debubbling [8]. The sampling rate of the CF analyser incorporating this cell is reduced by the dispersion of samples passing through the unsegmented zones of the flow system. The main contribution to the dispersion is from the peristaltic pump, the pump rollers squeezing the tubes and distorting the concentration profile. To reduce this interaction of the sample with the stream carrying it, the "pecking" technique [9] was used. Another possibility for minimizing the dispersion

Correspondence to: O.M. Petrukhin, D.I. Mendeleev Moscow Chemical Technology Institute, Miusskaya pl. 9, Moscow 125820 (Russia).

is to inject the sample slug into the air-segmented stream without passing it through the pump after the introduction. The objective of this work was to develop a flow analysis system combining the advantages of the injection technique and air segmentation with improved performance characteristics in comparison with conventional CFA and FIA systems.

EXPERIMENTAL

Reagents and solutions

All reagents were of analytical-reagent grade and solutions were prepared with distilled water and stored in polyethylene bottles. Stock ionic strength adjusting buffer (ISAB) containing 0.5 M CH_3COOH, 0.5 M NaCl and 2.25 g l^{-1} *trans*-1,2-diaminocyclohexane-*N*,*N*,*N*′,*N*′-tetraacetic acid with pH adjusted to 5.2 with sodium hydroxide solution was used for the measurements with fluoride-selective electrodes.

Flow cell

The measurements were made with a flow cell of modified wall-jet design with improved dynamic characteristics [8], which can be represented by

Ag/ AgCl	inner solution	membrane	sample	reference solution	membrane	inner solution	Ag/ AgCl

The single-crystal membranes of the custom-made fluoride-selective electrodes had the composition 1 mol% EuF_2–5 mol% SrF_2–94 mol% LaF_3 and the inner solution was 1×10^{-4} M NaF–2×10^{-1} M NaCl. The reference solution, pumped constantly through the cell, contained 1×10^{-4} M NaF and ISAB diluted in a 2:3 ratio.

Apparatus

A Reihelt E 25/WM K10 peristaltic pump was used for pumping the solutions and maintaining the air flow. The sampler was a Contiflo OL-610/11 equipped with an electronic control unit. Potentials were measured at room temperature with a Radelkis OP-208 pH/mV meter and recorded by a strip-chart recorder. Tygon tubing (0.76 and 1.65 mm i.d.) was used to construct the manifold.

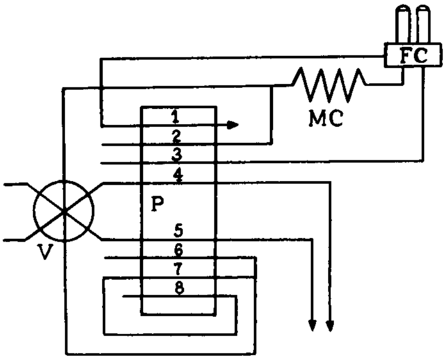

Fig. 1. Schematic diagram of the flow analyser. V = Injection valve; P = peristaltic pump; MC = mixing coil; FC = flow cell; 1 = differential pumping from the cell; 2 = buffer solution; 3 = reference solution; 4 = sample/wash flow; 5 = wash/sample flow; 6 = carrier; 7 = air flow (second tube); 8 = air flow (first tube). Arrows indicate the waste outlets. For details, see text.

Figure 1 shows a schematic diagram of the flow apparatus. A PTFE valve with a load/inject shaft rotation angle of 60° (Fig. 2) was used for sample injection, the bores of the valve being 1.5 mm in diameter.

RESULTS AND DISCUSSION

Preliminary experiments with a valve installed close to the inlet port of the flow cell showed that the dynamic characteristics of the cell permit sampling rates as high as 700–900 h^{-1}, depending on the fluoride concentration level and the flow-

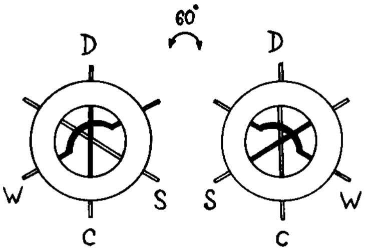

Fig. 2. Three-loop injection valve. W = Wash stream inlet port; S = sample stream inlet port; C = carrier stream inlet port; D = to detector.

rate. The performance of any routine flow analyser is always poorer owing to sample dispersion. The method of sample injection into the air-segmented stream proposed here results in a significant decrease in the carry-over in comparison with conventional CFA and FIA techniques. However, the application of an ordinary one-loop injector commonly used with flow manifolds reduces the sampling rate to 400–500 h^{-1} owing to the time nessesary for proper washing of the sampling line and the injection loop. This drawback can be overcome by the use of the dual sampling line manifold with a six-port injector shown in Fig. 1. Two samplers are operated by the electronic control unit so that when one of the sample probes is dipped into the sample container, the other is dipped into the wash vessel, the sample to wash ratio being 1:1. Such a technique can be also realised with one sampler, equipped with two probes. Utilization of two sampling probes allows one of the sample lines to be washed while the other one is supplying the sample to the injector. With the pump positioned downstream the sample/wash solutions are aspirated directly into the injector loops. This prevents distortion of the concentration profile by the pump rollers and reduces the carry-over.

Two injection loops with identical volumes introduce sample slugs into the carrier stream in rotation; the third loop volume (black in Fig. 2) serves merely to wash one of the sample lines while the other one is supplying the sample solution to the injector. This three-loop operation mode with injection, sample loading and washing carried out simultaneously provides minimum injector downtime, thus increasing the sample throughput.

During the operation of the set-up shown in Fig. 1, each continuous sample slug downstream of the valve is separated from the next one by a series of carrier and air segments. An attempt to segment the sample stream before introducing it into the valve resulted in a decrease in the analysis rate, primarily owing to the decreased volume of sample passing through the flow cell. Moreover, with air segmentation of the sample stream aspirated into the valve a uniform sequence of air bubbles could not be obtained. Hence the method utilizing the injection of continuous (unsegmented) sample slugs into the air-segmented carrier stream was chosen for the flow analyser operation. In this instance the buffer solution introduced into the stream dilutes the sample and carrier in different ratios. This has no discernible effect on the performance of the flow analyser, however, because the calibration solutions and the samples are diluted in the same proportions and a higher buffer concentration in the carrier solution separating consecutive samples is of minor significance.

Distilled water containing 0.1 vol.% of the non-ionic surfactant Brij-35 was used as a carrier solution instead of a baseline solution containing constant dilute or concentrated background levels of the measured ions. The use of distilled water as a carrier reduces the cell wash time and increases the sample throughput; the variable baseline caused by this approach is analytically insignificant in some instances, as discussed previously [8,10].

Air segments were injected into the stream each time a pump roller left the platen using the dual pump tube method [11]. The parameters chosen for the flow system (Fig. 1) after optimization experiments are listed in Table 1.

The mixing coil consisted of eight turns of a 40 cm × 1.5 mm i.d. glass tube. The total flow-rate directed to the detector part of the cell was 5.12 ml min^{-1} including the air flow, which is the optimum value for the flow cell used [8]. The

TABLE 1

Parameters of the flow system

Volume injected	0.1 ml
Carrier flow-rate	1.56 ml min^{-1}
Air flow-rate (first tube)	2.77 ml min^{-1}
Air flow-rate (second tube)	1.56 ml min^{-1}
Segmentation frequency	2 s^{-1}
Buffer solution flow-rate	2.00 ml min^{-1}
Reference solution flow-rate	1.56 ml min^{-1}
Sampling time	5 s
Sampling line wash time	5 s
Sampling rate	720 h^{-1} (360^{-1} h for each probe)
Valve rotation frequency (= injection rate)	720 h^{-1}

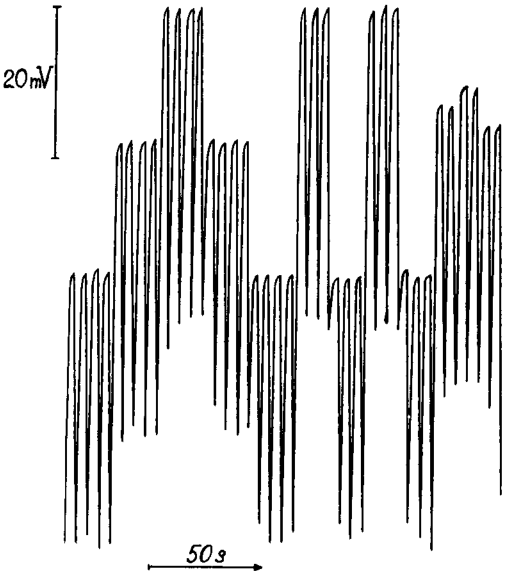

Fig. 3. Recordings of 2×10^{-5}, 4×10^{-5} and 8×10^{-5} M fluoride standards run in ascending and descending order followed by two interaction test patterns and duplicate determinations for water samples.

liquid level in the cell was kept constant by differential pumping with a flow-rate of 7.74 ml min^{-1}.

The performance of the proposed flow analyser was assessed by fluoride determinations in fluoridated drinking water. The calibration solutions contained 2×10^{-5}, 4×10^{-5} and 8×10^{-5} M fluoride, based on fluoride content recommended for the water after fluoridation [12]. Typical recordings for the analysis of aqueous fluoride standards in sets of four and three and fluoride determinations in water samples in duplicate are shown in Fig.3. With a sampling rate of 720 h^{-1} the calibration graph is linear and has a slope of 58 mV pF^{-1}, the relative standard deviation being better than 1%.

REFERENCES

1 E. Pungor, Z. Feher, G. Nagy and K. Toth, CRC Crit. Rev. Anal. Chem., 14 (1984) 175.
2 J. Ruzicka and E.H. Hansen, Flow Injection Analysis, Wiley, New York, 2nd ed., 1988.
3 G. Horvai and E. Pungor, CRC Crit. Rev. Anal. Chem., 17 (1987) 231.
4 E.H. Hansen and J. Ruzicka, J. Autom. Chem., 4 (1982) 193.
5 T. Buch-Rasmussen, Anal. Chem., 62 (1990) 932.
6 T. Buch-Rasmussen, Anal. Chim. Acta, 237 (1990) 405.
7 L.-C. Tian, X.-P. Sun, Y.-Y. Xu and Z.-L. Zhi, Anal. Chim. Acta, 238 (1990) 183.
8 J.A. Borzitsky, A.V. Dvinin, O.M. Petrukhin and Yu.I. Urusov, Anal. Chim. Acta, 258 (1992) 135.
9 C.J. Patton, M. Rabb and S.R. Crouch, Anal. Chem., 54 (1982) 1113.
10 J. Ruzicka, E.H. Hansen and E.A. Zagatto, Anal. Chim. Acta, 88 (1977) 1.
11 R.L. Habig, B.W. Schlein, L. Walters and R.E. Thiers, Clin. Chem. (Winston-Salem, N.C.), 15 (1969) 1045.
12 H.T. Dean, J. Am. Dent. Assoc., 52 (1956) 1.

Analytica Chimica Acta, 274 (1993) 129–140
Elsevier Science Publishers B.V., Amsterdam

Solid-phase extraction procedure for the determination of selenium by capillary gas chromatography

K. Johansson, U. Örnemark and Å. Olin

Department of Analytical Chemistry, University of Uppsala, P.O. Box 531, S-751 21 Uppsala (Sweden)

(Received 6th July 1992)

Abstract

A solid-phase extraction procedure to be used in the determination of selenium by gas chromatography with electron-capture detection (GC-ECD) was investigated. After derivatization of Se(IV) with 1,2-diamino-3,5-dibromobenzene the formed 4,6-dibromopiazselenol was adsorbed on a porous divinylbenzene polymer. Elution was performed with toluene. The proposed solid-phase extraction procedure was compared with a liquid–liquid extraction procedure and the overall efficiency was approximately 97% for sample volumes between 5 and 100 ml. Concordant results were obtained for natural water samples spiked with selenium between the GC-ECD procedure and a hydride generation atomic absorption spectrometric procedure. Removal of dissolved organic carbon in natural waters on XAD-8 and Dowex 1X8 prior to selenium determination was also studied.

Keywords: Atomic absorption spectrometry; Gas chromatography; Selenium; Solid-phase extraction; Waters

The low levels of Se(IV) present in natural waters [1–3] require analytical procedures having good accuracy at the ng l^{-1} level. Gas chromatography with electron capture detection (GC-ECD) [4–6] and hydride generation atomic absorption spectrometry (HG-AAS) [1,7] in conjunction with appropriate preconcentration steps are both suitable techniques for such determinations.

The determination of Se(IV) in water by GC-ECD is based on the formation of a volatile compound, a piazselenol, in the reaction between selenious acid and a substituted *o*-phenylenediamine. The piazselenol is normally extracted into an organic solvent before injection into the gas chromatograph. The extraction procedure makes it possible to preconcentrate the sample up to 500 times [8], leading to a detection limit below 1 ng l^{-1} of Se(IV) in the sample.

In the HG-AAS method, Se(IV) is reduced with sodium tetrahydroborate to volatile hydrogen selenide, which is collected at liquid nitrogen temperature. The preconcentrated hydrogen selenide is vaporized and selenium determined by AAS. The limit of detection is 1 to 2 orders of magnitude lower than for systems without preconcentration [9,10].

Both methods may be subject to interferences from dissolved organic material. In the HG-AAS method, Se(IV) and/or Se(VI) added to ground water [11], soil extracts [12–14] and extracts of biogenic material [15] have been lost. The interference is removed by wet digestion [11,12,15] but this prevents speciation. Another solution to this problem is to remove the interferent(s) on a sorbent before selenium determination. Roden and Tallman [11] demonstrated that the interferent, probably an organic constituent, could be

Correspondence to: K. Johansson, Department of Analytical Chemistry, University of Uppsala, P.O. Box 531, S-751 21 Uppsala (Sweden).

reversibly bound on the macroreticular polymeric resin XAD-8, while inorganic Se(IV) and Se(VI) were unretained. As reported by several authors [13–15], this sorbent will not always remove the interference completely.

In the GC-ECD method with liquid–liquid extraction, the main problem connected with the organic material is emulsion formation, making the phase separation time-consuming if not impossible. The interferences from organic material can be reduced by extracting the sample with an organic solvent or filtering it through a sorbent prior to the derivatization and liquid–liquid extraction. A sorbent can thus be used as a clean-up step in the GC-ECD method. However, it should also be possible to adsorb and collect the piazselenol from the aqueous phase. This technique is sometimes referred to as solid-phase extraction (SPE). SPE can be used to separate analyte and concomitants by adsorbing the former while the latter are unretained and is a special case of adsorption chromatography. In trace analysis, where SPE is used to accumulate the analyte, the distribution coefficient should be large for the analyte. It is also important that the adsorption capacity of the column is adequate, since the sample may contain other substances, that are also retained. Ideally, the analyte should be adsorbed as a narrow band at the top of the column, because then a short column can be used and the elution made in a small volume.

This paper reports on investigations of a SPE method in trace analysis of Se(IV) in water with GC-ECD. We also report on determinations with GC-ECD and HG-AAS of Se(IV) added to natural water, treated by filtration through XAD-8 or Dowex 1X8.

EXPERIMENTAL

Apparatus

For the gas chromatographic measurements a Shimadzu GC-14A gas chromatograph equipped with a constant current ^{63}Ni electron-capture detector was used. The column was DB-1701 (15 m × 0.25 mm i.d.) with a 0.25-μm film thickness (J&W Scientific). The chromatographic conditions were: carrier gas, helium at 40 cm s^{-1}; split vent, 60 ml min^{-1}; purge vent, 1 ml min^{-1}; make-up gas, nitrogen at 45 ml min^{-1}; injector temperature, 250°C; detector temperature, 325°C; and column temperature programme, 100°C held for 2 min, increased at 8°C min^{-1} to 175°C, held for 5 min, increased at 15°C min^{-1} to 265°C, held for 5 min.

The injections (0.5 μl sample + 1 μl toluene) were made in the splitless mode with a Shimadzu AOC-14 automatic injector, with a change to the split mode after 1 min. The peak areas were evaluated with a Shimadzu C-R5A integrator.

The HG-AAS apparatus with a cold trap is described elsewhere [7]. Hydride generation is accomplished by mixing the acidified sample with sodium tetrahydroborate in a flow system. The hydride is stripped from the aqueous phase and transported with nitrogen gas. Four glass U-tubes in series are used for gas–liquid separation, removal of water vapour and trapping of the hydride. Atomic absorption measurements were made with a Perkin-Elmer 3100 spectrometer equipped with the MHS-20 oven and containing a quartz cuvette at 800°C. The light source, an electrodeless discharge lamp, was operated at 7.6 W. The analytical wavelength was 196.0 nm and the spectral band-width 0.7 nm. Evaluation of peak areas and peak heights was made with the Model 3100 EDS software supplied by the manufacturer. No background correction was applied.

Determinations in the 1–10 μg l^{-1} range were performed with the HG-AAS instrumentation described by Pettersson et al. [9].

A Philips PU 8625 spectrophotometer equipped with a 40-mm flow through cell, a U4-XV peristaltic pump (Alitea AB) and a glass column, bed volume 1.1 ml, (Kabi-Pharmacia) were used in the study of the XAD-resins. The absorbance was measured at 420 nm.

Total dissolved organic carbon (TOC) in the water samples was determined on a Shimadzu 500 TOC analyzer by the National Environmental Protection Agency in Uppsala.

The equipment used for SPE is presented in Fig. 1. Five of these devices were connected in parallel to a water aspirator. The column (inner diameter 3/8″, volume 4 ml) was made of

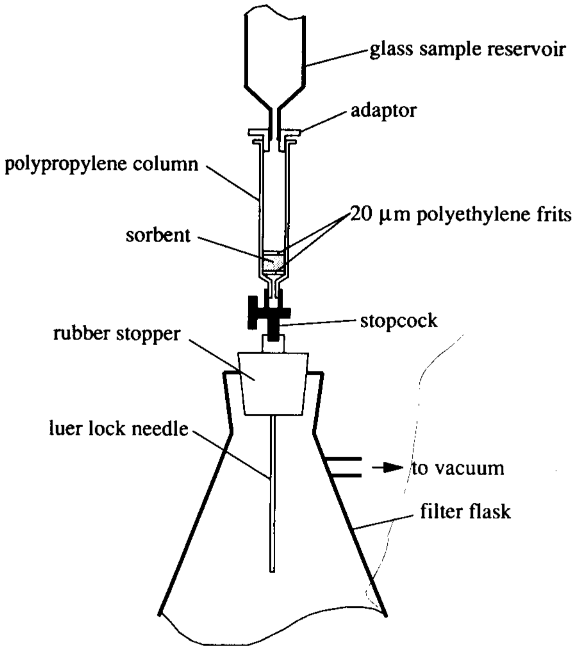

Fig. 1. Equipment used for solid-phase extraction.

polypropylene and contained two 20-μm polyethylene frits. The stopcock and adaptor were purchased from Analytichem (Harbour City, CA). The sample reservoir was made of glass.

The ion-exchanger tubes were made from Pyrex, length 200 mm, i.d. 8 mm and provided with a cylindrical funnel, length 70 mm and i.d. 42 mm, at the top. Flow was controlled by a clamp around a small piece of PVC tubing connected to the 1-mm drawn out tip. These tubes were also used in the recovery experiments for inorganic selenium on XAD-7 and XAD-8.

Chemicals and reagents

All chemicals were of analytical grade from Merck unless otherwise stated. Demineralized, destilled water passed through a Millipore 3 filter cartridge system, Milli-Q water, was used throughout. All glassware was cleaned in 4 M nitric acid and rinsed with Milli-Q water.

1,2-Diamino-3,5-dibromobenzene (Br_2-PDA). A 5.5 mM solution of Br_2-PDA in 0.5 M perchloric acid was prepared. The solution was purified by extraction with toluene and should preferably be kept in the dark. When 100 ml were extracted with 5 ml of toluene the Br_2-PDA concentration dropped to about 5.2 mM.

Selenium(IV). A stock standard solution, 1 g l^{-1} of Se(IV), was prepared from an ampoule of selenium dioxide in dilute nitric acid. Its concentration was checked by an amperometric titration with thiosulphate after addition of a large excess of iodide [16]. Working standard solutions were obtained by serial dilution of the stock standard solution and contained 2 ml l^{-1} of hydrochloric acid (37%, w/w).

Internal standard solution. This solution was prepared by dissolving lindane (99%) and aldrin (99%), both purchased from Applied Science Labs. (State College, PA), in toluene. The working solution contained 2.0 mg l^{-1} of lindane and 2.6 mg l^{-1} of aldrin.

Lindane and aldrin are insecticides and precautions should be taken to avoid inhalation and skin contact.

4,6-Dibromopiazselenol. This was synthesized according to the literature [5]. The synthesized piazselenol was analysed for selenium after wet digestion according to a variation of Gould's method [17] using a 10:1 (v/v) mixture of concentrated sulphuric acid and fuming nitric acid by the amperometric titration method mentioned above. The purity was 99.8 ± 0.4%. A stock standard solution containing 0.5 g l^{-1} of piazselenol was prepared by dissolving piazselenol in toluene. Working standard solutions were prepared by serial dilution with toluene.

Sodium tetrahydroborate. Sodium tetrahydroborate, 0.5% (w/v), was stabilized and purified as described elsewhere [7].

Hydrochloric acid. HCl, 37% (w/w), used in the cold trap system was diluted 1:1 and flushed with nitrogen prior to use.

Resins

Solid-phase extraction resin. The resin was a porous divinylbenzene polymer (PD-102-PE), 10 μm in diameter, with a narrow particle size distribution. It was supplied by Dyno Particles (Lillström) as a 10% (v/v) suspension in methanol. The resin was not further purified. The resin bed was packed as follows, see also Fig. 1. The upper

75-ml glass reservoir was detached, the stopcock closed and the frit at the bottom inserted. Since the particle size of the resin was 10 μm, a glass-fibre filter with a pore diameter of about 2 μm was inserted above the frit. The resin was added as a methanol slurry until the settled bed was approximately 4 mm. Then the second frit was inserted. The column was conditioned by draining the methanol followed by 5 ml of 0.25 M perchloric acid. The stopcock was closed when about 2 ml of perchloric acid were left above the upper frit, then the sample reservoir was attached. The column was effectively regenerated by passing 5 ml of methanol–perchloric acid (70–72%) (98 : 2) through the column. When not used, the column was filled with methanol and stored closed.

Ion-exchange resin. Dowex 1X8, (100–200 mesh analytical grade, Serva) was purchased from LabKemi (Stockholm). Fines were removed by decantation and the resin (100 g) was placed in a glass filter funnel and washed with 200 ml of 1 M sodium hydroxide added in portions followed by Milli-Q water to neutral. Conversion to the chloride form was achieved by passing 200 ml of 1 M hydrochloric acid followed by Milli-Q water. When no detectable chloride was found in the effluent the resin was dried over night at 50°C and then conditioned over calcium chloride hexahydrate and its saturated solution. A 2-g amount of the conditioned resin (dry weight) was slurried in a few ml of Milli-Q water and packed between plugs of quartz wool. The resin was washed with 10 ml of 1 M hydrochloric acid followed by Milli-Q water to approximately neutral effluent. Finally 25 ml of 0.025 M hydrochloric acid were passed through the column. The solution to be filtered was made 0.025 M with respect to hydrochloric acid and transferred to a volumetric flask. The flask was mounted upside down in the cylindrical funnel of the exchanger tube. The flow was adjusted to about 2 ml min^{-1}. The effluent was collected and analysed for Se(IV) and TOC.

XAD resins. XAD-2 (0.3–1 mm anal. gr.), XAD-4 (20–50 mesh pract.), XAD-7 (20–50 mesh pract.), XAD-8 (0.3–1 mm pract.), XAD-16 (13–80 mesh pract.) (Serva), were purchased from Techtum (Umeå). Fines were removed by decantation. The resin (100 g) was then slurried in 50 ml of methanol followed by addition of 50 ml of water. After deaeration with nitrogen gas the resin was stored refrigerated. A 7.5-ml column was prepared between plugs of quartz wool from the resin in the methanol–water (1 : 1) mixture. After washing of the resin with Milli-Q water to remove all methanol, 50 ml of 0.01 M hydrochloric acid were passed through the column. The solution to be filtered was made 0.01 M with respect to hydrochloric acid and passed through the column as described above at about 1 ml min^{-1}.

Solid-phase extraction of piazselenol

Standard procedure for the extractions. The Se(IV) was derivatized at room temperature or 100°C by adding Br_2-PDA to test solutions in 0.25 M perchloric acid so that the concentration became 0.1 mM. At room temperature the derivatization reaction was complete after 3 h and at 100°C after 5 min [6]. The SPE columns were conditioned as described above. The derivatized test solutions were passed through the columns at a flow-rate of 5 ml min^{-1} followed by 1.5 ml of 4 M perchloric acid. The columns were allowed to drain and were then spinned for 2 min to remove most of the liquid. The adsorbed piazselenol was eluted with 1 ml of toluene (flow-rate of 2 ml min^{-1}) into a test-tube with a PTFE-faced screw-cap containing 10 μl of the internal standard solution. The toluene eluate was washed with 1.5 ml of Milli-Q water and dried with anhydrous sodium sulphate prior to injection on the gas chromatograph.

Effect of sample volume. A stock standard solution containing 1 μg l^{-1} of Se(IV) in 0.25 M perchloric acid was prepared. Standard solutions were prepared by diluting 5-ml portions of the stock standard solution to 25, 50 and 100 ml with 0.25 M perchloric acid. The procedure from above was then followed. As a reference, a 5-ml portion of the stock standard solution was derivatized and extracted with 1 ml of toluene + 10 μl of the internal standard solution. The aqueous phase was discarded and the toluene phase was extracted with 1.5 ml of 4 M perchloric acid followed by 1.5 ml of Milli-Q water. Finally the toluene phase was dried with anhydrous sodium sulphate prior to injection.

Effect of sample flow-rate. 25-ml portions of a derivatized standard solution containing 200 ng l^{-1} of Se(IV) were passed through a conditioned SPE column at different flow-rates. The conditions were otherwise the same as described above.

Effect of elution flow-rate. 25-ml portions of the solution above [200 ng l^{-1} of derivatized Se(IV)] were passed through a conditioned SPE column at 5 ml min^{-1}. The flow-rate of toluene at the elution was varied, otherwise the conditions were the same as above.

Elution profile of piazselenol from the SPE column. 20 ml of a derivatized solution containing 10 $\mu g\ l^{-1}$ of Se(IV) were passed through a conditioned SPE column. The standard procedure was followed except at the elution, which was performed as follows. A total volume of 2.9 ml of toluene was passed through the column at a flow-rate of 2 ml min^{-1}. Fractions of approximately 0.5 ml were collected and diluted to 1 ml with toluene. The first fraction was further diluted 1:40. All volumes and dilutions were controlled by weighing.

Elution of excess of Br_2-PDA. 25 ml of derivatized standard solution, 160 ng l^{-1} of Se(IV), were passed through a conditioned SPE column at a flow-rate of 5 ml min^{-1} followed by 1.5 ml of either 0.25, 2, 4, 6 or 8 M of perchloric acid. Elution and analyses were performed according to the standard procedure.

Pretreatment of natural water samples

Natural water samples were collected as surface water from lakes and streams in the vicinity of Uppsala. After filtration through 0.45-μm membrane filter, samples were stored refrigerated in polyethylene bottles. Prior to the analysis 1 or 2 l portions of the samples were withdrawn, acidified to pH 2, spiked with selenite and deaerated with nitrogen. Each sample was then split into three equal portions of which two were subjected to the filtration procedures on XAD-8 and Dowex 1X8, respectively, as described above. Finally, the two effluents and untreated sample were analysed for Se(IV) with GC-ECD and HG-AAS and in addition analysed for TOC.

Determination of Se(IV) with GC-ECD

Sample preparation. 25 ml of the pretreated sample and 0.5 ml of perchloric acid (70–72%) were added to a conical flask. The flask was placed on an ordinary hot-plate and removed as soon as the sample started to boil. Immediately 0.5 ml of 5.2 mM Br_2-PDA was added and the mouth of the conical flask was covered with a watch-glass. The piazselenol formation was complete after 5 min and the sample was cooled to room temperature in a water bath.

Solid-phase extraction. The sample was quantitatively transferred to the sample reservoir and the sample was passed through the conditioned column at a flow-rate of 5 ml min^{-1}. When most of the sample had passed the column and the liquid level had reached the top of the sorbent, the stopcock was closed. The sample reservoir was detached and 1.5 ml of 4 M perchloric acid were added. The column was allowed to drain and then spinned for 2 min to remove most of the liquid. One ml of toluene was added to the column. A syringe was used to supply the pressure needed for the toluene to pass through the column. The effluent was collected in a test tube containing 10 μl of the internal standard solution and equipped with a PTFE-faced screw-cap. The toluene phase was washed with 1.5 ml of Milli-Q water (rapid phase separation was obtained by spinning the test-tube) and dried by adding anhydrous sodium sulphate prior to injection on the gas chromatograph.

Liquid–liquid extraction. The extraction was performed as described in Ref. 6.

Determination of Se(IV) with HG-AAS

To 25 ml of the sample containing < 5 ng of selenium, 5 ml of deaerated 6 M hydrochloric acid were added. The hydride trap was immersed into the liquid nitrogen and 30 s allowed for lowering of the temperature. The peristaltic pump was turned on. When the sample followed by small portions of 1 M hydrochloric acid to rinse the tubings had been consumed after 3 min, the pump was stopped. After 10 s the hydride was released by replacing the liquid nitrogen with ethanol at −15°C and the measuring cycle of the spectrometer was initiated. The cold ethanol was not removed until the whole peak had been monitored.

RESULTS AND DISCUSSION

Selection of solid-phase extraction sorbent

The selection of the SPE sorbent depends on the application. The two, perhaps, most commonly used types of sorbents today are bonded-phase silica and macroreticular polymeric resins. The bonded-phase sorbents based on silica particles have a limited working pH range, approximately between 2 and 7.5. Above pH 7.5, the silica substrate is susceptible to dissolution in aqueous solutions. Below pH 2 the silyl ether linkage is labile and the functional groups on the surface will begin to cleave, changing the sorptive properties in a non-reproducible fashion. The polymeric resins, on the other hand, are almost unaffected by extremes of pH.

The formation of the piazselenol occurs in a reaction between undissociated selenious acid and the monoprotonated diamine, and the derivatization should therefore be carried out at a pH where these species predominate. When Se(IV) is derivatized with Br_2-PDA, the reaction is carried out in 0.25 M perchloric acid [6]. This reaction medium makes polymeric resins best suited for the SPE.

The resin used, PD-102-PE, is a porous divinylbenzene polymer. It has a small particle size, 10 μm, which gives good mass transfer properties, and a narrow size distribution so that no problems with backpressure were experienced. No other sorbent was studied in detail.

Equipment used for the solid-phase extractions

The piazselenol does not adsorb only on the resin (divinylbenzene polymer) used, but also on other common polymeric materials. Different materials were cut into pieces and added to conical flasks together with an aqueous solution of derivatized Se(IV). The flasks were shaken for 3 h and the solution analysed. The results are presented in Table 1. The piazselenol was adsorbed on all the investigated materials except PTFE and glass. This makes the choice of material in the extraction equipment important. The equipment is presented in Fig. 1. The sample reservoir is made of glass to reduce the risk of loss of piazselenol due to adsorption on the walls. The column is made of polypropylene. However, when toluene was added to elute the adsorbed piazselenol from the sorbent, the wall of the column was also rinsed with the eluent.

TABLE 1

Adsorption of piazselenol on different materials
[Solutions of derivatized Se(IV) were shaken together with different materials cut into small pieces. The determination of Se(IV) was made after 3 h]

Material	Recovery (%)
PVC	4
Polyethylene	40
Polypropylene	70
Silicone	4
PTFE	99
Glass	96

Solid-phase extraction of piazselenol

The detection limit of a procedure for trace determination in water with a preconcentration step will depend on the enrichment factor. Since Se(IV) is often present at concentration below 100 ng l^{-1} in natural waters [1–3], considerable preconcentration might be necessary from a large sample volume. When SPE is used in trace analysis it is important that the rate of the sorption process is also fast at low analyte concentrations. If the sorption is slow, there should be a trend towards lower recoveries when the concentration of Se(IV) is decreased. Table 2 contains results on the SPE of 5 ng of Se(IV), derivatized at different temperatures and in different sample volumes. The results are presented as the ratio, R, between the peak areas of the piazselenol and the internal standard. The data in Table 2 do not indicate a trend in recovery with sample volume.

In a previous study [6] it was shown that the time for the derivatization reaction could be reduced from 3 h to 5 min by raising the temperature to 100°C. No adverse effects on the chromatograms were observed from the increase in derivatization temperature. To verify this obser-

TABLE 2

Effect of sample volume on solid-phase extraction of piazselenol

[5 ng of Se(IV) were added to 5, 25, 50 and 100 ml of 0.25 M perchloric acid and derivatized at 22°C or 100°C by adding Br_2-PDA to a concentration of 0.1 mM. The reference consisted of 5 ng of Se(IV) derivatized in 5 ml of 0.25 M perchloric acid and extracted with 1 ml of toluene. *R* is the ratio between the areas of the piazselenol and the aldrin peaks]

V_{tot} (ml)	[Se(IV)] ($ng\ l^{-1}$)	*R*	
		22°C	100°C
5	1000	1.055, 1.041	1.081, 1.048
25	200	1.054, 1.036	1.075, 1.064
50	100	0.982, 1.055	1.098, 1.046
100	50	1.048, 1.058	1.010, 1.012
Ref.	1000	1.098, 1.057	1.081, 1.090

vation for SPE, the derivatization was run at the two temperatures in parallel. No adverse effects were observed on the chromatograms or the performance of the SPE column. The values of *R* obtained with derivatization at 22°C, $R = 1.041 \pm 0.025$, and 100°C, $R = 1.054 \pm 0.032$ (mean ± S.D., $n = 8$), are not significantly different. These values are, however, lower than for the reference, $R = 1.082 \pm 0.018$. Since the recovery of derivatized Se(IV) at liquid–liquid extraction was earlier found to be nearly 100% [6], the difference in the *R* values indicates incomplete recovery of Se(IV) with the SPE procedure.

Further, the influence of sample flow-rate on the recovery of derivatized Se(IV) was investigated. The results are presented in Table 3. No influence of flow-rate on the recovery could be established. A flow-rate of 5 ml min^{-1} was used in most experiments.

TABLE 3

Effect of flow-rate on the adsorption of piazselenol

[25 ml of a solution containing 200 ng l^{-1} of derivatized Se(IV) were passed through an SPE column at different flow-rates. *R* is the ratio between the areas of the piazselenol and the aldrin peaks]

Flow-rate (ml min^{-1})	*R*
1.8	1.026, 1.089
4.2	1.041, 1.058
5.0	1.053, 1.063
6.1	1.061, 1.075
7.5	1.063, 1.075

TABLE 4

Effect of flow-rate on the desorption of piazselenol

[25 ml of a solution containing 200 ng l^{-1} of derivatized Se(IV) were passed through an SPE column. The flow-rate at the desorption of piazselenol with toluene was varied. *R* is the ratio between the areas of the piazselenol and the lindane peaks]

Flow-rate (ml min^{-1})	*R*
0.3	1.082
1	1.051
1.3	1.086
3	1.066

The adsorbed piazselenol from the SPE column was eluted with toluene. Toluene was successfully used in the liquid–liquid extraction of piazselenol [6] and was therefore chosen in the SPE. No other organic solvents were investigated. The flow-rate of toluene does not effect the recovery in the investigated range, Table 4. The elution profile exhibits some tailing, but when 2.9 ml had passed the column, approximately 98.5% of the piazselenol had been eluted in the first 0.6 ml of toluene, Table 5. One ml of toluene was added to the columns in all experiments and since the void volume of the column was approximately 0.15 ml, 0.85 ml passed through the column.

TABLE 5

Elution profile of desorbed piazselenol

[20 ml of a solution containing 10 $\mu g\ l^{-1}$ of derivatized Se(IV) were passed through an SPE column. The column was eluted with toluene and fractions of about 0.5 ml were collected and analysed. *R* is the ratio between the areas of the piazselenol and lindane peaks]

Total eluate volume (ml)	*R*
0.58	49.071 [a]
1.13	0.330
1.58	0.154
1.99	0.114
2.44	0.094
2.93	0.036

[a] The first fraction was diluted 1:40 before injection on the gas chromatograph. The calculated area ratio is compensated for the dilution.

The reason for the use of two internal standards, lindane and aldrin, was due to the fact that in some experiments a compound with a retention close to lindane appeared, which made the evaluation difficult. The use of aldrin as internal standard, instead of lindane, solved the problem. Aldrin is not back-extracted by 1.5 ml of 4 M perchloric acid followed by 1.5 ml of Milli-Q water or 5 ml of 0.25 M perchloric acid. Later, the origin of the interfering compound was fully investigated and traced to contaminated perchloric acid.

Clean-up procedure in the SPE method

With liquid–liquid extraction it has been reported that the piazselenol reaction yields byproducts, which together with excess of reagent, result in chromatographic peaks that may overlap the piazselenol peak [5,8,18]. However, no interference was observed when a capillary GC column was used [6]. Piazselenol and lindane were well separated from the byproducts and the reagent. However, a clean-up step could be included in order to minimize broad peaks from the reagent that appeared after the piazselenol peak [6]. In the clean-up step, the toluene phase was washed once with 6 M perchloric acid.

The same reagent peaks appeared in the SPE method. By treating the SPE column with perchloric acid before elution of the adsorbed piazselenol, these peaks were diminished. The effect of the concentration of perchloric acid on both the ligand peaks and the piazselenol peak was investigated by adding 0.25, 2, 4, 6 or 8 M perchloric acid to the column, Table 6 and Fig. 2. A higher concentration of perchloric acid yielded a cleaner chromatogram but when the concentration exceeded 6 M, losses of piazselenol were observed. This might be due to protonation of the piazselenol [19], changing the sorptive properties. Since the difference in the appearance of the chromatograms from columns treated with 4 or 6 M perchloric acid was small, 4 M perchloric acid was used.

TABLE 6

Clean-up step with perchloric acid

[25 ml of a solution containing 160 ng l^{-1} of derivatized Se(IV) were passed through an SPE column. The column was washed with 1.5 ml of a solution of perchloric acid before elution. *R* is the ratio between the areas of the piazselenol and the lindane peaks]

$HClO_4$ (M)	*R*
0.25	1.011, 1.019
2	1.005, 1.017
4	1.046, 1.014
6	0.950, 1.066
8	0.740, 0.676

Calibration of the SPE method

In the liquid–liquid extraction procedure it was possible to use standard solutions of synthesized piazselenol for calibration purpose, since there was good agreement between calibration graphs obtained from these solutions and derivatized standard solutions of Se(IV) [6]. In the proposed SPE method the recovery of Se(IV) is approximately 96–98% with the liquid–liquid extraction method as reference, Fig. 3. Consequently, the calibration should be carried out with standards of Se(IV) treated the same way as the sample. It should, however, also be possible to use standard solutions of synthesized piazselenol for calibration purpose if, in addition, one or two Se(IV) standards are analysed with the same procedure as the samples. The standards are evaluated with the calibration graph obtained from the synthesized piazselenol and the recovery calculated. The results from the samples are then corrected for the recovery.

Choice of XAD resin for removal of dissolved organic carbon

The uptake of organic matter was followed by pumping the fresh water sample through a column of the resin and measuring the absorbance at 420 nm. This experiment was similar to that described by Aiken et al. [20] for XAD-1, 2, 4, 7 and 8. According to the authors, fulvic acids are a major part of the coloured organic compounds present in natural waters. They found that resins based on styrene divinylbenzene copolymers (XAD-1, 2, 4 and 16) were less suitable than those based on acrylic ester polymers (XAD-7 and 8) for adsorption of fulvic acids. This was confirmed in our study. The degree of adsorption increased in the order XAD-4, 16, 2, 7 and 8. The position of XAD-16 is in agreement with the discussion in [20] on the influence of pore size and surface area on adsorption. Only small differences were noted between XAD-7 and XAD-8. The latter resin is known not to retain inorganic

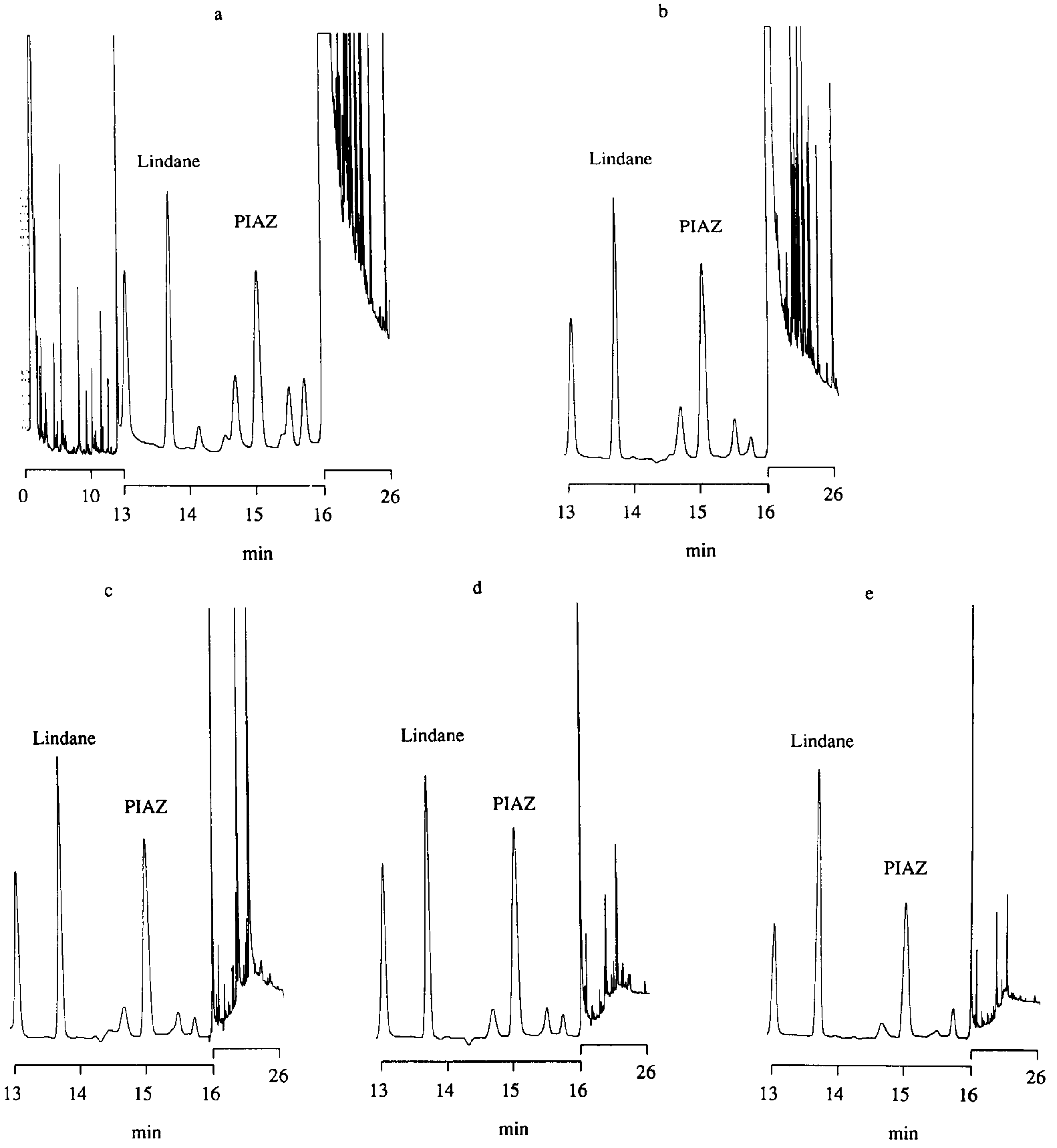

Fig. 2. Chromatograms of toluene eluates. 25 ml of a derivatized standard solution, 160 ng l^{-1} of Se (IV), were passed through an SPE column followed by cleaning with 1.5 ml of (a) 0.25 M, (b) 2 M, (c) 4 M, (d) 6 M or (e) 8 M of perchloric acid. In (a) the complete chromatogram is shown and in the others only the analytically relevant parts.

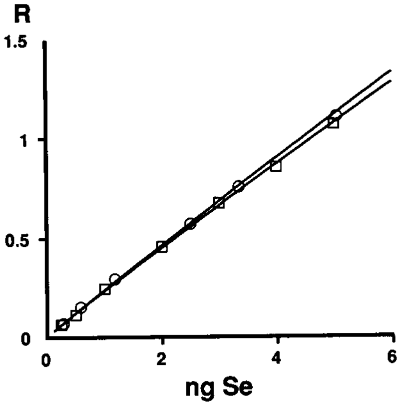

Fig. 3. Calibration graphs. R is the ratio between the areas of the piazselenol and the aldrin peaks. Results from (○) synthesized piazselenol standards and (□) 25 ml of derivatized selenium(IV) solutions passed through an SPE column.

selenium [11,13]. This was found to be the case also for XAD-7 at μg l^{-1} and ng l^{-1} levels (Table 7). XAD-8 was used in the subsequent filtration experiments since it is reported [20] not to suffer from bleeding as XAD-7 does. Blank levels of TOC were low, < 0.5 mg l^{-1} and 0.8 mg l^{-1} for XAD-8 and Dowex 1X8, respectively, using a 500-ml solution. Results from absorption measurements and TOC analysis of column effluents are presented in Table 8. The percentage of total organic carbon removed hardly exceeds 50%, whereas coloured material is adsorbed more effectively. A study of the behaviour of inorganic Se(IV) and Se(VI) on Dowex 1X8 is in progress in our laboratory. Under the conditions used in this work, i.e., addition of hydrochloric acid to 0.025 M, Se(IV) passes through the column while Se(VI) is retained. Our results indicate that the ion-exchange resin is as effective as XAD-8 for removal of coloured organics and other dissolved organic compounds. It can thus be an attractive alternative to XAD-7 and 8 since Se(IV) and (VI) can be separated at the same time as organic matter is removed.

TABLE 8

Adsorption of coloured organics and total dissolved organic material from water samples on Dowex 1×8 and XAD-8 [Coloured organics were determined by spectrophotometric measurements at 420 nm. Sample volume 330 ml (670 ml for sample V)]

Sample	TOC (mg l^{-1})	XAD-8		Dowex 1X8	
		Coloured (%)	TOC (%)	Coloured (%)	TOC (%)
(I) Lafssjön	26.1	89	61	69	52
(II) Sävjaån	17.4	85	52	93	45
(III) Ramsen	13.3	86	11	96	47
(IV) Trehörningen	15.1	83	16	94	46
(V) Flottsund	15.6	84	49	92	61

Determination of Se(IV) in spiked water

The five fresh water samples were not acidified on storage. Speciation changes and adsorption losses are therefore likely to have occurred [21]. The decrease in Se(IV) concentration for sample I after three months of storage was approximately 30% (Tables 9 and 10). Preliminary measurements indicated that the concentrations of Se(IV) were just a few nanograms per litre.

TABLE 7

Recovery of inorganic selenium (average and standard deviation) in 0.01 M hydrochloric acid after filtration through XAD-7 and XAD-8

(250 ml of a solution with inorganic selenium were passed through a 7.5 ml bed of XAD. The effluent was collected as 25 ml fractions and analysed for selenium using HG-AAS)

	XAD-7				XAD-8			
	Se(IV)		Se(VI)		Se(IV)		Se(VI)	
[Se]/(μg l^{-1})	2.00	0.040	2.00	0.060	2.00	0.040	2.00	0.080
Recovery (%)	94 ± 4	96 ± 5	101 ± 3	106 ± 10	100 ± 1	104 ± 3	102 ± 2	102 ± 6
Fractions analysed	9	5	9	5	9	7	8	7

TABLE 9

Determination of Se(IV) in water samples with GC-ECD
[Average and standard deviation (ng l^{-1}) from triplicate analysis SPE = Solid-phase extraction; Extr. = liquid–liquid extraction]

Sample	Added Se(IV) (ng l^{-1})	No pretreatment		XAD-8		Dowex 1X8	
		SPE	Extr.	SPE	Extr.	SPE	Extr.
(I) Lafssjön	80 [a]	54 ± 2	54 ± 3	54 ± 1	54 ± 2	53 ± 2	57 ± 1
(II) Sävjaån	60	57 ± 1	59 ± 2	58 ± 2	56 ± 2	57 ± 4	55 ± 1
(III) Ramsen	40	37 ± 2	41 ± 1	39 ± 3	41 ± 1	42 ± 3	42 ± 1
(IV) Trehörningen	20	18 ± 2	19 ± 1	19 ± 2	21 ± 1	18 ± 1	20.0 ± 0.2
(V) Flottsund	0	2.6 ± 0.3	3.3 ± 0.6	2.8	4.2 ± 0.1	3.1 ± 0.7	3.8 ± 0.2

[a] Se(IV) added 3 months prior to analysis.

The samples were therefore spiked with Se(IV) to concentration levels, where differences between methods and treatments could be better detected.

Analysis were carried out within 24 h after spiking. Determinations with the GC-ECD method and the HG-AAS method were performed by different persons.

GC-ECD. The water samples were analysed by the SPE and the liquid–liquid extraction methods and the results are presented in Table 9. There is no significant difference ($p = 0.05$) in the Se(IV) concentrations or in the precision between filtered or unfiltered samples. Selenium(IV) concentrations obtained with the two extraction methods indicate a somewhat higher mean value for the liquid–liquid extraction procedure but this difference is not significant. The major effect of the filtration of the water through XAD-8 or Dowex 1X8 was the faster and more distinct phase separation in the liquid–liquid extraction procedure. In the solid-phase extractions the same columns were used for samples that had been treated in the same way, e.g., all unfiltered samples passed through the same SPE columns. The regeneration of the columns appeared to work effectively. No accumulation of adsorbed coloured organic material was observed on either column and no deterioration in performance was noted after 15 loadings. Consequently, there appears to be no need to prefilter the samples through an adsorbing resin in the SPE method.

HG-AAS. Standard additions of Se(IV) were made to the unspiked waters and the slopes of the standard additions graphs were compared with the sensitivity determined from standards. No differences were found and subsequently the calibration graph was used in the evaluation of the Se(IV) concentrations. The results are given in Table 10. Significant higher results ($p = 0.05$) were noted for subsamples filtered through Dowex 1X8 despite the fact that this was not the general observation. Evaluations from peak height

TABLE 10

Determination of Se(IV) in water samples with HG-AAS
[Average and standard deviation (ng l^{-1}) from triplicate analysis. ND = Not detected]

Sample	Added Se(IV) (ng l^{-1})	No pretreatment		XAD-8		Dowex 1X8	
		Peak area	Peak height	Peak area	Peak height	Peak area	Peak height
(I) Lafssjön	80 [a]	59 ± 1	55 ± 2	59 ± 5	56 ± 2	58 ± 2	57 ± 3
(II) Sävjaån	60	62 ± 4	61 ± 4	58 ± 6	58 ± 2	65 ± 4	66 ± 2
(III) Ramsen	40	43 ± 2	43 ± 1	44 ± 1	44 ± 1	47 ± 3	47 ± 1
(IV) Trehörningen	20	23 ± 3	20.8 ± 0.4	21 ± 2	21.1 ± 0.5	23 ± 4	21.7 ± 0.4
(V) Flottsund	0	ND	1 ± 1	ND	2 ± 1	3 ± 2	4.5 ± 0.3

[a] Se(IV) added 3 months prior to analysis.

or peak area gave the same results, indicating the absence of volatile compounds causing spectral interferences [7].

Analysis of variance was performed on the results in Tables 9 and 10. There is a small but significant difference ($p = 0.05$) between the results obtained with the two methods. The over-all mean was 37.4 ng l^{-1} with the HG-AAS method compared to 34.8 for the GC-ECD method. It is noticeable that the analysis by HG-AAS generally gave a Se(IV) concentration higher than the spiked level of the samples while the results obtained with the GC-ECD method were somewhat lower. The reason for this difference is not known to the authors.

Conclusions

Solid-phase extraction using a polymeric sorbent can replace the liquid–liquid extraction of the piazselenol in the determination of Se(IV) in natural waters with GC-ECD. The SPE is less time-consuming than the liquid–liquid extraction and makes it possible to run several samples simultaneously. Problems with emulsion formation and/or precipitation of organic substances in the boundary layer between the two phases that sometimes occur in liquid–liquid extraction, are not present in SPE.

Removal of dissolved organic material is most effective on XAD-7 or XAD-8 which in addition do not retain inorganic selenium. The use of Dowex 1X8 allows a separation of inorganic Se(IV) and Se(VI) and it adsorbs dissolved organics as effectively as the XAD resins. Concordant result were obtained between GC-ECD and HG-AAS for fresh water samples spiked with Se(IV) at the ng l^{-1} level.

Thanks are due to Dynochrom Sweden Inc. for supplying the solid-phase extraction resin. This work has partly been supported by the Swedish Environmental Protection Board.

REFERENCES

1 G.A. Cutter, Anal. Chim. Acta, 98 (1978) 59.
2 H. Uchida, Y. Shimoishi and K. Tôei, Environ. Sci. Technol., 14 (1980) 541.
3 D. Tanzer and K.G. Heumann, Anal. Chem., 63 (1991) 1984.
4 S. Nakashima and K. Tôei, Talanta, 15 (1968) 1475.
5 Y. Shimoishi, J. Chromatogr., 136 (1977) 85.
6 K. Johansson and Å. Olin, J. Chromatogr., 589 (1992) 105.
7 U. Örnemark, J. Pettersson and Å. Olin, Talanta, 39 (1992) 1089.
8 Y. Shimoishi and K. Tôei, Anal. Chim. Acta, 100 (1978) 65.
9 J. Pettersson, L. Hansson and Å. Olin, Talanta, 33 (1986) 249.
10 V.E. Negretti de Brätter, P. Brätter and A. Tomiak, J. Trace Elem. Electrolytes Health Dis., 4 (1990) 41.
11 D.R. Roden and D.E. Tallman, Anal. Chem., 54 (1982) 307.
12 S.M. Workman and P.N. Soltanpour, Soil Sci. Soc. Am. J., 44 (1980) 1331.
13 J.L. Fio and R. Fujii, Soil Sci. Soc. Am. J., 54 (1990) 363.
14 M.M. Abrams and R.G. Burau, Commun. Soil Sci. Plant Anal., 20 (1989) 221.
15 G.A. Cutter, Anal. Chem., 57 (1985) 2951.
16 T.A. Bengtsson, unpublished results.
17 E.S. Gould, Anal. Chem., 23 (1951) 1502.
18 T. Stivje and G. Philippossian, Trav. Chim. Aliment. Hyg., 69 (1978) 74.
19 J. Nève, M. Hanocq and L. Molle, Microchim. Acta, 1 (1980) 41.
20 G.R. Aiken, E.M. Thurman and R.L. Malcolm, Anal. Chem., 51 (1979) 1799.
21 G.A. Cutter, Report EPRI EA-4641, Volume 1, June 1986.

Analytica Chimica Acta, 274 (1993) 141–146
Elsevier Science Publishers B.V., Amsterdam

Liquid–liquid extraction of transition metal ions with macrocyclic Schiff bases containing phenol or thiophene subunits

Shigeki Abe, Tyo Sone, Kazuhito Fujii and Masatoshi Endo

Department of Material Science and Engineering, Applied Chemistry Section, Yamagata University, 992 Yonezawa (Japan)

(Received 11th August 1992; revised manuscript received 13th October 1992)

Abstract

Two types of macrocyclic Schiff bases containing either thiophene or phenol subunits were synthesized and the effect of ligand atoms on the liquid–liquid extraction of bivalent transition metal ions was studied. The phenol groups in the macrocycle led to a large increase in the extraction of transition metal ions. The least stable manganese(II) complex was extracted quantitatively into nitrobenzene as an ion pair with tetraphenylborate ion at pH 9. Copper(II) was selectively extracted from weakly acidic media, permitting its separation from manganese(II), cobalt(II), nickel(II) and zinc(II). The composition of extracted copper(II) species was evaluated. The extractability of metal complexes with a cyclic tetraaza Schiff base has been compared with that of the corresponding acyclic Schiff base.

Keywords: Extraction; Schiff bases; Transition metal ions

In recent years an increasing number of macrocyclic compounds with oxygen, nitrogen and/or sulphur ligand atoms have been synthesized and their potential usefulness as an analytical extractant for hard and soft metal ions has been evaluated. Oxygen-containing crown ethers are mainly used for alkali and alkaline earth metal ion extraction, whereas thiacrown ethers are dedicated to the extraction of soft metal ions. Macrocyclic polyamines, possessing reactive secondary amines as the ligand, form stable cationic complexes with various metal ions. The most popular reagents of this class are tetraaza and hexaaza crown ethers. These compounds have been utilized for the extraction and spectrophotometric determination of silver(I), copper(II), zinc(II), cadmium(II), lead(II) and mercury(II) [1–4]. The kinetics of metal complexation, however, revealed that an increase in the size of macrocyclic amines is accompanied by a decrease in the reaction rate constant [5]. Thus, the slow complexation of metal ion with hexacyclene necessitated preheating for the quantitative extraction of most metal ions [4]. The use of polyoxa–polyaza crown ethers and macrocyclic formazans has also been investigated from analytical point of view [6–8].

In contrast, applications of macrocyclic Schiff bases to the extraction of transition metals have been restricted. Zolotov and co-workers [9,10] synthesized fifteen- and nineteen-membered polyoxa–polyaza Schiff bases for the liquid–liquid extraction of metal ions. The reagents showed high selectivity for silver(I). Fujiwara et al. [11] synthesized tetraaza Schiff bases and applied them to the extraction of copper(II). Recently, the extraction behaviour of copper(II) complexes with macrocyclic tetraaza Schiff bases has been reported [12].

Correspondence to: S. Abe, Department of Material Science and Engineering, Applied Chemistry Section, Yamagata University, 992 Yonezawa (Japan).

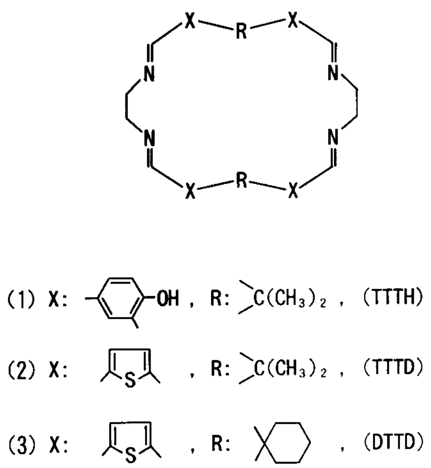

Fig. 1. Macrocyclic Schiff bases used as extractants for transition metal ions.

In this work, three novel macrocyclic Schiff bases containing thiophene or phenol subunits were designed (see Fig. 1) and tested for the ion-pair extraction of transition metals. The macrocycles, 12,12,27,27-tetramethyl-31,32,33,34-tetrathia-3,6,18,21-tetraazapentacyclo[26.2.1.$1^{8,11}$.$1^{13,16}$.$1^{23,26}$]tetratriaconta-1(30),2,6,8,10,13,15,17,21,23,25,28-dodecaene (TTTD), 12,27-dicyclohexyl-31,32,33,34-tetrathia-3,6,18,21-tetraazapentacyclo[26,2,1,$1^{8,11}$.$1^{13,16}$.$1^{23,26}$]tetratriaconta-1(30),2,6,8,10,13,15,17,21,23,25,28-dodecaene (DTTD) and 13,13,30,30-tetramethyl-9,17,26,34-tetrahydroxy-3,6,20,23-tetraazapentacyclo[29.3.1.$1^{8,12}$.$1^{14,18}$.$1^{25,29}$]octatriaconta-1(34),2,6,8,10,12,14,16,18,19,23,25,27,29,31,33-hexadecaene (TTTH) were used with tetraphenylborate (TPB) as the counter anion. The extractability of metal complexes by the cyclic tetraaza Schiff base was also compared with that of the corresponding acyclic Schiff base. These ligand molecules are effective extractants for manganese(II), nickel(II), cobalt(II), copper(II) and zinc(II). The phenol groups in the TTTH imparted considerable stability to the transition metal complexes. Thus the manganese (II)–TTTH complex, one of the least stable complexes of TTTH with transition metals, was quantitatively extracted into nitrobenzene. Copper(II) was selectively extracted from weakly acidic media, permitting the separation of copper from associated transition metals.

EXPERIMENTAL

Reagents and apparatus

All reagents were of analytical-reagent grade. Standard solutions of manganese(II), cobalt(II), nickel(II), copper(II) and zinc(II) were prepared by diluting the Standard Solutions for Atomic Absorption Spectrometry (Cica-Merck, 1000 μg ml^{-1}) with water. Solutions of extractants were prepared by dissolving appropriate amounts of macrocyclic Schiff bases in nitrobenzene. The counter-ion solutions (1.2×10^{-2} M) were prepared from sodium tetraphenylborate. Acetate buffer (pH 3–6) and borate buffer solutions (pH 7–11) were used. The ionic strength (0.1 M) was adjusted with sodium sulphate solution.

A Hitachi Model 180-80 atomic absorption spectrometer (acetylene–air flame) was used to determine the concentration of metal ions. The pH of aqueous phase was measured with a Toa HM-26S pH meter.

Preparation of macrocyclic Schiff bases

TTTD, a macrocyclic Schiff base containing thiophene subunits, was prepared according to the non-plate method described by Sone et al. [13]. Briefly, 2,2-bis(5-formyl-2-thienyl)propane and 1,2-diaminoethane were simultaneously added to chloroform solution over a period of 15 h while stirring and the solution was further stirred for 30 h at room temperature. The crude product was recrystallized with chloroform–hexane to give TTTD. The yield of TTTD was about 85%; yellow powder, m.p. 233–236°C. Mass spectrum (70 eV), m/z 576 (M$^+$); ^{1}H NMR (CDCl$_3$, 60 MHz), $\delta = 1.80$ (12H, s), 3.79 (8H, s), 6.74 (4H, d, $J = 3.6$ Hz), 6.99 (4H, d, $J = 3.6$ Hz) and 8.18 (4H, s); ^{13}C NMR (CDCl$_3$), $\delta = 32.41$, 40.92, 61.07, 123.61, 130.04, 155.83 and 158.09.

Macrocyclic DTTD and TTTH were prepared in a similar manner to TTTD. DTTD was prepared by the reaction of 1,1-bis(5-formyl-2-thienyl)cyclohexane with 1,2-diaminoethane. The product was dissolved in CDCl$_3$ and reprecipitated with hexane to give DTTD as a pale yellow powder, m.p. 230–232°C. Mass spectrum (70 eV), m/z 656 (M$^+$); ^{1}H NMR (CDCl$_3$, 60 MHz), $\delta = 8.17$ (4H, s), 6.98 (4H, d, $J = 4.0$ Hz), 6.71

TABLE 1

Effect of solvents on copper(II) extraction [a]

Solvent	Extraction (%)
Nitrobenzene	> 99
1-Nitropropane	95.2
2-Nitropropane	70.7
Chloroform	73.7

[a] [TTTD] = 1.0×10^{-3} M in the solvent; [Cu^{2+}] = 1.57×10^{-4} M; [TPB] = 2×10^{-3} M (pH 9).

(4H, d, $J = 4.0$ Hz), 3.75 (8H, s), 2.0–2.5 (8H, br s) and 1.3–1.5 (12H, br s). TTTH was prepared by the reaction of 2,2-bis(3-formyl-4-hydroxyphenyl)propane with 1,2-diaminoethane. The product was recrystallized from benzene as a pale yellow powder, m.p. 231–234°C. Mass spectrum (70 eV), m/z 616 (M^+); ^1H NMR ($CDCl_3$, 60 MHz), $\delta = 8.32$ (4H, s), 6.7–7.3 (12H, m), 3.82 (8H, s) and 1.55 (12H, s).

Preparation of acyclic Schiff base

Acyclic *N,N′*-bis{2-[1-(2-thienyl)cyclohexyl]-5-thenylidene}ethylenediamine (TED) was prepared as follows: a solution of 1,2-diaminoethane in $CDCl_3$ was added to a solution of 2 mol eq. of 1-(5-formyl-2-thienyl)-1-(2-thienyl)cyclohexane in $CDCl_3$ (100 ml) at room temperature. After stirring for 7 h, the mixture was concentrated to dryness. The residual mass was recrystallized from benzene–hexane to afford TED as pale yellow crystals, m.p. 151–152°C. Mass spectrum (70 eV), m/z 576 (M^+); ^1H NMR ($CDCl_3$, 60 MHz), $\delta = 8.20$ (2H, s), 6.7–7.3 (10H, m), 3.80 (4H, s), 2.1–2.5 (8H, br s) and 1.3–1.8 (12 H, br s).

Extraction procedures

To 1.00 ml of the sample solution (less than 50 μg of metal ion) in a 10-ml glass-stoppered tube, the following solutions were added: 1 ml of 0.05 M borate buffer solution (pH 9), 1 ml of 0.167 M sodium sulphate solution, 1 ml of 1.2×10^{-2} M tetraphenylborate and 1 ml of water. Then 5 ml of 1.5×10^{-3} M TTTH solution of nitrobenzene was added and the mixture was shaken mechanically for 20 min at room temperature. After phase separation, samples of the organic and aqueous phases were taken and the pH of the aqueous phase was measured. The metal ion concentration in organic and aqueous phases was determined by atomic absorption spectrometry.

RESULTS AND DISCUSSION

Optimization of extraction parameters

The experimental conditions were optimized with a fixed amount of metal ion and a single extraction step. First, a range of bulky univalent counter anions were examined, because the major factors responsible for the ion-pair extraction of transition metal ions are the natures of the counter ion and the solvent. Preliminary experiments showed that copper(II) and zinc(II) form stable ion-pair complexes with a macrocyclic Schiff base and TPB; they were quantitatively

TABLE 2

Extraction of metal ions with macrocyclic and acyclic Schiff bases [a]

Metal ion	Extraction (%)							
	pH 5				pH 9			
	TTTH	TTTD	DTTD	TED	TTTH	TTTD	DTTD	TED
Mn(II)	0	0	0	0	> 99	3	3	2
Co(II)	0	0	0	0	> 99	> 99	91	> 99
Ni(II)	0	0	0	0	> 99	> 99	> 99	> 99
Cu(II)	> 99	54	97	28	> 99 (90) [b]	> 99 (12) [b]	97 (16) [b]	98 (5) [b]
Zn(II)	0	0	0	0	> 99	97	> 99	98

[a] [Extractant] = 1.5×10^{-3} M in nitrobenzene; [M^{2+}] = 50 μg in 5 ml; [TPB] = 2.4×10^{-3} M. [b] Values in parentheses denote the percentage extractions in the absence of TPB counter anion.

extracted into the organic phase. Triphenylmethane dyes such as naphtholphthalein and thymolphthalein can be used as counter ions but are less effective. Virtually no copper(II) was extracted with TTTD when picrate or perchlorate was used as a counter anion. The extraction of copper(II) with TTTD ligand and different organic solvents decreased in the order nitrobenzene > 1-nitropropane > 2-nitropropane = chloroform (Table 1). 1,2-Dichloroethane was unsuitable because of the low solubility of macrocycles in it.

The role of macrocyclic Schiff bases on the metal ion extraction was ascertained at pH 5 and 9; copper(II) and other transition metal ions were not extracted by pure nitrobenzene from aqueous solution containing TPB. As a result, the combination of TPB and nitrobenzene provided the most efficient system for the extraction study of transition metals.

The effect of variation of the mechanical shaking time on the extraction showed that equilibrium was attained after 10 min of mechanical shaking, 20 min was adopted in the subsequent experiments.

Comparison of macrocyclic extractants

The extractabilities of the transition metal ions by means of the different systems are summarized in Table 2. In acidic media, only copper(II) was extracted by macrocyclic TTTH and DTTD, permitting its separation from the other transition metal ions. The potential usefulness of macrocyclic DTTD as an extractant was compared with that of the acyclic counterpart, TED. The extraction of copper(II) by DTTD was almost quantitative, whereas only 30% of copper(II) was extracted by acyclic TED. This greater stability of the metal complexes with macrocyclic Schiff base could be a result of stronger bonding by nitrogen and/or sulphur donor groups in DTTD due to its relatively fixed stereochemistry compared with the more flexible TED molecules.

From weakly alkaline solution (pH 9), manganese(II), cobalt(II), nickel(II), copper(II) and zinc(II) were extracted quantitatively by TTTH. The contribution of phenolic OH groups to the metal ion complexation is obvious by comparing TTTH with TTTD. Both compounds contain similar 26-membered cycles and have a fixed cavity of similar size. The manganese(II)–TTTH complex, the least stable complex of TTTH with transition metal ions, is completely extracted into nitrobenzene as an ion-pair complex. In contrast, Schiff bases containing no oxygen donor group, i.e., TTTD, DTTD and TED, showed negligible extractability for manganese(II). The coordination of pendant phenolate to metal ion has been demonstrated in the extraction system with the monoaza-15-crown-5 derivative [14]. Acyclic TED is relatively easy to prepare and finds wide application as an extractant. The extraction curves of metal ions with TED showed similar patterns to those observed with the TTTD extraction system; transition metal ions except manganese(II) were quantitatively extracted by TED at pH 9.

The organic solubility of macrocyclic TTTD was modified by the substitution of cyclohexyl groups for propyl units in the macrocyclic moiety. The prepared DTTD also acts as an effective extractant for transition metal ions at pH 9. The extraction of copper(II) by DTTD was also improved in weakly acidic media.

Extraction with TTTH

The extraction curves for manganese(II), cobalt(II), nickel(II), copper(II) and zinc(II) with TTTH as a function of pH are shown in Fig. 2. The extraction of copper(II) was complete over a wide pH range (3–10.5). Quantitative extractions

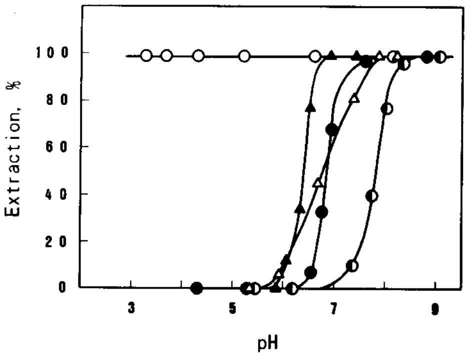

Fig. 2. Effect of pH on extractions. Metal–TTTH–TPB ion-paired complexes: ◐ = manganese(II); △ = cobalt(II); ▲ = nickel(II); ○ = copper(II); ● = zinc(II).

were also attained for manganese(II) at pH 8.5–9, cobalt(II) at pH 7.5–9, nickel(II) at pH 6.5–9 and zinc(II) at pH 7.5–10.5. When manganese(II), nickel(II) and cobalt(II) were extracted at pH > 9.5, precipitates were detected at the boundary of the aqueous and organic phases, which prevented the quantitative recovery of these elements. In contrast, copper(II) and zinc(II) complexes did not form any precipitate even at pH 10.5 and were extracted into the organic phase. The sequence of increasing extractability $Mn^{2+} < Co^{2+} < Ni^{2+} < Cu^{2+} > Zn^{2+}$ follows the order of the Irving–William series. These data agree with the previous finding that the tendency for coordination by the nitrogen-donor groups is more important for complexation than are the ionic dimensions. A similar extractability of metal ions has been documented in the polyaza macrocycle systems [4]. Quantitative extraction of manganese(II) with TTTH clearly demonstrated the analytical potential of TTTH as an extractant (cf., Table 2). The distribution ratio (D) for manganese(II) determined by atomic absorption spectrometry was > 100, which is in good agreement with that obtained by neutron activation analysis using the $^{55}Mn(n,\gamma)^{56}Mn$ reaction. The extraction of cadmium(II) was not quantitative; about 10% of the cadmium(II) remained in the aqueous phase at pH 9. Interestingly, about 90% of copper(II) was extracted by TTTD even in the absence of TPB counter ions (cf., Table 2). The proposed method is selective for the extraction of copper(II) at pH 5; the other transition metal ions (manganese, cobalt, nickel and zinc) remained in the aqueous phase. Hence the separation of copper from manganese, cobalt, nickel and zinc was satisfactory. No copper(II) was detected in the aqueous phase within the uncertainty of the measurements.

The composition of the extracted copper(II) species was estimated from a graph of log D versus log[TTTH] at fixed TPB and hydrogen ion concentrations. The slope was 1.5, indicating that the extracted copper(II) species contain one or two TTTH molecules (Fig. 3). Because TPB exists as a singly charged anion under the experimental conditions, the composition of the extracted species can be assumed to be $[Cu(TTTH)]^{2+}$-$[(TPB)_2]^{2-}$ or $[Cu(TTTH)_2]^{2+}[(TPB)_2]^{2-}$. In the thiophene-containing macrocycles, a 1:1 copper(II)–DTTD stoichiometry was confirmed by the log D vs. log[DTTD] plot. More detailed studies of the extraction mechanism are in progress to elucidate the steric effects on metal complexation.

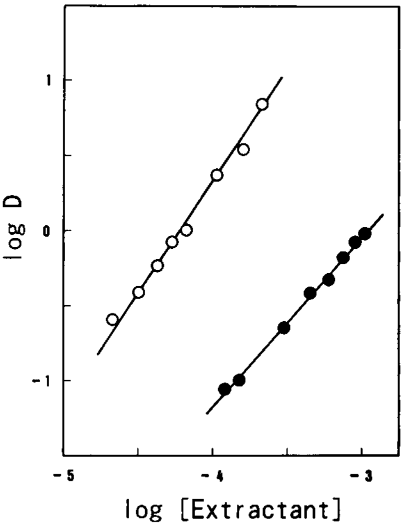

Fig. 3. Dependence of copper(II) distribution ratio on the concentration of extractant. ○ = TTTH system (pH 5); ● = DTTD system (pH 5).

In conclusion, the most effective extraction of the transition metals manganese(II), cobalt(II), nickel(II), copper(II) and zinc(II) was obtained by the use of TTTH as a ligand and TPB as a counter anion when nitrobenzene was used as the organic solvent. The proposed method permits the separation of copper from commonly associated transition metals at pH 5. The analytical utility of mixed donor macrocycles will motivate further developments of new types of extractants.

The authors acknowledge the technical assistance of Kazuaki Sato in synthesizing the macrocyclic Schiff bases.

REFERENCES

1 H. Handel, F.R. Muller and R. Guglielmetti, Helv. Chim. Acta, 66 (1983) 514.
2 W. Szczepaniak, B. Juskowiak and W. Ciszewska, Anal. Chim. Acta, 156 (1984) 235.

3 Z. Brzozka and T. Trybulowa, Anal. Chim. Acta, 172 (1985) 257.
4 S. Arpadjan, M. Mitewa and P.R. Bontchev, Talanta, 34 (1987) 953.
5 T.J. Riedo and T.A. Kaden, Helv. Chim. Acta, 62 (1979) 1089.
6 M.K. Beklemishev, L.I. Gorodilova, N.I. Shevtsov, L.M. Kardivarenko and N.M. Kuzmin, Zh. Anal. Khim., 44 (1989) 1058.
7 T. Kumamaru, Y. Nitta, H. Matsuo and E. Kimura, Bull. Chem. Soc. Jpn., 60 (1987) 1930.
8 N.V. Isakova, Yu. A. Zolotov and V.P. Ionov, Zh. Anal. Khim., 44 (1989) 1045.
9 E.I. Morosanova, Yu.A. Zolotov, V.A. Bodnya and A.A. Formanovskii, Mikrochim. Acta, III (1984) 389.
10 Yu.A. Zolotov, E.I. Morosanova, S.G. Dmitrienko, A.A. Formanovskii and G.V. Ivanov, Mikrochim. Acta, III (1984) 399.
11 M. Fujiwara, T. Matsushita and T. Shono, Polyhedron, 3 (1984) 1357.
12 N.V. Isakova, Yu.A. Zolotov and V.P. Ionova, Zh. Anal. Khim., 44 (1989) 859.
13 T. Sone, Y. Ohba and R. Watanabe, Bull. Chem. Soc. Jpn., 62 (1989) 1346.
14 Y. Katayama, R. Fukuda and M. Takagi, Anal. Chim. Acta, 185 (1986) 295.

Analytica Chimica Acta, 274 (1993) 147–162
Elsevier Science Publishers B.V., Amsterdam

Linear solvation energy relationships in reversed-phase liquid chromatography. Prediction of retention from a single solvent and a single solute parameter

Martí Rosés and Elisabeth Bosch

Departament de Química Analítica, Universitat de Barcelona, Diagonal 647, 08028 Barcelona (Spain)

(Received 7th April 1992; revised manuscript received 13th October 1992)

Abstract

The retention (log k') values for fifteen phenols with two different columns (C_{18}) and mobile phases (methanol–water and acetonitrile–water) were correlated with the solute and mobile phase solvatochromic parameters. From the results it is deduced that good linear relationships should be obtained between log k' and the Dimroth–Reichardt E_T^N parameter of the mobile phase. From these correlations it is demonstrated that, for a fixed column–mobile phase system, only a single solute parameter (p) and a single solvent parameter (E_T^N) are needed for the prediction of retention. Methods for computation of the column and mobile phase constants, solute p parameter and mobile phase E_T^N values are proposed. The prediction of retention was tested for three phenols (different from the original fifteen data set) with good agreement between the predicted and observed values.

Keywords: Liquid chromatography; Phenols; Retention; Solvation energy; Solvatochromic parameters

The accurate prediction of retention in reversed-phase liquid chromatography (RPLC) is an important aim. Many parameters have been proposed in order to define the strength of the mobile phase and to estimate the retention of solutes. Some of the most useful are the solvatochromic parameters. Solvatochromic parameters were developed for assessing solvent properties such as polarity and hydrogen bond donor and acceptor capabilities, and they can be easily measured from the UV–visible spectral shifts of an indicator probe.

The most widely used is the $E_T(30)$ scale proposed by Dimroth, Reichardt and co-workers [1,2]. Johnson et al. [3] showed that plots of log k' (k' = solute capacity factor) vs. the E_T value of the mobile phase are in general more linear than the plots of log k' vs. the volume fraction of organic modifier. Therefore, suitable prediction of retention for a specific solute can be achieved from the E_T of the mobile phase and the correlation parameters for this solute.

In a series of papers, Kamlet, Taft and coworkers [4–7] applied the linear solvation energy relationship (LSER) approach to retention in RPLC. LSER is based on the Kamlet–Taft multi-parameter scales [8–10] of solvatochromic polarity (π^*), hydrogen bond donor (α) and acceptor (β) abilities and the Hildebrand solubility parameter (δ_H). Cheong and Carr [11] have estimated the π^* and α values for the most often used mobile phase solvent mixtures and discussed the simple E_T approach. They concluded that good correlations of retention with a single solvent parameter can be observed only over a limited range of solvent composition, and that at

Correspondence to: E. Bosch, Departament de Química Analítica, Universitat de Barcelona, Diagonal 647, 08028 Barcelona (Spain).

least two parameters are needed to account for all the processes that control retention in RPLC [12].

In this work, the LSER approach was applied to retention of phenols using two different columns and mobile phases over the whole range of solvent compositions, from experimental and literature [13] data. Phenols were chosen because they have significant chromatographic applications and appropriate polarity and hydrogen bond properties.

From the LSER results obtained it is concluded that good log k' vs. E_T correlations could be obtained in the most often used composition range of the most common mobile phases (methanol–water and acetonitrile–water). Moreover, it is shown that the slope and intercept of the log k' vs. E_T plots are well correlated, and that good predictions of retention can be achieved from a single solvent parameter (E_T) and a single solute parameter (denoted p). The E_T value of the mobile phases can be easily calculated from the composition of the mobile phase by means of previously developed equations [14]. Methods for estimating the p values of solutes are proposed from the correlation with the solute properties (volume, polarity and hydrogen bond capabilities, or log P) or from the p value of the same solute using other columns and/or mobile phases.

LINEAR SOLVATION ENERGY RELATIONSHIPS AND RETENTION IN CHROMATOGRAPHY

The LSER approach to chromatographic retention has been defined by Cheong and Carr [12] and can be written as

$$\log k' = (\log k')_0 + m(\delta_m^2 - \delta_s^2)V_2/100 + s(\pi_m^* - \pi_s^*)\pi_2^* + a(\beta_m - \beta_s)\alpha_2 + b(\alpha_m - \alpha_s)\beta_2 \quad (1)$$

where $(\log k')_0$ is an independent term, m, s, a and b are the coefficients of the correlation, $V_2/100$ is the "normalized" volume of the solute, δ is the Hildebrand solubility parameter and π^*, α and β are the Kamlet–Taft solvatochromic parameters. As usual in the LSER chromatographic formalism [12], the subscripts s and m denote the stationary and mobile phase, respectively, and the subscripts 1 and 2 the solvent (mobile and stationary phases) and solute, respectively.

Equation 1 is usually simplified in two different ways. When a system with a fixed mobile phase (with a fixed composition) and a fixed column stationary phase is considered, the equation becomes

$$\log k' = (\log k')_0 + m_1V_2/100 + s_1\pi_2^* + a_1\alpha_2 + b_1\beta_2 \quad (2)$$

where the coefficients m_1, s_1, a_1 and b_1 depend on the stationary and mobile phase solubility (δ^2), polarity (π^*) and hydrogen bond basicity (β) and acidity (α), respectively. Equation 2 allows the correlation of the retentions of different solutes in the same column and mobile phase with the solute properties, and it has been widely verified [4–7].

On the other hand, for the same solute in the same column but with different mobile phase compositions, Eqn. 1 can be reduced to

$$\log k' = (\log k')_s + m_2\delta_m^2 + s_2\pi_m^* + a_2\beta_m + b_2\alpha_m \quad (3)$$

where $(\log k')_s$ depends on $(\log k')_0$ and on the parameters of the stationary phase, and m_2, s_2, a_2 and b_2 depend on the solute parameters. In Eqn. 3 the invariance of the properties of the stationary phase with the change in the mobile phase composition is assumed. However, it is well known that the stationary phase is partially solvated by the mobile phase, and therefore their properties change with changes in the mobile phase composition [3,12,15–17]. In spite of this, Eqn. 3 can be retained, as is demonstrated under Results and Discussion.

Hildebrand solubility parameters are known for many pure liquids, but they have not been determined for mixtures. However, linear relationships between δ^2 and π^* have been proposed [12,18]. Although these correlations apply for pure solvents, they can presumably be applied to binary solvent mixtures where δ and π^* change in a limited range. Assuming that there is a linear

TABLE 1

Solute parameters and retention values (log k') of phenols in the Spherisorb C_{18}/methanol–water system [a]

No.	Phenol	$V_2/100$	π_2^*	β_2	α_2	Log k'										
						MeOH(%)										
						100	90	80	70	60	50	40	30	20	10	0
1	Phenol	0.536	0.72	0.36	0.60	−0.87	−0.67	−0.47	−0.28	−0.05	0.16	0.38	0.61	0.82	1.03	1.32
2	4-Nitrophenol	0.676	1.01	0.33	0.82	−0.85	−0.64	−0.31	−0.19	0.08	0.33	0.62	0.88	1.11	1.38	1.76
3	3-Nitrophenol	0.676	1.06	0.31	0.79	−0.81	−0.60	−0.37	−0.15	0.13	0.38	0.66	0.93	1.17	1.44	
4	2-Chlorophenol	0.626	0.82	0.29	0.65	−0.79	−0.56	−0.42	−0.08	0.21	0.49	0.81	1.09	1.34	1.61	
5	2-Nitrophenol	0.676	1.10	0.27	0.05	−0.63	−0.40	−0.25	0.07	0.35	0.60	0.89	1.13	1.37	1.63	
6	2,4-Dinitrophenol	0.816		0.34		−0.85	−0.64	−0.31	−0.15	0.16	0.42	0.72	0.98	1.24	1.55	
7	4-Chlorophenol	0.626	0.72	0.25	0.67	−0.77	−0.55	−0.17	0.00	0.32	0.62	0.96	1.25	1.49		
8	3-Bromophenol	0.669	0.84	0.23	0.70	−0.70	−0.45	−0.19	0.09	0.43	0.75	1.07	1.38			
9	4-Bromophenol	0.669	0.79	0.25	0.67	−0.70	−0.47	−0.19	0.07	0.40	0.72	1.09	1.41			
10	2,6-Dichlorophenol	0.716	0.95	0.28	0.32	−0.74	−0.44	−0.07	0.12	0.45	0.78	1.15	1.48			
11	2,4-Dimethylphenol	0.732	0.64	0.39	0.53	−0.70	−0.45	−0.15	0.11	0.43	0.75	1.30				
12	4-Chloro-3-methylphenol	0.724	0.70	0.33	0.65	−0.67	−0.40	−0.11	0.19	0.54	0.90	1.40				
13	2,4-Dichlorophenol	0.716	0.95	0.20	0.72	−0.65	−0.33	0.01	0.29	0.66	1.02					
14	3,5-Dichlorophenol	0.716	0.95	0.13	0.77	−0.55	−0.22	0.01	0.46	0.86	1.24					
15	Pentachlorophenol	0.986	0.85	0.15	0.55	−0.11	0.24	0.67								

[a] $V_2/100$ from [20] or calculated by the simple additivity method described therein; π_2^*, α_2, and β_2 from [19].

relationship between δ_m^2 and π_m^* (and perhaps also with α_m and β_m), Eqn. 3 can be simplified to

$$\log k' = (\log k')'_s + s'_2\pi_m^* + a'_2\beta_m + b'_2\alpha_m \quad (4)$$

where the prime indicates that the intercept and the coefficients depend on the correlation of δ_m^2 with π_m^*, α_m and β_m for the particular mobile phase studied.

Further reduction of Eqn. 4 is not directly possible because the remaining Kamlet–Taft solvatochromic parameters measure different solvent effects and linear correlations between them have not been demonstrated. However, it has been shown that retention in RPLC does not depend strongly on the interaction of the solute hydrogen bond acidity α_2 with the solvent hydrogen bond basicity β_m [12] and, therefore, Eqn. 4 can be reduced to

$$\log k' = (\log k')'_s + s'_2\pi_m^* + b'_2\alpha_m \quad (5)$$

In order to obtain good linear relationships between log k' and the E_T value of the mobile phase, the observed correlation between E_T and α and π^* [9] should be fulfilled:

$$E_T^N = 0.009 + 0.415\pi^* + 0.465\alpha$$
$$n = 40,\ r = 0.984 \quad (6)$$

In this and the following equations, the normalized E_T^N parameter [2] is used instead of the $E_T(30)$ values in order to use similar units as for the other parameters. Equation 6 shows that E_T is equally sensitive to polarity (π^*) and hydrogen bond donation (α) of the solvent, and if the s'_2 and b'_2 coefficients of Eqn. 5 have similar values, good correlations of log k' vs. E_{Tm}^N are expected, according to the equation

$$\log k' = q + pE_{Tm}^N \quad (7)$$

EXPERIMENTAL

Apparatus and procedure

Retention data for the acetonitrile–water mobile phase on a 15 cm × 4.1 mm i.d. Unisil Q C_{18} column at 30°C were taken from the literature [13]. Retention data for the phenols in methanol–water (0.1 M in acetic acid) mobile phase were measured at 25°C on a 25 cm × 4.6 mm i.d. Spherisorb C_{18} column (Table 1). The chromatographic equipment used consisted of an ISCO (Lincoln, NE) Model 2350 dual-pump system with a 10-μl loop valve and a variable-wavelength V^4 absorbance detector (ISCO) set at 282 nm. The chromatographic system was controlled by Chemresearch Chromatographic Data Management System Controller software (ISCO) running on a Peceman AT Supermicro personal computer. Phenols were dissolved (20–200 mg l^{-1}) in pure methanol. Resorcinol in pure methanol was used as a dead volume marker.

TABLE 2

Solvatochromic parameters of mobile phases

Organic modifier (%, v/v)	Methanol–water				Acetonitrile–water			
	E_{Tm}^N	π_m^*	α_m	β_m	E_{Tm}^N	π_m^*	α_m	β_m
100	0.764	0.60	1.09	0.62	0.464	0.75	0.31	0.37
90	0.777	0.74	0.99	0.54	0.712	0.80	0.80	0.43
80	0.792	0.82	0.95	0.54	0.749	0.84	0.84	0.42
70	0.809	0.91	0.91	0.53	0.767	0.85	0.87	0.40
60	0.827	0.98	0.88	0.50	0.787	0.91	0.86	0.41
50	0.848	1.03	0.88	0.43	0.810	0.95	0.87	0.40
40	0.870	1.08	0.89	0.38	0.836	0.99	0.90	0.39
30	0.896	1.11	0.92	0.32	0.867	1.06	0.90	0.36
20	0.926	1.15	0.95	0.26	0.903	1.12	0.92	0.31
10	0.960	1.16	1.01	0.23	0.947	1.15	0.99	0.25
0	1.000	1.17	1.09	0.19	1.000	1.17	1.09	0.19

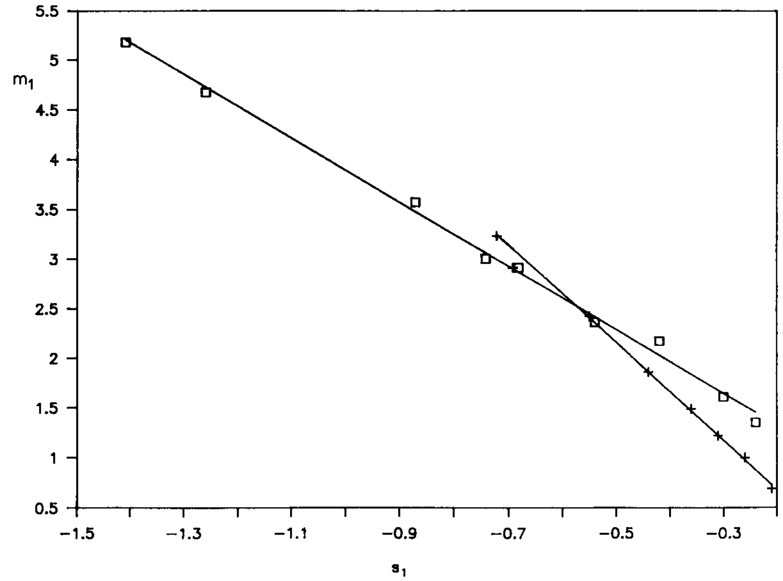

Fig. 1. Linear relationships between mobile phase solubility parameter (δ_m^2) and polarity (π_m^*) from log k' vs. solute parameters correlation coefficients m_1 and s_1 (Eqn. 2). □ = Spherisorb C_{18}/methanol–water; + = Unisil Q C_{18}/acetonitrile–water.

Reagents

Methanol (Merck, for chromatography), phenol (Carlo Erba, RPE, > 99.5, 2-chlorophenol and 4-chlorophenol (Carlo Erba, RPE, > 99%), 2,4-dichlorophenol and 3,5-dichlorophenol (Aldrich, > 99%), 3-bromophenol (Aldrich, > 97%), 2,4-dimethylphenol, 4-chloro-3-methylphenol and 2-nitrophenol (Scharlau, > 99.5%), 4-nitrophenol and 2,4-dinitrophenol (Scharlau, > 99%), pentachlorophenol (Scharlau, > 97%), 2,4,6-trichlorophenol (Scharlau, > 95%), 3-nitrophenol (Fluka, > 99%), 2,6-dichlorophenol (Fluka, 97%), 3-chlorophenol and 4-bromophenol (Merck, > 98%) and 2-methylphenol (Doesder) were used. Triply distilled water was used throughout.

Solvatochromic parameters

Table 1 shows the solute parameters [19,20] used in the correlations. Solvent solvatochromic parameters are presented in Table 2.

E_T^N values were calculated by means of the equations developed previously [14], which can be written as follows:

methanol–water:

$$E_{Tm}^N = 1.000 - 0.43v/(1 + 0.82v) \quad v = 0\text{–}1 \quad (8)$$

acetonitrile–water:

$$E_{Tm}^N = 1.000 - 0.59v/(1 + 1.1v) \quad v = 0\text{–}0.80 \quad (9)$$

$$E_{Tm}^N = 0.788 - 0.0111v/(1 - 0.966v) \quad v = 0.90\text{–}1 \quad (10)$$

where v is the volume fraction of the organic modifier.

The π^* values measured by Cheong and Carr [11] were used, α was computed form E_T^N and π^* values according to Eqn. 6 and β was interpolated from the values in mol-% given in [21].

RESULTS AND DISCUSSION

The results of the correlation of the log k' values for the phenols using the two studied columns and mobile phases with the solute parameters according to Eqn. 2 are presented in Table 3. The coefficient m_1 is positive and increases with increasing water content, indicating that an increase in the solubility parameter of the mobile phase or an increase in the volume of the solute increases the retention. The coefficients

TABLE 3

Correlation of log k' values with solute parameters (Eqn. 2)

Mobile phase	Organic modifier (%, v/v)	$(\text{Log } k')_0$	m_1	s_1	b_1	a_1	n	r
Methanol–water	100	-1.04 ± 0.05	1.35 ± 0.17	-0.24 ± 0.11	-1.01 ± 0.23	-0.17 ± 0.07	14	0.975
	90	-0.82 ± 0.05	1.61 ± 0.17	-0.30 ± 0.11	-1.33 ± 0.23	-0.19 ± 0.07	14	0.983
	80	-0.86 ± 0.06	2.17 ± 0.21	-0.42 ± 0.13	-1.34 ± 0.29	$(-0.11 \pm 0.09)^a$	14	0.982
	70	-0.37 ± 0.06	2.36 ± 0.32	-0.54 ± 0.13	-2.08 ± 0.27	-0.19 ± 0.08	13	0.972
	60	-0.20 ± 0.06	2.91 ± 0.36	-0.68 ± 0.14	-2.51 ± 0.30	-0.18 ± 0.09	13	0.977
	50	-0.05 ± 0.07	3.57 ± 0.39	-0.87 ± 0.15	-2.98 ± 0.33	$(-0.17 \pm 0.10)^a$	13	0.981
	40	-0.34 ± 0.05	4.67 ± 0.27	-1.26 ± 0.10	-1.99 ± 0.30	-0.28 ± 0.07	11	0.993
	30	-0.21 ± 0.03	5.18 ± 0.50	-1.41 ± 0.17	-2.10 ± 0.47	-0.30 ± 0.06	9	0.996
	20	1.23 ± 0.06	$(3.00 \pm 3.04)^a$	$(-0.74 \pm 0.90)^a$	$(-3.92 \pm 2.35)^a$	$(-0.10 \pm 0.25)^a$	6	0.994
Acetonitrile–water	90	-0.03 ± 0.02	0.69 ± 0.07	-0.21 ± 0.04	-0.59 ± 0.09	-0.12 ± 0.03	14	0.986
	80	-0.06 ± 0.02	1.00 ± 0.08	-0.26 ± 0.05	-0.67 ± 0.11	-0.16 ± 0.04	14	0.989
	70	0.07 ± 0.03	1.22 ± 0.10	-0.31 ± 0.07	-1.00 ± 0.14	-0.19 ± 0.04	14	0.989
	60	0.16 ± 0.03	1.49 ± 0.11	-0.36 ± 0.07	-1.25 ± 0.15	-0.22 ± 0.05	14	0.992
	50	0.26 ± 0.04	1.86 ± 0.13	-0.44 ± 0.08	-1.53 ± 0.18	-0.24 ± 0.06	14	0.992
	40	0.37 ± 0.05	2.42 ± 0.27	-0.55 ± 0.11	-1.97 ± 0.23	-0.24 ± 0.07	13	0.979
	30	0.47 ± 0.06	3.23 ± 0.33	-0.72 ± 0.13	-2.57 ± 0.27	-0.23 ± 0.08	13	0.983
	20	1.13 ± 0.03	2.91 ± 0.92	-0.69 ± 0.27	-3.22 ± 0.74	$(-0.14 \pm 0.08)^a$	8	0.997

[a] Values in parentheses are not statistically significant at the 95% confidence level by Student's t-test.

s_1, b_1 and a_1 are negative and decrease with increasing water content. Therefore, on increasing the polarity or hydrogen bond capabilities of the mobile phase or decreasing those of the solute, the retention increases. These conclusions agree with the general RPLC theory. Results for 20% (v/v) organic solvent in the mobile phase differ from the others, probably because of the small number of solute retention data, and therefore they have not been considered in the above comments.

From Table 3 it is deduced that the solvent properties most affecting the retention of phenols are the solubility parameter (high m_1 coefficient) and the hydrogen bond acidity (high b_1 coefficient). Solvent hydrogen bond basicity is the property that least affects retention (low a_1 coefficients). Therefore, the simplification of Eqn. 4 to Eqn. 5 is completely justified.

Solvent polarity (s_1 coefficients) also seems not to have much influence on the retention. However, the importance of solvent polarity comes from the correlation with the solvent solubility. Evidence for this correlation is presented in Fig. 1, where m_1 is plotted vs. s_1 for the different mobile phase compositions studied, and also in Table 4, where the correlation coefficients among the different coefficients for the different mobile phase compositions with organic modifier contents higher than 20% are presented. As can be seen, there is a good correlation ($r > 0.99$) between m_1 and s_1 for both mobile phases. There are also good correlations between m_1 and s_1 with b_1 in the acetonitrile–water system. General correlations for m_1, b_1 and a_1 are as follows:

methanol–water:

$$m_1 = (0.95 \pm 0.04) - (3.48 \pm 0.09)s_1 + (0.01 \pm 0.03)b_1 + (2.28 \pm 0.52)a_1$$

$$n = 8,\ r = 0.99975 \qquad (11)$$

acetonitrile–water:

$$m_1 = -(0.46 \pm 0.02) - (5.73 \pm 0.56)s_1 + (0.24 \pm 0.15)b_1 - (0.77 \pm 0.30)a_1$$

$$n = 8,\ r = 0.99990 \qquad (12)$$

For both correlations, the most significant term is s_1 (the coefficient a_1 is also significant, but the low a_1 values imply a low contribution of these terms to the overall correlations). Therefore, for both mobile phases a good correlation of δ^2 with π^* is expected, and Eqn. 3 can be reduced to Eqn. 4.

Correlation of log k' with the mobile phase parameters was done through Eqn. 4. The best correlations were obtained for solvent compositions with $\geqslant$ 30–50% (v/v) organic modifier in the methanol–water mobile phase and $\leqslant$ 70% (v/v) organic modifier in the acetonitrile–water mobile phase. The results are presented in Table 5. Because of the large retention of pentachlorophenol, not enough data were obtained in order to correlate this solute in the methanol–water system. Good correlations for this solute were obtained in acetonitrile–water in the solvent composition range available. However, the results are substantially different from those for the other phenols.

TABLE 4

Correlation coefficients of crossed correlation of m_1, s_1, b_1 and a_1 for different mobile phase compositions [a]

	r				
	m_1	s_1	b_1	a_1	
m_1		0.998	0.584	0.794	MeOH–H_2O
s_1	0.9997		0.562	0.827	
b_1	0.996	0.996		0.223	
a_1	0.785	0.776	0.803		
	MeCN–H_2O				

[a] Top right hand corner, correlation coefficients for methanol–water mobile phase; bottom left-hand corner, correlation coefficients for acetonitrile–water mobile phase.

TABLE 5

Correlation of log k' values with mobile phase solvatochromic parameters (Eqn. 4)

Mobile phase	Phenol [a]	$(\text{Log } k')'_s$	s'_2	b'_2	a'_2	n	r	Organic modifier range (%, v/v)
Methanol–water	1	−7.431 ± 0.023	4.19 ± 0.40	3.68 ± 0.52	(0.04 ± 0.44)[b]	8	0.9994	30–100
	2	−8.204 ± 0.053	4.74 ± 0.91	4.21 ± 1.20	(−0.15 ± 1.00)	8	0.9978	30–100
	3	−9.064 ± 0.032	5.08 ± 0.55	4.73 ± 0.72	(0.06 ± 0.60)	8	0.9992	30–100
	4	−11.333 ± 0.051	6.05 ± 0.89	6.28 ± 1.26	(0.09 ± 0.97)	7	0.9981	40–100
	5	−10.098 ± 0.045	5.60 ± 0.79	5.49 ± 1.11	(0.19 ± 0.86)	7	0.9984	40–100
	6	−9.485 ± 0.051	5.39 ± 0.89	4.82 ± 1.16	(0.22 ± 0.97)	8	0.9982	30–100
	7	−10.332 ± 0.058	5.93 ± 1.00	5.40 ± 1.32	(0.18 ± 1.10)	8	0.9981	30–100
	8	−12.157 ± 0.035	6.67 ± 0.66	7.07 ± 1.07	(−0.41 ± 0.70)	6	0.9992	50–100
	9	−11.951 ± 0.032	6.56 ± 0.56	6.72 ± 0.79	(−0.04 ± 0.61)	7	0.9994	40–100
	10	−9.366 ± 0.050	5.75 ± 0.86	5.04 ± 1.13	(−0.52 ± 0.94)	8	0.9988	30–100
	11	−11.639 ± 0.035	6.50 ± 0.68	6.57 ± 1.09	(−0.20 ± 0.72)	6	0.9991	50–100
	12	−13.268 ± 0.030	7.29 ± 0.53	7.89 ± 0.75	(−0.61 ± 0.58)	7	0.9996	40–100
	13	−12.047 ± 0.047	7.02 ± 0.90	6.86 ± 1.46	(−0.46 ± 0.96)	6	0.9988	50–100
	14	−15.659 ± 0.059	8.62 ± 1.13	9.26 ± 1.83	(−0.25 ± 1.20)	6	0.9985	50–100
Acetonitrile–water	1	−3.350 ± 0.005	2.24 ± 0.04	2.50 ± 0.18	−1.62 ± 0.15	7	0.999965	10–70
	2	−3.683 ± 0.005	2.88 ± 0.04	2.67 ± 0.16	−2.55 ± 0.14	7	0.999983	10–70
	3	−3.658 ± 0.003	2.89 ± 0.04	2.75 ± 0.16	−2.72 ± 0.09	6	0.999990	20–70
	4	−4.098 ± 0.002	3.10 ± 0.02	3.08 ± 0.09	−2.61 ± 0.06	6	0.999997	20–70
	5	−4.866 ± 0.009	3.37 ± 0.11	3.26 ± 0.46	−1.44 ± 0.28	6	0.999916	20–70
	6	−4.568 ± 0.004	3.45 ± 0.05	3.25 ± 0.21	−2.59 ± 0.22	5	0.999985	30–70
	7	−3.867 ± 0.007	3.31 ± 0.08	2.96 ± 0.35	−3.32 ± 0.21	6	0.999962	20–70
	8	−4.333 ± 0.003	3.61 ± 0.03	3.23 ± 0.13	−3.28 ± 0.08	6	0.999995	20–70
	9	−4.054 ± 0.006	3.50 ± 0.07	3.14 ± 0.32	−3.58 ± 0.19	6	0.999972	20–70
	10	−4.777 ± 0.002	3.83 ± 0.02	3.52 ± 0.09	−3.09 ± 0.09	5	0.999998	30–70
	11	−4.319 ± 0.003	3.54 ± 0.04	3.28 ± 0.18	−3.19 ± 0.19	5	0.999990	30–70
	12	−4.288 ± 0.008	3.86 ± 0.09	3.35 ± 0.40	−4.07 ± 0.42	5	0.999960	30–70
	13	−4.421 ± 0.011	4.06 ± 0.13	3.54 ± 0.56	−4.45 ± 0.59	5	0.999928	30–70
	14	−5.170 ± 0.007	4.53 ± 0.09	4.02 ± 0.37	−4.45 ± 0.39	5	0.999975	30–70
	15	6.764 ± 0.007	6.03 ± 0.08	−5.25 ± 0.40	−16.40 ± 0.86	5	0.999971	50–90

[a] See Table 1. [b] Values in parentheses are not statistically significant at the 95% confidence level by Student's t-test.

For methanol–water, a_2' is not statistically significant and s_2' is similar in value to b_2'. Therefore, a good correlation with E_T^N is expected for this system. The s_2' values for the acetonitrile–water are also similar to b_2', but a_2' is not meaningless for this system. Nevertheless, the very good correlations obtained for this mobile phase ($r > 0.9999$) suggest that although some correlation will be lost on neglecting a_2' terms, the remaining correlation will probably be still good.

One of the pitfalls with the Kamlet–Taft α_m, β_m and π_m^* parameters is that they can be measured with more than one solvatochromic indicator, and therefore the resulting parameter value can depend on the indicator used. This problem is especially important with solvent mixtures because of preferential solvation of the solvatochromic indicator used by one of the solvents of the mixture. The extent of the preferential solvation depends on the specific solute–solvent interactions, and therefore on the particular solvatochromic indicator used. Consequently, different α_m, β_m or π_m^* values can be obtained for the same solvent mixtures when measured with different solvatochromic indicators. One of the advantages of the $E_T(30)$ scale is that it is measured with a unique solvatochromic indicator, and therefore the $E_T(30)$ value is unambiguous, although the $E_T(30)$ indicator showed preferential solvation. A discussion of preferential solvation of the $E_T(30)$ indicator in 52 binary solvent mixtures (including those most often used in RPLC) is given in [14].

Preferential solvation of indicators explains the disparity of α_m values given in the literature [22,23] for methanol–water and acetonitrile–water solvent mixtures. Of course, the particular set of α_m (and β_m and π_m^*) values used in correlation affects the s_2', a_2' and b_2' coefficients in Eqn. 4. For example, when we use the α_m values obtained by Park et al. [22] employing bis[α-(2-pyridyl)benzylidine-3,4-dimethylaniline]bis(cyano)-iron(II) as indicator instead of our α_m values, we obtain b_2' coefficients about three times larger than s_2', no statistically significant a_2' coefficients for methanol–water and only significant s_2' coefficients for acetonitrile–water mobile phases. These results agree with those obtained by Park et al. [24] for monosubstituted phenols using their set of α_m values.

However, it is noteworthy that the conclusion that log k' should be well correlated with E_T^N is still valid. If α_m values for a solvent mixture calculated with any particular solvatochromic in-

TABLE 6

Correlation of log k' values with the E_T^N of the mobile phase [a]

Phenol [b]	Log P [c]	Methanol–water				Acetonitrile–water			
		q	p	n	r	q	p	n	r
1	1.48	−9.79 ± 0.03	11.7 ± 0.4	7	0.9976	−5.00 ± 0.04	6.6 ± 0.2	8	0.9968
2	1.95	−11.20 ± 0.06	13.6 ± 0.6	7	0.9953	−6.44 ± 0.06	8.5 ± 0.3	8	0.9955
3	2.00	−11.35 ± 0.03	13.8 ± 0.3	7	0.9990	−6.21 ± 0.05	8.2 ± 0.4	7	0.9947
4	2.16	−12.39 ± 0.04	15.2 ± 0.4	7	0.9984	−6.51 ± 0.05	8.7 ± 0.4	7	0.9955
5	1.77	−11.60 ± 0.04	14.4 ± 0.4	7	0.9979	−6.39 ± 0.03	8.7 ± 0.2	7	0.9986
6		−12.08 ± 0.05	14.8 ± 0.5	7	0.9969	−6.92 ± 0.04	9.2 ± 0.3	7	0.9971
7	2.42	−13.05 ± 0.06	16.1 ± 0.6	7	0.9967	−7.10 ± 0.06	9.5 ± 0.4	7	0.9946
8	2.63	−13.45 ± 0.03	16.7 ± 0.3	7	0.9991	−7.54 ± 0.06	10.1 ± 0.4	7	0.9951
9	2.60	−13.57 ± 0.02	16.9 ± 0.2	7	0.9997	−7.51 ± 0.07	10.1 ± 0.5	7	0.9941
10		−13.89 ± 0.06	17.3 ± 0.6	7	0.9967	−7.35 ± 0.04	10.0 ± 0.4	6	0.9967
11	2.30	−14.56 ± 0.05	18.1 ± 0.5	7	0.9978	−6.71 ± 0.05	9.1 ± 0.5	6	0.9935
12	3.10	−15.30 ± 0.03	19.2 ± 0.3	7	0.9994	−7.58 ± 0.05	10.2 ± 0.5	6	0.9945
13	3.15	−15.58 ± 0.04	19.6 ± 0.6	6	0.9979	−8.03 ± 0.05	10.9 ± 0.6	6	0.9948
14		−16.95 ± 0.04	21.5 ± 0.6	6	0.9984	−8.82 ± 0.06	12.0 ± 0.6	6	0.9956
15	5.06	−21.56 ± 0.06	28.1 ± 0.5	3	0.9998	−9.68 ± 0.06	13.6 ± 0.4	4	0.9992

[a] Correlation ranges: methanol–water > 30% methanol; acetonitrile–water, < 90% acetonitrile. [b] See Table 1. [c] Log P: the same values as used in [13], obtained from [25].

dicator do not agree with those calculated with E_T indicator, this means that Eqn. 6 cannot be applied to the former α_m values, and a new correlation must be established between E_T^N and the particular π^*, α and β values. Correlation of E_{Tm}^N values in Table 2 with the π_m^* and β_m values in Table 2 and the α_m values of Park et al. [22] in the range of application of Eqn. 4 (20–100% methanol for methanol–water and 10–80% acetonitrile for acetonitrile–water mobile phases) gives $E_T^N = (0.087 \pm 0.005) + (0.15 \pm 0.03)\pi^* + (0.56 \pm 0.17)\alpha + (0.02 \pm 0.13)\beta$, $n = 9$, $r = 0.997$, for methanol–water and $E_T^N = (0.391 \pm 0.006) + (0.35 \pm 0.09)\pi^* + (0.16 \pm 0.17)\alpha - (0.16 \pm 0.19)\beta$, $n = 8$, $r = 0.998$, for acetonitrile–water. Hence for methanol–water the β coefficient is not significant and the α coefficient is 3.7 times larger than the π^* coefficient. For acetonitrile–water only the π^* coefficient is significant. The relative size and significance of these coefficients agree with those of s_2', b_2' and a_2' when we use Park et al.'s α_m values in Eqn. 4, and therefore the same conclusion is obtained, i.e., good linear correlations are expected between log k' and E_T^N values.

Correlations of the phenols with the E_T^N of the mobile phase according to Eqn. 7 are presented in Table 6. Linear relationships between log k' and E_{Tm}^N are obtained for composition ranges with $> 30\%$ of organic modifier in methanol–water and $< 90\%$ in acetonitrile–water for all the solutes, including pentachlorophenol. These composition ranges cover the range usually employed for analytical applications in RPLC, and therefore good predictions of the retentions of analytes can be obtained from their p and q parameters and the E_T^N value of the mobile phase. In fact, only one parameter (p or q) is needed for each solute because both are very well correlated, as can be observed in Fig. 2, where q is plotted against p for both systems. The correlation of q and p in both systems is different according to the following expressions:

methanol–water:

$$q = -(1.35 \pm 0.07) - (0.724 \pm 0.005)p \quad n = 15, \ r = 0.9997 \tag{13}$$

acetonitrile–water:

$$q = -(0.66 \pm 0.08) - (0.674 \pm 0.013)p \quad n = 15, \ r = 0.9976 \tag{14}$$

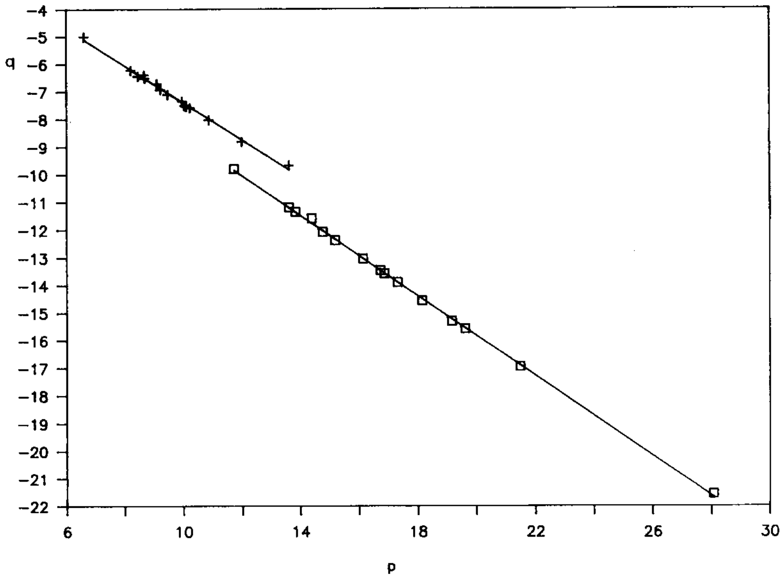

Fig. 2. Linear relationships between the intercept (q) and the slope (p) of correlations of log k' with E_T^N of the mobile phase (Eqn. 7). Symbols as in Fig. 1.

From Eqns. 13 and 14, Eqn. 7 can be written as

$$\log k' = -1.35 + p\left(E^N_{Tm} - 0.724\right) \quad (15)$$

for methanol-water and

$$\log k' = -0.66 + p\left(E^N_{Tm} - 0.674\right) \quad (16)$$

for acetonitrile-water. That is, log k' can be calculated from only one solute parameter (p) and one solvent parameter (E^N_{Tm}).

The meaning of the slope and intercept of the plot of q vs. p can be well understood if a general LSER for the E^N_T equation, similar to Eqn. 1, is considered:

$$\log k' = (\log k')_0 + r\left(E^N_{Tm} - E^N_{Ts}\right)p_2 \quad (17)$$

Comparison of Eqn. 17 with Eqns. 15 and 16 indicates that the slope of the q vs. p correlation would in fact be the E^N_T value of the stationary phase, and the intercept would be the log k' in a mobile phase with the same E^N_T value as the stationary phase.

The p_2 parameter is a hypothetical solute parameter that depends on the solute properties interacting with the solvent properties related to E^N_{Tm}. As demonstrated earlier, the significant solvent properties that have led to linear relationships between log k' and E^N_{Tm} are solvent hydrogen bond donor acidity, polarity and solubility parameter. Therefore, p_2 should depend on the solute volume, polarity and hydrogen bond acceptor basicity. The observed p parameter would also depend on these properties because it is the product of the unknown p_2 parameter (specific for each solute) and the fitting coefficient r (which depends on the studied system). This is supported by the linear correlation observed between the two sets of p parameters in Table 6 (see Fig. 3):

$$p_{\text{MeOH-H}_2\text{O}} = -(4.9 \pm 1.2) + (2.27 \pm 0.20) p_{\text{MeCN-H}_2\text{O}}$$

$$n = 15,\ r = 0.954 \quad (18)$$

The weakest point in the above reasoning is that it has been assumed that E^N_{Ts} is constant (with values of 0.724 and 0.674 for the two stationary phases studied). However, as has been pointed out earlier, the composition of stationary phases changes with change in the composition of the mobile phases and E^N_{Ts} is not constant. Variation of the polarity of the stationary phases has recently been demonstrated by Jones and Rutan [17], who measured the $E_T(30)$ values of silica and C_{18} stationary phases in thin-layer chromatography and methanol-water and acetoni-

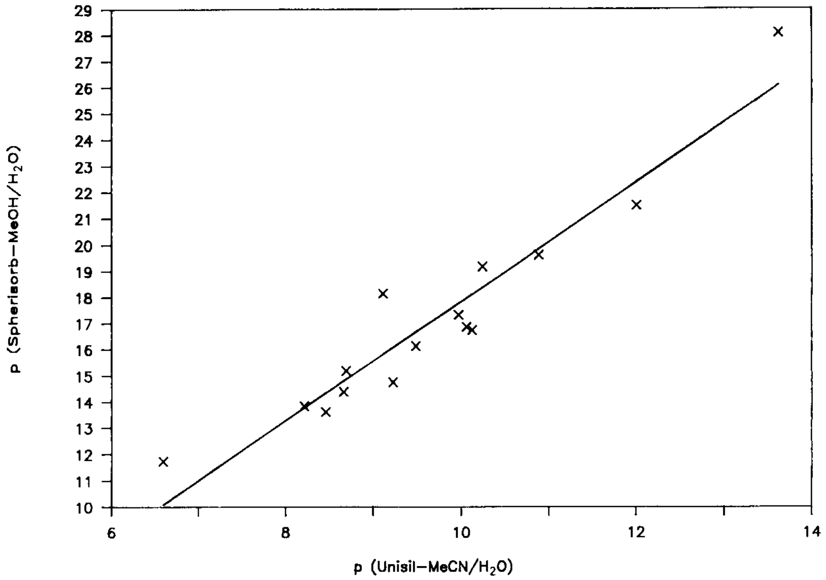

Fig. 3. Linear relationship between p values for Spherisorb C_{18}/methanol-water and Unisil Q C_{18}/acetonitrile-water.

trile–water mobile phases in the range 50–100% of organic modifier, and related the results to the mobile phase composition. However, if the E_T values of the stationary phases are plotted against the E_T values of the mobile phases (see Fig. 4), a linear relationship is obtained in the range 60–100% (v/v) for methanol–water and 60–90% (v/v) for acetonitrile–water.

Assuming a general linear relationship between the E_T^N values of the mobile and stationary phases, which for simplification can be written as

$$E_{Ts}^N = E_{T0}^N + (1 - p_1) E_{Tm}^N \tag{19}$$

and substituting Eqn. 19 in Eqn. 17,

$$\log k' = (\log k')_0 - rp_2 E_{T0}^N + rp_2 p_1 E_{Tm}^N \tag{20}$$

This equation is equivalent to Eqn. 7 with

$$q = (\log k')_0 - rp_2 E_{T0}^N \tag{21}$$

$$p = rp_1 p_2 \tag{22}$$

The two last equations show that there is a linear relationship between p and q and a proportionality between the p parameters in two different column–mobile phase systems. The parameter p depends on p_2, specific for each solute, and on rp_1, specific for each column–mobile phase, because the relationship between E_T^N values of stationary and mobile phases depends on both the particular mobile phase and column (e.g., kind of stationary phase and number of "active" points of the column that can absorb mobile phase). According to Eqn. 18, a linear relationship with a significant intercept (at the 95% confidence level by Students's t-test), instead of a proportionality, is obtained for the relationship between p values in the two column–mobile phase systems. However, assuming proportionality between the two p values:

$$p_{MeOH-H_2O} = (1.74 \pm 0.10) p_{MeCN-H_2O} \quad n = 15 \tag{23}$$

Statistically it is difficult to decide with only two p series whether they are proportional or linearly related. More work is being done with other solutes and columns, which is expected to clear this point.

Rearrangement of Eqn. 20 leads to

$$\log k' = (\log k')_0 + p(E_{Tm}^N - E_{T0}^N/p_1) \tag{24}$$

Comparison of Eqn. 24 with Eqns. 15, 16 and 17 shows that the term taken as the E_T^N value of the stationary phase is really a term that depends on

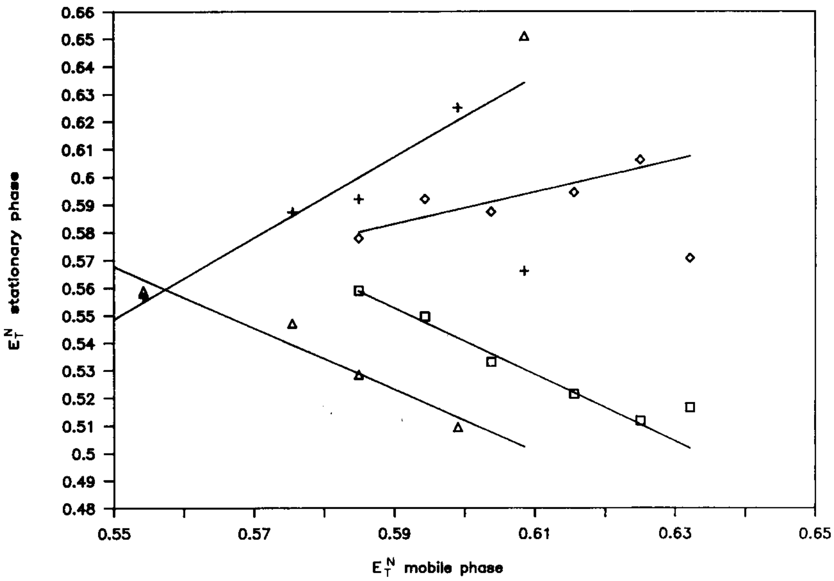

Fig. 4. Linear relationships between E_T^N values of stationary and mobile phases. □ = C_{18}/methanol–water; + = C_{18}/acetonitrile–water; ◇ = silica/methanol–water; △ = silica/acetonitrile–water. Data from [17].

the intercept and slope of the relationship between E_T^N values for the stationary and mobile phases.

Linear relationships between stationary and mobile phase solvatochromic parameters can be assumed for any other solvatochromic parameter, and these linear relationships justify the good correlations obtained between log k' and δ_m^2, π_m^*, β_m and α_m (Eqn. 3), in spite of the change in the solvatochromic parameters of the stationary phase on changing the mobile phase composition.

Prediction of retention in any column can be done from Eqn. 24 if the column–mobile phase-dependent terms (log $k')_0$ and E_{T0}^N/p_1, the solute–column–mobile phase-dependent term p and the mobile phase-dependent term E_{Tm}^N are known.

Calculation of E_{Tm}^N can be easily done from the mobile phase composition by means of Eqns. 9 and 10 developed previously [14]. Calculation of (log $k')_0$ and E_{T0}^N/p_1 can be achieved from standardization of the column–mobile phase with some solutes at different mobile phase compositions, correlation of the obtained log k' results with E_{Tm}^N and subsequent correlation of q with p parameters. Prediction of retention for other solutes in this column can then easily be done from their p values.

Estimation of the p values of solutes can be done in two ways: from their p values in other columns, or from the correlation of the p values with solute properties such as $V_2/100$, π_2^*, β_2 and α_2, or the partition coefficient in octanol–water (log P).

Correlation of the p values presented in Table 6 with the solute properties in Table 1 gives the following:

methanol–water:

$$p = (10.2 \pm 0.8) + (29.9 \pm 2.6)V_2/100 - (8.9 \pm 1.6)\pi_2^* - (22.5 \pm 3.6)\beta_2$$

$$n = 14, \quad r = 0.985 \qquad (25)$$

acetonitrile–water:

$$p = (8.9 \pm 0.4) + (9.7 \pm 1.4)V_2/100 - (2.6 \pm 0.9)\pi_2^* - (13.9 \pm 2.0)\beta_2$$

$$n = 14, \quad r = 0.976 \qquad (26)$$

As expected, the coefficients of α_2 are not significant (they are 0.1 ± 1.2 and 0.3 ± 0.7, respectively), showing that p does not depend on the hydrogen bond acidity of the solute. The most

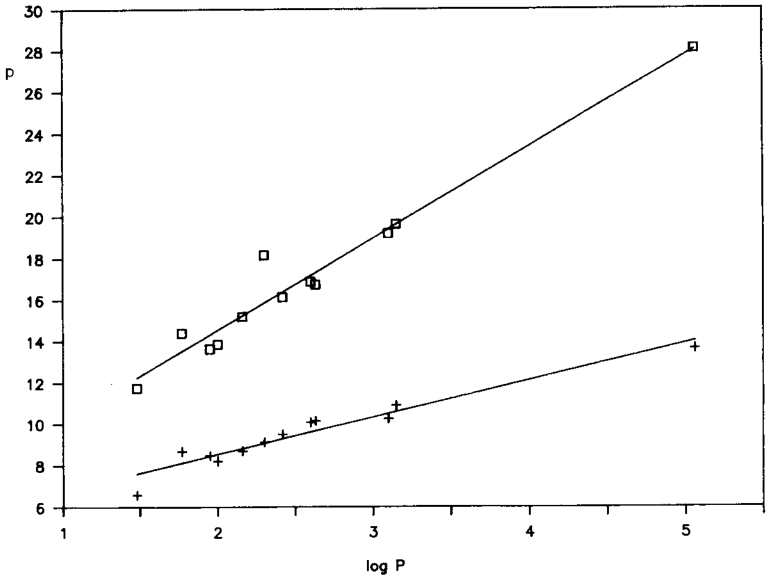

Fig. 5. Linear relationships between p values and octanol–water partition coefficients (log P). Symbols as in Fig. 1.

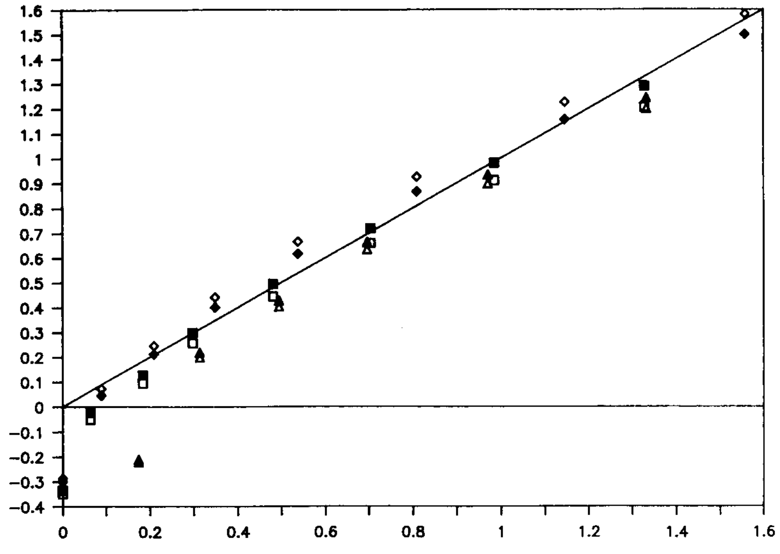

Fig. 6. Plot of predicted vs. observed log k' values for phenols for Unisil Q C_{18}/acetonitrile–water. □, ■ = 2-Methylphenol; ◇, ◆ = 3-chlorophenol; △, ▲ = 2,4,6-trichlorophenol. Open symbols, p values calculated from $V_2/100$, π_2^* and β_2; closed symbols, p values calculated from log P.

important coefficients are those of solute volume and hydrogen bond basicity. The coefficients of solute volume are positive and the coefficients of solute polarity and hydrogen bond basicity are negative, showing that an increase in the polarity or hydrogen bond properties of the solute or a

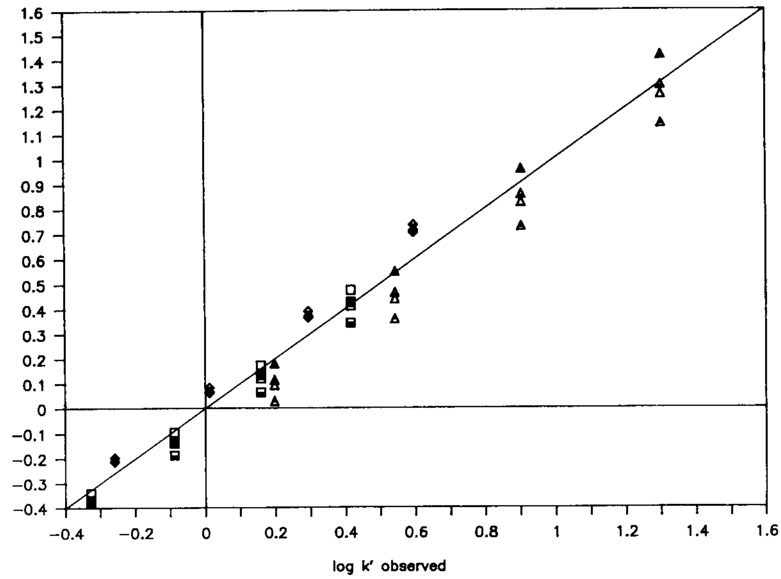

Fig. 7. Plot of predicted vs. observed log k' values for phenols for Spherisorb C_{18}/methanol–water. Symbols as in Fig. 6, plus ⬓, ⬘, ◭ = p values calculated from experimental p values for Unisil Q C_{18}/acetonitrile–water through Eqn. 18 and ⬒, ⬙, ◮ = p values calculated from experimental p values for Unisil Q C_{18}/acetonitrile–water through Eqn. 23.

TABLE 7

Predicted and observed p parameters of phenols

Parameter	2-Methyl phenol	3-Chloro-phenol	2,4,6-Tri-chlorophenol
Solute parameters			
$V_2/100$	0.634	0.626	0.806
π_2^*	0.68	0.77	1.00
α_2	0.52	0.69	0.35
β_2	0.37	0.23	0.19
Log P	1.97	2.48	3.79
Unisil Q C_{18} / acetonitrile – water			
p from $V_2/100$, π_2^*, α_2, β_2	8.1	9.8	11.5
p from log P	8.5	9.4	11.7
p observed	8.2 ± 0.3	9.6 ± 0.4	11.6 ± 0.5
Spherisorb C_{18} / methanol – water			
p from $V_2/100$, π_2^*, α_2, β_2	14.8	16.9	21.1
p from log P	14.4	16.6	22.4
p from Eqn. 18	13.7	16.9	21.4
p from Eqn. 23	14.3	16.7	20.2
p observed	14.7 ± 0.3	15.9 ± 0.1	22.1 ± 0.5

decrease in the solute volume produces a lower retention (lower p values) because of the higher polarity and hydrogen bond properties and the lower solubility parameter of the mobile phase.

A plot of p vs. log P is presented in Fig. 5. Correlation of p values with the log P values represented in Table 6 (which have been used earlier for prediction of retention in RPLC [13]) gives

methanol–water:

$$p = (5.7 \pm 0.9) + (4.41 \pm 0.28) \log P$$

$$n = 12, \quad r = 0.980 \tag{27}$$

acetonitrile–water:

$$p = (5.0 \pm 0.5) + (1.78 \pm 0.15) \log P$$

$$n = 12, \quad r = 0.966 \tag{28}$$

A practical example of the prediction of retention was done for 2-methylphenol, 3-chlorophenol and 2,4,6-trichlorophenol with both column–mobile phase systems. Table 7 presents the $V_2/100$, π_2^*, β_2 and α_2 [19,20] and log P [13] with the computed p values from Eqns. 25–28 and the observed values. For the Spherisorb C_{18}/methanol–water system, p values were also predicted from the experimental p values with the Unisil Q C_{18}/acetonitrile–water system through Eqns. 18 and 23. The agreement between the predicted and observed p values is very good; only 3-chlorophenol in the Spherisorb C_{18}/methanol–water system shows a p value slightly lower than predicted. Prediction of log k' was done from the estimated p values and Eqns. 15 and 16. Figures 6 and 7 show the predicted log k' values vs. the observed values for the Unisil Q C_{18}/ acetonitrile–water and Spherisorb C_{18}/ methanol–water systems, respectively.

From the results obtained it can be concluded that the proposed equations offer a good method for the prediction of retention in RPLC. This prediction can be achieved from a single solute parameter (p), which can be easily estimated from different sources, and a single mobile phase parameter (E_T^N). All the other parameters are constants of the column–mobile phase system used, and can be easily determined from retention measurements on a few solutes at different mobile phase compositions.

The authors thank Professor M.H. Abraham (University College London) for kindly providing the solute parameters of the phenols studied. Financial support from the DGICYT (Project PB88-0194) of the Spanish Government is also gratefully acknowledged.

REFERENCES

1 K. Dimroth, C. Reichardt, T. Siepmann and F. Bohlmann, Justus Liebigs Ann. Chem., 661 (1963) 1.
2 C. Reichardt, Solvents and Solvent Effects in Organic Chemistry, VCH, Weinheim, 2nd edn., 1988.
3 B.P. Johnson, M.G. Khaledi and J.G. Dorsey, Anal. Chem., 58 (1986) 2354.
4 P.C. Sadek, P.W. Carr, R.M. Doherty, M.J. Kamlet, R.W. Taft and M.H. Abraham, Anal. Chem., 57 (1985) 2971.
5 P.W. Carr, R.M. Doherty, M.J. Kamlet, R.W. Taft, W. Melander and C. Horvath, Anal. Chem., 58 (1986) 2674.
6 M.J. Kamlet, M.H. Abraham, P.W. Carr, R.M. Doherty and R.W. Taft, J. Chem. Soc., Perkin Trans. 2, (1988) 2087.
7 J.H. Park, P.W. Carr, M.H. Abraham, R.W. Taft, R.M. Doherty and M.J. Kamlet, Chromatographia, 25 (1988) 373.
8 M.J. Kamlet, J.L.M. Abboud, R.W. Taft, J. Am. Chem. Soc., 99 (1977) 6027.

9 M.J. Kamlet, J.L.M. Abboud and R.W. Taft, Prog. Phys. Org. Chem., 13 (1981) 485.
10 M.J. Kamlet, J.L.M. Abboud, M.H. Abraham and R.W. Taft, J. Org. Chem., 48 (1983) 2877.
11 W.J. Cheong and P.W. Carr, Anal. Chem., 60 (1988) 820.
12 W.J. Cheong and P.W. Carr, Anal. Chem., 61 (1989) 1524.
13 T. Hanai and J. Hubert, J. High Resolut. Chromatogr. Chromatogr. Commun., 6 (1983) 20.
14 E. Bosch and M. Rosés, J. Chem. Soc., Faraday Trans., in press.
15 C.R. Yonker, T.A. Zwier and M.F. Burke, J. Chromatogr., 241 (1982) 257.
16 C.R. Yonker, T.A. Zwier and M.F. Burke, J. Chromatogr., 241 (1982) 269.
17 J.L. Jones and S.C. Rutan, Anal. Chem., 63 (1991) 1318.
18 M.J. Kamlet, P.W. Carr, R.W. Taft and M.H. Abraham, J. Am. Chem. Soc., 103 (1981) 6062.
19 M.H. Abraham, personal communication, 1991.
20 M.J. Kamlet, R.M. Doherty, M.H. Abraham, Y. Marcus and R.W. Taft, J. Phys. Chem., 92 (1988) 5244.
21 T.M. Krygowski, P.K. Wrona, U. Zielkowska and C. Reichardt, Tetrahedron, 41 (1985) 4519.
22 J.H. Park, M.D. Jang and D.S. Kim, J. Chromatogr., 513 (1990) 107.
23 Y. Marcus and Y. Migron, J. Phys. Chem., 95 (1991) 400.
24 J.H. Park, M.D. Jang and D.S. Kim, Bull. Korean Chem. Soc., 11 (1990) 297.
25 A. Leo, C. Hansch and D. Elkins, Chem. Rev., 71 (1971) 526.

Analytica Chimica Acta, 274 (1993) 163–170
Elsevier Science Publishers B.V., Amsterdam

Simultaneous determination of trace metals in human hair by dynamic ion-exchange chromatography

A. Sturaro, G. Parvoli and L. Doretti
Ufficio Sicurezza e Prevenzione del CNR, Corso Stati Uniti 4, 35020 Padova (Italy)

S. Zanchetta and G. Allegri
Dipartimento di Scienze Farmaceutiche dell'Università di Padova, Via Marzolo 5, 35100 Padova (Italy)

G. Battiston
Istituto di Chimica e Tecnologia dei Radioelementi del CNR, Corso Stati Uniti 4, 35020 Padova (Italy)

(Received 26th February 1992; revised manuscript received 21th September 1992)

Abstract

The simultaneous determination of six metal ions (Cu^{2+}, Zn^{2+}, Ni^{2+}, Mn^{2+}, Co^{2+}, Pb^{2+}) by using dynamic ion-exchange chromatography is proposed. The method was applied to the analysis of human hair after HNO_3–$HClO_4$ digestion, with detection limits of ca. 1 $\mu g\ g^{-1}$ for all the metals examined, using Co as an internal standard. The quantitative data were confirmed by analysing the same hair samples by atomic absorption spectrometry and x-ray fluorescence spectrometry.

Keywords: Ion exchange; Liquid chromatography; Hair; Trace metals

Human hair represents an interesting biological matrix for studies in the organic [1] and inorganic [2] fields. In the recent years it has had an important role owing to the particular exogenous substances accumulating in its structure and that are linked to specific situations [3,4]. From an inorganic point of view, the determination of metallic elements may constitute a biological index for workplace [5–7] and environmental [8–10] pollution or the presence of specific diseases [11–13].

Various different techniques have been employed in the detection of trace metals present in human hair. Optical methods such as atomic absorption spectrometry (AAS) and atomic emission spectrometry (AES) have been widely used owing to their simplicity, negligible matrix effects and significant levels of sensitivity and precision. However, they need average sample volumes of several millilitres and the measurements must be repeated for each element because, in general, single-element hollow-cathode lamps are used [14,15]. Another technique applied to hair analysis is x-ray fluorescence (XRF) spectrometry. This technique is sensitive for those elements above Si, but does not give satisfactory results when measuring lighter elements [16,17]. Yet another method for trace metals in hair is mass spectrometry (MS). In this instance the instrument uses a

Correspondence to: A. Sturaro, Ufficio Sicurezza e Prevenzione del CNR, Corso Stati Uniti 4, 35020 Padova (Italy).

spark source, the specific ionic source for the sample having a high melting point and low partial pressure [18,19]. This technique is very sensitive and specific but may suffer from spectral interferences due to the overlap of ionic organic fragments with the spectral lines of the elements which are present. Neutron activation analysis (NAA), rarely employed in chemistry laboratories, may also be used [20,21].

Liquid chromatography (LC) has been used for the determination of metals as ions in aqueous solutions [22–24]. The classical LC configuration (pump, column and UV detector) with the addition, on-line, of a post-derivatization apparatus allows a wider field of application of this method. This technique, which applies the reversed-phase dynamic ion-exchange chromatographic principle, requires only a knowledge of the common LC system [25,26]. In this work, the use of this LC method for the detection and determination of trace metals in human hair is proposed.

EXPERIMENTAL

Materials and chemicals

Each hair sample was ashed with 2 ml of nitric acid (65%, v/v) and 1 ml of perchloric acid (60%, v/v) with low metal concentrations, purchased from Merck (Darmstadt). Decomposition took place in 30-ml PTFE FEP (ethylene–propylene fluorurate) bottles with hermetic caps supplied by Nalgene (Rochester, NY).

Standard solutions containing 2000 μg ml^{-1}, used to obtain the calibration graphs for each element, were prepared by diluting commercial Tritisol standards (Merck) to 500 ml.

LC eluent contained 0.433 g of sodium octanesulphonate (98%), 6.063 g of sodium hydrogentartrate (98%), 50 ml of acetonitrile and water (LC grade) to give 1 l. For the preparation of the post-column derivatization solution, 206 ml of ammonia solution (30%, v/v) (99.99 + % pure), 52 mg of monosodium 4-(2-pyridylazo)resorcinol (PAR), 58 ml of glacial acetic acid and water (LC grade) to bring the volume to 1 l were used [27]. All these chemicals were supplied by Aldrich (Stenheim, Germany).

Millex-GV filters (0.22 μm) were employed (Millipore, Milford, MA) for filtration of the samples, eluent and post-derivatization solution.

Wet ashing apparatus

Human hair and oxidizing acids contained in PTFE bottles were wet ashed in an autoclave at 115°C. After decomposition, the liquid phase was evaporated on a sand-bath at 150°C.

LC separation and detection system

All the measurements were made with a Waters (Milford, MA) LC system consisting of a Model 600 E MS pump, a U6K manual injector, a Model 441 UV detector and a Model 990 plus MS photodiode-array (PDA) detector. The acquisition and processing of the data were carried out with an NEC (Boxborough, MA) APC IV computer, and the chromatograms and the results for the samples analysed were reported in graphical form using a Waters Model 990 and an NEC CP6 Pinwriter printer. A Waters Delta-Pak RP-18 stainless-steel LC column (150 mm × 3.9 mm i.d.) was used with 5-μm spherical particles and 100-Å pore diameter [27].

Chromatographic conditions

The metals were separated at room temperature using the chromatographic eluent adjusted to pH 3.65 at a flow-rate of 0.75 ml min^{-1} and degassed with helium at a flow-rate of 20 ml min^{-1}. The UV 441 detector recorded at a fixed wavelength of 546 nm with a sensitivity of 0.5 a.u.f.s. The PDA detector conditions were wavelength scan 470–600 nm, scan time 2 s, sensitivity 0.3 a.u.f.s. and resolution 1.4 nm. Quantitative analysis was carried out at 546 and 492 nm for the UV 441 and PDA detectors, respectively. The injection volume for all the samples was 100 μl.

Post-derivatization system

An RDM (reagent delivery module) post-column derivatization apparatus was supplied by Waters. This consisted of a T-connector which allowed the addition of a reagent to the column eluate, so that the examined metals had a reasonable absorbance in the UV region [28]. Such system was set up after the LC column and programmed at a post-derivatization solution flow-rate of 0.4 ml min^{-1}.

Preparation of standard solutions

Seven standard solutions, containing the different concentrations reported in Table 1 for Cu, Zn, Pb, Ni and Mn, were prepared to obtain the calibration graphs for the five metals examined. The chromatographic eluent was used for the preparation of the above solutions in 10 ml volumetric flasks. The solutions reported in Table 1 were equivalent to particular concentrations of each metal, defined as μg g^{-1} in the hair. All the solutions contained 0.4 μg ml^{-1} Co as an internal standard. Three absorbance measurements, related to each concentration level of the standard solutions, were recorded to allow statistical treatment of the data.

Preparation of samples

The human hair samples, not subjected to any chemical treatment, were collected from healthy people in the age range 6–40 years. The hair was washed with Aquet (Manostat, NY) non-ionic detergent solution (1%, v/v) and extracted with diethyl ether in a Soxhlet apparatus for 5 h so as to eliminate the presence of lipids and pollutants from environment such as dust, which may adhere superficially to hair [29]. After drying at 105°C for 12 h, the hair was pulverized by means of PTFE pellets.

A 200-mg amount of each hair sample was placed in a PTFE container and 2 ml of concentrated HNO_3 were added at room temperature. The bottles were left open for a few minutes until the appearance of brown fumes due to the oxidation of the more easily decomposed components.

The bottles were then hermetically sealed and placed in an autoclave at 115°C for 1 h. After cooling and having eliminated the smoke, 1 ml of concentrated $HClO_4$ was added to the bottles, repeating the above procedure in the autoclave. The liquid phase was completely evaporated on a sand-bath at 150°C.

The solid residue was dissolved in 10 ml of chromatographic eluent and the solution was filtered through a 0.22-μm membrane. A 20-μl volume of internal standard solution (200 μg ml^{-1} Co) was added to the solution before it was injected into the chromatograph.

AAS and XRF conditions

The same human hair samples, after digestion according to the above procedures, were analysed by an independent method to verify the LC data. An atomic absorption spectrometer (Varian Model AA 275; Techtron, Springvale, Australia) equipped with single-element hollow-cathode lamps was used for the determination of Cu and Zn at the detection wavelengths of 324.7 and 213.9 nm, respectively, using an air–acetylene flame. A total reflection x-ray fluorescence (TXRF) spectrometer was used for the determination of all six elements investigated, with Co as the internal standard. This instrument consisted of an EXTRA II module (R. Seifert, Ahrensburg, Germany) with double-beam excitation (molybdenum and tungsten tubes), an x-ray generator, an Si(Li) detector, an automatic sample changer and a computer-controlled multi-channel anal-

TABLE 1

Cu, Pb, Zn, Ni and Mn concentrations in the standard solutions used to obtain the calibration graphs

Solution	Cu		Pb		Zn		Ni		Mn	
	μg ml^{-1}	μg g^{-1}	μg ml^{-1}	μg g^{-1}	μg ml^{-1}	μg g^{-1}	μg ml^{-1}	μg g^{-1}	μg ml^{-1}	μg g^{-1}
1	0.04	2	0.1	5	1	50	0.02	1	0.002	0.1
2	0.10	5	0.2	10	2	100	0.04	2	0.004	0.2
3	0.20	10	0.5	25	4	200	0.10	5	0.010	0.5
4	0.40	20	1.0	50	6	300	0.20	10	0.016	0.8
5	0.80	40	2.0	100	8	400	0.30	15	0.020	1.0
6	1.20	60	3.0	150	10	500	0.40	20	0.030	1.5
7	1.60	80	4.0	200	12	600	0.50	25	0.040	2.0

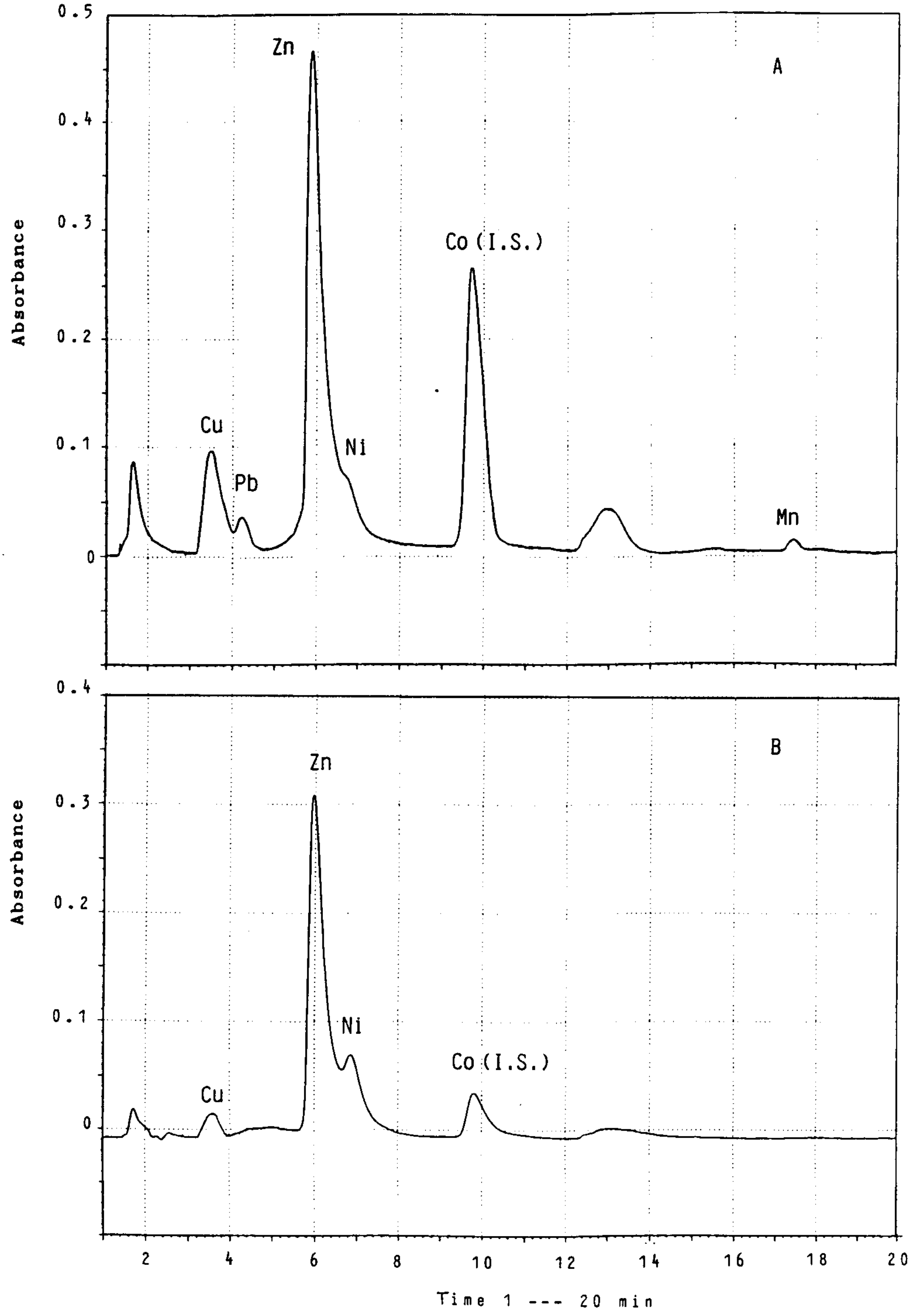

Fig. 1. Typical liquid chromatogram for the determination of Cu, Pb, Zn, Ni and Mn in human hair samples measured at (A) 546 and (B) 492 nm (Co internal standard).

yser system. The sample solutions (10 μl) were placed on the sample carrier (quartz disc) as a thin film obtained by evaporation of the solvent.

RESULTS AND DISCUSSION

Optimization of sample preparation

Organic compounds present in the samples or chromatographic eluent may contaminate the LC column when used in this type of analysis. The effects of this contamination result in the broadening of the peaks with a consequent decrease in their height, especially for the Cu and Ni peaks. As a result, a certain degree of sensitivity is lost with a subsequent higher detection limit, in that the peak height/area ratio is less favourable, and even where there are significantly high concentrations it is more difficult to distinguish this from the noise.

The main source of organic compounds is the sample itself, as the wet ashing is incomplete. Therefore, optimization of the decomposition phase is essential if the results are to be reproduced and accurate analyses of large numbers of samples are to be carried out. To ensure the least possible contamination the hair samples should be treated with a more aggressive oxidizing acid at a sufficiently high temperature, which results in better ashing. To this end, it was found that using 2 ml of HNO_3 first, followed by the addition of 1 ml of $HClO_4$ in two separate steps for each sample, gave the best results. In fact, when these two oxidizing agents were used together, the degradation of the hair sample was worse, owing to the strong action of the $HClO_4$ on easily oxidizable components and thus left fractions to be ashed that could not be degraded by the weaker HNO_3. By using the two acids in successive steps, the less powerful HNO_3 oxidized the more reactive components of the matrix, leaving the stronger $HClO_4$ acid to degrade completely the remaining, more resistant components. An interesting study which deals with partial wet ashing has been reported by Wurfels et al. [30].

To avoid any organic contamination of the chromatographic column, a precolumn (Nova-Pak RP-18, Waters) was connected on-line. Replacing such a device periodically, meant that the efficiency of the column was not compromised, as the unwanted effect of the organic compounds was eliminated. Using the precolumn also ensured the absence of organic compounds in the chromatographic eluent, which could represent a considerable source of contamination owing to its large volume.

Because of the low detection levels obtained with this LC method, considerable care should be taken to prevent any metal contamination by reagents or by the containers themselves. With reference to this latter point, only extremely pure acids should be used in order to avoid further increasing the levels of metals in the human hair samples. During our experiment, it was seen that the acid used could lead to an increase in the Ni peak by as much as 60% over its real value, although the Cu and Zn peaks were less affected because of their higher concentrations in the original samples.

Another factor affecting the analysis, was the kind of material of which the containers were made [31]. The adsorption and release of metals were possible phenomena that could arise between the solution and container material. It has been emphasized that the adsorption is influenced by the solution pH and that, in particular, pH values $\leqslant 4$ minimize such effects [32–34]. This phenomenon was negligible in these experiments owing to the low conservation time and the pH normally used ($\leqslant 3.65$). Choosing the materials for the bottles was important because of the release effects [31]. Among all the materials available, PTFE ensures minimum contamination of the samples [31]. Therefore, in all sample preparation phases this container material was used.

The injection volume required (100 μl) allowed the selection of a suitable dilution of the sample so as to exceed the detection limit for all the metals.

Performance of the method

Hair analysis by the LC method allowed the detection of Cu^{2+}, Pb^{2+}, Zn^{2+}, Ni^{2+} and Mn^{2+} in each chromatographic run of 25 min. Figure 1 shows a typical chromatogram, with Co as the internal standard.

TABLE 2

Detection limits for Cu, Pb, Zn, Ni and Mn elements according to the LC method

Element	Detection limit	
	ng ml^{-1}	$\mu g\ g^{-1}$
Cu	20	1
Pb	40	2
Zn	20	1
Ni	20	1
Mn	3	0.15

[a] Minimum area = 0.001 absorbance · min.

TABLE 3

Calibration equations $y = (a \times \text{concentration}) + b$ and concentration ranges ($\mu g\ g^{-1}$) for Cu, Pb, Zn, Ni and Mn metals, where y = metal area/internal standard area

Element	$a \times 10^3$	b	R^2	Concentration range ($\mu g\ g^{-1}$)
Zn	5.44	0.131	0.9962	50–600
Cu	17.78	−0.019	0.9972	2–80
Ni	6.01	−0.001	0.9964	1–25
Pb	11.09	−0.047	0.9989	5–200
Mn	25.33	0.0032	0.9849	0.1–2

[a] Seven triplicate determinations.

The presence of the very intense Cu peak interfered with the detection of Pb, which was present only at low concentrations, because the former immediately preceded the Pb peak in the chromatographic run. A similar situation was found with regard to the Zn–Ni pair. However, to detect the Ni peak effectively PDA detection was used, which reduced the interference by the Zn peak. The 546-nm wavelength of the UV filter detector was reliably sensitive with reference to all the metals except the Ni complex. The 492-nm PDA wavelength was more sensitive with respect to Ni as this wavelength represents the maximum absorbance value for this element only.

The validity of the method was confirmed by the high sensitivity of detection, which gave concentration values a few ng ml^{-1} for all the metals under examination. Table 2 gives the detection limits for all the elements recorded with a signal-to-noise ratio of 3, corresponding to an area of about 0.001 absorbance · min.

Linear calibration graphs were constructed for all the metal ions at the various concentration levels in the range of interest. The equations representing the seven sets of experimental data indicated good linearity as verified by the R^2 values (Table 3). The relative standard deviations (R.S.D.), calculated on three replicate determinations of the same concentration for all the metals are reported in Table 4.

According to the literature [35], the precision of data relating to biological samples should be in the region of R.S.D. $\leqslant 20\%$. A comparison between the limits of detection and determination limits is reported in Table 5 for the two units of measurement (ng ml^{-1} and $\mu g\ g^{-1}$). The quanti-

TABLE 4

Relative standard deviations ($n = 3$) for each concentration value of the Cu, Pb, Zn, Ni and Mn solutions

Zn		Cu		Ni		Pb		Mn	
Concentration ($\mu g\ g^{-1}$)	R.S.D. (%)	Concentration ($\mu g\ g^{-1}$)	R.S.D. (%)	Concentration ($\mu g\ g^{-1}$)	R.S.D. (%)	Concentration ($\mu g\ g^{-1}$)	R.S.D. (%)	Concentration ($\mu g\ g^{-1}$)	R.S.D. (%)
600	3.5	80	3.2	25	3.6	200	2.1	2	7.7
500	4.0	60	4.0	20	4.3	150	2.6	1.5	9.6
400	4.7	40	5.6	15	5.4	100	3.8	1.0	13.5
300	6.1	20	10.9	10	7.8	50	7.2	0.8	16.6
200	8.9	10	21.7	5	15.3	25	14.4	0.5	25.9
100	17.4	5	43.2	2	38.0	10	35.8	0.2	64.0
50	34.6	2	108	1	76.0	5	71.7	0.1	128.0

TABLE 5

Comparison between the detection and determination limits in the LC determination of Cu, Pb, Zn, Ni and Mn in hair [a]

Element	Detection limits		Determination limits	
	ng ml^{-1}	μg g^{-1}	ng ml^{-1}	μg g^{-1}
Cu	20	1	220	11
Pb	40	2	360	18
Zn	20	1	1700	86
Ni	20	1	76	3.8
Mn	3	0.15	13	0.65

[a] Minimum area = 0.001 absorbance·min. R.S.D. = 20%.

tative detection of more abundant elements such as Zn, Cu and Pb shows high limit values, because they were strictly linked to the particular concentration range, used to obtain the calibration graphs corresponding to the real concentrations in human hair.

Evaluation of the method

The accuracy of the LC method was verified by comparing the data with those obtained for the same hair samples using AAS and XRF. These two methods were chosen because they represent the most widely used approaches in the investigation of trace metals in human hair [2].

Table 6 shows the average concentrations (μg g^{-1}), the range of values found for Zn, Cu, Ni, Mn and Pb by the three methods on a total of 30 human hair samples and the percentage differences between the LC and the AAS and XRF results. The measurements done with AAS allowed the detection only of Cu and Zn because these elements were present in appreciable concentrations in the amount of hair analysed (200 mg). The average values obtained with the three different methods for Zn and Cu compared well, thus confirming the validity of the RP-LC system for the quantitative analysis of this particular and complex matrix.

For Ni, Mn and Pb there were differences between the values obtained by LC and XRF, with the XRF data having higher values. If from a qualitative point of view the presence of these metals was verified, an R.S.D. > 20% must be attributed to the data for Ni and Pb because their levels were below the determination limits, as reported in Table 5.

Further, LC, unlike the XRF method, did not detect the presence of Pb in all the samples analysed, probably owing to the interference of the high and close Cu peak. The LC values for the Mn were sufficiently reliable and compared well with those obtained by XRF, considering the low concentration of this metal in human hair.

Conclusions

The proposed method for the determination of trace metals in human hair has certain advantages, mainly owing to the wide availability of LC instruments. The high precision and accuracy and the low detection limits make this technique suitable for the simultaneous determination of a number of elements found together even in complex matrices. The LC study of six elements (Cu, Zn, Ni, Mn, Pb and Co as internal standard) in human hair was significant for Zn, Cu and Mn but not for Ni and Pb because their concentration

TABLE 6

Cu, Pb, Zn, Ni and Mn average concentration values and range determined in the same human hair samples using LC, XRF and AAS and average percentage differences between the LC and the XRF and AAS results

Method	Parameter	Zn	Cu	Ni	Mn	Pb
LC	Average concentration (μg g^{-1}) [a]	238 ± 12	16 ± 1	1.2 ± 0.1	0.8 ± 0.1	7 ± 1
	Range (μg g^{-1})	189–319	11–22	1.0–1.8	0.6–1.3	5–9
XRF	Average concentration (μg g^{-1}) [a]	226 ± 13	16 ± 1	2.2 ± 0.2	1.1 ± 0.1	7.7 ± 0.6
	Range (μg g^{-1})	171–314	10–21	1.4–3.2	0.7–1.8	6.5–8.7
	Difference from LC (%)	5.6	5.5	90	36	19
AAS	Average concentration (μg g^{-1}) [a]	235 ± 16	16 ± 1	–	–	–
	Range (μg g^{-1})	169–350	11–22	–	–	–
	Difference from LC (%)	6.6	7.7	–	–	–

[a] Mean ± S.D. ($n = 30$).

levels were lower than the determination limits. The results obtained were confirmed by analysing the same hair samples by AAS and XRF.

REFERENCES

1 H.B. Matthews, J.J. Domanski and F.E. Guthrie, Xenobiotica, 6 (1976) 425.
2 V. Valkovic, Human Hair, Vol. I–II, CRC, Boca Raton, FL, 1988.
3 F. Tagliaro, P. Traldi, B. Pelli, S. Maschio, C. Neri and M. Marigo, in G. Piemonte, F. Tagliaro, M. Marigo and A. Frigerio (Eds.), Developments in Analytical Methods in Pharmaceutical, Biomedical and Forensic Sciences, Plenum, New York, 1987, pp. 115–127.
4 S. Forshufvud, Nature, 300 (1982) 680.
5 U. Tomza, T. Janicki and S. Kossman, Radiochem. Radioanal. Lett., 58 (1983) 209.
6 W. Grund, W.D. Schneider and W. Wiesener, J. Radioanal. Chem., 58 (1980) 319.
7 L. Raghupathy and V.N. Sharma, Sci. Total Environ., 41 (1985) 73.
8 T. Takeuchi, Y. Nakano, S. Ohmori, A. Aoki and M. Kasuya, J. Radioanal. Nucl. Chem., 144 (1990) 97.
9 G. Balazova, P. Truska, O. Palusova and M. Ursinyova, Cesk. Hyg., 30 (1985) 383.
10 V. Bencko, T. Geist, D. Arbetova and D.M. Dharmadikari, Spurenelemente Symposium, 4th, Friedrich Schiller University, Jena, 1983, p. 355.
11 G. Vivoli, P. Borella, M. Bergomi and G. Fantuzzi, Sci. Total Environ., 66 (1987) 55.
12 Y. Sha, P. Liu, R. Zhang, G. Liu, Z. Zhang, Y. Feng, G. Liu, G. Sun and S. Wang, Nucl. Instrum. Methods Phys. Res., B22 (1987) 191.
13 D. Shore, R.I. Henkin, N.R. Nelson, R.P. Agarwal and R.J. Wyatt, J. Am. Geriatr. Soc., 32 (1984) 892.
14 G. Bagliano, F. Benischek and I. Huber, Anal. Chim. Acta, 123 (1981) 45.
15 G. Allegri, C. Costa, M. Biasolo, R. Arban, A. Bertazzo, E.L. Cardin De Stefani, Ital. J. Biochem., 39 (1990) 209.
16 H. Kubo, Phys. Med. Biol., 26 (1981) 867.
17 M. Folin, E. Contiero and I. Calliari, Ann. Chim. (Rome), 81 (1991) 39.
18 J.P. Yurachek, G.G. Clemena and W.W. Harrison, Anal. Chem., 41 (1969) 1666.
19 V. Valkovic, Trace Element Analysis, Halsted Press, New York, 1975.
20 L.C. Bate, W.B. Healy and G. Ludwigt, N.Z.J. Sci., 9 (1966) 559.
21 J. Osbrusnik and V. Bencko, Radiochem. Radioanal. Lett., 38 (1979) 189.
22 M. Adachi, K. Oguma and R. Kuroda, Chromatographia, 29 (1990) 579.
23 D.J. Barkley and T.E. Dahms, in P.A. Williams and M.J. Hudson (Eds.), Recent Developments in Ion Exchange, Elsevier Applied Science, London, 1987, pp. 396–401.
24 M. Deacon, M.R. Smith and R.G. Leonard, Analyst, 116 (1991) 897.
25 R.M. Cassidy and S. Elchuk, Anal. Chem., 54 (1982) 1558.
26 J. Krol, Waters Ion Chromatography Notes, Vol. 2, Waters Chromatography Division, Millipore, Milford, MA, 1988, pp. 3–5.
27 Ion Chromatography Cookbook, Waters Chromatography Division, Millipore, Milford, MA, 1990.
28 A. Siriraks, H.M. Kingston and J.M. Riviello, Anal. Chem., 62 (1990) 1185.
29 W.W. Harrison, J.P. Yurachek and C.A. Benson, Clin. Chim. Acta, 23 (1969) 83.
30 M. Wurfels, E. Jackwerth and M. Stoeppler, Anal. Chim. Acta, 226 (1989) 1, 17.
31 J.C. Van Loon, Selected Methods of Trace Metal Analysis: Biological and Environmental Samples, Wiley, New York, 1985.
32 A.W. Struempler, Anal. Chem., 45 (1973) 2251.
33 K.S. Subramanian, C.L. Chakrabarti, J.E. Sveiras and I.S. Maines, Anal. Chem., 50 (1978) 444.
34 P. Benes and A. Garba, Radiochim. Acta, 5 (1966) 99.
35 J. Chamberlain, Analysis of Drugs in Biological Fluids, CRC, Boca Raton, FL, 1987, pp. 156–160.

Analytica Chimica Acta, 274 (1993) 171–177
Elsevier Science Publishers B.V., Amsterdam

Effect of relative humidity on the performance of a platinum–lead denuder for the adsorption of nitrobenzene

C.L.P. Thomas and J.F. Alder

Department of Instrumentation and Analytical Science, UMIST, P.O. Box 88, Manchester M60 1QD (UK)

(Received 24th July 1992; revised manuscript received 26th October 1992)

Abstract

A platinum–lead coated annular denuder has been tested with humid atmospheres laden with nitrobenzene. Atmospheres in the range 20–99% relative humidity at 12.5°C laden with 16 μg m^{-3} nitrobenzene were employed. Measurements of the nitrobenzene leaving the denuder were made by a gas chromatograph fitted with an electron capture detector. Results demonstrate the dramatic effect of high relative humidity on the performance of the denuder. Above 47% relative humidity the denuder showed immediate breakthrough of nitrobenzene and a greatly reduced capacity compared with relative humidity of $\leq$ 20%. It is believed that the presence of multilayers of sorbed water on the metal surface is the reason for the reduced efficiency of the denuder.

Keywords: Gas chromatography; Humidity effects; Platinum–lead denuder

Previous work in this laboratory [1,2] and elsewhere (reviewed in Ref. 3) has demonstrated the potential of annular denuder tubes for selective sorption of organic vapours and gases from the atmosphere.

The concentration and determination of trace gases in the atmosphere using active surfaces as either sensors or concentrators cannot be considered in isolation from the influence of water vapour on the system employed. Water vapour is present in the air in the 10 g m^{-3} range at usual atmospheric temperatures, pressures and altitude [4]. This is a three orders greater concentration than the occupational exposure limit for nitrobenzene (5 mg m^{-3}) [5] which was the target analyte in these studies [1]. One would expect, therefore, an influence of water vapour on the performance of denuder tube concentrators towards nitrobenzene.

Water vapour adsorbs onto metal surfaces readily, and the enthalpy change which accompanies non-dissociative H_2O adsorption does not vary widely for different metals, being typically -50 kJ mol^{-1} [6, p. 241], on a smooth surface. The enthalpy of adsorption on an atomically rough surface will be 10–20 kJ mol^{-1} greater than this [6, p. 265]. The platinum–lead surface used in this work was grey, as opposed to shiny [1] and it is likely therefore that the surface was atomically rough. The adsorption of water onto the metal surface is followed by rapid surface diffusion, with the tendency to form water clusters, however it is not necessary to assume high mobility of the adsorbed water. According to Thiel and Madey [6, p. 254], "all available evidence indicates that adsorption of H_2O on metals is not activated; adsorption probabilities are close to unity and not temperature dependent

---

Correspondence to: C.L.P. Thomas, Department of Instrumentation and Analytical Science, UMIST, P.O. Box 88, Manchester M60 1QD (UK).

below the onset of desorption". The adsorption kinetics of water apparently reflect the fact that it is energetically equivalent to chemisorb directly at the metal, or to hydrogen bond with other water molecules. Multilayers can start to form even before the first layer is saturated [1]. On atomically rough surfaces, it is believed that the adsorbed water molecules occupy positions at the top of the ridges or steps of the surface [6, p. 265]. One therefore has a picture of the metal surface exposed to high concentrations of water vapour (g m^{-3}) at atmospheric temperature and pressure as being covered to a large extent with a quite strongly adsorbed water film. For nitrobenzene to be adsorbed on this surface it would need to penetrate this film, displace water, and be itself adsorbed onto the metal surface. Concurrent work in this laboratory [7] has demonstrated similar effects with the sorption of chloropicrin onto wetted carbon surfaces, and demonstrated (on a macro-scale) that chloropicrin does indeed displace water both from capillaries and the open surface of the carbon. One might cautiously imagine a similar situation on the platinum–lead surface.

In the present study the effect of wetting the surface of the platinum–lead denuder tube described elsewhere [1,2], was investigated, to determine the degradation in concentration efficiency that would occur.

EXPERIMENTAL

The experimental arrangement and details of the procedures employed for measuring the nitrobenzene breakthrough curves have been described in detail elsewhere [1]. The apparatus was modified (Fig. 1) to incorporate the humidity generator which is described in detail in another paper [8]. Briefly, a PTFE permeation tube containing 0.1 g of nitrobenzene is maintained at 30°C in an oven. The nitrobenzene source is placed in a gas line with a constant flow of dried oxygen-free nitrogen over it. The approximate release rate was 370 pg s^{-1} and the resulting test atmosphere was passed to a stainless steel four-way valve for switching into and out of the test apparatus. Detection of the nitrobenzene was with a electron capture detector (Chrompak, London).

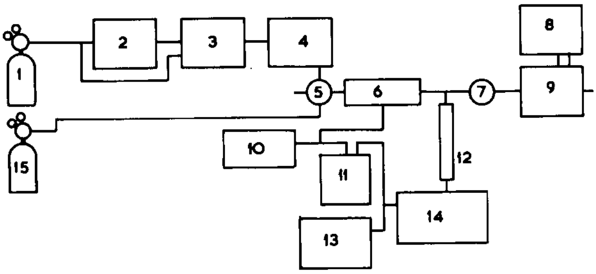

Fig. 1. Experimental rig [1,8]. 1 = Air; 2 = humidifier; 3 = humidity controller; 4 = nitrobenzene vapour generator; 5 = 4-way inlet valve; 6 = denuder tube in induction heater; 7 = exhaust valve; 8 = chart recorder; 9 = humidity meter; 10 = thermometer; 11 = chart recorder; 12 = heated sample transfer line; 13 = integrator; 14 = gas chromatograph; 15 = nitrogen, oxygen free and dried. Most pipework was stainless steel with a few connections in PTFE tubing and glass.

The humid atmospheres were generated by blending a humid air stream with a dry air stream in a solenoid operated mixing valve (Fig. 2). The valve was driven by a programmable controller

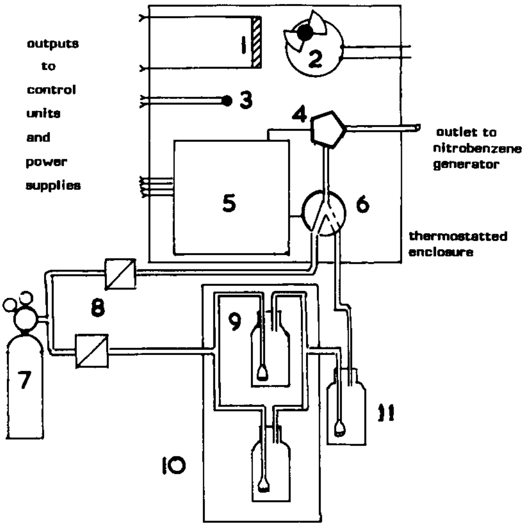

Fig. 2. Humidifier and humidity controller [8]. 1 = Heater; 2 = fan; 3 = thermistor; 4 = humidity sensor; 5 = humidity control unit; 6 = solenoid operated switching valve; 7 = air; 8 = flow controller sand meters; 9 = bubblers containing water; 10 = constant temperature water bath; 11 = mist trap. Most pipework was stainless steel with a few connections in PTFE and glass.

which adjusted the mixing ratio. The blended air was passed through a mixing coil to a humidity sensor (Panametrics, Surrey) and the response of the sensor was fed back to the humidity controller. The relative humidity was checked with a Vaisala (Cambridge) HM132 humidity sensor. The controller was capable of maintaining the relative humidity (RH) to within ± 0.5% RH over the range 0–80% RH at 23–25°C. The calibrated humid atmosphere and the nitrobenzene test atmosphere, of known concentration, were then mixed and passed into the platinum–lead coated denuder tube. The denuder was of a somewhat different design to that used previously [1], and consisted of two parts, an outer thimble and an inner finger, both made from fused silica (Fig. 3). The outer thimble was fitted with a B19 ground glass socket and two side arms. Its internal surfaces were frosted by grinding with an abrasive paste. The inner finger was fitted with a B19 ground socket and had a co-axial inlet. Its outer surfaces were frosted by sandblasting. Before gold and platinum–lead surfaces were applied the frosted quartz surfaces were thoroughly cleaned by washing with Decon 75 (BDH, Poole) followed by rinsing with doubly distilled water. The denuder sections were then dried in an oven for approximately 1 h at 70°C.

The gold surface was applied to the collection surface using Liquid Brightgold (Englehard, Cinderford), a ceramic finishing product. Liquid Brightgold was painted onto the frosted surfaces and allowed to dry at room temperature. The quartz pieces were then placed into an oven and heated to approximately 550°C for 5 h. This procedure was repeated to ensure an adequate gold support for the electrodeposition of the platinum–lead surfaces. After the final application the units were rinsed in doubly distilled water and dried overnight at 70°C.

Platinum–lead surfaces were produced in the same way as previously reported [1].

The complete unit was held within the water-cooled coil of a 3-kW induction heater (Inductelec, Sheffield). The denuder unit could be rapidly heated in the coil to a desorption temperature of 300°C in 20 s. On completion of desorption the denuder unit was cooled back to a constant temperature of 12.5°C. The temperature of the unit was monitored with a thermocouple during the course of the experiments.

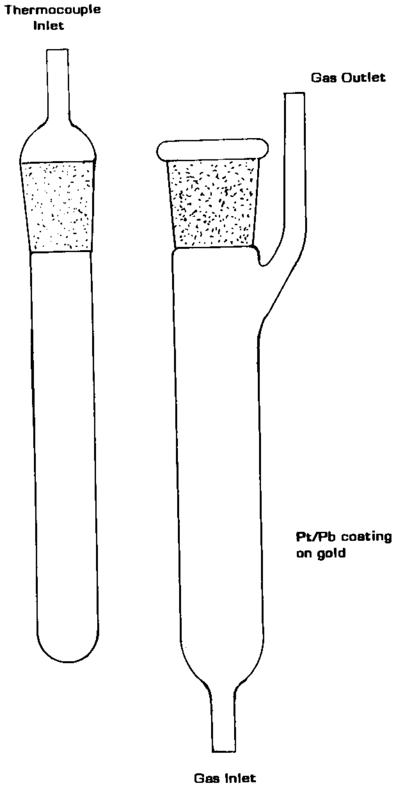

Fig. 3. Denuder tube assembly. Made from transparent fused silica with B19 cone and socket. The outside of the male tube and the inside of the female tube are coated with platinum–lead [1] laid down on gold. A thermocouple is placed inside the male tube in thermal contact with the wall. The whole assembly is fitted within the induction heater coil, gas connections are made with compression fittings.

Procedures

The relative humidity of the test atmosphere was the only variable parameter in these tests. All other variables were fixed and are given in Table 1. Breakthrough curves and desorption profiles were obtained for each of the humidities studied. Each run comprised three parts: conditioning, challenge and calibration.

Conditioning. Prior to a test the denuder was thermally desorbed in accordance with previously described procedures [1]. The resulting desorp-

TABLE 1

Instrumental and experimental parameters

Instrumental	
Gas chromatograph model	Packard 437A
Oven temperature	120°C
Detector temperature	250°C
Injector and sample valve temperature	175°C
Column	10 m × 0.53 mm i.d. WCOT fused-silica coated with CP Sil 19CB
Inlet pressure	100 kPa
Carrier gas flow-rate	23.8 $cm^3 min^{-1}$
Make-up gas flow-rate	41.8 $cm^3 min^{-1}$
Experimental	
Denuder tube temperature	12.5°C
Sample flow-rate	1427 $cm^3 min^{-1}$
Nitrobenzene concentration	16 $\mu g m^{-3}$
Desorption gas flow-rate	28.3 $cm^3 min^{-1}$
Sample volume	42.81 dm^3
Humidifier inlet pressure	1.5 bar
Dry air inlet pressure	4 bar
Sample transfer line temperature	150°C

tion profile was scrutinised for evidence of desorbed nitrobenzene and if present in anything other than trace amounts, the desorption procedure was repeated until an acceptable blank was obtained.

Challenge. At the beginning of each test a relative humidity test atmosphere was selected and passed to the four-way inlet valve of the denuder tube, where it was exhausted and the inlet RH recorded. Once the RH was stable the outlet valve of the denuder was opened, the inlet valve switched over to its sample position, and the gas chromatograph programme was started. Throughout the sample period the relative humidity at the denuder tube outlet was monitored. At 120 s before the end of the sample period the integrator and the gas chromatograph were stopped, and their parameters adjusted for the thermal desorption sequence. The induction heater parameters were then set and the digital thermometer, which monitored the temperature inside the male component of the denuder, turned on and adjusted to the appropriate scale. At the end of the sample period the four-way inlet valve was set to the desorption position before the outlet valve was shut off. The denuder was then purged for 30 s before it was thermally desorbed.

Calibration. After the thermal desorption procedure was finished the sample inlet of the gas chromatograph was connected to the exhaust of the four-way inlet valve and a series of calibration samples taken. This process was repeated after every other run unless the baseline signal of the electron capture detector had shifted significantly.

RESULTS AND DISCUSSION

The conditioning step was incorporated because the desorption procedure had been developed for use with dry test atmospheres (RH $\leq$ 5% at 12.5°C). In the present experiments relatively large quantities of water vapour were passed through the system, so the additional blank desorption step was incorporated to ensure that the initial condition of the system was the same for all tests.

Quantities of water were seen to condense within the side arm of the denuder during the desorption procedure following sampling of high relative humidity test atmospheres (RH > 70% at 12.5°C). The condensate was only cleared after the second desorption procedure (i.e., the next conditioning run).

In two of these conditioning runs significant quantities of nitrobenzene were detected. Prior to these tests the system had been shut down overnight or longer. Furthermore, the mass of analyte desorbed seemed to be dependent on the recent history of the denuder tube, and the length of time the system had been shut down with purge gas flowing through it.

Examples of the desorption profiles are given in Figure 4. The source of nitrobenzene could be attributed to the release of absorbed analyte from the PTFE tubing connecting the denuder tube to the rest of the system. In Fig. 4A, the desorption profile has two peaks, suggesting two adsorption mechanisms at work within the unit. It seems likely that the analyte was adsorbed in significant

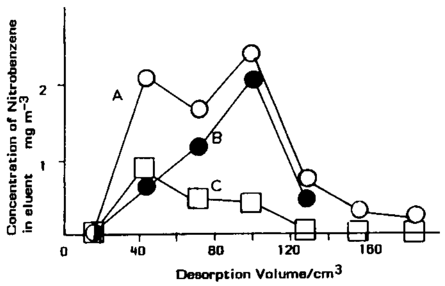

Fig. 4. Desorption profiles and their relationship to history of denuder exposure. A (○), 200 ng nitrobenzene desorbed, first desorption after system had been shut down for 31 days. B (●), 12 ng nitrobenzene desorbed, second desorption, after "A"; shift in maximum indicates desorption from silica. C (□), 44 ng nitrobenzene desorbed, system had been shut down for 14 h. Maximum corresponds to desorption from Pt–Pb surface. Last run had been with air of RH 21.1% at 12.5°C.

quantities on the fused silica and metal surfaces of the denuder tube. The second peak would be associated with the silica surfaces, for these would be indirectly heated by the platinum–lead collection surfaces and so their temperature would lag behind in the desorption cycle. Figure 4B is the profile obtained from a second blank desorption run immediately after that described above. The maximum of this desorption profile is shifted towards a larger desorption volume of 100 cm^3. This indicates that analyte was still being released from silica surfaces. Profiles 4A and 4B may be compared to the profile shown in Figure 4C, obtained after the system had been left standing overnight after sampling a nitrobenzene test atmosphere with an RH of 20% at 12.5°C; two peaks are discernible. When conditioning runs were performed after the system had sampled high humidity atmospheres (RH $\geq$ 70% at 12.5°C) containing nitrobenzene, and then been left to stand overnight, no nitrobenzene was observed in the desorption profile these results support the findings that the wetted silica and PTFE surfaces do not sorb significant amounts of nitrobenzene.

Breakthrough profiles

A sample of breakthrough profiles for nitrobenzene-laden air at various relative humidities is given in Fig. 5. There is a marked trend in the curves from the classic sigmoid shape at 21% RH, to immediate breakthrough at 47%, and then decreasing capacity at higher RH. The 70% RH profile was obtained after the denuder had been exposed to nitrobenzene in dry air. The initial peak indicates removal of nitrobenzene from the non-heated parts of the denuder, the

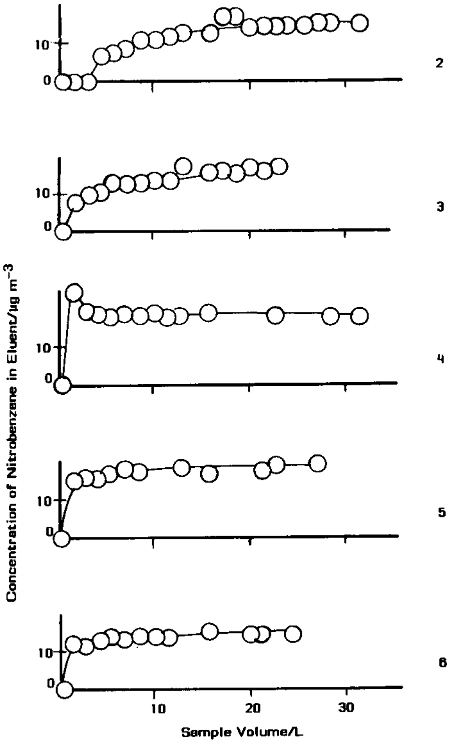

Fig. 5. Denuder breakthrough profiles for nitrobenzene laden air at different relative humidities. Conditions (B.V. = breakthrough volume, in l; E.V. = equilibration volume, in l; M.R. = mass retained, in ng; M.D. = mass desorbed, in ng): Run 1, RH = < 0.1, B.V. = 4, E.V. = not measured, M.R. = not measured, M.D. = 188. Run 2, RH = 21.1, B.V. = 3.00–4.43, E.V. = 27.5, M.R. = 130, M.D. = 112. Run 3, RH = 47.0, B.V. = < 1.57, E.V. = 20, M.R. = 82, M.D. = 82. Run 4, RH = 70.0, B.V. = < 1.57, E.V. = < 1.57, M.R. = not measured, M.D. = 1.1. Run 5, RH = 80.0, B.V. = < 1.57, E.V. = < 1.57, M.R. = not measured, M.D. = 4.8. Run 6, RH = 99.1, B.V. = < 1.57 E.V. = 7.5, M.R. = not measured, M.D. = 5.8. Run 7 not shown, saturated, B.V. = < 1.57, E.V. = 10, M.R. = 29, M.D. = 14. Run 8 not shown, saturated, B.V. = < 1.57, E.V. = not measured, M.R. = not measured, M.D. = 17. The profile obtained for < 0.5% RH is not shown, it is very similar to profile 2. Two other profiles were obtained with the vapour saturated which were almost identical to the plot of Run 5, and are therefore not shown.

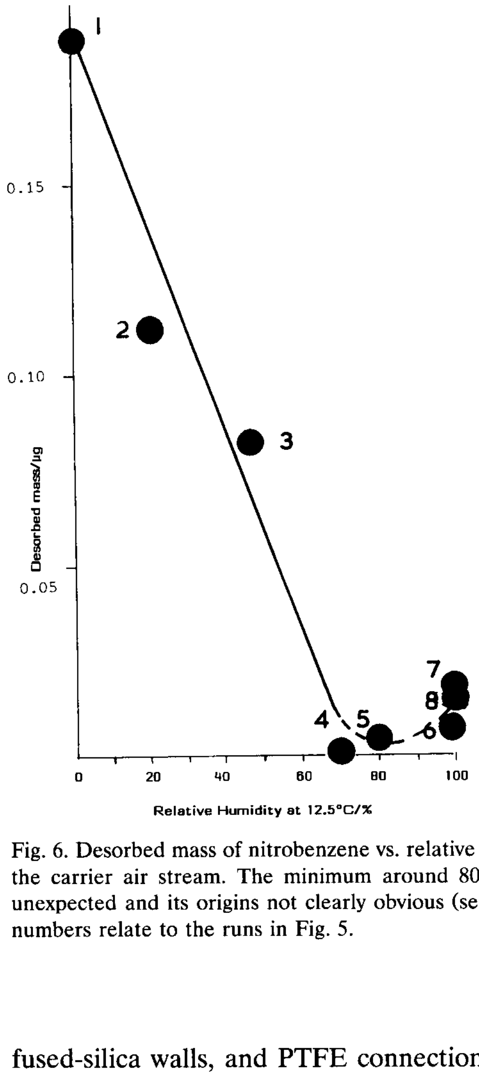

Fig. 6. Desorbed mass of nitrobenzene vs. relative humidity of the carrier air stream. The minimum around 80% RH was unexpected and its origins not clearly obvious (see text). The numbers relate to the runs in Fig. 5.

fused-silica walls, and PTFE connections. This is a typical example of the phenomenon which was observed regularly in the work. By 99% RH (at 12.5°C) the breakthrough profile had achieved its limiting shape, with almost immediate breakthrough and minimal adsorption capacity.

Desorbed mass of nitrobenzene

The plot of desorbed mass of nitrobenzene from the denuder during the desorption cycle vs. relative humidity of the ambient air is shown in Fig. 6. The small increase at 99% RH (at 12.5°C) may be due to condensation of water into a liquid film with dissolution of the nitrobenzene in the water. The actual surface area of the denuder is quite large (ca. 100 cm^2) and the amount of nitrobenzene desorbed is 20 ng, so this is a possible explanation, although it is not entirely convincing. In view of the propensity of water to form multilayers even with only partial coverage [6, p. 254], one would expect the curve to decrease asymptotically rather than go through a minimum as was observed. Another explanation might be the condensation of a nitrobenzene hydrate from the gas phase in the aerosol formed, with subsequent sorption onto the water film. This effect could be due to experimental error however, and the point should be investigated further.

Conclusions

It is clear that humidity disrupts the concentration of nitrobenzene by the denuder tube; the capacity of the denuder tube decreases linearly by 1.2% for each 1% increase in relative humidity at 12.5°C (Fig. 6). The disruption of denuder tube operation by relative humidity has been previously reported [9], and the collection surfaces were heated to reduce the effect. As important however are the implications for other active surfaces, such as are employed on piezoelectric, semiconductor or potentiomeric sensors, where not only will the sensor be affected by the presence of water vapour, the response sensitivity to nitrobenzene (and like compounds) will be reduced.

This work was supported by the Procurement Executive, Ministry of Defence, to which the authors are grateful.

REFERENCES

1 C.L.P. Thomas and J.F. Alder, Anal. Chim. Acta, 217 (1989) 289.
2 J. McEntee, C.L.P. Thomas and J.F. Alder, Anal. Chim. Acta, 226 (1989) 145.
3 Z. Ali, C.L.P. Thomas and J.F. Alder, Analyst, 114 (1989) 759.
4 R.C. Weast (Ed.), Handbook of Chemistry and Physics, CRC Press, Boca Raton, FL, 1979, p. E41.

5 Health and Safety Executive, Guidance Note EG40/87, Occupational Exposure Limits, HM Stationary Office, London, 1987.
6 Surface Sci. Rep., 7 (1987).
7 P.J.C. Anstice, N. Halliday and J.F. Alder, Ads. Sci. Tech., 7 (1990) 107.
8 C.L.P. Thomas, J.F. Alder, P.R. Fielden, A.R.M. Przybylko, R.D. Snook and A.F.R. Watson, Anal. Chim. Acta, 274 (1993) 179.
9 M. Ferm, Atmos. Environ., 20 (1985) 1193.

Analytica Chimica Acta, 274 (1993) 179–183
Elsevier Science Publishers B.V., Amsterdam

Precision humidifier for dynamic test atmosphere generators

C.L.P. Thomas, J.F. Alder, P.R. Fielden, A.R.M. Przybylko, R.D. Snook and A.F.R. Watson

Department of Instrumentation and Analytical Science, University of Manchester Institute of Science and Technology, P.O. Box 88, Manchester M60 1QD (UK)

(Received 24th July 1992; revised manuscript received 26th October 1992)

Abstract

A low-cost precision humidity generation technique capable of producing constant humidity atmospheres at variable flow-rates is described. The stability of the humidity generation was to within ±0.5% relative humidity at ambient temperature per hour over a continuously variable range of humidity, from 0 to 80% relative humidity at ambient temperature.

Keywords: Atmospheric monitoring; Humidity generator

Atmospheric monitoring systems must be able to tolerate a range of water vapour concentrations in their operating environment. Accurate characterisation of a sensor with respect to changes in relative humidity (RH) is an essential stage of prototype and method development. Many workers have used saturated salt solutions to generate standard RH atmospheres, either through recirculating or static headspace techniques [1]. While being convenient, saturated salt solutions may be regarded as unsuitable sources for three reasons: they require a long equilibration time, the carry over of salt aerosol or particulates often disrupts test instrumentation in a non-quantifiable manner, and they are difficult to use in conjunction with dynamic test atmosphere generation techniques. The last reason is especially important when sensing systems are to be evaluated for their response to toxic vapours, where dynamic methods are preferred for test atmosphere generation [2]. An alternative approach, embodied in some commercial equipment, involves blending streams of wet and dry air with humidity control being achieved through the variation of the mixing ratio. Such systems operate at a fixed flow making them cumbersome to use for dynamic test atmosphere generation, where the concentration of the analyte is often controlled through adjustment of gas flows.

Harvey et al. [3] highlighted the need for low-cost precision RH generators. In order to evaluate a series of RH sensors and designs a generator was developed to produce static standard RH atmospheres in a thermostatic container. A pump recirculated air through a bubbler and then back to the test enclosure. The pump was operated on a feedback control loop based on the signal of a relative humidity sensor located in the test enclosure. Although the authors reported some problems with condensation, their data indicated a system capable of generating stable test atmospheres with short equilibration times.

The work described here is based in part on the approach described above. Two streams of

Correspondence to: C.L.P. Thomas, Department of Instrumentation and Analytical Science, UMIST, P.O. Box 88, Manchester M60 1QD (UK).

purified air, one saturated with water vapour and the other one dry, were mixed by solenoid actuated valve switching between the two streams. The eluting gas streams were then fed into a short mixing column. The signal from a relative humidity sensor located downstream of the valve and mixing assembly was used to control the mark space ratio of the valve, and hence the proportion of dry and wet air switched into the mixing column.

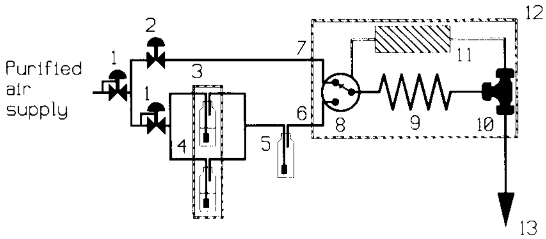

Fig. 1. Schematic diagram of the humidity generator. 1 = Pressure regulator; 2 = needle valve; 3 = water bath at 318 K; 4 = epoxy lined aluminium bubblers; 5 = condensor; 6 = wet air inlet at > 95% RH, 308 K; 7 = dry air inlet at < 1% RH, 308 K; 8 = switching valve; 9 = mixing coil, 200 mm of 3.2 mm o.d. PTFE tubing; 10 = swagelok T-union in 316 stainless-steel housing humidity sensor fixed into a PTFE ferrule; 11 = humidity control electronics; 12 = thermostatic housing at 308 K; 13 = outlet.

DESCRIPTION OF THE HUMIDITY GENERATOR

The humidity generator was based on three interacting systems: a conditioned pressurised air supply, temperature regulation, and humidity control. Cylinder air (BOC, Guildford) was cleaned and dried, using standard gas chromatography gas treatment systems (Chrompack, London), before it was split into two streams. One was passed through a secondary regulator before entering a humidification assembly, after which it was connected to the inlet of a mixing valve. The other air line was passed directly to the mixing valve inlet. The flow through the mixing valve was controlled by needle valves located upstream of the mixing assembly. The combined action of the mixing valve and flow controls enables a continuously variable range of standard RH test atmospheres to be produced at variable flow-rates. Figure 1 is a schematic diagram of the whole system.

Temperature regulation

All the humidity control components were maintained at a constant temperature of 308 K. This was an essential feature of the design. The control signal from the humidity sensor was based on capacitance changes caused by the absorption of water into a polymer film producing a shift in the dielectric constant of the sensing element. Variations in the temperature of the sensor would have interfered in the sensing mechanism and led to an irreproducible and unstable response from the whole humidity generation system.

Temperature control was achieved by using a 40 Ω Nichrome wire heater, run from the feedback signal produced by a thermistor located in the thermostatic enclosure. All the components were supplied by RS Components (Corby), and standard circuit designs and construction techniques were used to produce a temperature controller of the required precision [4]. A fan mounted inside the enclosure was run continuously to ensure an even temperature distribution, and the temperature was maintained to a stability of better than ±0.5 K. It should be noted that if ambient temperatures were to approach 308 K then additional cooling might be required. This unit was not used under such conditions and this aspect of the design was not investigated further.

Humidity control

Humidity control was achieved using a miniature solenoid-actuated valve (Lee Products, UK) that rapidly switched between the wet and dry air streams. The gas from the valve outlet was mixed in a turbulent flow in PTFE tubing, 10 cm long and 1.56 mm o.d. (Phase Separations, Deeside) before entering the humidity sensor cell. The humidity sensor was a Minicap II (Panametrics, Surrey) and was fitted into a Swagelok T-Union (Manchester Valves and Fittings, Warrington) using a one-piece 6.4 mm PTFE ferrule and epoxy resin (Phase Separations). The test atmosphere then exited the sensor cell and was passed through the walls of the enclosure using 3.2 mm o.d. PTFE tubing (Phase Separations). Figure 2 is a schematic diagram of the humidity sensing and control circuitry.

Humidity generation

Wet air was generated by using two bubblers in parallel. The pressure at the inlet to the bubblers was maintained at 0.67 bar by a pressure regulator. This was to ensure that excessive pressure build-up did not occur within the humidifier when the mixing valve shut down the wet air supply to the mixing column. The flow was then split and passed through two glass bubblers immersed in high purity water (18 $M\Omega\ cm^{-2}$). The two air streams were combined before being sent to a condenser. Here entrained aerosol was removed and the temperature of the humidified air equilibrated with ambient temperature, before it was passed to the wet input of the mixing valve. The bubblers were housed in a water bath maintained at 316 K and this enabled $> 95\%$ RH at ambient temperature to be generated. The bubbler reservoirs were made from aluminium containers internally coated with an epoxy based lacquer to prevent dissolution of the aluminium walls into the water. These containers were subjected to a static hydraulic pressure test to 2.01 bar on one of the units before use to ensure their suitability for pressurised operation.

SYSTEM EVALUATION

Experimental procedure

To assess the performance of the humidity generator its outlet was connected to a Vaisala HM132 humidity and temperature sensor (RS Components, Corby) using a simple nylon test cell. The internal volume of this cell was minimised so that short term fluctuations in the stability of the generator could be precisely recorded. The sensor was calibrated prior to these tests in accordance with the manufacturer's instructions, using a series of saturated salt solutions.

The performance of the system was then evaluated with respect to the reproducibility of operation and the stability of the test atmospheres generated.

Reproducibility study

The precision with which the unit could be set to generate a fixed humidity atmosphere in the absence of any external monitoring was determined. A series of set points at regular intervals across the humidity generator operating range was selected. The relative humidity of the test atmosphere produced at each of the set points was subsequently recorded, along with its temperature. At the end of the test the whole system

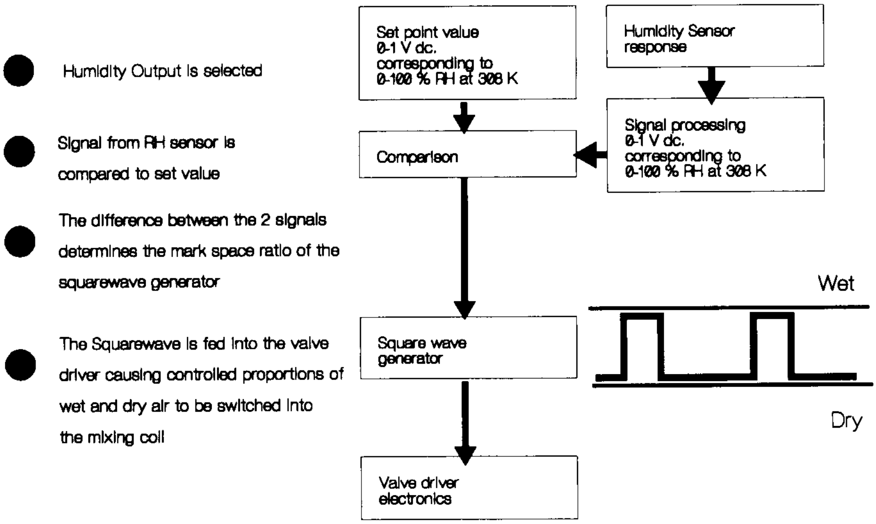

Fig. 2. Schematic diagram of the humidity control electronics.

was shut down. The test was then repeated a further eight times.

Data from the relative humidity meter were obtained at ambient temperature, which varied between 296.0 K and 298.3 K during these trials. In order to assess the performance of the system these data were converted to mole fractions of water vapour in air and hence to mass per unit volume concentration of water in air, [H_2O].

The RH of an atmosphere at a specified temperature T is:

$$\mathrm{RH}_T = 100\frac{P_{\mathrm{H_2O}}}{\mathrm{SVP}_T} \qquad (1)$$

where $P_{\mathrm{H_2O}}$ is the partial pressure in mmHg of the water vapour in the atmosphere and SVP_T is the saturated vapour pressure of water at temperature T.

Hence the mole fraction $X_{\mathrm{H_2O}}$ of water in a test atmosphere at 760 mmHg may be approximated by the expression:

$$X_{\mathrm{H_2O}} \approx \left[\frac{\mathrm{SVP}_T}{100\mathrm{RH}_T}\right]\left[760 - \frac{\mathrm{SVP}_T}{100\mathrm{RH}_T}\right]^{-1} \qquad (2)$$

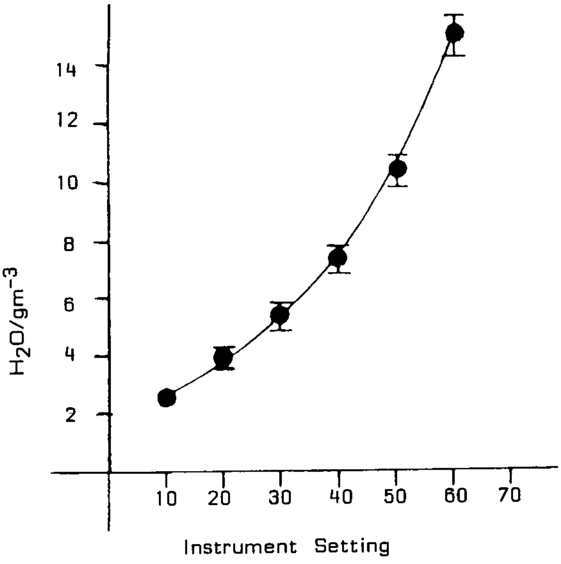

Fig. 3. Reproducibility study. 99% confidence limits marked.

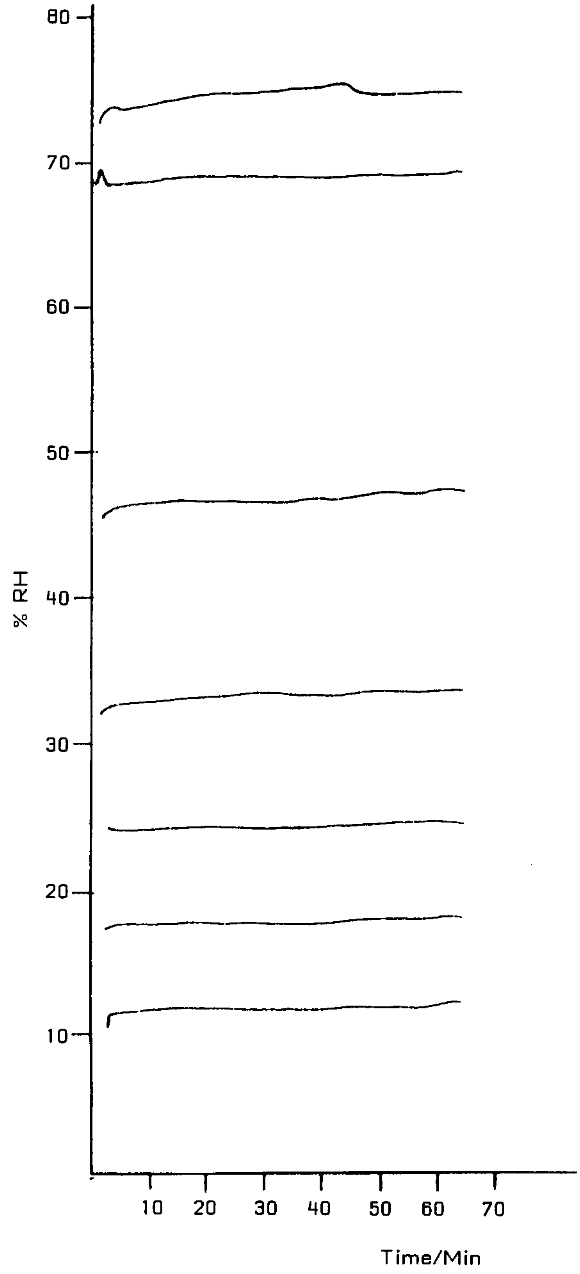

Fig. 4. Stability study showing the stability of the %RH at 308 K of 7 test atmospheres in the range 10–75% RH at 308 K over a test period of 1 h at a flow of $\mathrm{dm^3\ min^{-1}}$.

The mass of water $M_{\mathrm{H_2O}}$ in 1 m^3 of air at 25°C at 760 mmHg may be estimated by:

$$M_{\mathrm{H_2O}} \approx X_{\mathrm{H_2O}}\left(\frac{m_{\mathrm{H_2O}}}{V_{\mathrm{m}}}\right) \qquad (3)$$

The molar mass of water m_{H_2O} is 18 g and the molar volume V_m, is approximately 0.024 m^3 at 25°C, 760 mmHg pressure.
Hence:

$$[H_2O] \approx 750 X_{H_2O} \quad (4)$$

In these tests the errors caused by slight fluctuations in temperature away from 298 K and variations in pressure about 760 mmHg were calculated to be in the range 1–5% of the calculated concentration, and the data obtained are presented in Fig. 3. The 99% confidence limits are shown in Fig. 3 and these indicate that the humidity generator could be set to within ±10% of the set point value.

Stability study

Seven tests were conducted to assess the stability of the generator under normal operating conditions. In each study the outlet flow was set at 1 dm^3 min^{-1}, and a humidity valve set, ranging between 10 and 75% RH at 308 K. The humidity of the outlet flow was then continuously monitored for 1 h, a typical sensor test cycle time.

The results of this trial are given in Fig. 4, where it can be seen that the water concentrations of the test atmospheres were maintained to a stability of ±0.5% RH at 308 K.

Further tests were undertaken to establish the speed at which stable RH generation was achieved when the instrument setting was changed. These investigations revealed that instantaneous changes of greater than ±10% RH at 308 K required a period of approximately 2 min before the humidity stability was recovered.

Further instability was observed when the unit was first switched on and the generator was heating up to its operating temperature. Under normal operating conditions the unit required 90 min to stabilise to its operating temperature and any test atmosphere produced in this period was not stable in respect of its RH.

The lifetime of the unit is dependent on the valve used. With the valves specified above, the generator has an expected service interval of 400 h of continuous operation.

The system described enables precise and stable dynamic humid atmospheres to be generated at low cost. This means that chemical sensing systems, sampling techniques and atmospheric monitoring methods for the determination of low levels of toxic gases may now be evaluated and calibrated in the laboratory under conditions that are closely tailored to their eventual operating environment. Furthermore, its use may be further extended through the use of computer control to enable accurate temperature and humidity programming of test atmospheres to be achieved. This would allow aspects of climatic cycles and weather patterns to be physically reproduced in the laboratory. The development of such a system would be an obvious continuation of this work.

The authors gratefully acknowledge the support given to A.R.M. Przybylko by the SERC and Chelsea Instruments Ltd. through the Total Technology Award Scheme. Our work in this area is also supported by the Procurement Executive, Ministry of Defence, UK.

REFERENCES

1 K.M. Ganzer and R. Rebenfeld, Am. Lab., 19 (1987) 40.
2 P.R. Fielden and G.M. Greenway, Anal. Chem., 61 (1989) 1993.
3 I. Harvey, G. Coles and J. Watson, Sensors Actuators, 16 (1989) 393.
4 P. Horowitz and W. Hill, The Art of Electronics, Cambridge University Press, London, 1987.

Hyphenated Techniques in Supercritical Fluid Chromatography and Extraction

edited by **K. Jinno,** Toyohashi University of Technology, Toyohashi, Japan

Journal of Chromatography Library Volume 53

This is the first book to focus on the latest developments in hyphenated techniques using supercritical fluids. The advantages of SFC in hyphenation with various detection modes, such as, FTIR, MS, MPD and ICP and others are clearly featured throughout the book. Special attention is paid to coupling of SFE with GC or SFC.

In this edited volume, chapters are written by leading experts in the field. The book will be of interest to professionals in academia, as well as to those researchers working in an industrial environment, such as analytical instrumentation, pharmaceuticals, agriculture, food, petrochemicals and environmental.

Contents:

1. General Detection Problems in SFC *(H.H. Hill, D.A. Atkinson).*
2. Fourier Transform Ion Mobility Spectrometry for Detection after SFC *(H.H. Hill, E.E. Tarver).*
3. Advances in Capillary SFC-MS *(J.D. Pinkston, D.J. Bowling).*
4. Advances in Semi Micro Packed Column SFC and Its Hyphenation *(M. Takeuchi, T. Saito).*
5. Flow Cell SFC-FT-IR *(L.T. Taylor, E.M. Calvey).*
6. SFC-FT-IR Measurements Involving Elimination of the Mobile Phase *(P.R. Griffiths et al.).*
7. Practical Applications of SFC-FTIR *(K.D. Bartle et al.).*
8. Recycle Supercritical Fluid Chromatography - On-line Photodiode-Array Multiwavelength UV/VIS Spectrometry/IR Spectrometry/Gas Chromatography *(M. Saito, Y. Yamauchi).*
9. Inductively Coupled Plasma Atomic Emission Spectrometric Detection in Supercritical Fluid Chromatography *(K. Jinno).*
10. Microwave Plasma Detection SFC *(D.R. Luffer, M.V. Novotny).*
11. Multidimensional SFE and SFC *(J.M. Levy, M. Ashraf-Khorassani).*
12. Advances in Supercritical Fluid Extraction (SFE) *(S.B. Hawthorne et al.).*
13. Introduction of Directly Coupled SFE/GC Analysis *(T. Maeda, T. Hobo).*
14. SFE, SFE/GC and SFE/SFC: Instrumentation and Applications *(M.-L. Riekkola et al.).*
15. Computer Enhanced Hyphenation in Chromatography - Present and Future *(E.R. Baumeister, C.L. Wilkins).*

Subject Index.

1992 x + 334 pages
Price: US $ 157.00/ Dfl. 275.00
ISBN 0-444-88794-6

ELSEVIER
SCIENCE PUBLISHERS

ORDER INFORMATION
For USA and Canada
ELSEVIER SCIENCE PUBLISHERS
Judy Weislogel
P.O. Box 945
Madison Square Station,
New York, NY 10160-0757
Tel: (212) 989 5800
Fax: (212) 633 3880

In all other countries
ELSEVIER SCIENCE PUBLISHERS
P.O. Box 211
1000 AE Amsterdam
The Netherlands
Tel: (+31-20) 5803 753
Fax: (+31-20) 5803 705

US$ prices are valid only for the USA & Canada and are subject to exchange fluctuations; in all other countries the Dutch guilder price (Dfl.), is definitive. Books are sent postfree if prepaid.

711/414\141\0001-00

Data Handling in Science and Technology Volume 8

Design and Optimization in Organic Synthesis

by **R. Carlson**, Department of Organic Chemistry, Umeå University, Umeå, Sweden

This is the first general textbook on experimental design and optimization in organic synthesis. The book presents a unified methodology for carrying out systematic studies when the objective is to develop efficient and optimum synthetic methods. Strategies are included both for exploring the experimental conditions and for systematic studies of entire reaction systems (substrates, reagent(s) and solvents). The methodology is based on multivariate statistical techniques.

The following topics are treated in depth: classical two-level designs for screening experiments, gradient methods (steepest ascent, simplex methods) as well as response surface techniques for optimization, principal components analysis and PLS modelling.

The book is intended as a hands-on text for chemists and engineers engaged in developing synthetic methods in industrial research, e.g. in fine chemicals and pharmaceuticals production, as well as for advanced undergraduate students, graduate students, and researchers in an academic environment.

Contents:
1. Introduction: Strategies on different levels in organic synthesis. 2. Experimental study of reaction conditions. Initial remarks. 3. Models as tools. 4. General outline for screening experiments. 5. Two-level factorial designs. 6. Two-level fractional factorial design. 7. Other designs for screening experiments. 8. Summary of screening experiments. 9. Introduction to optimization. 10. Steepest ascent. 11. Simplex methods. 12. Response surface methods. 13. Summary of strategies to explore the experimental space. 14. The reaction space. 15. Principal properties. 16. Strategies for the selection of test systems. 17. Quantitative relations between observed responses and experimental variations. 18. A method for determining a suitable order of introducing reagents in "one-pot" procedures. 19. Concluding remarks. Appendices. Index.

1992 xvi + 536 pages

Price: US $ 169.00 / Dfl. 330.00

ISBN 0-444-89201-X

Elsevier Science Publishers

P.O. Box 211, 1000 AE Amsterdam, The Netherlands
P.O. Box 882, Madison Square Station, New York, NY 10159, USA

PUBLICATION SCHEDULE FOR 1993

	S'92	O'92	N'92	D'92	J	F	M	A	M	J	J	A
Analytica Chimica Acta	267/1 267/2	268/1 268/2	269/1 269/2	270/1 270/2	271/1 271/2	272/1 272/2 273/1-2	274/1 274/2	275/1-2 276/1	276/2 277/1	277/2 278/1 278/2	279/1 279/2	280/1 280/2
Vibrational Spectroscopy		4/1			4/2		4/3					

INFORMATION FOR AUTHORS

Manuscripts. The language of the journal is English. English linguistic improvement is provided as part of the normal editorial processing. Authors should submit three copies of the manuscript in clear double-spaced typing on one side of the paper only. *Vibrational Spectroscopy* also accepts papers in English only.

Abstract. All papers and reviews begin with an Abstract (50–250 words) which should comprise a factual account of the contents of the paper, with emphasis on new information.

Figures. Figures should be prepared in black waterproof drawing ink on drawing or tracing paper of the same size as that on which the manuscript is typed. One original (or sharp glossy print) and two photostat (or other) copies are required. Attention should be given to line thickness, lettering (which should be kept to a minimum) and spacing on axes of graphs, to ensure suitability for reduction in size on printing. Axes of a graph should be clearly labelled, along the axes, outside the graph itself. All figures should be numbered with Arabic numerals, and require descriptive legends which should be typed on a separate sheet of paper. Simple straight-line graphs are not acceptable, because they can readily be described in the text by means of an equation or a sentence. Claims of linearity should be supported by regression data that include slope, intercept, standard deviations of the slope and intercept, standard error and the number of data points; correlation coefficients are optional.

Photographs should be glossy prints and be as rich in contrast as possible; colour photographs cannot be accepted. Line diagrams are generally preferred to photographs of equipment.

Computer outputs for reproduction as figures must be good quality on blank paper, and should preferably be submitted as glossy prints.

Nomenclature, abbreviations and symbols. In general, the recommendations of the International Union of Pure and Applied Chemistry (IUPAC) should be followed, and attention should be given to the recommendations of the Analytical Chemistry Division in the journal *Pure and Applied Chemistry* (see also *IUPAC Compendium of Analytical Nomenclature, Definitive Rules*, 1987).

References. The references should be collected at the end of the paper, numbered in the order of their appearance in the text (*not* alphabetically) and typed on a separate sheet.

Reprints. Fifty reprints will be supplied free of charge. Additional reprints (minimum 100) can be ordered. An order form containing price quotations will be sent to the authors together with the proofs of their article.

Papers dealing with vibrational spectroscopy should be sent to: Dr J.G. Grasselli, 150 Greentree Road, Chagrin Falls, OH 44022, U.S.A. Telefax: (+1-216) 2473360 (Americas, Canada, Australia and New Zealand) or Dr J.H. van der Maas, Department of Analytical Molecule Spectrometry, Faculty of Chemistry, University of Utrecht, P.O. Box 80083, 3508 TB Utrecht, The Netherlands. Telefax: (+31-30) 518219 (all other countries).

0003-2670/93/$06.00

This issue is printed on acid-free paper.

PRINTED IN THE NETHERLANDS

CATALOGUE 1993 ON CD-ROM

Elsevier Science Publishers - the world's largest scientific publisher - presents for the first time details of all its publications on CD-ROM

ADVANTAGES

- ➢ Easy to use.
- ➢ Get more comprehensive information than ever before.
- ➢ Make fast and effective searches.
- ➢ Find what you want even with incomplete information.
- ➢ Compile special lists of products without typing.
- ➢ Improve your control of scientific product information.
- ➢ Enhance service to clients.

PRODUCT DESCRIPTION

The CD-ROM contains descriptions of all Elsevier products.

- ➢ All the journals, with complete information about journal editors and editorial boards
- ➢ Listings of recently published papers for many journals
- ➢ Complete descriptions and contents lists of book titles
- ➢ Independent reviews of published books
- ➢ Forthcoming title information
- ➢ Book series
- ➢ All other products, e.g. software, CDs, dictionaries, wallcharts.

In addition, the CD-ROM features easy-to-use search tools, making the information accessible and useful. For example, searches can be made by subject area, by year of publication, by author/editor or title and by "free text" search.

Full book and journal information can be printed to initiate your order.

If you do not find what you need, or wish to know more about Elsevier's publishing programme, the CD-ROM can supply you with the name, address and fax number of the correct person to contact.

AUDIENCE

Librarians, booksellers, researchers, agents and information specialists.

SYSTEM REQUIREMENTS

The CD-ROM has been designed to run under Microsoft® Windows™ 3.0, on IBM PC-ATs and compatibles. The CD-ROM is Microsoft® Windows™ 3.1 compatible.

The minimum requirements are:

- ➢ IBM or IBM-compatible PC with a 80286 or higher processor
- ➢ 2 MB or more RAM
- ➢ MS-DOS® 3.3 or higher installed
- ➢ Microsoft® Windows™ 3.0 (or 3.1) installed
- ➢ Microsoft® Windows™ compatible mouse or other pointing device
- ➢ VGA graphics adapter (colour or monochrome)
- ➢ Hard disk with at least 2 MB free disk space
- ➢ CD-ROM drive which is accessible from Microsoft® Windows™
- ➢ For faster operation a 80386SX or higher processor is recommended, as well as a fast CD-ROM drive (access time less than 0.4 seconds).

The CD-ROM can be installed in a local area network.

For further information please contact

ELSEVIER SCIENCE PUBLISHERS
Attn. Vivian Wong Swie San
Marketing Services Department
P.O. Box 211
1000 AE Amsterdam
The Netherlands
FAX: (020) 5862 425

In the USA & Canada
Journal Information Center
P.O. Box 882
Madison Square Station
New York, NY 10159, USA
FAX: (212) 633 3764

ELSEVIER
SCIENCE PUBLISHERS

711/414\141\0001-00

0003-2670(19930301)274:1;1-M

23 มีค. ๓๖

24 [illegible].ค. ๓[illegible]